

Abstract

Title of dissertation: Neutral Gas Outflows and Inflows in Local AGN & High- z Lyman- α Emitters in COSMOS

Hannah Bowen Krug, Doctor of Philosophy, 2013

Dissertation directed by: Professor Sylvain Veilleux
Department of Astronomy

This thesis is composed of two parts: (1) a search for neutral gas outflows and inflows in local active galactic nuclei (AGN) and ultraluminous infrared galaxies (ULIRGs), and (2) a deep and wide imaging search for high-redshift Lyman- α emitters (LAEs). In the first part, we utilize the R-C spectrograph on the Mayall 4m telescope at Kitt Peak National Observatory (KPNO) to look for Na I D absorption. Galactic outflows are thought to play a major role in galactic feedback and evolution, and previous studies of neutral gas have shown that galactic winds occur in most galaxies with high infrared (IR) luminosities. However, in composite systems where a starburst coexists with an active galactic nucleus (AGN), it is unclear whether the starburst or the AGN is driving the outflows. This thesis attempts to answer that question by looking at samples of Seyfert galaxies, Palomar-Green quasistellar objects (PG QSOs), and ULIRGs.

We first describe the results from a search for Na I D outflows in 35 IR-faint Seyferts. We find that the outflow detection rates for IR-faint Seyferts are substantially lower than those of IR-luminous Seyferts. The outflow kinematics of Seyfert 2s resemble those of starburst galaxies, while the outflow velocities in Seyfert 1s are significantly larger. Taken together, these results suggest that the AGN does not play a significant role in driving the outflows in most Seyferts, except the high-velocity outflows seen in Seyfert 1s. We also find high rates of detection of inflows in IR-faint Seyferts.

We then perform the same analysis on a sample of 28 PG QSOs and 10 ULIRGs; this sample was taken from a survey of gas-rich mergers. When we combine our data with our Seyfert study results, as well as previous work, we note three important trends. We find that outflows in IR-luminous AGN and IR-luminous starbursts appear to be driven by fundamentally different processes, the AGN and star formation, respectively. We find the same distinction for outflows in AGN with optical spectral types of Type 1 (AGN) and Type 2 (star formation). We note fundamental differences between outflows in objects which have already undergone mergers versus those which have not.

In the second part of this thesis, we search for $z = 7.7$ LAEs in the COSMOS field. These objects are useful probes of the epoch of reionization, as the Ly α line should be attenuated by the intergalactic medium (IGM) at low to moderate neutral hydrogen fractions (x_{HI}). We have utilized two ultra-narrowband filters on the NEWFIRM camera in order to isolate LAEs at $z = 7.7$. We find 5σ detections of four candidate LAEs in a survey volume of $2.8 \times 10^4 \text{ Mpc}^3$. Using these results to construct a Ly α luminosity function (LF) and comparing to previously established LFs at $z = 5.7$ and $z = 6.5$, we find no conclusive evidence for evolution of x_{HI} over $5.7 < z < 7.7$.

Finally, we use a combination of imaging and spectroscopy to follow up those results, noting that, while imaging can rule out a candidate from being considered a high-redshift LAE, only spectroscopy can confirm that a target is indeed at $z = 7.7$. Imaging follow-up has essentially ruled out one candidate. We then perform spectroscopic follow-up with GNIRS on the Gemini-North telescope on our second-brightest candidate. We fail to detect that candidate after 2.5 hours of integration; spectroscopic follow-up performed by collaborators on our two brightest candidates also yielded non-detections. We are thus left with only one viable $z = 7.7$ candidate. Such null results are consistent with other attempts detailed in the literature, implying that reionization is still ongoing.

**Neutral Gas Outflows and Inflows in Local AGN & High- z
Lyman- α Emitters in COSMOS**

by

Hannah Bowen Krug

Dissertation submitted to the Faculty of the Graduate School of the
University of Maryland, College Park in partial fulfillment
of the requirements for the degree of
Doctor of Philosophy
2013

Advisory Committee:
Professor Sylvain Veilleux, Chair
Professor Stuart Vogel
Professor Alberto Bolatto
Professor Stacy McGaugh
Professor Robert Hudson

© Copyright by
Hannah Bowen Krug
2013

Preface

Much of this work has either been previously published or has been presented at conferences across the world.

Chapter 2 was published in *The Astrophysical Journal*, Volume 708, Issue 2, pp. 1145-1161 (2010), under the title *Neutral Gas Outflows and Inflows in Infrared-faint Seyfert Galaxies* (Hannah B. Krug, David S.N. Rupke, & Sylvain Veilleux). Additionally, this work was presented with a poster of the same title at the *Assembly, Gas Content, and Star Formation History of Galaxies* meeting at NRAO headquarters in Charlottesville, VA, in September 2009, as well as at the AAS Winter Meeting in Washington, D.C., in January, 2010.

Chapter 4 was published in *The Astrophysical Journal*, Volume 745, Issue 2, pp. 122-131 (2012), under the title *Searching for $z \sim 7.7$ Ly α Emitters in the COSMOS Field with NEWFIRM* (Hannah B. Krug, Sylvain Veilleux, V. Tilvi, S. Malhotra, J. Rhoads, P. Hibon, R. Swaters, R. Probst, A. Dey, M. Dickinson, & B.T. Jannuzi). This work was also presented as a poster of the same title in July, 2011 at the *New Horizons for High Redshifts* meeting in Cambridge, U.K. Talks entitled *Searching for High-Redshift Ly α Emitters in the COSMOS Field with NEWFIRM* were presented in June, 2011 at the COSMOS Annual Team Meeting in Zurich, Switzerland, and at the AAS Winter Meeting in Austin, TX, in January 2012.

Chapter 3 is in preparation for submission to *The Astrophysical Journal* (Hannah B. Krug, Sylvain Veilleux, Margaret Trippe, Marcio Meléndez, and David S. N. Rupke).

Dedication

For my parents, Mary & Warren Krug.

Acknowledgments

There are a number of people who have greatly supported me throughout these past six years, without whom I probably would not have made it this far. First and foremost, I'd like to thank my advisor, Dr. Sylvain Veilleux. Sylvain has supported me through every step of this process, including sending me on observing runs as early as my first year, as well as trusting me to give a talk in his stead (and my first professional talk, no less!) at an international meeting. He has been particularly supportive of my choice to go into teaching, which I appreciate more than I can say. I have learned so much from him and loved working on these projects, and am very glad that I asked to work with him way back on my UMD visit in 2007. I am also grateful to his fish for not dying during my many extended periods of house-sitting, plant-watering, and fish-feeding.

I would also like to thank the rest of my committee, Dr. Stuart Vogel, Dr. Alberto "El Supremo" Bolatto, and Dr. Stacy McGaugh. Stuart has not only been a great scientific mentor, he has also been an incredible department chair, supporting the graduate students in every possible way, and he went above and beyond in assisting me during my job search. Alberto was a phenomenal teacher, making ISM the most entertaining and enlightening two and a half hours of my week back in second year, and is definitely one of my favorite people in the department. Stacy was also an excellent teacher as well as a great person to TA for, giving us the freedom to be creative with our teaching and helping me start to realize that this was a career I might want. I would like to express my appreciation for the support of two

other members of the department faculty: Dr. Cole Miller and Ms. Grace Deming. Cole was my first contact in the department (having admitted me!) and has always been someone to whom I felt like I could go for help with any problem, be it related to astronomy, personal issues, or sports trivia, despite the fact that he has always humbled me on the basketball court. Grace gave me the opportunity to teach in my fifth year that led directly to my realization that I wanted to spend my life in education, and I cannot thank her enough for that. I also owe a debt of gratitude to former Maryland graduate student / postdoc Dr. David Rupke, who developed the methods used in two of my chapters and who helped guide me through my second year project.

There are a number of other friends that I would like to thank, both in and out of the department. I would like to thank my three best external friends, Julie, Emily, and Saheli, for keeping me sane throughout these last several years and reminding me that there is life outside of astronomy. Department-wise, Lisa Wei has always been my sounding board and partner in chicken-consumption-related crime, Jithin “J-Dawg” George was an excellent roommate and is an even better friend, Mike “Mickey D” McDonald has more astronomy knowledge than any peer I’ve ever met and is always willing to share it, and Alex McCormick has always provided me with the outlet I’ve needed for discussing and watching sports. Other astronomy folks that I’d like to thank for being great friends and supporters are my fellow former Poobahs, Matthew and Mike K., new Poobah Taro, Stacy, Ashley, Katie P., Megan, Che-Yu, Katie J., Kory, Kim, and my fellow front-row sitting Astro 101 TAs: Gabriele, Vicki, and Krista.

I would be remiss if I failed to thank the group of people without whom I would have no competitive outlet, my winter nights would be empty, and my office walls would be bare: the Maryland men's basketball team. Anyone who knows me knows that going to Terps games has been my absolute favorite pastime of the last six years, and watching them has kept me going through many a period of scientific frustrations. In particular, getting to watch Greivis Vasquez play in person for three years got me through many tough times and inspired me to always strive for better.

Finally, the most important section of these acknowledgments, the people who have been there for me through it all: my family. My parents have supported me since day one, instilling me with a love for learning and general edification that has never left me. They put me through Yale without hesitation and have always encouraged me in every endeavor. I would be nowhere without the love and support they have given me. I would also like to thank my brother Andrew for being my role model growing up and for always pushing me to think deeply and critically. His telling me that I should go to Yale is what put me on this path and led me back to my childhood love of astronomy. And last, but most certainly not least, I have to thank Ashlee, my rock, the reason I was able to make it through these last two years, the reason I will make it through all the years to come. I could not have done this without you.

Table of Contents

| | |
|--|-----------|
| List of Tables | x |
| List of Figures | xi |
| List of Abbreviations | xiii |
| 1 Introduction | 1 |
| 1.1 Active Galactic Nuclei | 1 |
| 1.1.1 Seyferts | 4 |
| 1.1.2 PG QSOs | 6 |
| 1.2 ULIRGs & LIRGs | 8 |
| 1.3 Galactic Mergers | 10 |
| 1.4 Galactic Outflows & Feedback | 13 |
| 1.5 The High-Redshift Universe | 16 |
| 1.5.1 Reionization | 19 |
| 1.5.2 Lyman- α Emitters | 22 |
| 1.5.3 Cosmological Evolution Survey | 23 |
| 1.6 Observatories & Instruments Used in this Thesis | 24 |
| 1.6.1 Kitt Peak National Observatory Mayall 4-meter Telescope | 24 |
| 1.6.1.1 Ritchey-Chrétien Spectrograph | 24 |
| 1.6.1.2 NEWFIRM | 25 |
| 1.6.2 Gemini Observatory | 26 |
| 1.6.2.1 GNIRS | 26 |
| 1.6.3 Infrared Astronomical Satellite and Infrared Space Observatory | 27 |
| 1.6.4 Subaru Telescope | 28 |
| 1.6.5 United Kingdom Infrared Telescope | 29 |
| 1.6.6 Canada France Hawaii Telescope | 29 |
| 1.6.7 Hubble Space Telescope | 30 |
| 1.6.7.1 Advanced Camera for Surveys | 31 |
| 1.6.8 UltraVISTA | 31 |
| 1.7 Outline of Thesis | 32 |
| 2 Neutral Gas Outflows and Inflows in Infrared-Faint Seyfert Galaxies | 37 |
| 2.1 Introduction | 37 |
| 2.2 Sample | 40 |
| 2.2.1 Redshifts | 41 |
| 2.2.2 Star Formation Rates | 41 |
| 2.2.3 Spectral Types | 42 |
| 2.3 OBSERVATIONS | 42 |
| 2.4 ANALYSIS | 43 |
| 2.4.1 Line Fitting | 43 |
| 2.4.2 Velocities | 48 |
| 2.4.3 Column Densities | 50 |

| | | |
|---------|--|-----|
| 2.4.4 | Stellar Na I D Contribution | 51 |
| 2.5 | RESULTS: OUTFLOWS | 52 |
| 2.5.1 | Seyfert 2 | 52 |
| 2.5.2 | Seyfert 1 | 58 |
| 2.6 | RESULTS: INFLOWS | 63 |
| 2.6.1 | Seyfert 2 | 63 |
| 2.6.2 | Seyfert 1 | 64 |
| 2.7 | DISCUSSION | 64 |
| 2.7.1 | Outflows | 64 |
| 2.7.1.1 | Comparison with Previous Studies | 64 |
| 2.7.1.2 | Outflow Dynamics | 70 |
| 2.7.2 | Inflows | 76 |
| 2.7.2.1 | Comparison with Previous Studies | 76 |
| 2.7.2.2 | Search for Connection between Inflows and Nuclear Structures | 77 |
| 2.7.2.3 | Inflow Dynamics | 80 |
| 2.8 | SUMMARY | 82 |
| 3 | Neutral Gas Outflows and Inflows in PG QSOs and ULIRGs | 95 |
| 3.1 | INTRODUCTION | 95 |
| 3.2 | SAMPLE | 99 |
| 3.2.1 | Redshifts | 100 |
| 3.2.2 | Far-Infrared Luminosities and Star Formation Rates | 101 |
| 3.2.3 | Bolometric and AGN Luminosities | 102 |
| 3.2.4 | Spectral Types | 103 |
| 3.2.5 | Interaction Classes | 104 |
| 3.3 | OBSERVATIONS | 105 |
| 3.4 | ANALYSIS | 106 |
| 3.4.1 | Line Fitting | 106 |
| 3.4.2 | Velocities | 129 |
| 3.4.3 | Column Densities | 132 |
| 3.4.4 | Stellar Na I D Contribution | 132 |
| 3.5 | RESULTS AND DISCUSSION: OUTFLOWS | 135 |
| 3.5.1 | Detection Rates | 135 |
| 3.5.2 | Kinematics | 140 |
| 3.5.3 | Dynamics | 150 |
| 3.6 | RESULTS AND DISCUSSION: INFLOWS | 160 |
| 3.6.1 | Detection Rates | 160 |
| 3.6.2 | Kinematics | 163 |
| 3.6.3 | Dynamics | 165 |
| 3.7 | SUMMARY | 167 |

| | | |
|-------|--|-----|
| 4 | Searching for $z=7.7$ Ly α -Emitters in the COSMOS Field with NEWFIRM | 189 |
| 4.1 | INTRODUCTION | 189 |
| 4.2 | OBSERVATIONS AND DATA | 194 |
| 4.2.1 | Observations with NEWFIRM | 194 |
| 4.2.2 | Data Reduction | 196 |
| 4.2.3 | Photometric Calibration | 198 |
| 4.2.4 | Limiting Magnitude | 199 |
| 4.3 | CANDIDATE Ly α EMITTERS | 200 |
| 4.3.1 | Selection Criteria | 200 |
| 4.3.2 | Results | 203 |
| 4.3.3 | Ly α Equivalent Widths | 205 |
| 4.4 | POSSIBLE SAMPLE CONTAMINATION | 208 |
| 4.4.1 | Foreground Emission Line Sources | 208 |
| 4.4.2 | Other Possible Contaminants | 211 |
| 4.5 | MONTE CARLO SIMULATIONS | 213 |
| 4.6 | $z = 7.7$ Ly α LUMINOSITY FUNCTION | 216 |
| 4.7 | SUMMARY | 220 |
| 5 | $z=7.7$ Ly α Emitter Candidates: Imaging and Spectroscopic Follow-up | 225 |
| 5.1 | INTRODUCTION | 225 |
| 5.2 | IMAGING FOLLOW-UP | 227 |
| 5.2.1 | <i>Hubble</i> ACS <i>I</i> -Band Data | 227 |
| 5.2.2 | CFHT <i>H</i> -Band Data | 228 |
| 5.2.3 | UltraVISTA <i>Y</i> -, <i>J</i> -, <i>H</i> -, and <i>K</i> -Band Data | 229 |
| 5.3 | SPECTROSCOPIC FOLLOW-UP | 230 |
| 5.3.1 | Gemini GNIRS Spectroscopy | 230 |
| 5.3.2 | Additional Spectroscopic Follow-up | 235 |
| 5.4 | DISCUSSION | 236 |
| 5.5 | SUMMARY | 239 |
| 6 | Summary | 241 |
| 6.1 | OBJECTIVES | 241 |
| 6.2 | RESULTS | 244 |
| | Bibliography | 249 |

List of Tables

| | | |
|------|---|-----|
| 2.1 | Galaxy properties and observing logs: Seyfert 2s | 84 |
| 2.2 | Galaxy properties and observing logs: Seyfert 1s | 85 |
| 2.3 | Properties of individual velocity components: Seyfert 2s | 86 |
| 2.4 | Properties of individual velocity components: Seyfert 1s | 87 |
| 2.5 | Outflow: individual objects (Seyfert 1s and 2s) | 88 |
| 2.6 | Outflow: average properties | 89 |
| 2.7 | Inflow: individual objects | 90 |
| 2.8 | Inflow: average properties | 91 |
| 2.9 | Statistical comparisons of kinematic parameters: IR-faint and IR-luminous Seyfert galaxies. | 92 |
| 2.10 | Statistical comparisons of kinematic parameters: all galaxies. | 93 |
| 2.11 | Statistical comparisons of kinematic parameters: galaxies with outflows | 94 |
| 2.12 | Statistical comparisons of kinematic parameters: Seyfert 1s vs Seyfert 2s with inflows | 94 |
| | | |
| 3.1 | Galaxy properties | 171 |
| 3.2 | Observing logs | 173 |
| 3.3 | Properties of individual velocity components (fit 1) | 175 |
| 3.4 | H α fit parameters | 176 |
| 3.5 | He I fit parameters | 178 |
| 3.6 | Outflow: individual objects | 183 |
| 3.7 | Outflow: average properties | 184 |
| 3.8 | Outflow: average properties (combined sample) | 185 |
| 3.9 | Inflow: individual objects | 186 |
| 3.10 | Inflow: average properties (combined sample) | 187 |
| 3.11 | Statistical comparisons of kinematic parameters (combined sample) . | 188 |
| | | |
| 4.1 | Comparison to previous high- z searches | 223 |
| 4.2 | Properties of four candidate Ly α emitters | 224 |

List of Figures

| | | |
|------|---|-----|
| 1.1 | Unified model of AGN | 2 |
| 1.2 | Comparison of Seyfert 1 and Seyfert 2 spectra | 6 |
| 1.3 | Numerical simulations of merging galaxies | 12 |
| 1.4 | Numerical simulations of galactic wind | 14 |
| 1.5 | Numerical simulations of star formation in the early universe | 18 |
| 1.6 | Illustration of the reionization of hydrogen in the IGM | 21 |
| 1.7 | NEWFIRM field of view compared with Gemini fields of view | 25 |
| 1.8 | A typical raw image of a faint galaxy taken in cross-dispersed mode with GNIRS | 27 |
| | | |
| 2.1 | Deblended He I and Na I D complex examples. | 46 |
| 2.2 | Reduced χ^2 comparison for free- and fixed-parameter fits: Seyfert 1s and 2s | 47 |
| 2.3 | Δv comparison for free- and fixed-parameter fits: Seyfert 1s and 2s . | 49 |
| 2.4 | Comparing stellar population synthesis models to fits: Seyfert 1s and 2s | 53 |
| 2.5 | Seyfert 2 galaxy spectra | 54 |
| 2.6 | BELA plots: Seyfert 1s and 2s | 59 |
| 2.7 | Seyfert 1 galaxy spectra | 60 |
| 2.8 | Outflow detection histogram: Seyfert 1s and 2s | 66 |
| 2.9 | Velocity component histograms: Seyfert 1s and 2s | 68 |
| 2.10 | Outflow velocity versus circular velocity and L_{FIR} : Seyfert 1s and 2s . | 71 |
| 2.11 | Mass outflow rate versus circular velocity and L_{FIR} : Seyfert 1s and 2s | 73 |
| 2.12 | Inflow velocity versus circular velocity and L_{FIR} : Seyfert 1s and 2s . . | 78 |
| | | |
| 3.1 | PG QSO spectra (fit 1) | 108 |
| 3.2 | ULIRG spectra (fit 1) | 112 |
| 3.3 | PG QSO $\text{H}\alpha$ spectra | 116 |
| 3.4 | ULIRG $\text{H}\alpha$ spectra | 120 |
| 3.5 | Fixed PG QSO spectra (fit 4) | 122 |
| 3.6 | Fixed ULIRG spectra (fit 4) | 126 |
| 3.7 | Reduced χ^2 comparison for free- and fixed-parameter fits: PG QSOs and ULIRGs | 130 |
| 3.8 | Δv comparison for free- and fixed-parameter fits: PG QSOs and ULIRGs | 131 |
| 3.9 | Comparing stellar population synthesis models to fits: PG QSOs and ULIRGs | 134 |
| 3.10 | Outflow detection percentages versus L_{FIR} (combined sample) | 139 |
| 3.11 | Outflow detection percentages per bin versus L_{AGN} (combined sample) | 141 |
| 3.12 | Velocity histogram (combined sample) | 144 |
| 3.13 | Outflow Δv_{max} plots (combined sample) | 146 |
| 3.14 | Δv_{max} versus L_{AGN} (combined sample) | 148 |
| 3.15 | Outflow dynamics vs L_{FIR} plots: far-IR luminosity grouping | 154 |

| | | |
|------|---|-----|
| 3.16 | Outflow dynamics vs v_{circ} plots: far-IR luminosity grouping | 155 |
| 3.17 | Outflow dynamics vs L_{FIR} plots: spectral type grouping | 156 |
| 3.18 | Outflow dynamics vs v_{circ} plots: spectral type grouping | 157 |
| 3.19 | Outflow dynamics vs L_{FIR} plots: interaction class grouping | 158 |
| 3.20 | Outflow dynamics vs v_{circ} plots: interaction class grouping | 159 |
| 3.21 | $\dot{p}/(L_{AGN}/c)$ vs Δv_{max} : IR-luminous starbursts and IR-luminous AGN | 161 |
| 3.22 | Inflow detection percentages versus L_{FIR} : far-IR luminosity grouping | 164 |
| 3.23 | Inflow Δv_{max} plots: far-IR luminosity grouping | 166 |
| 4.1 | NEWFIRM ultra-narrowband filter diagrams | 195 |
| 4.2 | Completeness calculations used to determine UNB filter limiting mag- nitudes | 200 |
| 4.3 | $z=7.7$ Ly α candidate image cutouts | 206 |
| 4.4 | Monte Carlo simulation results calculating expected Ly α sources . . . | 217 |
| 4.5 | $z=7.7$ Ly α luminosity function | 219 |
| 5.1 | 2.5 hour continuum subtracted GNIRS spectrum, candidate #2 . . . | 234 |

List of Abbreviations

| | |
|---------|---|
| A&A | Astronomy & Astrophysics |
| A&AS | Astronomy & Astrophysics Supplements |
| ACS | Advanced Camera for Surveys |
| AGN | Active Galactic Nucleus/Nuclei |
| AJ | The Astronomical Journal |
| ApJ | The Astrophysical Journal |
| ApJL | The Astrophysical Journal Letters |
| ApJS | The Astrophysical Journal Supplements |
| Ap&SS | Astrophysics & Space Science |
| ARA&A | Annual Review of Astronomy & Astrophysics |
| CASSIS | Cornell Atlas of Spitzer IRS Sources |
| CFHT | Canada France Hawaii Telescope |
| FIR | Far-infrared |
| GNIRS | Gemini Near-Infrared Spectrograph |
| HST | Hubble Space Telescope |
| IGM | Intergalactic Medium |
| IR | Infrared |
| IRAS | Infrared Astronomical Satellite |
| ISM | Interstellar Medium |
| ISO | Infrared Space Observatory |
| LAE | Lyman α Emitter |
| LIRGs | Luminous Infrared Galaxies |
| MmSAI | Memorie della Societa Astronomica Italiana |
| MNRAS | Monthly Notices of the Royal Astronomical Society |
| NED | NASA/IPAC Extragalactic Database |
| NEWFIRM | NOAO Extremely-Wide Field Infrared Mosaic Imager |
| NOAO | National Optical Astronomy Observatory |
| PASJ | Publications of the Astronomical Society of Japan |
| PASP | Publications of the Astronomical Society of the Pacific |
| PG QSOs | Palomar Green Quasi-Stellar Objects |
| QJRAS | Quarterly Journal of the Royal Astronomical Society |
| SDSS | Sloan Digital Sky Survey |
| SFR | Star Formation Rate |
| UKIRT | United Kingdom Infrared Telescope |
| ULIRGs | Ultraluminous Infrared Galaxies |

Chapter 1

Introduction

1.1 Active Galactic Nuclei

Active galactic nuclei, or AGN, are among the most energetic and interesting objects in the universe. They are particularly notable as they exhibit extremely high luminosities, yet often appear star-like, as all the energy comes from a very small region. To produce the energies and variabilities measured, complex physics is required. There are several different types of AGN (two will be described in the following sections and studied in this thesis), yet it is theorized that the same general mechanisms power all AGN, but the way we classify them depends on their orientation. This theory is known as the unified model. The groundwork for this model was laid out in Antonucci & Miller (1985), in which the authors determined that NGC 1068, a Seyfert 2 galaxy, resembled a Seyfert 1 galaxy when studied in polarized light (see Section 1.1.1 for descriptions of these two types), and thus proposed a physical model based on those similarities. This model was described in detail in two reviews by Antonucci (1993) and Urry & Padovani (1995), and will be summarized here; it will also be supplemented by Frank, King, & Raine (2002). Figure 1.1 shows an illustration of AGN structure in the unified model.

The principal power source is believed to be a supermassive black hole, located at the center of the AGN host. The extreme gravitational potential causes the

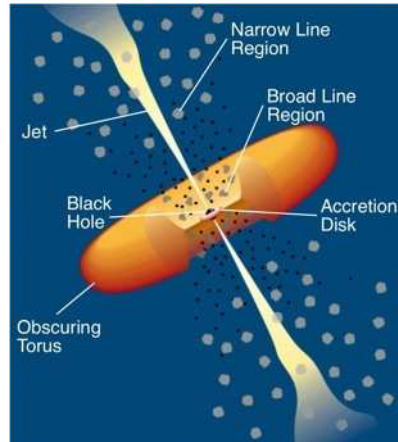


Figure 1.1: The generally held picture of the physical structure of the AGN in a unified model, adapted from Urry & Padovani (1995). A supermassive black hole is located in the center of the galaxy and is surrounded by an accretion disk. Broad emission lines measured in AGN spectra are produced by clouds in the broad line region, or potentially by the accretion disk. A thick, obscuring dust torus surrounds the accretion disk and broad line region and blocks those from view along certain lines of sight. Narrow lines are produced in clouds further from the black hole, in the narrow line region. Radio jets extend from the black hole, here pictured perpendicularly, though that is not always the case.

high AGN luminosity, as the supermassive black hole pulls matter toward it. An accretion disk forms as material is pulled toward the black hole and loses angular momentum. The accretion disk is typically visible in the ultraviolet regime, but can occasionally be observed in X-ray. The broad line region (BLR) is from whence observed broad emission lines in AGN spectra are produced, as clouds of gas are pulled by the gravitational potential of the black hole, thus broadening optical and ultraviolet line profiles. Surrounding the central black hole, the accretion disk, and the BLR is an obscuring torus of gas and dust. This torus blocks optical and ultraviolet light from being observed along lines of sight parallel to it. The narrow line (NLR) region exists in the area above the dust torus, where gas clouds are pulled by the gravitational potential but not to the same extent that clouds are in the BLR. Thus the clouds do not move as quickly as those in the BLR, but move enough to produce emission lines that are broader than those in ordinary galaxies. The emission lines are believed to be produced by photoionization of gas, arising from UV emission from the central supermassive black hole and accretion disk. Finally, jets emerge from the accretion disk, typically radio jets produced by synchrotron radiation which are relativistically beamed and collimated along the pole of the disk. In this picture, Type 1 AGN (including Seyfert 1s and QSOs, as described in the following section) are those observed via lines of sight along the jet and perpendicular to the torus, as these objects show broad emission lines (from the BLR) and bright continua (from the accretion disk). Type 2 AGN (including Seyfert 2s) are those observed via lines of sight along the torus and perpendicular to the jet, and thus have fainter continua and lack broad lines, as the accretion disk

and BLR are obscured by the torus. When viewed in polarized light, many Type 2 AGN reveal a hidden broad line region resembling those found in Type 1 AGN; this discovery gave rise to this model [Antonucci & Miller (1985), Antonucci (1993), Urry & Padovani (1995), Frank et al. (2002)]

1.1.1 Seyferts

The characterization of a Seyfert galaxy dates back to 1943, when Carl Seyfert found six galaxies with high excitation, broadened emission lines. He found that the widths of the lines tended to increase with absolute magnitude of the galaxy nucleus [Seyfert (1943)]. Markarian added roughly 700 galaxies to this sample starting in the late 1960s (e.g., Markarian (1967,69), Markarian et al. (1971)). The traditionally held definition of a Seyfert galaxy is two-fold. First, in terms of morphology, a Seyfert appears in observations to be a normal bright star, but one which is located inside a faint, nebulous envelope. The ratio of nucleus luminosity to galaxy luminosity is significantly higher than an ordinary galaxy, which shows gradual luminosity changes over its full extent [Weedman (1977)]. Second, in terms of spectroscopy, Seyferts must show strong, broad emission lines, as described in the original discovery paper [Seyfert (1943)]. Seyferts are by far the most commonly observed AGN, yet make up no more than a few percent of giant spiral galaxies [Simkin et al. (1980)]. In Osterbrock (1989), the space density of luminous spirals is listed as 10^{-2} per Mpc^{-3} , whereas the space density of Seyfert galaxies is only 10^{-4} per Mpc^{-3} (the number is 10^{-7} per Mpc^{-3} for QSOs; see Section 1.1.2).

Seyferts can be subdivided further into two types, defined based on the properties of their emission lines. A Seyfert is classified as type 1 if it has very broad permitted lines, but whose forbidden lines are narrower (though still broader than ordinary galaxies) [Khachikian & Weedman (1974)]. A typical Seyfert 1 has broad permitted lines (e.g., He I) of widths up to 10^4 km s⁻¹, whereas FWHMs of forbidden lines (e.g., [O III]) are closer to 10^2 km s⁻¹ [Osterbrock (1984)]. This is predicted to be due to extreme densities in the broad line regions of Seyfert 1s, collisionally de-exciting forbidden lines and preventing them from gaining the same widths as the permitted lines [Osterbrock (1984)]. All line widths for Seyfert 2s are similar to each other, and generally of similar widths to the Seyfert 1 forbidden lines ($\sim 10^2$ km s⁻¹), though again are significantly broader than ordinary, non-active galaxies [Osterbrock (1984)]. Seyferts whose line widths are in between the two extreme cases of Seyfert 1 and Seyfert 2 are classified with intermediate numbers (e.g., 1.5, 1.8) depending on the relative strength of the narrow and broad line regions [Osterbrock (1977)]. Seyfert 2s tend to exhibit weaker, smoother continua than Seyfert 1s [Osterbrock (1978)]. Figure 1.2 shows a comparison between the spectrum of a Seyfert 1 (Mrk 1243) and a Seyfert 2 (Mrk 1157). Note the significantly broader permitted lines in the Seyfert 1 spectrum, as well as the more complex continuum.

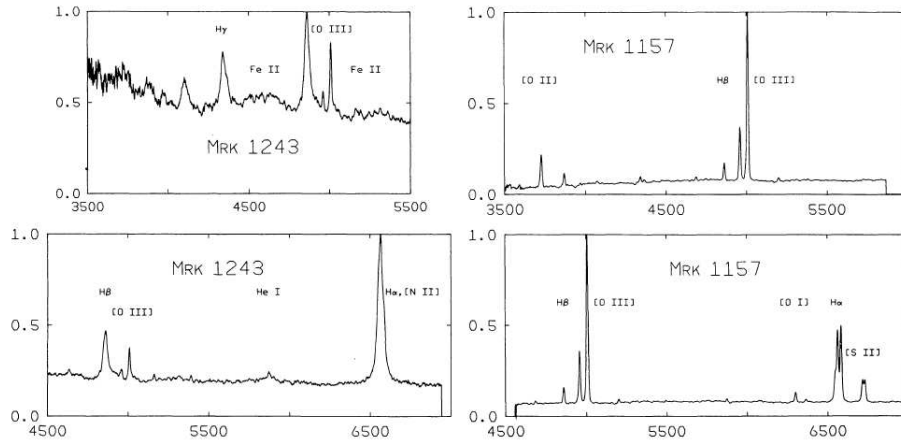


Figure 1.2: Comparison between an example Seyfert 1 spectrum (left, Mrk 1243) and an example Seyfert 2 spectrum (right, Mrk 1157), taken from Osterbrock (1984). The vertical scale is relative energy flux in flux units per unit wavelength interval, and the horizontal scale is wavelength in \AA . Note that the Seyfert 1 has much broader permitted lines than the Seyfert 2, as well as a more complex, stronger, heavily-featured continuum.

1.1.2 PG QSOs

The initial discovery of quasi-stellar objects, or QSOs, was made in 1960, when radio observations produced measurements of flux which did not appear to have an optical counterpart. The only measurable optical emission near the radio emission of 3C 48, the first reported QSO, was what appeared to be a nebulous 16th magnitude star [Sandage (1960), Burbidge (1967)]. A better picture began to emerge when 3C 273 was discovered, as it displayed two radio lobes with a faint optical jet in between [Hazard et al. (1963), Schmidt (1963), Burbidge (1967)]. Broadened emission lines were measured in the spectra. Initial classifications of QSOs made in 1964 included those objects which were star-like, yet identified via radio, which showed optical variability, which had large UV flux, which had measurable

broad emission lines, and whose spectral lines were measured to have high redshifts [Schmidt (1964)]. The high redshifts measured via QSO emission lines were initially baffling, as redshifts that high (measured up to $z = 2.012$ in 1965) were unexpected, and astronomers had a hard time believing these were genuine cosmological redshifts [Burbidge (1967)]. In fact, it was initially posited that QSOs were objects ejected from the nucleus of the Milky Way in some great cataclysm [Terrell (1964)], or similarly ejected from nearby radio galaxies [Hoyle & Burbidge (1966)] or peculiar galaxies [Arp (1966)]. The energies and sizes required by the variability measurements were likewise intriguing and unexplainable upon initial discovery, though relativistic speeds [Rees (1966)] and synchrotron radiation were beginning to be considered [Sligh (1963), Williams (1963)].

Once it was realized that QSOs were likely powered by the same physical phenomenon as Seyfert galaxies and thus QSOs were AGN, just significantly more luminous, rarer, and at higher redshift than typical active galaxies, QSOs began to be studied in detail [Osterbrock (1984)]. The PG QSO sample, as used in Chapter 3, was taken from the Palomar-Green Catalog of Ultraviolet Excess Stellar Objects, a statistically complete sample which observed 266 fields, for a total coverage of over 10000 square degrees [Green et al. (1986)]. This catalog primarily identified hot subdwarf stars, but 5.4% of the 1800 UV excess objects measured were spectroscopically classified to be QSOs. The PG Bright Quasar Sample, consisting of the QSOs identified in Green (1986), was looked at individually by Schmidt & Green (1983), and chosen via morphological and spectroscopic criteria: PG QSOs must appear to be star-like (the bulk of the optical light coming from within a circle of $2''$) and they

must have broad emission lines and high redshift. The spectroscopic criterion for PG QSOs is very similar to that of Seyferts, but with a redshift cutoff of $z > 0.025$ [Schmidt & Green (1983)]. The initial PG QSO sample of 92 objects showed an increasing space density with higher redshifts. In particular, the sample used in Chapter 3, as selected by the Quasar and Evolution Study [Schweitzer et al. (2006)], was drawn from Guyon et al. (2006), which identified the 28 most local and brightest QSOs from the BQS sample ($z \leq 0.3, B \leq 16.3$), in particular because these QSOs have existing multiwavelength observations, which allows for comparisons of their global properties. This work found significant correlations between host luminosity and host morphology (the most luminous QSOs being found in ellipticals, whereas the fainter QSOs are hosted in disks) [Guyon et al. (2006)]. Further studies of QSOs will be described in Chapter 3.

1.2 ULIRGs & LIRGs

Luminous infrared galaxies (LIRGs) and ultraluminous infrared galaxies (ULIRGs) are defined strictly by their infrared luminosity: $L_{\text{IR}} > 10^{11} L_{\odot}$ for LIRGs, $L_{\text{IR}} > 10^{12} L_{\odot}$ for ULIRGs, where infrared luminosity is calculated via a combination of IRAS flux densities [Sanders & Mirabel (1996)]. These objects were first categorized by the *Infrared Astronomical Satellite*, IRAS; galaxies whose infrared luminosities were stronger than their remaining overall luminosity had begun to be studied as early as the late 1960s [Low & Kleinmann (1968), Kleinmann & Low (1970), Rieke & Low (1972)], but not in such large numbers as were revealed by IRAS.

LIRGs have been found to be as common as Seyferts, with ULIRGs twice as common as QSOs with comparable luminosities [Sanders & Mirabel (1996)]. Multi-wavelength observations have revealed a number of LIRG & ULIRG properties and the sources of such high luminosities. Optical and near-infrared spectroscopy have revealed that most of the *IRAS* objects show evidence for strong starbursts enshrouded in dust [Elston et al. (1985)]. SED modeling of infrared emission in objects with strong infrared luminosity also indicates a strong starburst component (e.g., Helou (1986), Rowan-Robinson & Efstathiou (1993)). Spectroscopy has also shown that many LIRGs and ULIRGs host AGN, with significant increases in Seyfert percentages with increasing infrared luminosity [Kim et al. (1995), Veilleux et al. (1995)]. Roughly 30% of local ULIRGs have shown evidence of AGNs [Veilleux et al. (1999a), Veilleux et al. (1999b)]. It remains unclear whether ULIRGs are powered by AGN or starbursts, as though infrared spectra would imply that AGN may be dominating [Veilleux et al. (1999a), Veilleux et al. (1999b), Armus et al. (2007)], it is possible that there is significant, dust-obscured star formation in these objects [Teng et al. (2005), Teng et al. (2009)]. Optical and near-infrared imaging studies have revealed the morphologies of these objects and found that roughly 25% of LIRGs and nearly all ULIRGs are undergoing galaxy interactions/mergers (e.g., Soifer et al. (1984), Sanders et al. (1988), Kim et al. (1995), Clements et al. (1996), Murphy et al. (1996), Veilleux et al. (2002,06)). Gas measurements illustrate this picture as well, as during the merger process (see Section 1.3), significant amounts of gas fall in to the center of ULIRGs, evident in CO detections implying very high column densities [Rupke et al. (2008),

Evans et al. (2002)]. Sanders has posited that ULIRGs undergoing mergers present a transitional phase, perhaps becoming optically bright quasars [Sanders et al. (1988)]. This will be discussed further in Chapter 3.

1.3 Galactic Mergers

The commonly held picture of galactic mergers has been developed primarily through numerical simulations and is well described in Mihos & Hernquist (1996) and Mihos (1999), and interaction classes based on this picture were defined in Veilleux et al. (2002); we will summarize this picture here. The initial phase of a merger, or interaction class I [Veilleux et al. (2002)], is known as either “pre-collision” or “first approach.” During this phase, galaxies experience their first responses to one another: the dark halos of the two galaxies cross, and the orbital motions of the galaxies are altered. In interaction class II, “first contact,” the disks of the galaxies overlap, but there is still no morphological change in either galaxy. Interaction class III, defined as “pre-merger” by Veilleux et al. (2002), encompasses several stages as described in Mihos (1999). First, “impact” results when each galaxy begins feeling the tidal force from the other, leading to both morphological distortion, primarily in the form of tidal tails or bridges, and shocks in the ISM. Next, “gravitational response” occurs after the two galaxies separate out of their initial collision, and disk self-gravity makes the distortions stronger. At this point, distortions are believed to result in gaseous infall, providing fuel to trigger star formation and AGN activity [Barnes & Hernquist (1996), Hopkins et al. (2005), Hopkins et al. (2006a)]. Galax-

ies then enter the “hanging out” phase, in which the dynamical friction of the dark matter halos causes the galaxies to begin spiraling into one another, eventually leading to a full merger. Veilleux et al. (2002) split interaction class III into two branches, a, “wide binary,” and b, “close binary,” based on the apparent separation of the two galaxies. Next, we get interaction class IV: “merger.” Here the two galaxies have coalesced together to form one, often dusty, nucleus, though tidal tails are still present. This class is split into a, “diffuse merger,” and b, “compact merger,” depending upon the extent of the infrared luminosity. Finally, we get interaction class V, “old merger” or “relaxation,” in which the merger remnant core has relaxed and there are no obvious signs of tidal tails, yet it is clear from the morphology of the remnant core that the system has been previously disrupted. Strong regions of star formation are often seen. Figure 1.3 shows snapshots of a numerical simulation, run by Mihos & Hernquist (1996), illustrating what two merging galaxies might look like during several of these stages. It also shows a more recent simulation by Hopkins et al. (2006), in which the quasar turning on is readily apparent.

As described in the previous section, galactic interactions and mergers are so common in ULIRGs (nearly 100% in most samples) that ULIRGs provide an excellent laboratory for the study of mergers. These ULIRGs are often in the final two interaction classes [Mihos (1999)], and thus study of star formation and AGN in ULIRGs can provide observational evidence for the merger picture described above; we investigate these relationships in Chapter 3.

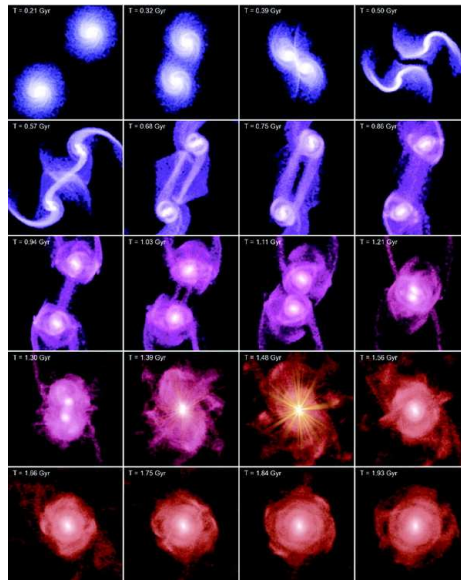
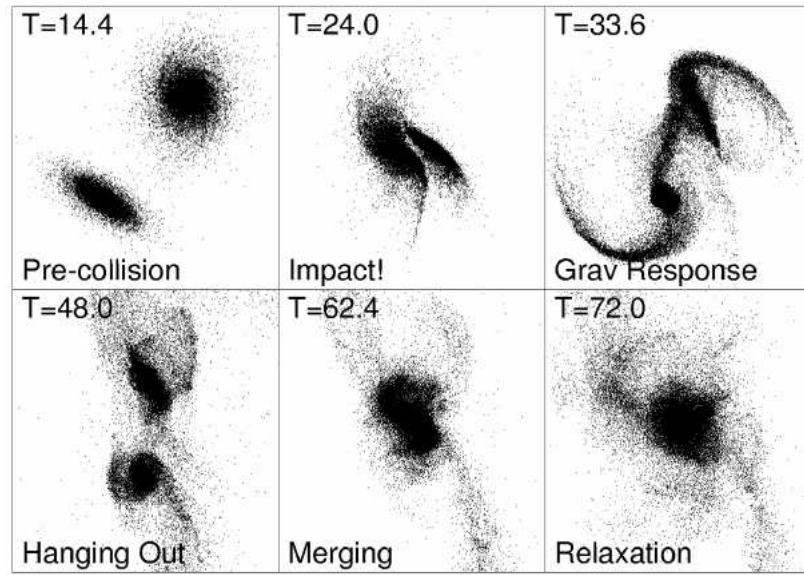


Figure 1.3: Top: Snapshots of a numerical simulation of merging galaxies, run by Mihos & Hernquist (1996) and taken from Mihos (1999), illustrating what two galaxies might look like in the pre-collision, impact, gravitational response, hanging out, merging, and relaxation phases. Bottom: Time sequence from a Hopkins et al. (2006) galaxy merger simulation. Pixel brightness corresponds to stellar mass density, whereas color indicates baryonic gas fraction (blue: 20%, red: <5%). The optical quasar is clearly illustrated at $T=1.39$ and 1.48 Gyr.

1.4 Galactic Outflows & Feedback

Galactic-scale winds were an unknown phenomenon before the early 1960s, when evidence for outflowing, galaxy-scale gas was discovered in several elliptical galaxies and when evidence for a central explosion in M82 was found [Osterbrock (1960), Lynds & Sandage (1963), Burke (1968)]. Galactic outflows are now found to be prevalent at both low- and high-redshifts, and while the physics of these winds has been well studied, it remains unclear whether AGN or starbursts are the primary drivers of these outflows [Veilleux et al. (2005)]. The basic physics behind these galactic-scale winds is outlined in the review article by Veilleux, Cecil, & Bland-Hawthorn (2005) and will be summarized here.

The central engine of the galactic-scale wind, either an AGN or a starburst, deposits mechanical energy into the surrounding ISM, which in turn over-pressurizes a hot gas cavity in that ISM [Chevalier & Clegg (1985)]. When the pressure in that cavity becomes greater than the pressure of the ISM surrounding the bubble, the bubble will begin behaving like one driven by a stellar wind and will begin expanding [Castor et al. (1975), Ostriker & McKee (1988)]. The bubble begins to shock the ISM and to sweep up shocked gas from the ISM as it moves along, which in turn slows the bubble's expansion to below the velocity of the wind. At this point, what is known as the "free expansion" phase of the wind has ended, and a five-zoned structure develops: in zone 1, the energy from the central engine is being deposited into the ISM; in zone 2, material outflows supersonically; in zone 3, there is hot, shocked wind; in zone 4, there is a thin, dense, shocked

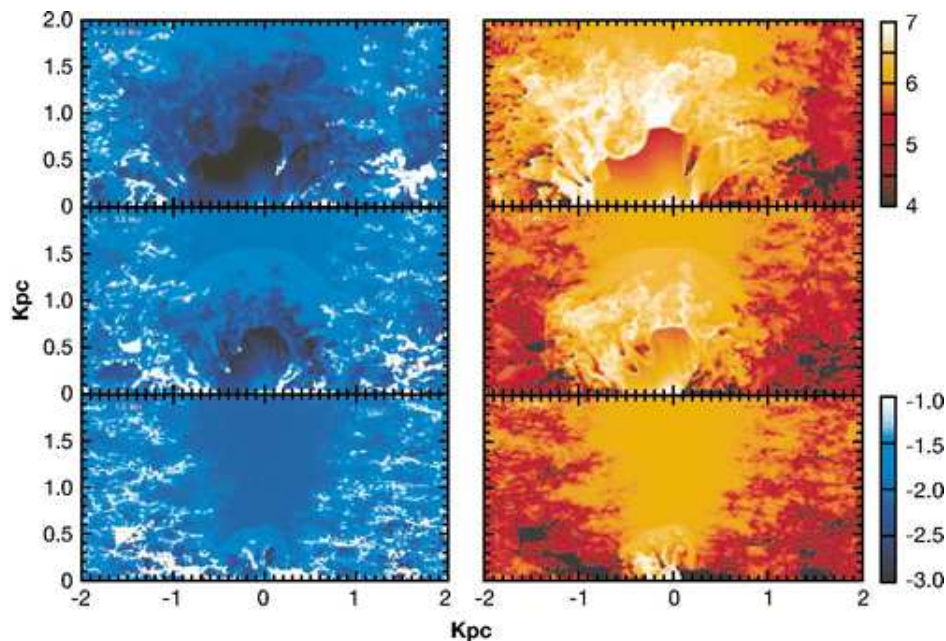


Figure 1.4: Hydrodynamical simulation, performed by J. Cooper, G. Bicknell, R. Sutherland, and J. Bland-Hawthorn, as published in Veilleux, Cecil, & Bland-Hawthorn (2005), of a starburst-driven outflow into the ISM. The blue panel is log-density and the red panel is log-temperature; time evolves from bottom to top.

ISM shell accumulated as the material moves outward; in zone 5, the ISM remains undisturbed. If radiative losses are primarily negligible, the bubble is said to be energy-conserving [Castor et al. (1975)], if not, the bubble is momentum-conserving [Steigman et al. (1975), Koo & McKee (1992)], and decelerates much more quickly than the energy-conserving winds. At this point, if the bubble reaches the scale height of the disk, it will reaccelerate, Rayleigh-Taylor instabilities will cause it to fragment, and the fragments and shocked wind will be released into the halo of the galaxy (a simulation of this is shown in Figure 1.4).

If the central engine of the galactic winds is starbursts, it has been found

that supernovae explosions resulting from those starbursts are typically dominant in galactic winds. Only in certain cases, in which the starbursts are very young ($< 10^7$ years), high-mass ($> 60M_{\odot}$), and metal-rich ($Z > Z_{\odot}$), do stellar winds play a significant role in galactic outflows [Veilleux et al. (2005)]. If the central engine is an AGN, black hole accretion and radiative processes are believed to power the outflows. Radiation released in black hole accretion can impart radiation pressure onto the gas of the ISM through electron scattering, dust grain scattering, scattering in atomic resonance lines, and photoionization. The radiation of the AGN can also cause runaway heating in gas surrounding the AGN, which could in turn lead to winds [Krolik et al. (1981), Begelman (1985)]. Finally, the magnetic fields generated by the accretion disks of the AGN can power and potentially collimate galactic-scale winds, particularly in galaxies with strong radio emission [Blandford & Payne (1982), Zensus (1997), Worrall (2005)]. One of the major goals of this thesis is to attempt to use observational evidence to determine which is the central engine in Seyferts and ULIRGs: the AGN or starbursts?

Galactic, particularly AGN-driven, winds are often invoked to answer questions involving galactic feedback, particularly the cutoff at the bright-end of the extragalactic luminosity function (e.g., Dekel & Silk (1986), Somerville & Primack (1999), Benson et al. (2003), Hopkins et al. (2006b)) and the extremely close correlation between central black hole mass and bulge mass in elliptical galaxies (e.g., Silk & Rees (1998), Ferrarese & Merritt (2000), Murray et al. (2005), Fabian (2012)). In order to play a significant role in feedback, AGN winds need to have sufficiently high velocities (to get $L_{wind} \sim L_{Edd}$), and winds of $\sim 1000 \text{ km s}^{-1}$ are believed to

be insufficient [Blustin et al. (2005), Fabian (2012)]. Wind powers of 5-10% of the accretion power can be sufficient to play a role in feedback, which has been observed in some quasars [Dunn et al. (2010), Moe et al. (2009), Saez et al. (2009)]. As described in Fabian (2012), several recent observations of high-redshift quasars have shown evidence for AGN feedback occurring. Cano-Díaz et al. (2012) find evidence for suppressed star formation around a $z = 2.4$ quasar with high-velocity [O III] outflows, and Maiolino et al. (2012) have measured a $z = 6.4$ quasar with an outflow strong enough ($\dot{M} > 3500 M_{\odot} \text{ yr}^{-1}$) and extended enough (~ 16 kpc) to eject all of the molecular gas of the host galaxy in barely more than a megayear. In Chapters 2 and 3, we will attempt to quantify the potential role that the galactic outflows we observe could be playing in galactic feedback.

1.5 The High-Redshift Universe

Knowledge of the early universe primarily exists in the realm of theory to this day, as current observational instruments are not yet sufficient to reliably probe the dark ages. The James Webb Space Telescope (JWST) and the Thirty Meter Telescope (TMT) will play a significant role in increasing our observational knowledge, and the Atacama Large Millimeter Array (ALMA) is already beginning to make contributions to that knowledge base [Bromm & Yoshida (2011)]. In the meantime, we turn to theory and simulations for a general picture of the early days of the universe, after inflation but prior to the era of massive galaxies. The first galaxies are believed to have formed just ~ 100 Myr after the Big Bang, following the formation

of the first stars [Rees (1993), Loeb & Barkana (2001)]. In a Λ cold dark matter cosmology (Λ CDM), we expect to see hierarchical galaxy formation, in which structure forms from bottom-up: small dark matter halos merge into larger halos, and thus we progress from stars to small galaxies to larger galaxies [Blumenthal et al. (1984), Springel et al. (2005b), Bromm & Yoshida (2011)]. In order for an object to form, gas clouds must reach a mass of roughly the Jeans mass, approximately $10^4 M_\odot$ [Jeans (1928)], and thus gravitational pressure can dominate over gas pressure and cause the cloud to collapse [Couchman & Rees (1986), Ostriker & Gnedin (1996)]. The first stars were believed to have formed via trace amounts of molecular hydrogen, which condensed among cold gas in a dark halo [Galli & Palla (1998), Bromm et al. (2009)]. Figure 1.5 shows a simulation of formation of a protostar, taken from Yoshida et al. (2008) via Bromm et al. (2009). The simulation shows gas distribution in and around *a*, the minihalo, *b*, the self-gravitating cloud which condenses into the star, *c*, the core of the molecular star-forming cloud, and *d*, the resulting protostar itself. According to numerical simulations, this would have occurred at $z \sim 20 - 30$, in dark matter “minihalos” of $\sim 10^6 M_\odot$ [Tegmark et al. (1997), Abel et al. (2002), Bromm et al. (2002), Yoshida et al. (2006)]. Radiative feedback from these first stars is believed to have been vitally important, as these early stars should have been massive enough and bright enough for their UV radiation to destroy all H_2 remaining in the surrounding cloud, thus preventing the formation of more stars from that cloud [Omukai & Nishi (1999)]; simulations predict that there could have been over a 10 Myr between periods of star formation because of that feedback [Yoshida et al. (2007), Alvarez et al. (2009), Bromm & Yoshida (2011)].

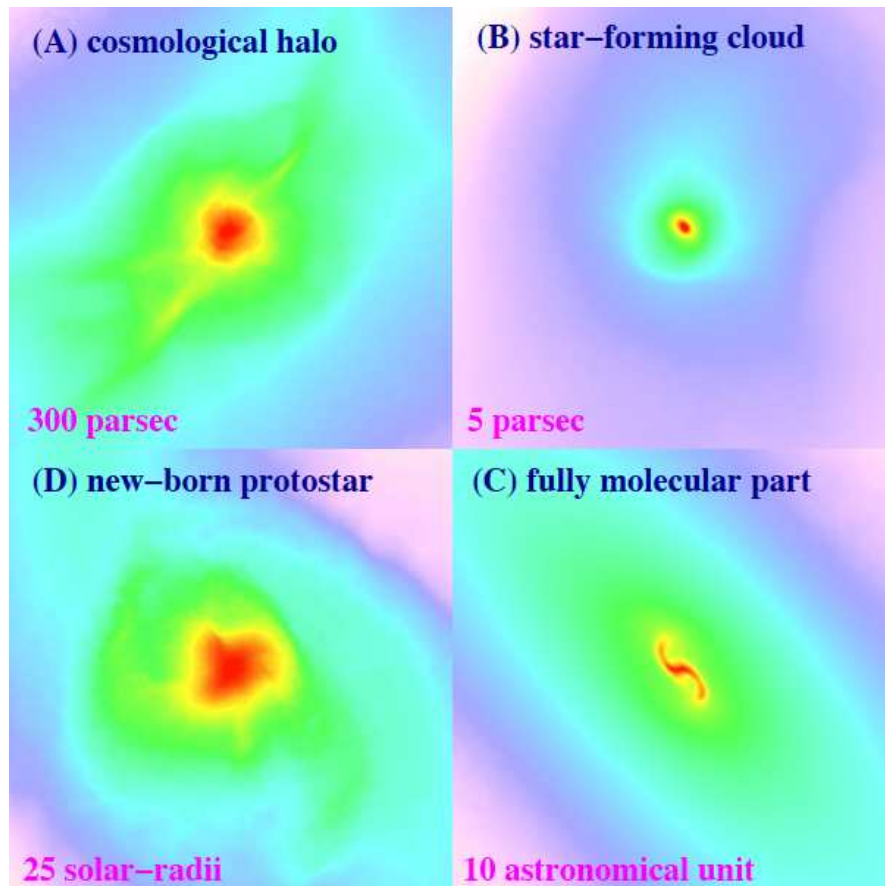


Figure 1.5: Snapshots of a simulation from Yoshida et al. (2008) showing formation of a protostar in the early universe. Colors reflect the large-scale gas distribution in four different stages as labeled in the plot.

That negative feedback from the formation and supernovae of the initial stars has led to some disagreement over how the first galaxies formed [Bromm & Yoshida (2011)]. Some simulations predict that the minihalos in which the first stars formed, as described above, were the hosts of the very first galaxies, although this requires a very different initial mass function than what we observe today [Ricotti et al. (2002a), Ricotti et al. (2002b), Ricotti et al. (2008)]. These simulations would predict that the first galaxies formed at $z > 40$ [Naoz et al. (2006)]. But, if negative feedback plays a substantial role, as described above, photoionization and supernovae would leave the minihalo with no gas unless the minihalo is sufficiently massive [Alvarez et al. (2006), Greif et al. (2007), Bromm & Yoshida (2011)]. In this case, the first galaxies would form at closer to $z > 15$ [Miralda-Escudé (2003)]. Regardless, the formation of the first galaxies led to the reionization epoch, which will be described below.

1.5.1 Reionization

Prior to the formation of the first radiating sources, the universe was in the midst of a “dark ages,” entirely opaque to photons, the only radiation emanating from the cosmic microwave background [Loeb & Barkana (2001)]. The ionization potential of hydrogen is 13.6 eV, and nuclear fusion releases nearly a million times more energy per hydrogen atom; when one takes into account the number of emitted photons with higher energy than the hydrogen ionization potential, only 10^{-4} of the total baryonic mass of the universe is required to condense into stars

or black holes in order for the entire universe to be ionized [Bromm et al. (2001), Loeb & Barkana (2001)]. The reionization of hydrogen in the universe is believed to occur in several different phases, with terminology defined in Gnedin (2000); these phases are described in depth in Loeb & Barkana (2001), which we will summarize here.

When the first individual sources have formed, the universe is said to have been in the “pre-overlap” phase, in which isolated stars and quasars begin ionizing the media surrounding them. The initial ionizing sources are found in the highest-density regions of the universe, because the initial objects which form live in the most massive halos, and so recombinations often occur as the ionizing radiation propagates through the high-density medium. Thus the highest density media can remain somewhat neutral, despite the presence of ionizing sources. The lower-density media are easily ionized and stay that way, and thus there are two phases in the IGM – a neutral phase and an ionized phase – during the pre-overlap stage of reionization. This stage is thought to last a long time, from when initial sources turn on, at $z \sim 30$, to roughly ~ 10 , when the second phase of reionization begins.

Next comes the “overlap” phase, which is much quicker compared to the initial pre-overlap phase. As the name indicates, during this phase, the H II bubbles formed by the individual ionizing sources start overlapping, allowing the ionizing radiation to spread more quickly. Recombination in high-density regions is now too slow to keep those regions neutral, because those regions are subject to ionizing radiation from multiple sources. These first two phases are illustrated in Figure 1.6, taken from Loeb & Barkana (2001). The overlap phase is considered to be over when H

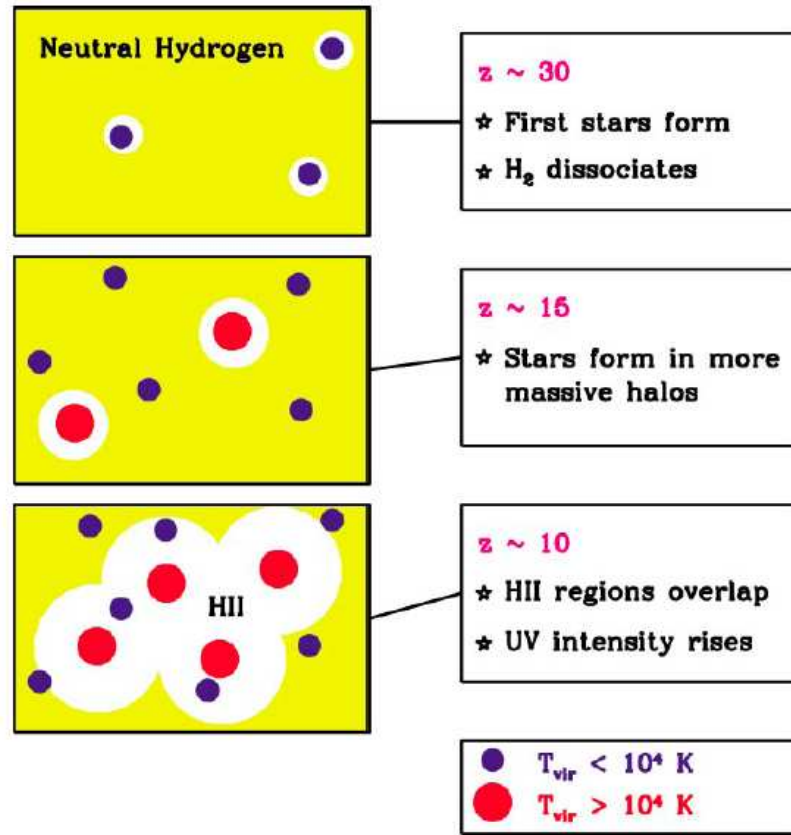


Figure 1.6: A figure from Loeb & Barkana (2001) illustrating the pre-overlap and overlap phases of the reionization of hydrogen in the IGM. Yellow represents neutral hydrogen, white represents ionized (H II) regions, and red and purple indicate the masses of the halos in which the ionizing sources have formed.

H II regions are dominant, and everything is ionized except for isolated clouds which are high enough density to shield themselves from the ionizing radiation; this is considered the “moment of reionization.”

The universe then enters the “post-overlap” phase, which remains ongoing even in the local universe. Galaxy formation continues and more and more high-density, formerly neutral regions become ionized. The most important point in this phase

is what Madau et al. (1999) describe as the “breakthrough redshift,” occurring at $z \sim 1.6$, when every ionizing source becomes visible to every other ionizing source.

While these stages are fairly well understood from a theoretical perspective, the moment of reionization is, to this day, very poorly constrained (see Section 4.1 for further details). Our work in Chapters 4 and 5 attempts to put further constraints on the moment of reionization via a search for $z \sim 8$ Lyman- α emitters, which will be described in the following section.

1.5.2 Lyman- α Emitters

The earliest galaxies are expected to be undergoing heavy, rapid star formation, and thus are predicted to be producing substantial amounts of Ly α emission [Partridge & Peebles (1967), Pritchett (1994), Rhoads et al. (2000)]. In particular, the lack of dust in the early interstellar medium should also lead to pronounced Ly α emission [Oh (1999), Tumlinson & Shull (2000)]. This Ly α emission becomes a unique probe of reionization because H α and He II $\lambda 1640$, two other lines commonly produced in these early stars, will simply propagate through the neutral IGM [Oh (1999)]. For Ly α photons, however, the neutral IGM presents a significant problem; with its optical depth of $\sim 10^5$ during in the pre-overlap and overlap phases before the moment of reionization [Gunn & Peterson (1965)], the neutral IGM prevents essentially any Ly α photons from propagating through [Loeb & Barkana (2001)]. Those Ly α photons become absorbed by the neutral IGM and re-emitted. Each time this occurs, the Hubble expansion of the IGM causes the

photon to redshift slightly [Loeb & Barkana (2001)]. This results in a Ly α emission line profile which has a characteristic red asymmetry, detailed in Rhoads et al. (2004). As will be discussed further in Chapter 4, the Ly α line is thus an excellent probe of the neutral hydrogen fraction in the IGM, as prior to reionization, Ly α flux should be completely suppressed; no Ly α flux emitted prior to the epoch of reionization should be observable today.

1.5.3 Cosmological Evolution Survey

In order to find such Ly α emitters and thus probe the previously described reionization epoch in Chapters 4 & 5, we undergo an observational probe of the Cosmological Evolution Survey (COSMOS) field. This 2 square degree field (centered at 10:00:28.6, +02:12:21.0 in J2000 coordinates) was chosen to be fairly sparse locally in order to be able to probe large scale structure as well as, like the name suggests, the cosmic evolution of galaxies. It is being observed via a comprehensive, multi-wavelength survey using both ground and space telescopes; this is an international effort, being spearheaded by researchers at Caltech ¹. The four primary science goals of COSMOS are 1, to quantify large scale structure evolution, on scales of galaxies, clusters, and dark matter, in terms of redshift; 2, to determine how galaxies and stars form and evolve as functions of redshift and large scale structure; 3, to map the distribution of dark matter from the local universe out to $z \sim 1$; and 4, to probe AGN evolution ². Of these science goals, our work falls most closely under

¹<http://cosmos.astro.caltech.edu/index.html>

²<http://cosmos.astro.caltech.edu/astronomer/tech.html>

the second, as we attempt in Chapters 4 & 5 to find some of the earliest galaxies, whose radiation fields are believed to have played a major role in the evolution of the early universe.

1.6 Observatories & Instruments Used in this Thesis

In this section, we detail the various observatories and instruments used to obtain the data taken in this thesis.

1.6.1 Kitt Peak National Observatory Mayall 4-meter Telescope

The Mayall 4-meter telescope, located near the summit of the Kitt Peak National Observatory (KPNO) in Tucson, Arizona, was the primary telescope used for Chapters 2, 3, and 4 of this thesis. It is a Cassegrain reflecting, prime focus telescope (focal ratio $f/2.7$) on an equatorial mounting, built in 1973, and used for optical and infrared observations ³.

1.6.1.1 Ritchey-Chrétien Spectrograph

The Ritchey-Chrétien (R-C) spectrograph on the KPNO 4-m telescope was the primary instrument used for observations in Chapters 2 and 3. It has a resolution range of 300-5000, with a 5.4" slit at 0.69" per pixel. It makes use of a T2KB CCD. The typical system throughput is 11-14%. We used the KPC-18C, 790 lines/mm grating in the first order, with a wavelength coverage of 1700 Å. This

³http://www.noao.edu/outreach/kptour/mayall_fact.html

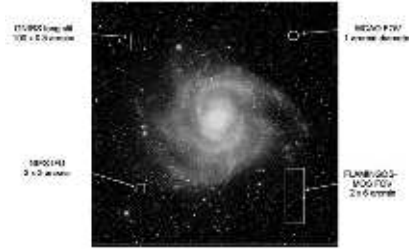


Figure 1.7: A single, dithered NEWFIRM field of view, compared to the fields of view of various Gemini instruments. This image was taken from the NEWFIRM website, <http://www.noao.edu/ets/newfirm/>.

grating disperses at 1.14 \AA per pixel, which corresponds to a resolution of 2.9 \AA^4 .

1.6.1.2 NEWFIRM

NEWFIRM, the NOAO Extremely Wide-Field Infrared Mosaic imager, was the primary instrument used for the observations detailed in Chapter 4. It has a 28×28 arcminute field of view, which is shown in comparison to Gemini fields of view in Figure 1.7. The detector uses four 2048×2048 InSb arrays ($40''/\text{pixel}$), arranged in a 2×2 mosaic, with a 35 arcsecond wide gap forming a cross in the middle of the mosaic⁵. In addition to the gap between the arrays, there is a significant semicircular defect, roughly 100 pixels in radius, in the upper left quadrant, making significant dithering a necessity. With ultra-narrowband filters, rings from sky lines, particularly OH, can become present in the data; this phenomenon is described in detail in Chapter 4, as well as the specifics of the ultra-narrowband filters.

⁴<http://www.noao.edu/kpno/manuals/l2mspect/node8.html>

⁵http://www.noao.edu/ets/newfirm/documents/Quick_Guide_for_Proposal_Preparation.pdf

1.6.2 Gemini Observatory

The Gemini Observatory is made up of two identical 8.1-meter altitude-azimuth telescopes: Gemini-North is located on Mauna Kea on the Big Island of Hawaii, and Gemini-South is located on Cerro Pachón in Chile. The telescopes are reflecting Cassegrain telescopes, and the 8.1-meter primary and 1-meter secondary mirrors are both coated with high-reflectivity silver. Silver coatings reduce thermal emission of the mirrors and are thus ideal for infrared astronomy⁶. In Chapter 5, we use the Gemini-North telescope to perform infrared spectroscopic observations, using the instrument described in the following section.

1.6.2.1 GNIRS

GNIRS, the Gemini Near-Infrared Spectrograph, can be used in long-slit, single order mode, with an overall range of 1.0-5.4 μm across the orders, or in short-slit, cross-dispersed mode, which gives complete coverage of 0.9-2.5 μm across the orders and a resolution of roughly 1700. In the observations described in Chapter 5, we made use of the 31.7 lines/mm grating with orders 3-6 in cross-dispersed mode, which include the *X*-band (1.03-1.17 μm), *J*-band (1.17-1.37 μm), *H*-band (1.49-1.80 μm), and *K*-band (1.91-2.49 μm)⁷. Figure 1.8 shows a raw image of a typical galaxy, observed with GNIRS in cross-dispersed mode. With the 0.45" camera (3 pixel slit widths) in this configuration, we get a resolution of \sim 1070-1130.

⁶<http://www.gemini.edu/sciops/telescopes-and-sites>

⁷<http://www.gemini.edu/sciops/instruments/gnirs/spectroscopy>

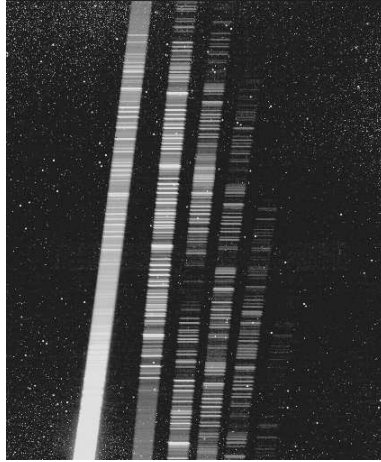


Figure 1.8: A raw image of a typical faint galaxy, taken with GNIRS in cross-dispersed mode. Orders run from 3-8 and go left to right, and within the order, wavelength increases downwards. This image taken from <http://www.gemini.edu/sciops/instruments/gnirs/spectroscopy/crossdispersed-xd-spectroscopy>.

1.6.3 Infrared Astronomical Satellite and Infrared Space Observatory

In Chapters 2 and 3, we use flux densities from the Infrared Astronomical Satellite (IRAS) and the Infrared Space Observatory (ISO) to calculate near-infrared and infrared fluxes, along with their respective luminosities. IRAS, a mutual endeavor between the United States, the United Kingdom, and the Netherlands, was a survey satellite which took its observations in 1983 and was able to survey all but 4% of the sky. It operated in four wavelength bands (12, 25, 60, and 100 μm) and produced unbiased survey catalogs of over 250,000 sources, including the IRAS Faint Source Catalog and the IRAS Point Source Catalog⁸. IRAS was responsible for a number of extremely important scientific discoveries, including detections of roughly 75,000

⁸<http://irsa.ipac.caltech.edu/IRASdocs/exp.sup/ch1/A.html>

ULIRGs (our ULIRG sample consists primarily of IRAS discoveries), dusty disks around stars, the first probe of the core of the Milky Way, and measurements which were used to prove that the Milky Way is a barred spiral⁹.

ISO, a European Space Agency satellite, was a natural follow-up to IRAS, and operated from 1995-1998. The operating range of ISO was larger than that of IRAS, from 2.5-240 μm , and had much improved detectors; sensitivity and resolution increases over IRAS have been quoted at up to 1000 and 100 times better, respectively. ISO did not observe as many sources as IRAS – only $\sim 30,000$ – but was able to probe much deeper on the sources it observed¹⁰.

1.6.4 Subaru Telescope

The Subaru Telescope, operated by the National Astronomical Observatory of Japan, is an 8.2-meter reflecting telescope located on the summit of Mauna Kea on the Big Island of Hawaii. The telescope has four focal points; the instrument with which data used in Chapter 4 was taken, Suprime-Cam, is located at the prime focus¹¹. The Subaru Prime Focus Camera (Suprime-Cam) is an extremely wide-field imager, covering a 34' x 27' field of view, and made up of a 5 x 2 mosaic of ten rectangular 2048 x 4096 CCDs. Each CCD chip has a 14-16 arcminute gap between it and the next chip¹². The data used in Chapter 4 were taken by the COSMOS team in the $Bj-$, $r+-$, and $i+-$ bands. These bands are centered at 0.45, 0.63, and

⁹http://www.ipac.caltech.edu/outreach/Edu/iras_discoveries.html

¹⁰http://www.esa.int/Our_Activities/Space_Science/ISO_overview

¹¹<http://www.naoj.org/Introduction/telescope.html>

¹²<http://www.naoj.org/Observing/Instruments/SCam/>

0.76 μm , respectively, with 10.4, 5.8, and 7.5 hours total integration in the three respective bands. Average seeing was 0.95'' for Bj , 1.05'' for $r+$, and 0.95 for $i+$ ¹³.

1.6.5 United Kingdom Infrared Telescope

The United Kingdom Infrared Telescope, or UKIRT, is a 3.8 meter telescope on the summit of Mauna Kea on Hawaii's Big Island, and is operated by the Joint Astronomy Centre. UKIRT has only one instrument, WFCAM, which is a wide field, near-infrared camera, whose sole design is to perform observations for large-scale surveys. The camera is made up of a mosaic of four HgCdTe 2048 x 2048 CCD arrays, and there are gaps of nearly 13 arcminutes between each chip. Four exposures taken with WFCAM can cover an area of 0.75 square degrees on the night sky¹⁴. Data used in Chapter 4 was taken by the COSMOS team during the period of December 2005 and June 2007, using WFCAM's J -band; this band is centered at 1.2 μm and has a bandwidth of 0.16 μm . Average seeing of this data set was 1.74''¹⁵.

1.6.6 Canada France Hawaii Telescope

Chapter 5 of this thesis describes data taken with the Canada France Hawaii Telescope, or CFHT. This telescope is a 3.6 meter optical/infrared telescope which, like Subaru, Gemini-N, and UKIRT, is located on the summit of Mauna Kea. The

¹³http://irsa.ipac.caltech.edu/data/COSMOS/images/subaru/SUBARU_INFO.txt

¹⁴http://www.jach.hawaii.edu/UKIRT/instruments/wfcam/user_guide/description.html

¹⁵http://irsa.ipac.caltech.edu/data/COSMOS/images/ukirt/UKIRT_INFO.txt

observatory is operated via a joint collaboration of the National Research Council of Canada, the Centre National de la Recherche Scientifique of France, and the University of Hawaii. The data referenced in Chapter 5 were taken using WIRCam, a near-infrared mosaic with a 20 square arcminute field of view. It is mounted at the prime focus of CFHT and consists of four 2048 x 2048 CCDs, laid out in a 2 x 2 mosaic¹⁶. The data we have used were taken by the COSMOS team between October 2007 and January 2009 and make use of the WIRCam *H*-band. This band is centered at a wavelength of 1.63 μm and spans a width of 0.28 μm . The average seeing for this data set was 0.8''¹⁷.

1.6.7 Hubble Space Telescope

The Hubble Space Telescope (HST) has been operating since 1990 under the aegis of the National Aeronautics and Space Administration and the European Space Agency, and has been arguably the most successful and important astronomical observatory ever built, both in terms of scientific discoveries and capturing the interest of the public. Its five servicing missions have resulted in a number of instruments being used on HST, and at present, three cameras and two spectrographs are available for use by the scientific community¹⁸. This thesis makes use of one of those cameras, which will be described below.

¹⁶<http://www.cfht.hawaii.edu/Instruments/Imaging/WIRCam/>

¹⁷http://irsa.ipac.caltech.edu/data/COSMOS/images/cfht/CFHT_INFO_H.txt

¹⁸http://www.stsci.edu/hst/HST_overview

1.6.7.1 Advanced Camera for Surveys

The Advanced Camera for Surveys (ACS) is a third-generation instrument on the Hubble Space Telescope that was used to take data referenced in Chapter 5. It has three channels: a wide field channel, with a 202" x 202" field of view, a high resolution channel, with a 29" x 26" field of view, and a solar blind channel, with a 34.6" x 30.8" field of view. The overall wavelength range of ACS is 0.12-1.1 μm ¹⁹. The COSMOS team data used specifically the WFC and focused on the *I*-band, via the F814W filter, covering roughly a 2 square degree area of the sky. There were 261 total orbits in this particular cycle of data, each consisting of four, 500 second exposures²⁰.

1.6.8 UltraVISTA

The UltraVISTA survey is utilizing the new VISTA (Visible and Infrared Survey Telescope for Astronomy) surveys telescope, a 4-m wide field telescope located at Cerro Paranal in Chile, which is operated by the European Southern Observatory. It uses a near infrared camera with a 1.65 degree field of view, mounted at a Cassegrain focus, and can operate in bands *Z* through *K*²¹. The UltraVISTA program is a survey of the COSMOS field which intends to obtain ultra-deep near-IR imaging over a five year span; it begins with a deep, 212 hour survey of the full 1.5 square degrees of COSMOS, and will conclude with an ultra-deep, 1408 hour

¹⁹<http://www.stsci.edu/hst/acs/Detector/>

²⁰<http://www.stsci.edu/~koekemoe/cosmos/>

²¹<http://www.vista.ac.uk/>

survey of half of the COSMOS field. The initial data release which we have used in Chapter 5 encompasses the Y , J , H , and K bands, and has an average exposure of 12 hours per pixel across the full 1.5 square degrees of the COSMOS field being imaged by this survey²².

1.7 Outline of Thesis

Chapters 2 and 3 make up part one of this thesis, a search for neutral gas outflows and inflows in local AGN and ULIRGs. This part attempts to answer several major questions:

- What role does far-infrared luminosity play in the detection of and velocities in large-scale outflows in local AGN and ULIRGs?
- Does star formation rate or host galaxy mass play a bigger role in the properties of those outflows?
- What is the primary mechanism powering large-scale outflows in local AGN and ULIRGs: starbursts or AGN?
- Does AGN type, AGN luminosity, or merger stage influence outflow detection rates and velocities in these objects?
- Are there any trends between host galaxy properties and the presence of strong inflows in local AGN, and could those inflows be powering the AGN?

²²http://www.eso.org/sci/observing/phase3/data_releases/ultravista_dr1.html

Chapters 4 and 5 make up part two of this thesis, an attempt to find high-redshift Ly α emitters in the COSMOS field. The questions which we attempt to answer in those chapters are as follows.

- Can ultra-narrowband surveys which have previously detected $z \sim 5 - 7$ Ly α emitters effectively detect such objects at $z \sim 8$?
- Has the Ly α luminosity function, and thus the state of the IGM and progress of the reionization epoch, evolved over $5.7 < z < 7.7$?
- Can we spectroscopically confirm these high-redshift targets?
- Is present-day ground-based telescope technology sufficient for the detection and confirmation of such faint, high-redshift targets?

We attempt to answer these questions via the methodologies described here. In Chapter 2, we use the R-C spectrograph on the KPNO 4m telescope to measure Na I D absorption in a sample of infrared-faint Seyfert galaxies. Blueshifted (redshifted) Na I D absorption is an unambiguous indicator of outflowing (inflowing) Na I D material, as there must be a continuum source behind the absorber. Clumps of Na I D become entrained in the galactic-scale outflow or inflow. We look at an equally divided sample of infrared-faint Seyfert 1s and 2s and compare the results with a previously-performed study of infrared-luminous Seyfert 1s and 2s, along with infrared luminous starburst ULIRGs and LIRGs, to attempt to determine whether the main driver in galactic-scale outflows is starbursts, the AGN, or some combination thereof. We look for trends in detection rate and velocity with far-

infrared luminosity, a probe of star formation rate, and with circular velocity where possible, a probe of host galaxy mass. We also attempt to estimate the values of dynamical quantities of these outflows, such as mass, momentum, energy, and rates thereof, and to determine what role these outflows could play in galactic feedback. We also measure an unusually high percentage of inflows in these objects, and again estimate dynamical quantities to determine whether the inflows we are measuring could in fact be powering the AGN in these objects. We perform rigorous statistical tests to back up our claims.

In Chapter 3, we continue the neutral gas outflow & inflow study as performed in Chapter 2, but using a new sample of PG QSOs and ULIRGs. This data set was taken from the QUEST sample, which is attempting to compare local PG QSOs and ULIRGs involved in gas-rich mergers to thus clarify the presently-held picture of the gas-rich merger sequence. We combine this data set with the data sets used in Chapter 2 to look for further correlations between outflow detection rates and velocities with far-infrared luminosity, with optical spectral type, and with interaction class, to help inform the merger sequence picture. We again estimate dynamical quantities for both outflows and inflows in an attempt to quantify both contribution to galactic feedback and the possibility of AGN fueling. Rigorous statistical tests are again performed to confirm these results.

In Chapter 4, we switch to the high-redshift universe and describe a search for $z = 7.7$ Ly α emitters in the COSMOS field. We use the extremely-wide field imager, NEWFIRM, on the KPNO 4m telescope, with two ultra-narrowband near-infrared filters, centered at 1.056 and 1.063 μm to correspond to $z = 7.7$ Ly α emission. We

use an extremely deep ultra-narrowband data set – 100 hours of total integration time, split between the two filters – , as well as broadband J data (taken from UKIRT) and broadband optical data (taken from Subaru), to identify targets with strong narrowband line emission, an infrared excess over the J -band, and no flux in optical. These features are characteristic of high- z Ly α emitters. We use a Monte Carlo simulation to estimate the number of sources we should find at this redshift, based on currently held Ly α luminosity functions at lower z . We then use our potential high- z candidates to calculate a Ly α luminosity function at $z = 7.7$ and compare it to other luminosity functions at $z \leq 7.7$ in an attempt to determine the evolution of the neutral hydrogen fraction of the IGM and the progression of the epoch of reionization at that time.

In Chapter 5, we follow-up the results of Chapter 4 by attempting to confirm that our $z = 7.7$ candidates are in fact high- z Ly α emitters, rather than a foreground emitter at lower redshift. We use three broadband imaging data sets to either rule out a candidate, if optical flux is measured (*HST* ACS I -band data), or to attempt to detect the candidate’s continuum (CFHT H -band data, UltraVISTA Y -, J -, H -, and K -band data). We then perform spectroscopic follow-up – the only way to completely confirm redshift – on one of our candidates using GNIRS on Gemini-North, and we obtain further spectroscopic follow-up on that and another candidate via our collaborators (LUCI on LBT, MOSFIRE on Keck). We discuss the results of these follow-up attempts and what that would mean for the evolution of the IGM and of the reionization epoch.

In Chapter 6, we summarize the goals of this thesis and the results of each chapter.

Chapter 2

Neutral Gas Outflows and Inflows in Infrared-Faint Seyfert Galaxies

2.1 Introduction

Galactic-scale gas outflows appear to play an important role in the evolution of the universe, possibly providing an explanation for a number of cosmological questions (Veilleux et al. (2005) and references therein). These galactic outflows are frequently observed in local galaxies with high star formation rates and/or an active nucleus, often extending on a scale of order of a few kiloparsecs or larger.

The high frequency of outflows measured in high-redshift, actively star-forming objects such as Lyman break galaxies suggests that outflows are a common stage in galactic evolution, with wind velocities decreasing over time [Shapley et al. (2003), Ferrara & Ricotti (2006)]. Such outflows may be responsible for the deficit of baryons seen in our own Milky Way galaxy and the mass-metallicity relation in external galaxies, if winds are capable of preferentially ejecting metals into the intergalactic medium ([Larson (1974), Garnett (2002), Tremonti et al. (2004)]). The intergalactic medium can be heated as well as enriched with metals by these galactic outflows, since energy inputs into the IGM on the order of 10^{56} ergs have been measured from galaxies with strong outflows [Croston et al. (2008)]. Additionally, outflows may quench star formation by heating up cold gas and ejecting it from the host [Binney (2004), Scannapieco et al. (2005)]. Specifically, AGN-

powered outflows have been proposed as the cause of the drop in AGN luminosity at low redshift and the cutoff at high luminosity of the galaxy luminosity function [Somerville & Primack (1999), Cole et al. (2000), Thacker et al. (2006)]. These winds may also limit black hole and spheroid growth, and be responsible for the observed tight correlation between black hole mass and galactic spheroid mass [Ferrarese & Merritt (2000), McLure & Dunlop (2002), Granato et al. (2004)]. Finally, winds driven by AGN and/or starbursts may help remove enough nuclear material with low angular momentum early on in the evolution of gas-rich system to aid in the formation of large disks with high specific angular momentum, more in line with the observations [Binney et al. (2001), Kormendy & Kennicutt (2004)].

Studies performed on actively star-forming galaxies, near and far, have revealed that outflow energetics increase with infrared (8-1000 μm) luminosity, L_{IR} , or equivalently, star formation rate (Martin (2005), Rupke et al. (2005a), hereafter RVS05a; Rupke et al. (2005b), hereafter RVS05b; Sato et al. (2009), Weiner et al. (2009)). Outflows have also been detected in composite galaxies with both starbursts and AGN (e.g., Irwin & Saikia (2003), Hota & Saikia (2006)). Seyfert 1 composites show significantly higher outflow velocities than pure starbursts and Seyfert 2 composites (Rupke et al. (2005c), hereafter RVS05c). Hydrodynamical simulations of starburst-driven outflows (e.g., Thacker et al. (2006), Cooper et al. (2008)) have difficulties reproducing the very high velocities detected in Seyfert 1 composites. The AGN in these objects thus appear to play a significant role in driving these outflows, at least on small scales [Crenshaw et al. (2003b)]. The situation in Seyfert 2 composites is more ambiguous – the AGN or starburst or both could

be powering the outflow in these systems [Schiano (1985)].

The focus of this chapter is on “pure” Seyfert galaxies with weak infrared starbursts. Our sample consists of 35 galaxies that are faint in the infrared ($10^{9.9} < L_{\text{IR}}/L_{\odot} < 10^{11.2}$), equally split between Seyfert 1s and Seyfert 2s. We compare the results from our study with those from previous studies of starburst and Seyfert ultraluminous infrared galaxies (ULIRGs; $L_{\text{IR}}/L_{\odot} \geq 10^{12}$) and luminous infrared galaxies (LIRGs; $10^{11} < L_{\text{IR}}/L_{\odot} < 10^{12}$) to isolate the role of the AGN in powering these outflows. As in previous studies, the IR-faint objects were observed in the Na I D $\lambda\lambda 5890, 5896$ doublet absorption feature. This Na feature has a low ionization potential (5.1 eV), so it probes neutral gas, and it can be used to study the ISM due to its high interstellar abundance. All objects in the sample have $z < 0.05$, and thus the Na I D feature is found in the optical. Velocity components in Na I D absorption are unambiguous indicators of outflowing (blueshifted velocities) or inflowing (redshifted velocities) gas, as there must be a continuum source behind the absorber.

The organization of this chapter is as follows. The sample is described in Section 2.2, including methods of selection and sample properties in terms of redshifts, star formation rates, and spectral types. The observations are discussed in Section 2.3. Section 2.4 describes the line fitting, the derivations of the velocities and column densities, and estimates of the expected stellar contributions to the measured Na I D absorption. In Section 2.5 we present the results on outflows, starting with the Seyfert 2s and followed by the Seyfert 1s. Next, Section 2.6 describes the results on inflows in the same fashion as Section 2.5. This is followed by a discussion of

the implications of our findings in Section 2.7, including comparisons with previous studies, dynamical estimates, and possible connections between inflows and nuclear structures. We conclude in Section 2.8 with a summary of our findings.

All calculations in this chapter assume cosmological parameter values as used in RVS05b and c, with $H_0 = 75 \text{ km s}^{-1} \text{ Mpc}^{-1}$, $\Omega_m = 0.3$, and $\Omega_\Lambda = 0.7$. All wavelengths quoted are vacuum wavelengths.

2.2 Sample

The objects in the sample were selected using three main criteria: They had to be optically classified as Seyferts and had to be faint in the infrared ($L_{\text{IR}} \sim < 10^{11} L_\odot$). All objects in the sample were also selected to have $z < 0.05$ to focus on the brightest sources and obtain reliable measurements.

Most galaxies in the sample are well-studied Seyfert galaxies with extensive ancillary data (e.g., Whittle (1992a), Nelson & Whittle (1995)). Roughly equal numbers of Seyfert 1 and Seyfert 2 galaxies were chosen to allow meaningful comparisons with the study of RVS05c on ULIRG Seyferts. The bolometric luminosities of the AGN in the present sample are well matched to those in the composite systems of RVS05c. This allows us to make direct comparisons between the two samples. Basic properties for the galaxies in our sample can be found in Tables 2.8 and 2.8. The last column in that table lists the references used for the compilation.

2.2.1 Redshifts

Not all objects in this survey have well-constrained published redshift measurements, so preference was given to values from stellar absorption lines [Nelson & Whittle (1995), Wegner et al. (2003)] when possible, followed by redshifts taken from HI lines [Nelson & Whittle (1995), Springob et al. (2005)]. Redshifts measured from data in the present survey were used if neither of the preceding were available, but were given low priority due to systematic errors ($\sim 10^{-4}$) associated with these measurements (e.g. it is possible that part of the narrow line region (NLR) is outflowing so the velocities based on the narrow emission lines are not necessarily representative of the systemic velocity). In this case, IRAF was used to measure central wavelength of various emission lines, including [OI] $\lambda\lambda 6300, 6364$, [NII] $\lambda\lambda 6548, 6583$, and [SII] $\lambda\lambda 6716, 6731$, and redshifts were calculated from those values.

2.2.2 Star Formation Rates

To estimate the star formation rates in these objects, we use their far-infrared luminosity, $L(40-120 \mu\text{m})$, under the assumption that the AGN does not contribute significantly to L_{FIR} [Schweitzer et al. (2006)]. This is probably a good first-order approximation although AGN may contribute $\sim 10-20\%$ to L_{FIR} [Netzer et al. (2007)]. L_{FIR} is calculated using the prescription of Sanders & Mirabel (1996), using data from the *IRAS* Faint Source and *IRAS* Point Source Catalogs. L_{FIR} is then used to calculate SFR using the relation in Kennicutt (1998), $SFR = L_{\text{FIR}} / (5.8 \times 10^9 L_{\odot})$

$M_{\odot} \text{ yr}^{-1}$. The far-infrared luminosities and star formation rates of the objects in our sample are listed in Tables 2.8 and 2.8.

2.2.3 Spectral Types

Spectral classifications were taken from the NASA Extragalactic Database¹ and confirmed through examination of emission lines in the spectra and references in the literature. Seyfert 1 – 1.5 were labeled Seyfert 1s for the purpose of this study, while Seyfert 1.8 – 2 were labeled Seyfert 2s. This is in keeping with the classification scheme of RVS05c and allows for comparisons of our results on Seyfert 1 and Seyfert 2 galaxies with those of previous studies.

2.3 OBSERVATIONS

All observations were taken over the course of three different observing runs on the Kitt Peak 4-meter telescope. Observing runs, exposure times, and slit position angles for all objects are listed in Tables 2.8 and 2.8. All data were taken using the Ritchey-Chrétien Spectrograph with a moderate-resolution grating, KPC-18C, in the first order along with the GG-475 blocking filter. The wavelength range was 1700 Å, allowing measurements of both the Na I D absorption doublet and H α + [NII] emission complex in the same exposure. This combination provides an average resolution of 85 km s⁻¹ with a 1.25" slit. Median signal-to-noise ratio near Na I D was 85 per Å and ranged from 23 to 337 per Å, with seeing ranging from

¹<http://nedwww.ipac.caltech.edu/index.html>

~ 1 to $2''$ on average.

2.4 ANALYSIS

2.4.1 Line Fitting

Extraction and fitting procedures were performed as described in the original study (RVS05a), but the basic procedure will be outlined here; the method uses assumptions similar to those in a curve of growth analysis but does explicitly fit the line profiles. The spectral extraction was done while keeping a constant physical aperture size of ~ 3 kpc; this aperture size was selected to match the seeing and therefore reduce host galaxy contamination as much as possible. The reduction and calibration were performed using standard IRAF reduction packages. HeNeAr lamps were used for wavelength calibration and stars such as G191-B2B and BD+25 4655 were used as flux standards.

Once the spectra were reduced and calibrated, the region containing the Na I D absorption doublet, as well as the neighboring He I $\lambda 5876$ emission line, was isolated. A Levenberg-Marquardt fitting routine was used to fit one to two components to the He I emission and the Na I D absorption doublet line profile. For emission lines, the formula used to fit the intensity of the line was:

$$I(\lambda) = 1 + Ae^{((\lambda-\lambda_0)c/(\lambda_0b))^2} \quad (2.1)$$

where the amplitude, A , the Doppler parameter, b ($b = \sqrt{2}\sigma$), and the central wavelength, λ_0 , were free parameters. For absorption lines, the formula used to fit

was:

$$I(\lambda) = 1 - C_f(\lambda) + C_f(\lambda)e^{-\tau_1(\lambda)-\tau_2(\lambda)}, \quad (2.2)$$

where C_f is the covering fraction of the line (see Section 2.7.1.2), and τ_1 and τ_2 represent the optical depths of each of the two lines of the Na I D doublet; τ_1 corresponds to the line at 5896 Å, and $\tau_2 = 2\tau_1$. In general, the optical depth τ_i is given by:

$$\tau_i(\lambda) = \tau_{i,0}e^{-(\lambda-\lambda_{i,0})^2/(\lambda_{i,0}b/c)^2}. \quad (2.3)$$

Equations 2 and 3 were used to fit each line of the Na I D doublet. For each Na I D doublet pair, the covering fraction, C_f , central optical depth and wavelength of the red line (τ_1 and $\lambda_{0,1}$), and line width, b , were free parameters in the fit. Covering fraction was assumed to be independent of wavelength (and the same for both doublet lines), and the optical depths of the two doublet lines are fixed by atomic physics (as stated above: $\tau_2 = 2\tau_1$). Because of these constraints, and the assumption of a Gaussian in optical depth space, both C_f and τ can be constrained simultaneously for each doublet. It should be noted, however, that there is still some anticorrelation between C_f and τ in the fit due to uncertainty in line shape and relative intensities. In the case of multiple, Gaussian velocity components, each velocity component arises in both lines of the doublet, so that C_f and τ can be constrained independently for each velocity component.

Initial guesses for these parameters were supplied to the fitting program and a best fit was determined and plotted. Either one or two components were used to fit the He I emission line. Unless an absorption fit with two separate velocity compo-

nents (corresponding to two separate Na I D doublets) was considerably better than a fit with one velocity component, only one velocity component (one Na I D doublet) was used to fit the absorption features. Only six objects showed convincing evidence for a two velocity components in absorption. Examples of the deblending of the Na I D feature for two Seyfert 1 and two Seyfert 2 objects can be seen in Figure 2.1. After fitting was performed, a Monte Carlo simulation with 1000 iterations was then run, in order to determine the parameter errors.

Particular care is needed when fitting the He I emission at 5876 \AA , since the He I emission line in these objects is generally quite broad and has multiple components. So, for those objects showing He I emission lines, the $H\alpha + [\text{NII}]$ complex was also examined to verify the accuracy of the fit to He I. An interpolation script was written in IDL to subtract out the $[\text{NII}] \lambda\lambda 6548, 6583$ features and thus isolate the $H\alpha$ line. The resulting $H\alpha$ line was generally fit using two components, one narrow and one broad. The He I + Na I D complex was then refit, but this time parameters for He I emission lines were constrained to be those of the $H\alpha$ line. The results from the fits with fully fixed parameters (“fixed”) were then compared to those from the fits with free-floating parameters (“free”); agreement is observed within 2-5%. Again, the errors on these parameters were determined from the Monte Carlo simulations after all fits were completed. The reduced χ^2 for the two types of fits are compared in Figure 2.2. There are fewer points farther away from a reduced χ^2 of unity for the free-floating fit. We therefore choose to use the results from the free-floating fits in the following discussion (this is further justified in the next section).

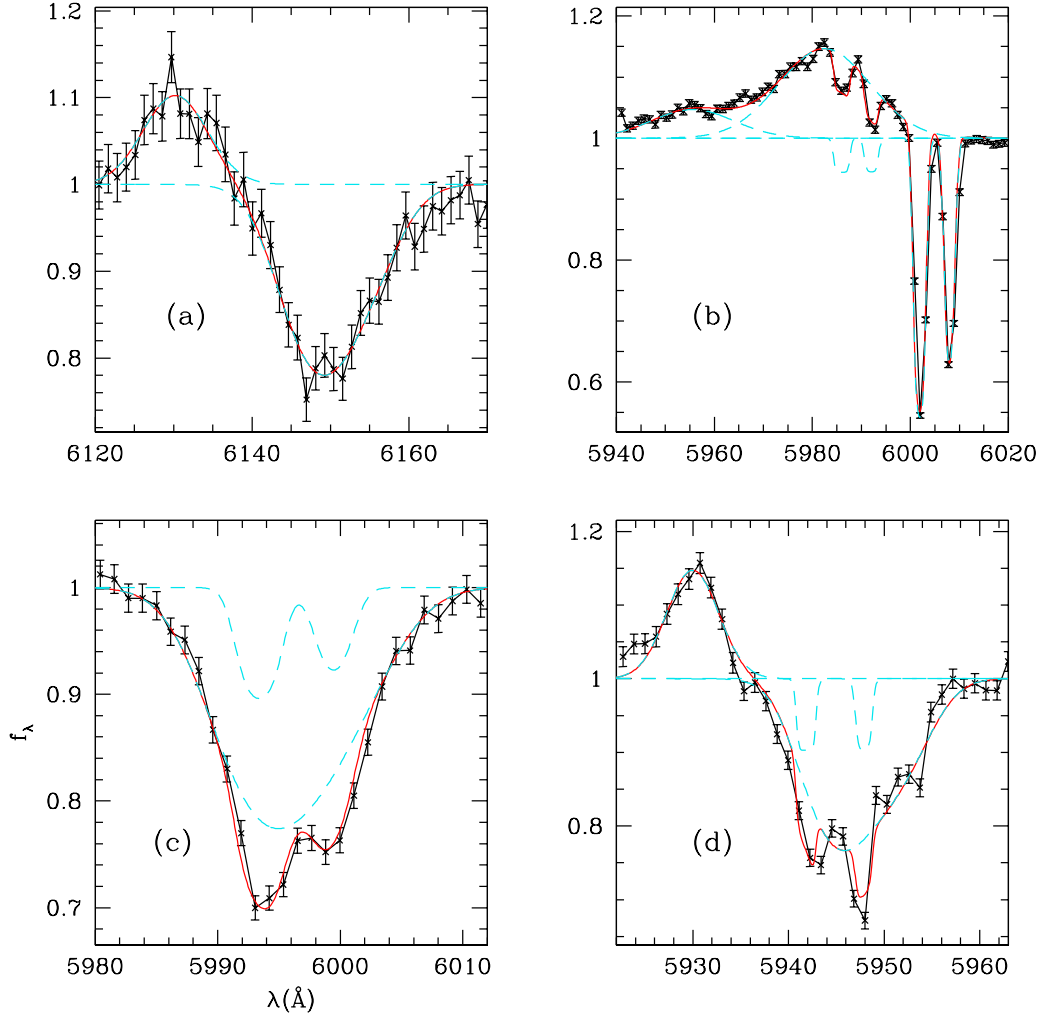


Figure 2.1: Binned data showing the He I and Na I D complexes, plotted on an intensity versus wavelength scale, for four objects. In all cases, blue dashed lines correspond to the individual He I or Na I D line fits, with solid red lines showing the combined He I and Na I D fit for the object. Panels (a) and (b) show two Seyfert 1 galaxies, Mrk 506 and Mrk 6. Mrk 506 is fit with one He I and one Na I D velocity component. Mrk 6 is fit with two He I components and two Na I D velocity components. Panels (c) and (d) show two Seyfert 2 galaxies, Akn 79 and NGC 3786. Akn 79 does not have a resolvable He I line; two Na I D components, one narrow and one broad, are used in the fit. NGC 3786 is fit with one He I component and two Na I D, one narrow and one broad. Note that the data for NGC 3786 are low signal-to-noise compared to most other objects, and thus the lines are not quite as well constrained.

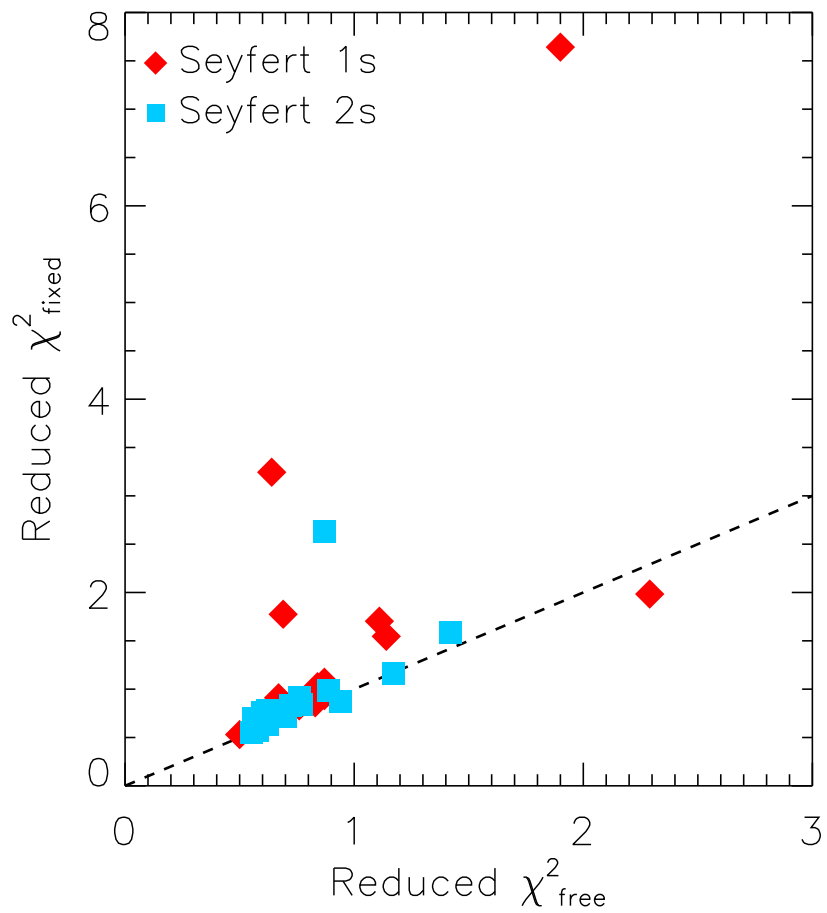


Figure 2.2: Reduced χ^2 values for free-floating and $\text{H}\alpha$ -fixed He I parameter fits. See Section 2.4.1 for an explanation of these fits. The dashed black line corresponds to equal χ^2 values. The free fits generally give lower χ^2 . The results from these fits were adopted in the present study.

2.4.2 Velocities

Once fitting was done, velocities for these Na I D absorption lines were calculated, relative to the systemic velocities using redshifts as outlined in Section 2.2.1. In the following, Δv is the velocity difference between the Na I D velocity centroid measured in the fit and the systemic Na I D velocity. Errors were propagated through both from the fit and the redshift measurement. A “maximum” velocity of $\Delta v_{max} \equiv \Delta v - \text{FWHM}/2$, which takes into account both the shift and width of the absorption line, was also computed. Values of Δv and Δv_{max} were compared for values resulting from the free He I fit and the fixed He I fit in order to determine the impact of fixing the He I parameters to those of H α . Plots of those comparisons are displayed in Figure 2.3. The agreement is good, with only three objects showing values that are not equal within the uncertainties. Of those, only one has $|\Delta v_{\text{free}} - \Delta v_{\text{fixed}}| > 50 \text{ km s}^{-1}$, which would change its outflow or inflow classification. In all three of those outlying cases, the He I line appears to be broader than the H α line. This is plausible, since all of these objects are Seyfert 1 galaxies and so collisional and radiative transfer effects in the broad line region may affect the He I profile in a different way than the H α profile. As there is little significant difference between the free-floating and fully-fixed fits, our adoption of the free-floating fits in Section 2.4.1 seems appropriate.

After velocities were calculated, a detection criterion of $\Delta v < -50 \text{ km s}^{-1}$ was used to determine whether or not an object possesses an outflow. Similarly, $\Delta v > 50 \text{ km s}^{-1}$ was used as the cutoff for the detection of an inflow. A $2\text{-}\sigma$ threshold in

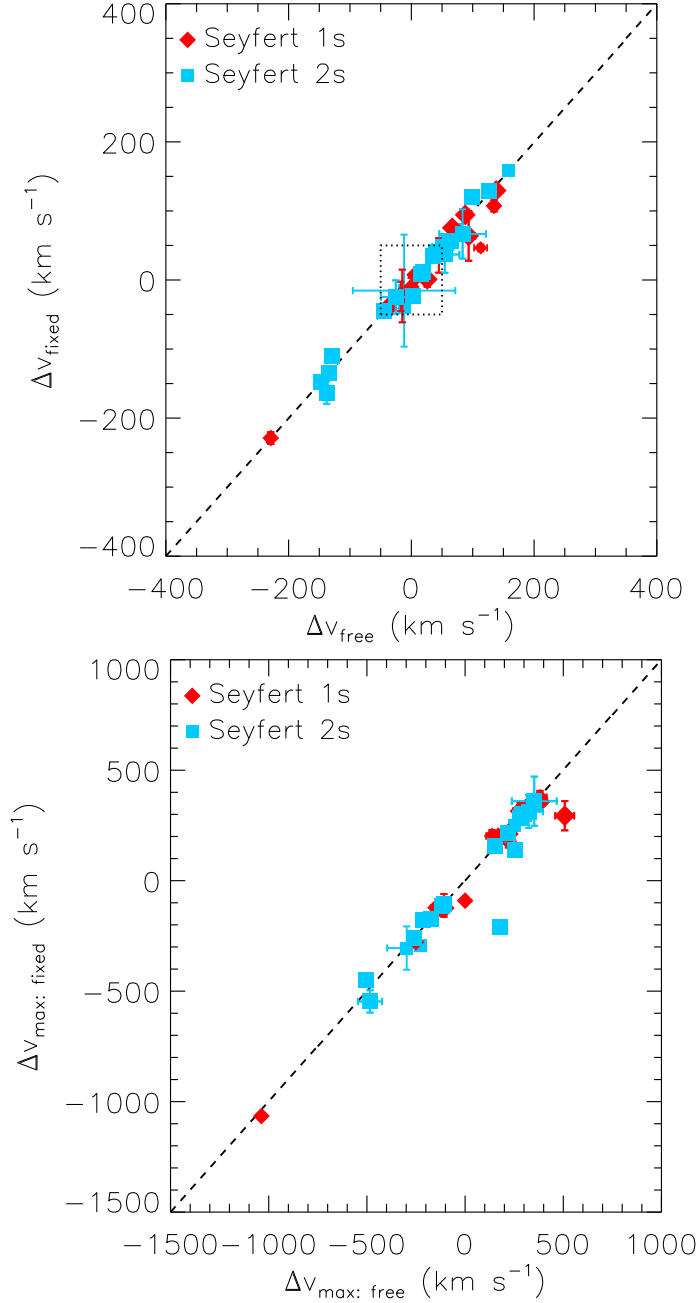


Figure 2.3: Top: Δv for $H\alpha$ -fixed He I fit versus Δv for free-floating He I fit. Smaller points are objects with larger redshift uncertainty. Dashed black line through center corresponds to equal fixed and free values, and all points outside dashed black box have $|\Delta v| > 50 \text{ km s}^{-1}$. Bottom: Same, but for Δv_{max} . The two types of fits give very similar results.

measurement uncertainty ($|\Delta v| > 2\delta(\Delta v)$, where $\delta(\Delta v)$ is the measurement error) was also required for inflow/outflow classification, but this did not eliminate any objects from being classified as showing inflow or outflow. As outlined in the initial study (RVS05a), the 50 km s⁻¹ cutoff accounts for potential contamination from errors in wavelength calibration ($\sim < 10$ km s⁻¹), fitting (~ 10 km s⁻¹), redshift measurements (~ 10 -15 km s⁻¹), and the possibility of small blue- and redshifts due to gas in rotation. Fit parameters and derived velocities are listed in Tables 2.8 and 2.8.

2.4.3 Column Densities

The optical depth τ and Doppler parameter b as determined by the fitting function were used to calculate column densities of Na I D and H along the line of sight. As described in Spitzer (1978), the column density of Na I D in cm⁻² is given by:

$$N(\text{Na I D}) = \frac{\tau_{1,c} b}{1.497 \times 10^{-15} \lambda_1 f_1}, \quad (2.4)$$

where f_1 is the oscillator strength, λ_1 is the rest frame vacuum wavelength (\AA), and $\tau_{1,c}$ is the central optical depth of the Na I D $\lambda 5896$ line. The Doppler parameter, b , is in units of km s⁻¹. Values of $f_1 = 0.3180$ and $\lambda_1 = 5897.55 \text{ \AA}$ were taken from Morton (1991).

To properly calculate the column density of hydrogen, we must correct for the effects of dust depletion and ionization. This process is also outlined in RVS05a, and uses empirical results that assume Galactic depletion and an ionization fraction

of 0.9. The formula used is:

$$N(\text{H}) = N(\text{Na I})(1 - y)^{-1}10^{-(a+b)} \quad (2.5)$$

Column densities are again given in cm^{-2} , y is the ionization fraction, and a and b are the Na abundance and depletion onto dust in the object for which calculations are being performed, respectively. Whereas a near-IR luminosity-metallicity relation was used to determine Na abundance in the previous RVS05b and RVS05c studies, we here assume that these objects have solar Na abundance. Calculated column densities for each object can be found in Tables 2.8 and 2.8.

2.4.4 Stellar Na I D Contribution

Stellar Na I D absorption may contribute to the observed Na I D feature. Stellar features from other elements may also contaminate the measurements if they are located close to the Na I D feature. The original study used a scaling relation between Na I D and Mg I b equivalent width to determine the stellar Na I D contribution, as Na and Mg are created in a similar fashion (RVS05a). However, the spectral range for our data begins at roughly 5500 Å and so does not include that Mg I b triplet, so we must use the other method outlined in that study: stellar population synthesis models. As in RVS05a, we used the population synthesis code (Sed@.0 ²) of González Delgado et al. (2005), which combines a young (40 Myr), instantaneous burst stellar population with an old (10 Gyr) population. One model uses a stellar mass ratio of 10%/90% for young *versus* old populations, and the other

²<http://www.iaa.es/~rosa/> and <http://www.iaa.es/~mcs/sed@>

uses 1%/99%. In order to enhance weak stellar features, the spectra were boxcar smoothed by 150 km s^{-1} and convolved with a $\sigma = 200 \text{ km s}^{-1}$ Gaussian. Our spectra were emission subtracted, using fitting parameters to remove He I and leave only the Na I D absorption. They were then overlaid with the stellar population synthesis models.

Almost all objects with suspected outflows or inflows showed absorption that was much deeper than the stellar absorption alone. The extreme examples of Mrk 352 and Mrk 6 are shown in Figure 2.4. In Mrk 352, the results from stellar population synthesis show a high likelihood that the bulk of the Na I D absorption is stellar. In contrast, Mrk 6 shows a definite high-velocity outflow.

2.5 RESULTS: OUTFLOWS

2.5.1 Seyfert 2

Figure 2.5 shows the He I and Na I D complexes for all of the 17 Seyfert 2 galaxies in this study, plotted on a velocity scale based on Na I D $\lambda 5890$ systemic. Tables 2.5 and 2.8 list the measured properties for each Na I D outflow velocity component and overall outflow averages, combined with data for Seyfert ULIRGs from RVS05c.

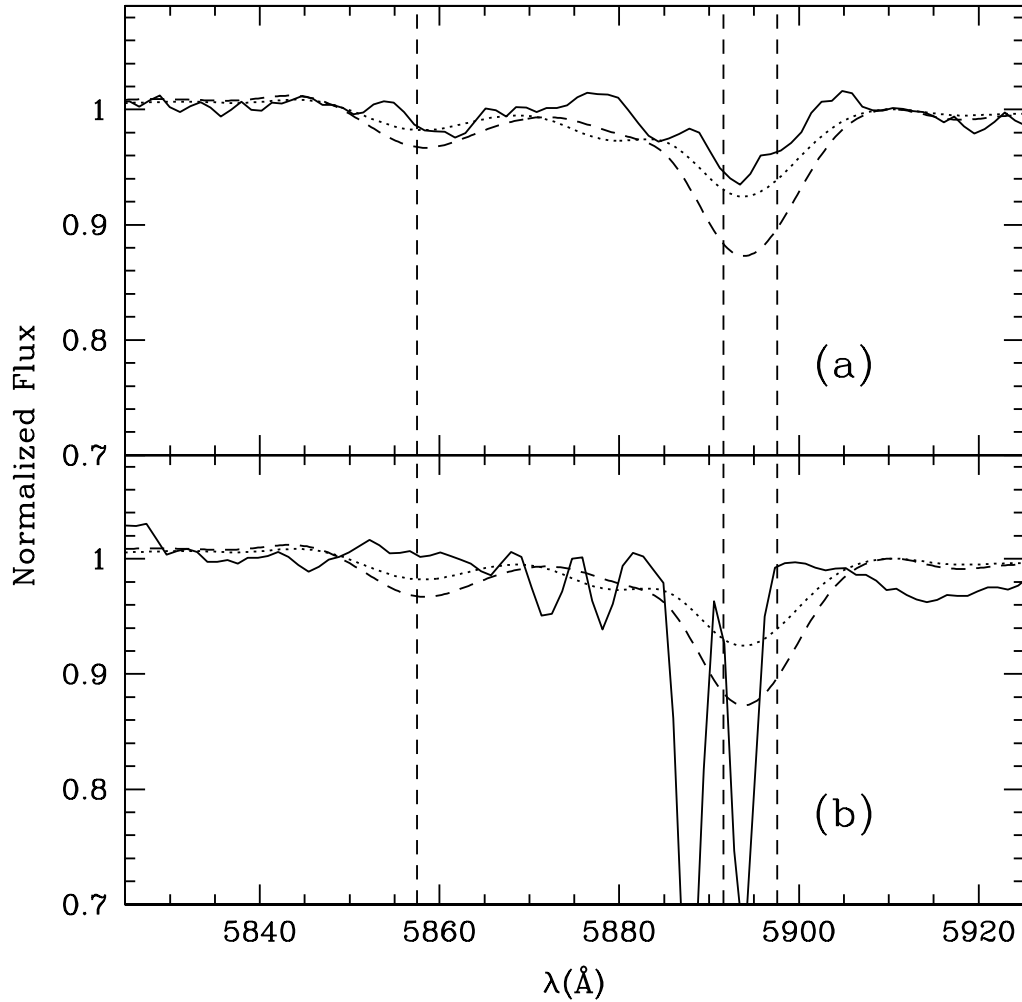


Figure 2.4: Spectra of two Seyfert 1 galaxies, (a) Mrk 352 and (b) Mrk 6, in the Na I D region. These spectra were He I emission line subtracted, boxcar smoothed, and normalized to unity at 5910 Å. The dotted line shows the 10/90 model (10%/90% stellar mass ratio for a young 40 Myr instantaneous burst population compared to an older 10 Gyr population) and the dashed line shows the 1/99 model (1%/99% young to old stellar mass ratio), as outlined in Section 2.4.4. Strong stellar features are marked with dashed vertical lines. Mrk 352 shows absorption that is weaker than the stellar models, suggesting that the absorption is only stellar or atmospheric (the feature at ~ 5880 Å was also determined to be atmospheric). In contrast, Mrk 6 shows very strong absorption, which is consistent with predominant interstellar origin.

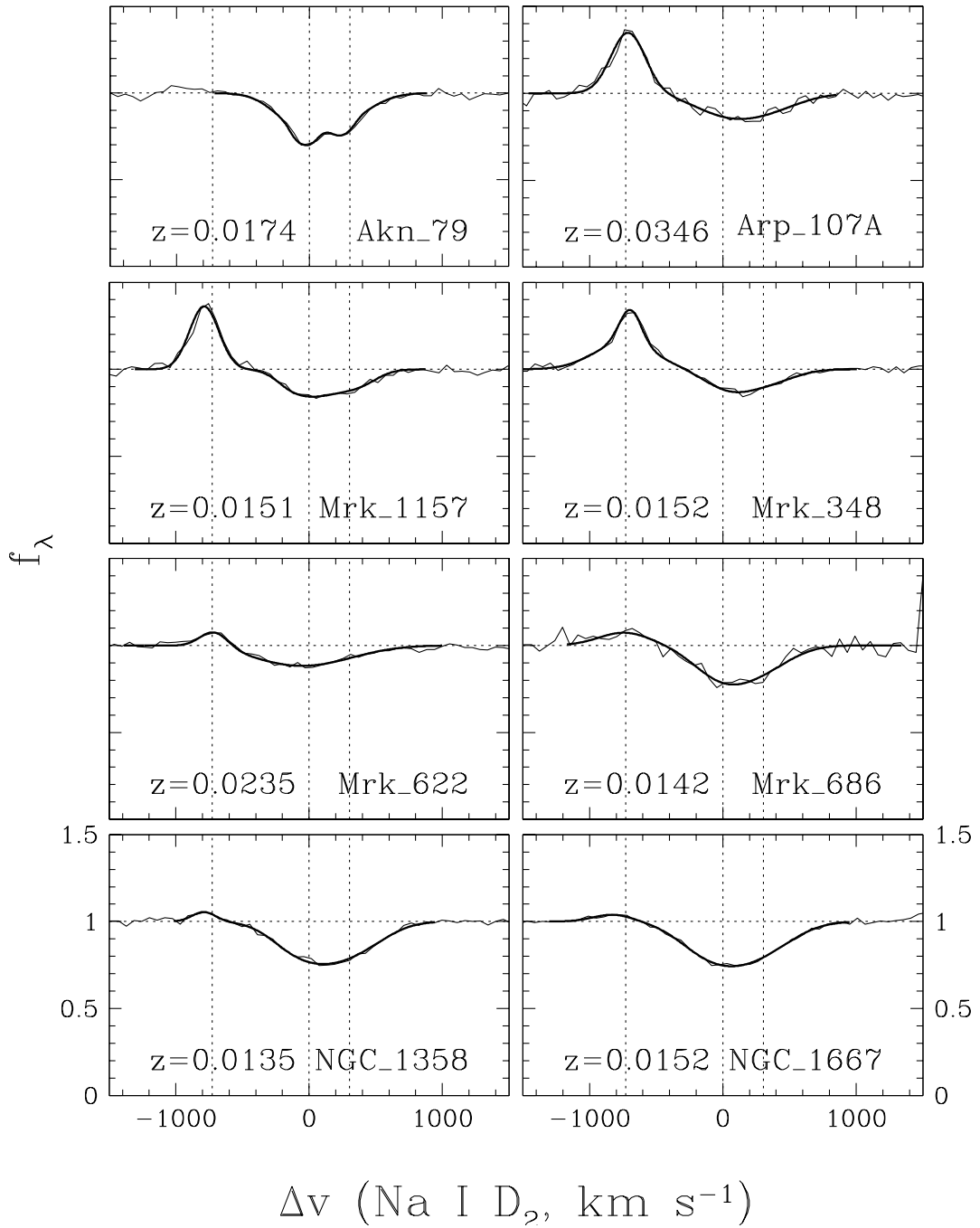
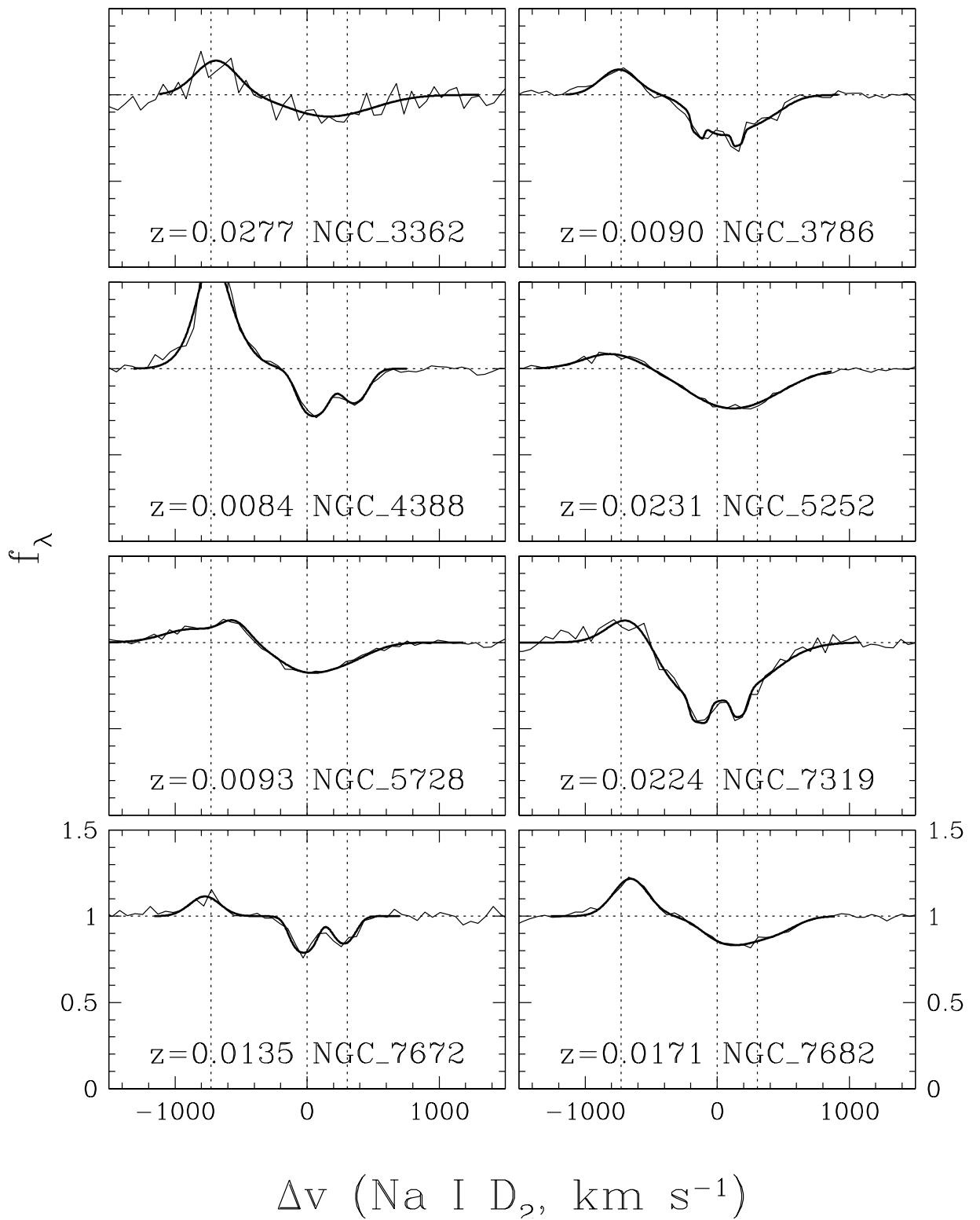
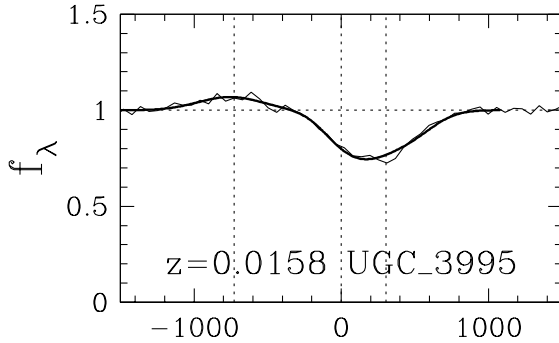


Figure 2.5: Spectra of the He I emission + Na I D absorption region in infrared-faint Seyfert 2 galaxies. These spectra are plotted on a velocity scale based on the systemic Na I D $\lambda 5890$ velocity. The thin lines are smoothed original spectra, and thick lines are fits to the data. The vertical dotted lines show the locations of the Na I D $\lambda\lambda 5890, 5896$ doublet and He I $\lambda 5876$ emission line in the object's rest frame.





$$\Delta v \text{ (Na I D}_2\text{, km s}^{-1}\text{)}$$

Out of a total of 17 Seyfert 2 galaxies, we detected blueshifted Na I D absorption with $\Delta v < -50 \text{ km s}^{-1}$ in 3 objects, for an outflow rate of $18 \pm 9\%$. No objects were ruled out by the $2\text{-}\sigma$ criterion in measurement uncertainty, which requires $|\Delta v| > 2\delta(\Delta v)$ for a detection (see Section 2.4.2). Of those objects which fit the outflow criteria, only one, NGC 7319, showed convincing evidence for two velocity components in absorption. The implications of this low detection rate are discussed in Section 2.7.1.

Velocities for these objects were all within 20 km s^{-1} of each other, ranging from -130 to -148 km s^{-1} . The maximum velocity, $\Delta v_{max} \equiv \Delta v - \text{FWHM}/2$, showed a much larger range (due to the broader range of Doppler parameters), from -176 to -504 km s^{-1} , with NGC 7319 showing the largest Δv_{max} (Table 2.8). We further discuss these results in Section 2.7.1.

Previous studies have shown that it is common for Seyfert 2 galaxies to have asymmetric emission lines with extended blue wings. These asymmetries are generally believed to be the result of outflowing gas in the narrow line region of the AGN, and outflowing gas in the NLR has been spatially resolved in both Seyfert 1 and

Seyfert 2 galaxies [Walker (1968), Wilson & Ulvestad (1987), Ebstein et al. (1989), Veilleux et al. (1991a,91b,91c), Ruiz et al. (2005)]. This emission line asymmetry, however, is not an unambiguous indicator of outflow in the way absorption is since one cannot differentiate between outflowing line-emitting material in front of the nucleus from infalling material on the far side of the nucleus. Blue-wing emission asymmetries can only be interpreted as outflow if we are absolutely sure we are not seeing the opposite side of the object [Rodríguez-Ardila et al. (2006)]. The primary focus of our study is blueshifted Na I D absorption, but it is of interest to look for blue-wing emission line asymmetry in our Seyfert 2 galaxies to see if it is at all correlated with our findings on Na I D outflows. In RVS05c, 75% of Seyfert 2 nuclei showed blue emission-line asymmetry (BELA), compared to a 45% Na I D outflow detection rate.

We have used [NII] $\lambda\lambda 6548, 6583$ to look for BELA in our objects (the high-ionization [OIII] $\lambda 5007$ line most commonly used in BELA detection is not within our wavelength range). The [NII] $\lambda\lambda 6548, 6583$ lines were separated from $H\alpha$ by taking the blue wing of the [NII] $\lambda 6548$ line and the red wing of the [NII] $\lambda 6583$ line, and plotting them together about $\Delta v = 0$. The two wings were then scaled appropriately to match each other in intensity, and BELA determination was done by visual inspection. 5 out of 17 Seyfert 2 galaxies (29%) showed evidence for BELA. The most obvious case of BELA is NGC 5252. Of those which show BELA, only one (NGC 7319) has been determined to have an Na I D outflow, and one (Mrk 348) actually shows a Na I D inflow (Section 2.6.1), though it is the least asymmetric of all the BELA objects. Those five objects, along with a comparison object with

a Na I D outflow but no BELA (Mrk 622), are shown in Figure 2.6. Another object (NGC 3786; not shown in the figure) shows prominent red-wing asymmetry; this object presents an Na I D outflow rather than an inflow. Overall, we find no obvious correlation between emission and absorption signatures of outflow, although the statistics are poor. Moreover, we cannot formally rule out the possibility that the difference in outflow and BELA detection rates is simply due to our use of [NII] as a BELA probe since BELAs are more often seen in high-ionization lines like [OIII] than in low-ionization lines like [NII] [Veilleux (1991a)].

2.5.2 Seyfert 1

Figure 2.7 shows the He I and Na I D complexes for all of the 18 Seyfert 1 galaxies in this study, plotted on a velocity scale relative to Na I D $\lambda 5890$ systemic. As for the Seyfert 2 galaxies, Tables 2.5 and 2.8 list the measured properties for each Na I D outflow velocity component and overall outflow averages.

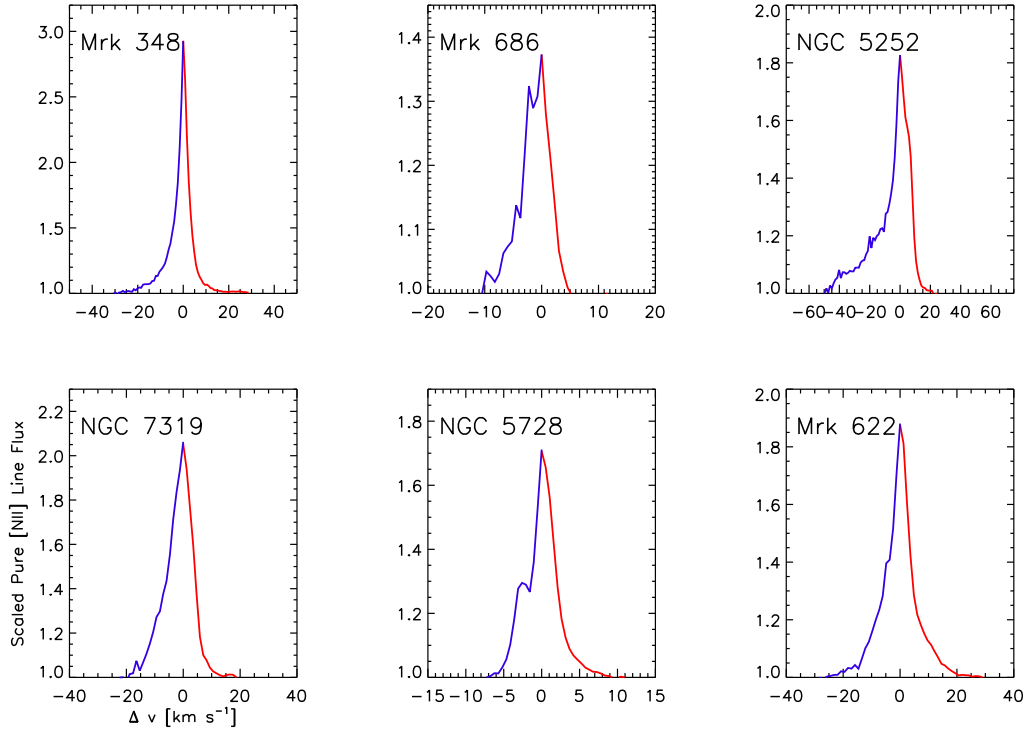


Figure 2.6: Plots showing the [NII] $\lambda 6548$ line for $\Delta v < 0$ and (properly scaled) [NII] $\lambda 6583$ line for $\Delta v > 0$ in 5 Seyfert 2 galaxies suspected of having blue emission-line asymmetry. The velocity scale is relative to systemic, and colors correspond to blue wing and red wing. The first four objects have noticeable blue-wing asymmetry, and the fifth (NGC 5728) shows a prominent blue bump in the emission line. The lower right panel (Mrk 622) is an example of an object which does not show an obvious asymmetry.

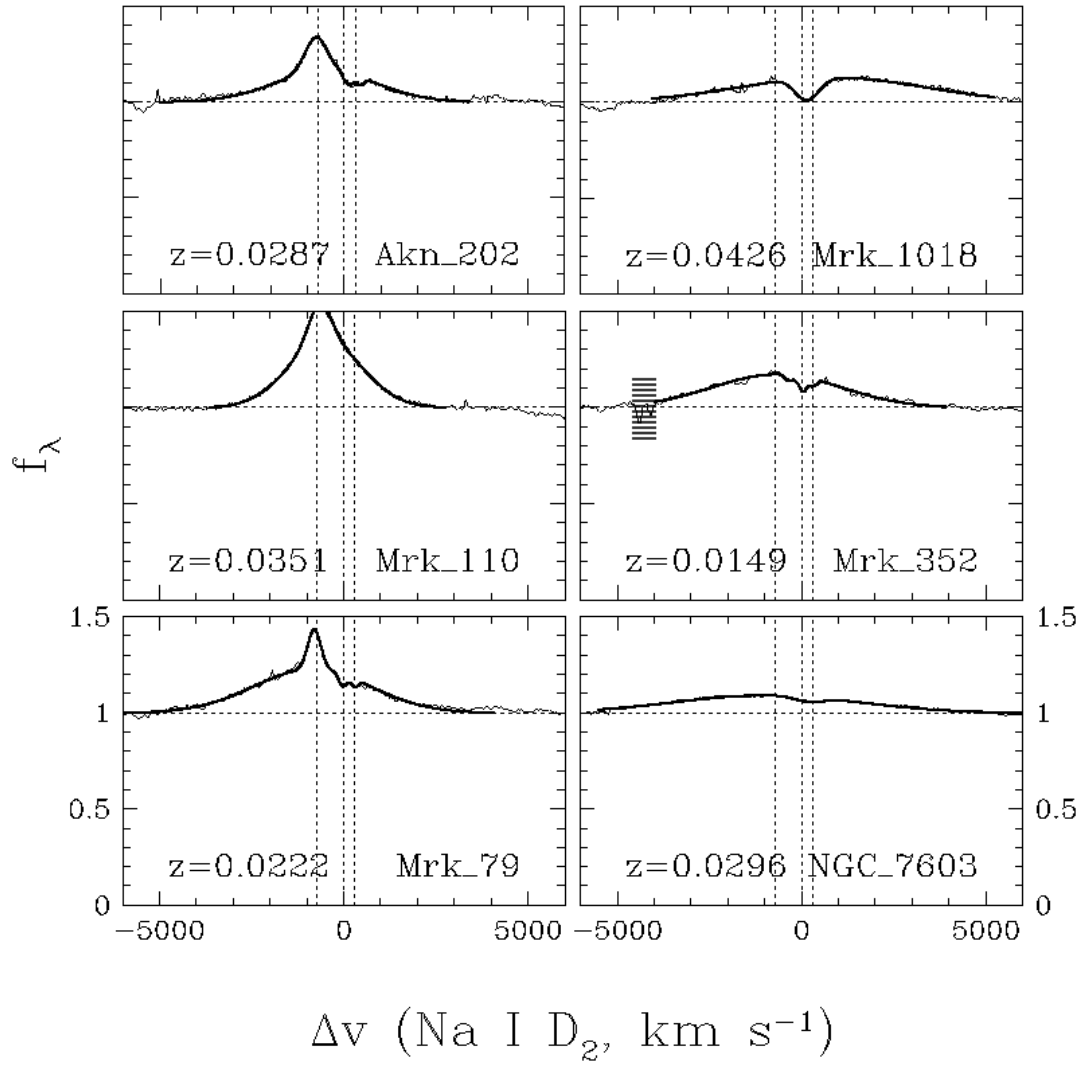
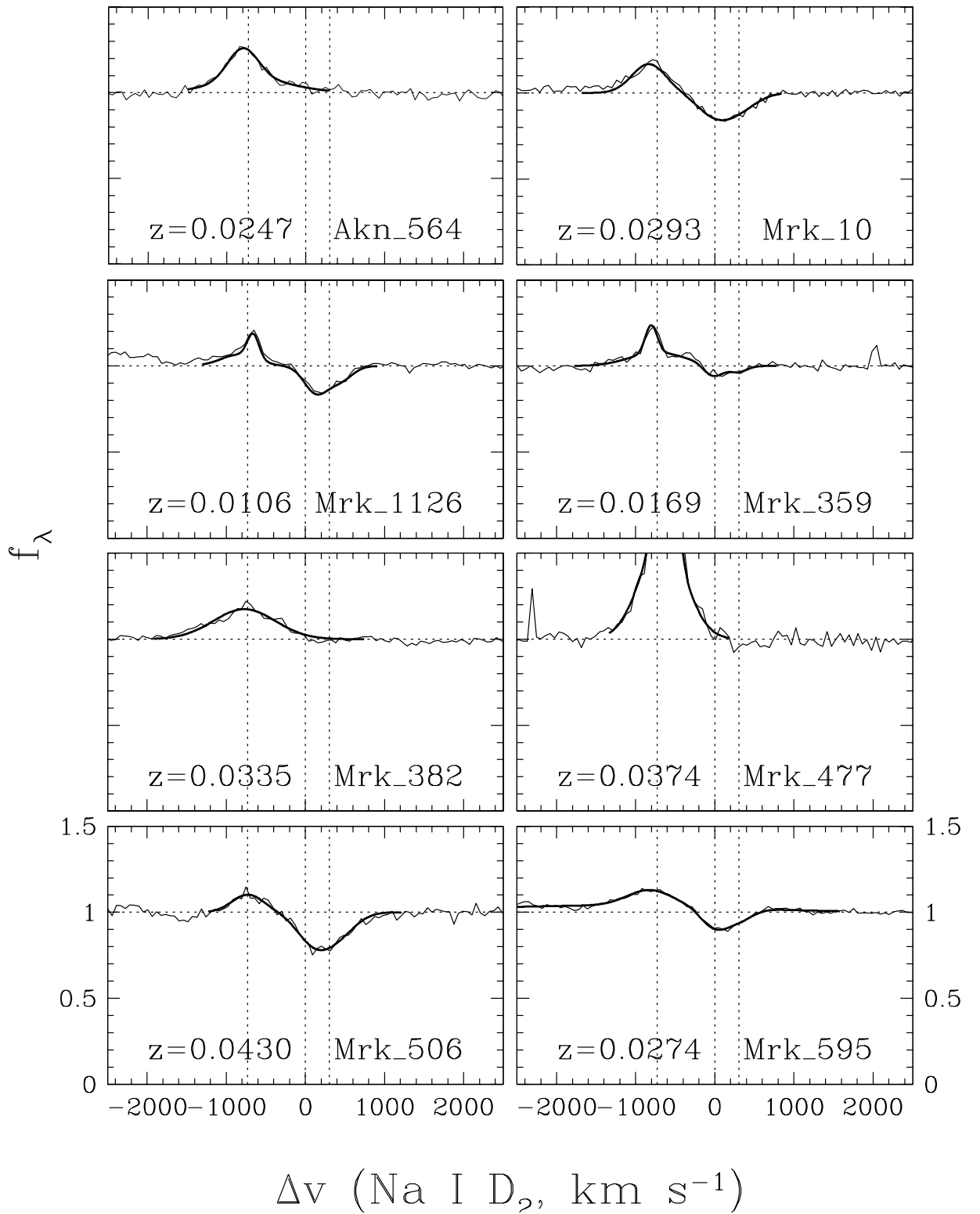
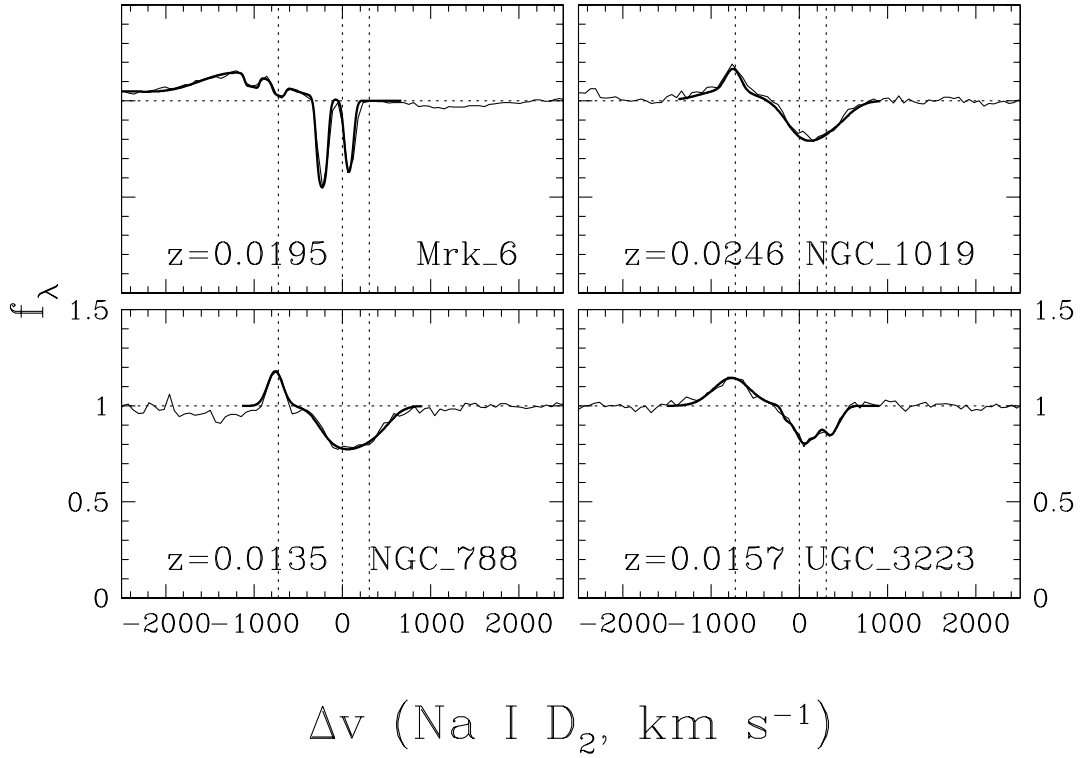


Figure 2.7: Spectra of the He I emission + Na I D absorption region in infrared-faint Seyfert 1 galaxies. See Figure 2.5 for details. A region of horizontal lines is used to block out atmospheric absorption in the case of Mrk 352.





Only 1 of the 18 Seyfert 1 galaxies was found to have blueshifted absorption with $\Delta v < -50 \text{ km s}^{-1}$, and as with Seyfert 2 inflows, the $2\text{-}\sigma$ criterion did not eliminate any objects (Section 2.4.2). The outflow detection rate is therefore only $6 \pm 6\%$.

Mrk 6 was the only Seyfert 1 galaxy determined to have an outflow. Two velocity components were detected, each with a velocity higher than those for the Seyfert 2 galaxies: one component with -229 km s^{-1} and one with -1024 km s^{-1} , giving a $\Delta v_{max} = -1037 \text{ km s}^{-1}$ (Table 2.8). See Section 2.7.1 for a discussion of these results.

2.6 RESULTS: INFLOWS

While only a few objects in our sample showed blueshifted Na I D absorption, a large percentage of objects in each Seyfert group showed redshifted Na I D absorption. We consider this redshifted absorption to be an unambiguous indicator of inflow, in the same way that blueshifted absorption is an unambiguous outflow indicator, since the continuum source (in this case the galaxy nucleus) must be behind the absorber. This section describes the results on inflow detection rates and kinematics. Table 2.7 lists the measured properties of these inflows in individual objects. The implications of these results are discussed in Section 2.7.2.

2.6.1 Seyfert 2

The same general detection criteria used for determining outflows were used for determining inflows: We required a redshifted absorption of $\Delta v > 50 \text{ km s}^{-1}$, along with the $2\text{-}\sigma$ criterion (Section 2.4.2). Out of the 17 Seyfert 2 galaxies, 6 showed Na I D inflow, for a detection rate of $35 \pm 11\%$. Velocities for these six objects spanned the range from 51 to 127 km s^{-1} . The maximum velocity, where in the case of inflows $\Delta v_{max} \equiv \Delta v + \text{FWHM}/2$, ranged from 155 to 352 km s^{-1} . The largest Δv was measured for UGC 3995, although NGC 3362 has a slightly larger Δv_{max} than UGC 3995 due to the difference in Doppler parameter. The average properties of these inflows are listed in Table 2.8 and discussed further in Section 2.7.2.

2.6.2 Seyfert 1

Of the 18 Seyfert 1 galaxies, 7 showed Na I D inflow, for a detection rate of $39 \pm 12\%$, i.e. similar to that of the Seyfert 2s. Again, no objects were ruled out by the 2σ criterion (Section 2.4.2). The Seyfert 1 inflow velocities spanned a similar range to those of the Seyfert 2 velocities, from 67 to 138 km s⁻¹. The Seyfert 1 Δv_{max} values showed a broader range than that of Seyfert 2, from 169 to 507 km s⁻¹, and while Mrk 1126 has the highest Δv , NGC 7603 has the highest Δv_{max} . Again, the average inflow properties are listed in Table 2.8 and the results are discussed further in Section 2.7.2.

2.7 DISCUSSION

2.7.1 Outflows

2.7.1.1 Comparison with Previous Studies

Since the purpose of this study is to determine whether starbursts or AGN are the primary mechanism behind galactic outflows, it is important to compare the results determined here to those of RVS05c for the ULIRG Seyferts – galaxies with both starburst and AGN. As seen in Table 2.8, the detection rates for the IR-faint Seyfert 2s and Seyfert 1s are only $18\% \pm 9\%$ and $6\% \pm 6\%$, respectively, but rates were as high as $45\% \pm 11\%$ and $50\% \pm 20\%$ for the IR-luminous Seyfert 2s and 1s (RVS05c). Our detection rates are even lower in comparison to non-Seyfert ULIRGs, since rates of $80\% \pm 7\%$ and $46\% \pm 13\%$ were measured for low- z

and high- z ULIRGs in RVS05b, and a rate of 83% was reported in Martin (2005). Poststarburst galaxies have also been found to have high outflow detection rates on the order of 70% [Tremonti et al. (2007)]. The measured outflow detection rates in the IR-faint Seyfert galaxies are therefore considerably smaller than those of pure starbursting galaxies, poststarbursts, and AGN + starburst composites.

Previous observations have indicated that the outflow detection rate increases with infrared luminosity (RVS05b, [Sato et al. (2009)]). Figure 2.8 shows the outflow detection rates of the IR-faint Seyferts in our sample as well as the the IR-luminous Seyferts and starburst ULIRGs and LIRGs of RVS05b and RVS05c as a function of L_{FIR} . The increase in outflow detection rate with L_{FIR} is apparent, despite the limited range in L_{FIR} . As L_{FIR} is correlated with the star formation rate, this increase in the detection rate with L_{FIR} suggests that star formation in all of these systems is the main driver of neutral outflows detected in Na I . Geometry could also be playing a role, since AGN winds with smaller opening angles (higher collimation) would reduce the detection rate (see Section 2.7.1.2).

Histograms showing the distributions of all (negative and positive) velocities in our current data as well as those of RVS05b and RVS05c provide another point of comparison (Figure 2.9). The left panel compares the velocities of IR-faint Seyfert galaxy components from this study to the Seyfert and starburst ULIRGs & LIRGs of RVS05b and RVS05c. We can safely rule out rotation as being a primary cause for the motion of the Na I D gas based on the fact that we do not observe a symmetry about zero velocity in these histograms. Were rotation the dominant gas motion, we should observe roughly equal amounts of blueshifted and redshifted gas in each

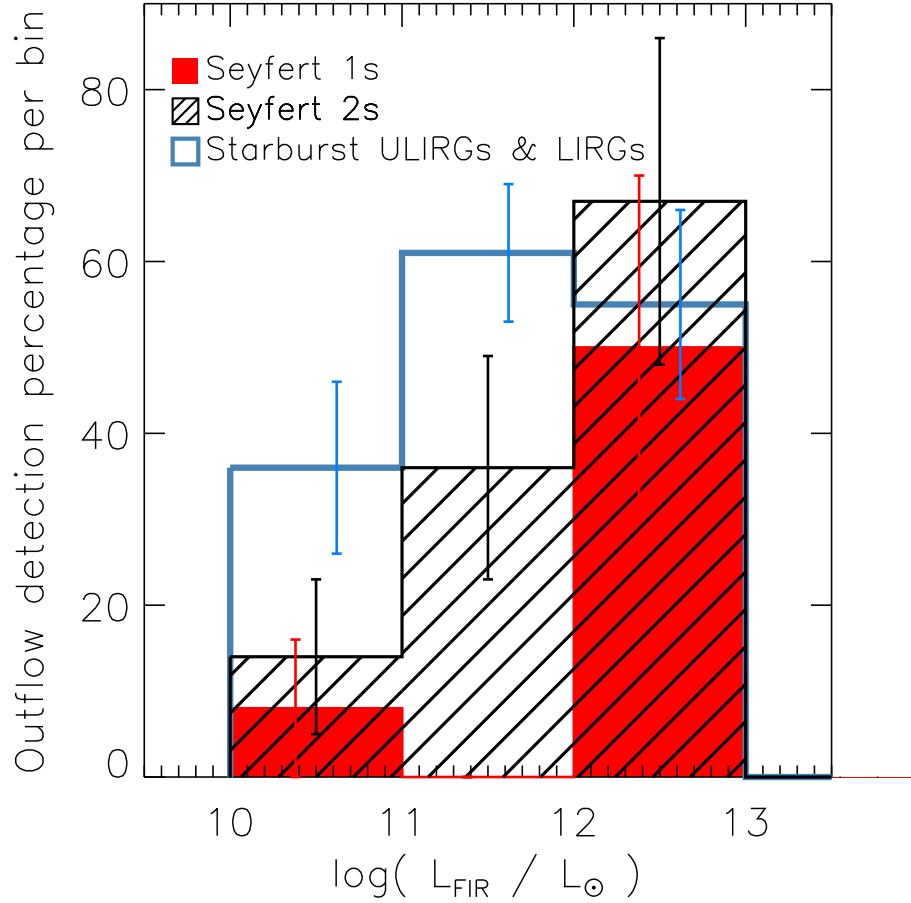


Figure 2.8: Histogram showing the fraction of Seyfert 1s, Seyfert 2s, and starburst ULIRGs and LIRGs with outflows as a function of L_{FIR} . The Seyfert categories include both IR-faint Seyferts from this study and IR-luminous Seyferts from RVS05c. Starburst ULIRGs & LIRGs are from RVS05b. The error bars are 1σ , assuming a binomial distribution. Note the trend of increasing outflow detection rate with increasing L_{FIR} for both starbursts and Seyferts.

object and in the overall distributions shown in Figure 8, assuming the Na I D gas is distributed more or less symmetrically around the center of rotation and is unaffected by severe differential obscuration. Negative velocities are found in a much higher percentage of IR-luminous objects (Seyferts of RVS05c and starbursts of RVS05b) than IR-faint objects, again indicating that outflows are both stronger and more frequent on average in objects with high SFR. The right panel in Figure 2.9 combines together the IR-faint and IR-luminous Seyferts from this study and RVS05c and compares them to the starbursts of RVS05b. In terms of the negative velocities, the results for Seyfert 1 and Seyfert 2 galaxies are quite different, with Seyfert 2 galaxies showing similar outflow percentages to those of the ULIRGs & LIRGs. This suggests a physical connection between the mechanisms that drive outflows in Seyfert 2s and starbursting galaxies and a physical difference between the mechanisms that cause outflows in Seyfert 1s and Seyfert 2s. Interestingly, studies of *ionized* gas outflows have not found such a dichotomy in velocities between Seyfert 1s and Seyfert 2s (e.g., Ruiz et al. (2001,05), Veilleux et al. (2005), Das et al. (2007), and references therein). This suggests that the neutral gas probed by our Na I D observations is not kinematically related to the ionized material of the NLR. This difference is even more obvious when we also consider our results on positive (inflow) velocities (Section 2.7.2.1).

Rigorous statistical tests confirm these results. Kolmogorov-Smirnov (K-S) and Kuiper tests were both used, as the K-S test has an inherent bias in terms of differences in the mean and the Kuiper test does not. Low values reported by both of these tests can help rule out two sets of data having the same parent distribution.

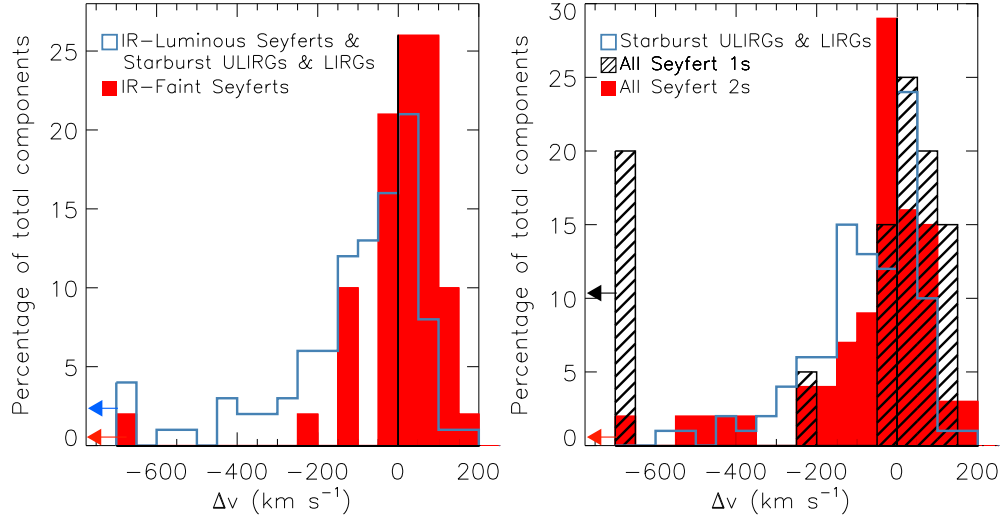


Figure 2.9: Top: Histogram showing the percentage of velocity components as a function of Δv for the IR-faint Seyferts from this study, the IR-luminous Seyferts from RVS05c, and the starburst ULIRGs & LIRGs from RVS05b. Objects at $\Delta v = -700$ km s⁻¹ actually have $\Delta v \leq -700$ km s⁻¹; the axis is truncated since most components have $\Delta v > -700$ km s⁻¹. Solid black line at $\Delta v = 0$ highlights the division between inflows and outflows. Note the lack (excess) of outflowing (infalling) components in IR-faint Seyferts relative to the other objects. Bottom: Same as left, but the IR-faint Seyferts from this study and IR-luminous Seyferts from RVS05c have been combined together and divided into Seyfert types. Note the excess of infalling and high-velocity outflowing components among Seyfert 1 galaxies.

Results of these tests are listed in Table 2.9. The small values of $P(\text{null})$ for Δv and Δv_{max} when comparing IR-faint and IR-luminous Seyferts suggest that they do not come from the same parent distribution. A more significant comparison comes from combining together the results for the IR-faint Seyfert galaxies from this study and those for the IR-luminous Seyfert galaxies from RVS05c, and comparing them with those for the starburst ULIRGs and LIRGs from RVS05b. The same statistical tests were performed on these distributions, first using all velocities, then the outflowing components only. The results are listed in Tables 2.10 and 2.11, respectively. The results in Table 2.10 indicate that Seyferts and starbursts do not share the same parent velocity distributions; we return to this point in Section 2.7.2. When considering only the outflowing components, all comparisons show low probability of originating from the same parent distribution except when the Seyfert 2 galaxies are compared with the starburst ULIRGs & LIRGs. In that case, both the K-S and Kuiper tests return large $P(\text{null})$ values. This confirms quantitatively that the outflows in these two classes of objects may arise from the same physical process.

Figure 2.10 displays plots showing Δv_{max} as a function of far-IR luminosity (correlated with star formation rate) and of galactic circular velocity (correlated with galactic mass) for Seyferts from this study, IR-luminous Seyferts from RVS05c, starburst LIRGs & ULIRGs from RVS05b, and four starburst dwarf galaxies from Schwartz & Martin (2004). The four dwarfs were added in order to see if low-mass galaxies follow the same trends as high-mass systems. The IR-faint Seyfert 2 galaxies seem to follow the same trends as the IR-bright galaxies, with Δv_{max} increasing with

both SFR and galactic mass, while the outflow velocities of all Seyfert 1 galaxies lie above these trends. This again suggests a fundamental difference in the way the winds in IR-faint/bright Seyfert 1 galaxies are powered compared with the winds in IR-faint/bright Seyfert 2 and starburst galaxies. We return to this issue in Section 2.7.1.2.

2.7.1.2 Outflow Dynamics

Another useful comparison between IR-faint and IR-luminous Seyferts is to look at the dynamical properties in addition to the kinematics. Using calculated covering fraction, column density, and velocities, we can estimate the mass, momentum, and kinetic energy of the neutral gas phase of the ISM being probed by those winds. We follow the method outlined in the original study (RVS05b), which made the assumption that the outflows are spherically symmetric mass-conserving free winds, with a velocity and instantaneous mass outflow rate which do not depend on radius within the wind and which are zero outside the wind. This method also assumed that the wind is a thin shell with a uniform radius of 5 kpc. This value was based on actual spatial measurements in some of the objects of RVS05c, but such spatial measurements are not available for our IR-faint Seyfert galaxies. In the present study, we use a 5 kpc radius for both the Seyfert 2 and Seyfert 1 galaxies. This is different from the radius of 10 pc that was used for the Seyfert 1 galaxies in the original study (RVS05c); the radius in IR-faint Seyfert 1s was chosen to be the same as for IR-faint Seyfert 2s to facilitate comparisons within the IR-faint

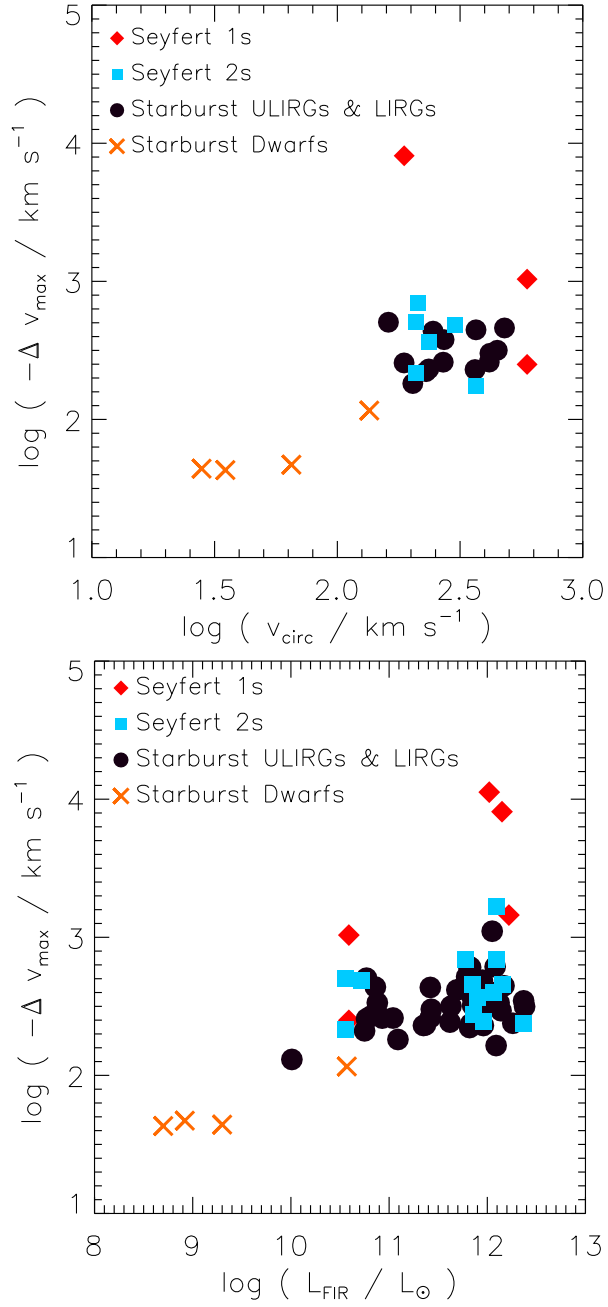


Figure 2.10: Top: Maximum outflow velocity versus circular velocity. The Seyfert 1 and Seyfert 2 categories include data from this study and from RVS05c (both IR-faint and IR-luminous Seyferts). The starburst ULIRG & LIRG category is composed of data from RVS05b. The data on the starburst dwarfs are from Schwartz & Martin (2004). Bottom: Same as left, but for maximum outflow velocity versus L_{FIR} . The outflow kinematics in Seyfert 2s (1s) are similar to (different from) those of the starburst ULIRGs and LIRGs.

sample, and to that end, the IR-luminous Seyfert 1 dynamical values from RVS05c have been scaled up to a 5 kpc radius as well. These results should be considered order-of-magnitude estimates since they are based on a number of largely unproven assumptions. We have not listed all results here; selected results can be seen in Figure 2.11.

For the objects in the present study, we assume a modest value of 0.3 for the large-scale opening angle (C_Ω), which is the typical value for local disk winds [Veilleux et al. (2005)]. Following the method of RVS05b, the covering fraction is used to parameterize the clumpiness of the wind, or it may reflect the global solid angle subtended by the wind when viewed from the galactic center. Using the value of $\langle C_f \rangle$ as listed in Table 2.8, this yields a global covering factor of $\Omega \sim 0.1$ for both Seyfert 1s and Seyfert 2s. These values are not well constrained, especially for the Seyfert 1s since only one outflow was detected in this type of Seyfert. The Ω value is inconsistent with values of $\Omega \sim 0.5-1.0$ calculated by Crenshaw et al. (2003b) from UV absorption lines in local Seyfert 1s. This low Ω value could imply that the winds we are seeing are collimated rather than wide-angle, and thus our lack of outflow detection in some of these objects may be due to their orientation relative to us rather than a complete lack of neutral gas outflow. The influence of host galaxy inclination on column density was explored using extinction-corrected axis ratios from the de Vaucouleurs Third Reference Catalog [de Vaucouleurs et al. (1995)], but no conclusion could be drawn due to small-number statistics. Additionally, these Ω values will be low in comparison to values from other studies; there is contribution here from the background galaxy, and many of the outflows we have

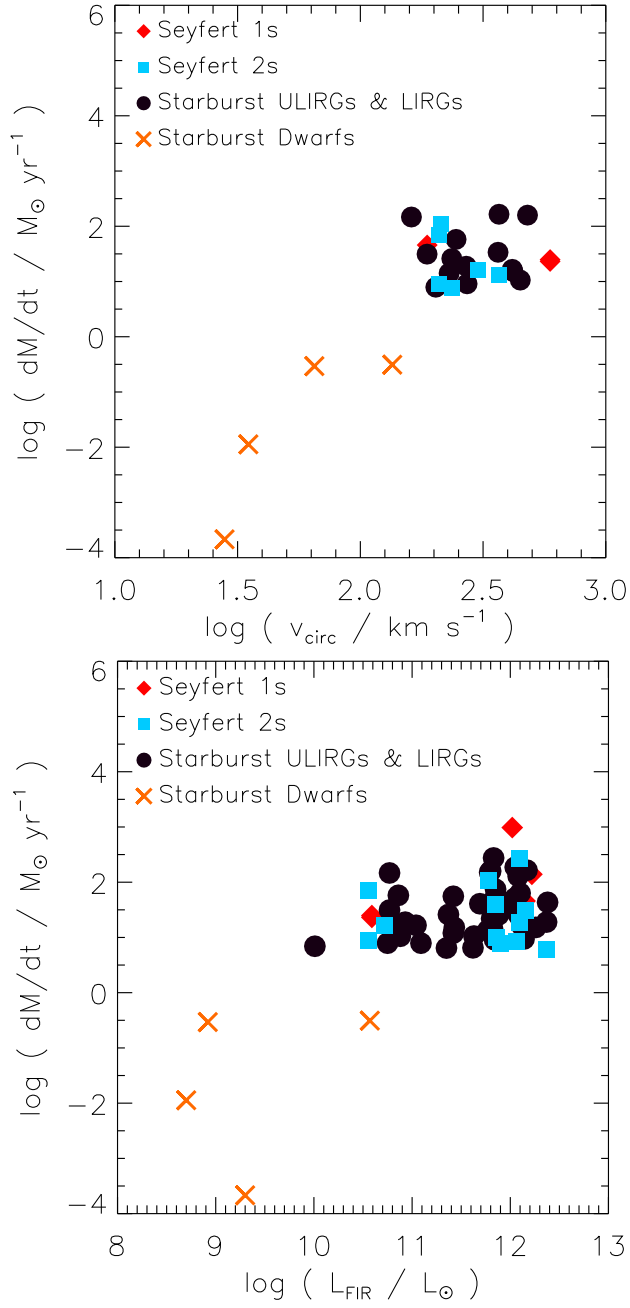


Figure 2.11: Top: Mass outflow rate versus circular velocity. See Figure 2.10 for descriptions of the various categories. Bottom: Same as left, but for mass outflow rate versus L_{FIR} .

found are small-scale. Comparisons with the results of UV absorption line studies should be considered with caution, though, since UV absorbers are typically of much higher ionization (NV, CIV) and likely located much closer to the AGN than Na I D absorbing material. The Na I D absorbers may also be affected more strongly by host galaxy contamination than the UV absorbers. Blueshifted absorption lines have also been detected in X-ray spectra for a number of Seyfert galaxies, including Mrk 6, with column densities of significantly higher order of magnitude than we have found here for Na I D in the optical (e.g., Mathur et al. (1995), Feldmeier et al. (1999), Monier et al. (2001), Krongold et al. (2003), Vaughn & Uttley (2008)). Again, we caution comparing these results with our own, as it has been noted that these X-ray lines are much higher ionization (OVII, OVIII) and are often intrinsically related to the aforementioned UV absorption lines.

One particularly interesting dynamical quantity is the mass outflow rate, since galactic outflows may contribute to the IGM enrichment and are possibly a quencher of star formation [Tremonti et al. (2007)]. Plots of dM/dt for the IR-faint Seyferts, IR-luminous Seyferts, and starbursting LIRGs and ULIRGS from RVS05b and RVS05c, and the dwarfs of Schwartz & Martin (all calculations are based on a absorber radius of 5 kpc) are presented in Figure 2.11. We see a general trend of mass outflow rate increasing with both L_{FIR} and galactic mass. There is a considerable difference in the mean dM/dt rates between IR-luminous Seyfert 1s and IR-luminous Seyfert 2s. The momentum and energy, as well as outflow rates for those quantities, are also significantly higher for IR-luminous Seyfert 1s than IR-luminous Seyfert 2s and all IR-faint Seyferts. The overall good agreement in

detection rate and kinematics between IR-faint and IR-bright Seyfert 2s and starburst ULIRGs & LIRGs (Figures 2.8-2.11) suggests that the outflows in all of these objects are powered by star formation, while the marked differences when IR-faint Seyfert 1 galaxies are considered suggest that the AGN plays an important role in driving the (generally high velocity) outflows in Seyfert 1 galaxies. Escape fractions were not calculated here since too few objects have outflow velocity components.

We can also look at energy outflow rates in order to determine what role these outflows could play in galactic feedback. The rates that we have calculated can be found in Table 2.5, though it must be cautioned that these numbers are a function of our uncertain Ω value, as well as our assumed absorber radius of 5 kpc. For the Seyfert 2 outflows, the average energy outflow rate was found to be $\sim 10^{41.1} \left(\frac{\Omega}{0.1}\right) \left(\frac{r}{5 \text{ kpc}}\right) \text{ ergs s}^{-1}$, or $\sim 10^8 \left(\frac{\Omega}{0.1}\right) \left(\frac{r}{5 \text{ kpc}}\right) L_{\odot}$. In comparison to the average bolometric luminosity for these objects ($\sim 10^{10} L_{\odot}$, taken from Woo & Urry (2002)), the energy outflow rates are only $\sim 1\%$ of the host galaxy luminosity. This indicates that outflow energetics in our Seyfert 2 galaxies are not strong enough to play a large role in galactic feedback. The findings of Schlesinger et al. (2009) for Mrk 573 are in agreement with our conclusion. For the only Seyfert 1 galaxy that we have found to have an outflow, Mrk 6, the energy outflow rate of its lower velocity component ($10^{41.6} \left(\frac{\Omega}{0.1}\right) \left(\frac{r}{5 \text{ kpc}}\right) \text{ ergs s}^{-1}$) is again $\sim 1\%$ of the host bolometric luminosity. This indicates that this Seyfert 1 outflow is also not energetic enough to play a vital role in galactic feedback, and thus previous findings are consistent with our results [Krongold et al. (2007)]. If we look at the higher velocity outflow found in Mrk 6, its energy outflow rate ($10^{42.9} \left(\frac{\Omega}{0.1}\right) \left(\frac{r}{5 \text{ kpc}}\right) \text{ ergs s}^{-1}$) is $\sim 5\%$ of the host bolometric

luminosity, which is higher than for the Seyfert 2 galaxies but again likely not strong enough to influence the evolution of its environment. However, one should note that these values are all highly dependent on the calculated value of Ω and assumed value of r and are thus uncertain in comparison to our measured velocities.

2.7.2 Inflows

2.7.2.1 Comparison with Previous Studies

An unexpected result of the present study is the high detection rate of inflows in IR-faint Seyferts ($39\% \pm 12\%$ for Seyfert 1s, $35\% \pm 11\%$ for Seyfert 2s). In contrast, only $\sim 15\%$ of the IR-luminous objects in RVS05b and RVS05c showed redshifted Na I D absorption. This difference is clearly seen in the left panel of Figure 2.9. Interestingly, a recent search for outflows in the AEGIS database has also revealed an excess of inflows among AGN-powered systems [Sato et al. (2009)]. Inflow has been observed in at least one Seyfert 1 galaxy, NGC 5548, using ionized gas detected in the UV, though detections have not been reported for such a large number of objects as we have found here [Mathur et al. (1999)]. There has been one tentative observation of redshifted X-ray absorption in a Seyfert 1 galaxy, but the authors caution that the significance of the absorption line they have measured is highly uncertain [Dadina et al. (2005)].

When we examine the inflow data on the IR-faint galaxies alone, we find no significant correlation between Δv_{max} and galactic mass (left panel in Figure 2.12). Neither is there any obvious trend with Seyfert type or far-infrared luminosity (right

panel of Figure 2.12), in contrast to the trends seen for the outflowing gas. Additionally, we see inflows in nearly the same fraction of Seyfert 1s and Seyfert 2s, indicating no particular trend with Seyfert type. As for the detected outflows, the influence of host galaxy inclination on column density was explored using extinction-corrected axis ratios [de Vaucouleurs et al. (1995)], but again, no conclusion could be drawn due to small-number statistics.

Next, the velocity distributions of the inflowing components for the IR-faint and IR-luminous Seyfert 1 galaxies were combined together and compared with the combined distribution of IR-faint and IR-luminous Seyfert 2 galaxies. K-S and Kuiper tests were performed on Δv , Δv_{max} , and Doppler parameter, following the same procedure as in Section 2.7.1, and the results are listed in Table 2.12. They confirm the lack of obvious differences in the inflow properties between the two types of Seyfert galaxies.

2.7.2.2 Search for Connection between Inflows and Nuclear Structures

The Na I absorption infall velocities often extend to relatively high values so we favor a nuclear location for this gas rather than a galactic origin (e.g. galactic fountains, Ferrara & Ricotti (2006)). Nuclear accretion of cool gas like Na I with $T \sim 100$ K can provide fuel not only for star formation but also for nuclear activity [Struve et al. (2008)]. Various mechanisms have been proposed to help reduce the large angular momentum of the gas in the nuclei of galaxies. These include nu-

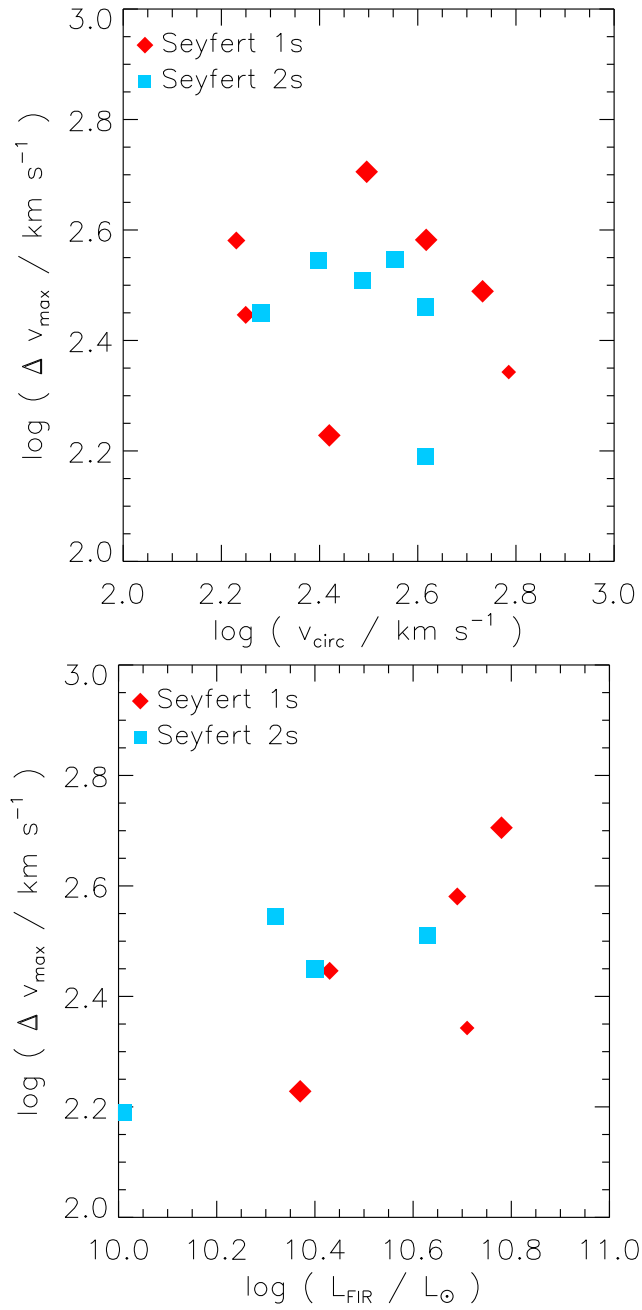


Figure 2.12: Top: Δv_{\max} versus circular velocity for inflows detected in IR-faint Seyfert galaxies. Smaller points are those with uncertain redshifts. Bottom: Same as left, but for Δv_{\max} vs. L_{FIR} . No obvious trend is seen.

clear ($\sim < 1$ kpc) bars and spirals [Pogge & Martini (2002), Martini et al. (2003a), Martini et al. (2003b), Davies et al. (2009)] and gravitational interactions with neighboring galaxies [Crenshaw et al. (2003a)]. Nuclear bars are thought to form when a large galactic bar forces gas inwards, creating a gaseous disk, and instability causes formation of a small gas bar near the nucleus [Shlosman et al. (1989), Martini et al. (2001)]. Stellar bars could also accomplish the same thing. Both bar types are capable of removing angular momentum from gas rotating near the nucleus [Martini et al. (2001)]. Nuclear spirals have been proposed as another AGN fueling mechanism since shock fronts that occur at their boundaries can take away angular momentum from local gas and cause material to fall in towards the black hole [Martini et al. (2003b)]. However, these nuclear structures do not necessarily lead to AGN fueling since they are present in a equally large fraction of non-active galaxies [Pogge & Martini (2002)]. Star formation may occur in these objects and disrupt AGN-fueling inflows [Davies et al. (2009)].

We revisit this issue here by looking for the presence of nuclear spirals or bars in the IR-faint Seyfert galaxies with inflow signature. We have compared our results to nuclear structure surveys done by three different groups [Malkan et al. (1998), Martini et al. (2003a), Deo et al. (2006)]. Nuclear dust structures in objects in common with these studies are classified into five distinct morphological categories (see Column (11) of Tables 2.8 and 2.8): irregular dust, dust filaments, nuclear dust ring, nuclear dust bar, and nuclear dust spiral. Of the thirteen objects which show inflows, five show evidence for nuclear dust spirals, bars, or rings, one shows evidence for dust filaments, one for irregular dust, and six show no sign of nu-

clear dust structure. The significant fraction of objects that show both inflows and nuclear dust spirals, bars, rings, and/or filaments lends credence to the idea of a connection between morphology and kinematics. Of the seven objects with irregular dust or no dust, five have nearby companion galaxies, so tidal forces due to interactions with these companions may cause AGN fueling [Rafanelli et al. (1995), Henriksen & Cousineau (1999), Smith et al. (2007)]. This leaves only two objects with inflow which do not show nuclear structure or a companion: Akn 202 and Mrk 1018. There are also two objects in our study with nuclear dust structure that show measurable *outflow* rather than inflow (NGC 3786 and NGC 7319), and thus whether we measure outflow rather than inflow may be a consequence of our line of sight to the nucleus (inflow and outflow may be occurring in different planes, or in the same plane but over a different range of azimuthal angles), rather than a lack of inflow in the object. Measurements of the line-of-sight velocity field with a resolution of ~ 10 s of pc will be needed to disentangle the geometry of the inflows/outflows detected in our data (e.g., the study of NGC 1097 by Davies et al. (2009), van de Ven & Fathi (2010)).

2.7.2.3 Inflow Dynamics

The same method used to calculate mass, momentum, and kinetic energy for outflows (Section 2.7.1.2) was used for inflows, but the characteristic absorber radius was reduced to 1 kpc, a rough upper limit to the scale of the circumnuclear structures (nuclear bars/spirals) believed to be responsible for feeding the AGN

(Section 2.7.2.2, Martini et al. (2003a)). Again, these dynamical quantities are rather uncertain, but are calculated to find out at least roughly how these inflows compare with the mass accretion rates necessary to power the AGN in these systems. Table 2.7 lists the mass, momentum, and kinetic energy calculated for all objects with measured inflows. The mass accretion rate for these inflows ranges from just under $1 \left(\frac{r}{1 \text{ kpc}}\right) M_{\odot} \text{ yr}^{-1}$ to just under $5 \left(\frac{r}{1 \text{ kpc}}\right) M_{\odot} \text{ yr}^{-1}$. For comparison, the mass accretion rate needed to power an AGN is $\dot{M} = L_{\text{bol}}/c^2\eta$, where L_{bol} is the bolometric luminosity of the AGN, \dot{M} is the mass accretion rate, c is the speed of light, and η is an efficiency factor dictating how much of the rest mass of the material being accreted is turned into radiation. If we take η to be ≈ 0.1 [Riffel et al. (2008)] and allow the bolometric luminosity to be $\sim 10^{44} \text{ ergs s}^{-1}$, typical for Seyfert galaxies [Padovani & Rafanelli (1988), Crenshaw et al. (2003b)], then we find that a mass accretion rate of $\dot{M} \sim 10^{-2} M_{\odot} \text{ yr}^{-1}$ is required. Even with our rough order of magnitude estimates, the mass accretion rates of all of our observed Na I D inflows are well above the amount necessary to power the AGN. Thus the inflows that we are measuring carry enough material to fuel the AGN in these objects, even if only $\sim 1\%$ of this material makes its way down to the AGN. The total infalling mass of $\sim 10^7 \left(\frac{r}{1 \text{ kpc}}\right) M_{\odot}$, estimated from our data, is enough to sustain nuclear activity over typical AGN lifetimes ($\sim 10^7 - 10^8 \text{ yrs}$; Mouri & Taniguchi (2002), Croom et al. (2004)).

2.8 SUMMARY

The main results from our study of Na I D absorption in infrared-faint Seyfert 1 and Seyfert 2 galaxies can be summarized as follows:

- *Outflow Detection Rates and Kinematics:* The rates of detection of outflows in IR-faint Seyfert 1 and 2 galaxies are lower than previously found in IR-bright Seyferts. Outflows were found in $\sim 18\%$ of IR-faint Seyfert 2s in our sample, compared with $\sim 45\%$ among the Seyfert 2 ULIRGs of RVS05c. Only one out of 18 Seyfert 1 galaxies in our sample shows evidence for a wind, far lower than the $\sim 50\%$ reported for Seyfert 1 ULIRGs in RVS05c. Interestingly, the outflow detection rate and velocities of IR-faint Seyferts follow the same trends with infrared luminosity and galaxy mass as IR-bright systems. The outflow kinematics of Seyfert 2 galaxies resemble those of starburst galaxies, while the outflow velocities in Seyfert 1 galaxies are significantly larger. These results suggest that the AGN is contributing to the neutral outflows in Seyfert 1 systems, while the starburst is the main driver of the outflows in all Seyfert 2 galaxies. Differences in wind angular extent (e.g. AGN-driven outflows in Seyfert 1s are more collimated than starburst-driven outflows) may also explain some of these results.
- *Outflow Dynamical Estimates:* The mass, momentum, and kinetic energy of the material involved in these outflows were estimated assuming a constant characteristic radius of 5 kpc. The dynamical properties of the outflows in Seyfert 2 galaxies are similar to those of the starburst ULIRGs & LIRGs,

but differ significantly from those of the Seyfert 1s. This again suggests a fundamental physical difference between the outflows of Seyfert 1s and those in the other objects. An attempt to determine the influence of host galaxy inclination on these outflows was inconclusive. Measured energetic rates do not appear large enough to play a significant role in galactic feedback, but these values are uncertain.

- *Inflow Detection Rates and Kinematics:* A striking result of this study is the high rate of detection of spatially-unresolved redshifted Na I D absorption, which we interpret as nuclear inflows (39% and 35% inflow detection rates for Seyfert 2s and 1s), with maximum velocities (321 and 291 km s⁻¹ on average). This is evidence for the existence of some mechanism capable of removing angular momentum from the circumnuclear gas in these objects. Nuclear bars and spirals, as well as interactions with nearby galaxies, may play a role in this process.
- *Inflow Dynamical Estimates:* Mass, momentum, and kinetic energy were estimated for the inflows, using a characteristic radius of 1 kpc, consistent with the observed sizes of nuclear bars and spirals in these systems. While these estimates are uncertain, we find that the total infalling mass and infalling mass rates are more than enough to power the AGN in these systems for typical AGN lifetimes. As with the outflows, an attempt was made to determine the influence of inclination on column density, but no conclusion could be drawn.

Table 2.1: Galaxy properties and observing logs: Seyfert 2s.

| Name (1) | z (2) | L_{IR} (3) | L_{FIR} (4) | SFR (5) | v_c (6) | W_{eq} (7) | Run (8) | t_{exp} (9) | PA (10) | Structure (11) | Refs (12) |
|-------------|----------------------|------------------------|-------------------------|------------|--------------|-----------------|-------------|------------------|------------|-------------------|--------------|
| Akn 79 | 0.01743 | ... | ... | ... | 231 | 3.43 | 2005 Sep 05 | 4500 | 0 | - | 1 |
| Arp 107A | 0.03463 | 10.63 | 10.09 | 2.14 | 308 | 2.20 | 2006 Apr 02 | 5400 | 0 | - | 1 |
| Mrk 348 | 0.01516 | 10.40 | 9.89 | 1.33 | 191 | 1.53 | 2006 Nov 23 | 4800 | 0 | - | 1 |
| Mrk 622 | 0.02347 | 10.72 | 10.26 | 3.15 | 301 | 2.03 | 2006 Apr 02 | 5400 | 0 | I | 1,4,7 |
| Mrk 686 | 0.01420 | 10.04 | 9.64 | 0.76 | 558 | 2.98 | 2006 Mar 31 | 4500 | 90 | S | 1,5,6 |
| Mrk 1157 | 0.01510 | 10.41 | 10.13 | 2.32 | 585 | 1.99 | 2005 Sep 04 | 3540 | 0 | R | 1,4,7 |
| NGC 1358 | 0.01351 | 10.35 | 9.37 | 0.41 | 299 | 3.73 | 2006 Nov 21 | 4800 | 0 | - | 1 |
| NGC 1667 | 0.01517 ^a | 10.97 | 10.66 | 7.84 | 580 | 3.99 | 2006 Nov 21 | 4800 | 0 | S | 1,4,6 |
| NGC 3362 | 0.02767 | ... | ... | ... | 358 | 1.92 | 2006 Mar 31 | 4500 | 90 | F | 1,7 |
| NGC 3786 | 0.00903 | ... | ... | ... | 367 | 3.11 | 2006 Apr 02 | 5400 | 22 | R,S | 1,6,8 |
| NGC 4388 | 0.00839 | 10.41 | 10.34 | 3.78 | 414 | 2.27 | 2006 Apr 02 | 5400 | 0 | I | 1,5,6 |
| NGC 5252 | 0.02308 | 10.39 | 9.84 | 1.18 | 340 | 3.72 | 2006 Apr 02 | 5400 | 0 | R,S | 1,6,7 |
| NGC 5728 | 0.00932 ^a | 10.60 | 10.32 | 3.63 | 434 | 2.25 | 2006 Apr 02 | 3600 | 0 | - | 2,4 |
| NGC 7319 | 0.02236 | 10.56 | 10.21 | 2.83 | 210 | 6.61 | 2005 Sep 08 | 3240 | 0 | F | 1,7 |
| NGC 7672 | 0.01348 | 9.91 | 9.64 | 0.76 | 363 | 1.39 | 2006 Nov 21 | 7200 | 0 | - | 1,4 |
| NGC 7682 | 0.01707 | ... | ... | ... | 412 | 2.06 | 2006 Nov 21 | 6000 | 0 | S | 1,6 |
| UGC 3995 | 0.01575 | 10.32 | 9.76 | 0.99 | 250 | 3.25 | 2006 Mar 31 | 4800 | 90 | - | 1,4 |

Col.(2): Heliocentric redshift. All redshifts are based on stellar measurements except (a) HI 21-cm measurements, or (b) measured from the emission lines in our data. Col.(3): Infrared luminosity, in logarithmic units of L_{\odot} . Col.(4): Far-infrared luminosity, in logarithmic units of L_{\odot} (see Section 2.2.2). Col.(5): Star formation rate, computed from the far-infrared luminosity (Section 2.2.2). Col.(6): Circular velocity, equal to $\sqrt{2}\sigma$, v_{rot} , or the quadratic combination if both are available. Col.(7): Rest-frame equivalent width of Na I D as computed from our model fits. Col.(8): Observing dates (Section 2.3). Instrument used was the R-C Spectrograph on the KPNO 4m. Col.(9): Total exposure time in seconds. Col.(10): Slit position angle. Col.(11): Letters indicate dust structure around nucleus (see Section 2.7.2.2): (B) nuclear dust bar, (F) dust filaments, (I) irregular dust, (R) nuclear dust ring, (S) nuclear dust spiral. Col.(12): Reference.
(1) [Nelson & Whittle (1995)]; (2) [Springob et al. (2005)]; (3) [Whittle (1992a)]; (4) IRAS Faint Source Catalog; (5) IRAS Point Source Catalog; (6) [Martini et al. (2003a)]; (7) [Malkan et al. (1998)]; (8) [Deo et al. (2006)].

Table 2.2: Galaxy properties and observing logs: Seyfert 1s.

| Name (1) | z (2) | L_{IR} (3) | L_{FIR} (4) | SFR (5) | v_c (6) | W_{eq} (7) | Run (8) | t_{exp} (9) | PA (10) | Structure (11) | Refs (12) |
|-------------|----------------------|------------------------|-------------------------|------------|--------------|-----------------|-------------|------------------|------------|-------------------|--------------|
| Akn 202 | 0.02872 ^b | 10.71 | 10.15 | 2.43 | 610 | 0.44 | 2006 Nov 23 | 6000 | 0 | - | 4 |
| Akn 564 | 0.02468 ^a | 10.75 | 10.14 | 2.40 | 443 | 0.00 | 2005 Sep 08 | 2040 | 0 | - | 2,5 |
| Mrk 6 | 0.01951 ^a | 10.59 | 10.09 | 2.14 | 593 | 1.08 | 2006 Nov 21 | 6000 | 0 | I | 1,4,7 |
| Mrk 10 | 0.02925 | 10.78 | 10.38 | 4.14 | 620 | 2.18 | 2006 Nov 21 | 3600 | 0 | - | 1 |
| Mrk 79 | 0.02221 ^a | 10.85 | 10.33 | 3.68 | 356 | 0.39 | 2006 Nov 22 | 4800 | 0 | S | 1,4,8 |
| Mrk 110 | 0.03513 ^b | ... | ... | ... | 147 | 0.00 | 2006 Nov 22 | 3600 | 0 | - | - |
| Mrk 352 | 0.01486 ^a | ... | ... | ... | 300 | 0.60 | 2006 Nov 22 | 7200 | 0 | - | 2 |
| Mrk 359 | 0.01694 | 10.35 | 9.96 | 1.59 | 235 | 0.55 | 2005 Sep 05 | 2700 | 0 | S | 2,5,8 |
| Mrk 382 | 0.03348 ^b | 10.72 | 10.00 | 1.73 | ... | 0.00 | 2006 Nov 23 | 4800 | 0 | B,S | 3,7,8 |
| Mrk 477 | 0.03744 ^b | 11.14 | 10.72 | 9.01 | ... | 0.00 | 2006 Mar 31 | 3926 | 90 | - | 4 |
| Mrk 506 | 0.04303 ^a | 10.69 | 10.12 | 2.30 | 170 | 2.96 | 2005 Sep 08 | 4830 | 27 | - | 1 |
| Mrk 595 | 0.02739 ^b | 10.64 | 10.28 | 3.31 | 444 | 1.41 | 2006 Nov 23 | 6000 | 0 | S | 3,8 |
| Mrk 1018 | 0.04263 | ... | ... | ... | 414 | 1.58 | 2006 Nov 23 | 6000 | 0 | - | 1 |
| Mrk 1126 | 0.01057 | ... | ... | ... | 540 | 1.70 | 2006 Nov 22 | 7200 | 0 | S | 1,8 |
| NGC 788 | 0.01350 | 10.04 | 9.38 | 0.41 | 226 | 3.20 | 2005 Sep 04 | 2700 | 0 | S | 1,6 |
| NGC 1019 | 0.02460 ^a | 10.43 | 9.97 | 1.62 | 178 | 2.63 | 2006 Nov 22 | 6000 | 0 | B,R,S | 2,7,8 |
| NGC 7603 | 0.02956 | 10.78 | 10.41 | 4.43 | 313 | 0.45 | 2006 Nov 23 | 7200 | 0 | R,S | 1,4,8 |
| UGC 3223 | 0.01567 | 10.37 | 10.09 | 2.13 | 263 | 1.66 | 2006 Nov 22 | 6000 | 0 | S | 1,4,8 |

See Table 2.8 for column descriptions.

Table 2.3: Properties of individual velocity components: Seyfert 2s.

| Name (1) | $\lambda_{1,c}$ (\AA) (2) | Δv (km s^{-1}) (3) | b (km s^{-1}) (4) | $\tau_{1,c}$ (5) | C_f (6) | $N(\text{Na I})$ (cm^{-2}) (7) | $N(\text{H})$ (cm^{-2}) (8) |
|-------------|--|---|--------------------------------------|------------------------|------------------------|---|--|
| Akn 79 | 5999.47 | -44 ± 5 | 85 ± 19 | $1.07^{+0.50}_{-0.21}$ | $0.12^{+0.06}_{-0.02}$ | $13.44^{+0.28}_{-0.20}$ | $21.08^{+0.43}_{-0.43}$ |
| ... | 5999.86 | -25 ± 7 | 280 ± 22 | $0.27^{+0.04}_{-0.04}$ | $0.48^{+0.07}_{-0.06}$ | $13.42^{+0.12}_{-0.12}$ | $21.06^{+0.18}_{-0.18}$ |
| Arp 107A | 6102.90 | 54 ± 24 | 323 ± 59 | $0.07^{+0.05}_{-0.01}$ | $0.92^{+0.04}_{-0.01}$ | $12.94^{+0.25}_{-0.09}$ | $20.58^{+0.25}_{-0.09}$ |
| Mrk 348 | 5988.26 | 65 ± 4 | 261 ± 25 | $0.06^{+0.01}_{-0.01}$ | $1.00^{+0.01}_{-0.01}$ | $12.74^{+0.08}_{-0.06}$ | $20.38^{+0.08}_{-0.06}$ |
| Mrk 622 | 6033.19 | -138 ± 10 | 416 ± 62 | $0.09^{+0.04}_{-0.01}$ | $0.55^{+0.23}_{-0.02}$ | $13.13^{+0.16}_{-0.07}$ | $20.77^{+0.16}_{-0.07}$ |
| Mrk 686 | 5981.63 | 16 ± 5 | 287 ± 34 | $0.10^{+0.04}_{-0.01}$ | $1.00^{+0.01}_{-0.01}$ | $13.05^{+0.25}_{-0.11}$ | $20.69^{+0.31}_{-0.17}$ |
| Mrk 1157 | 5986.67 | 3 ± 2 | 211 ± 20 | $0.83^{+0.17}_{-0.13}$ | $0.19^{+0.04}_{-0.03}$ | $13.79^{+0.17}_{-0.13}$ | $21.43^{+0.23}_{-0.20}$ |
| NGC 1358 | 5977.92 | 35 ± 6 | 320 ± 19 | $0.43^{+0.05}_{-0.05}$ | $0.37^{+0.04}_{-0.04}$ | $13.69^{+0.08}_{-0.08}$ | $21.33^{+0.15}_{-0.15}$ |
| NGC 1667 | 5986.79 | -12 ± 84 | 343 ± 19 | $0.32^{+0.03}_{-0.03}$ | $0.46^{+0.05}_{-0.05}$ | $13.59^{+0.06}_{-0.06}$ | $21.23^{+0.13}_{-0.13}$ |
| NGC 3362 | 6062.43 | 84 ± 38 | 323 ± 92 | $0.05^{+0.07}_{-0.01}$ | $1.00^{+0.01}_{-0.01}$ | $12.83^{+0.39}_{-0.16}$ | $20.47^{+0.39}_{-0.16}$ |
| NGC 3786 | 5947.88 | -148 ± 5 | 34 ± 3 | $5.00^{+0.36}_{-2.00}$ | $0.10^{+0.01}_{-0.04}$ | $>13.76^{+0.05}_{-0.23}$ | $>21.40^{+0.05}_{-0.23}$ |
| ... | 5951.19 | 19 ± 2 | 239 ± 14 | $0.34^{+0.04}_{-0.03}$ | $0.44^{+0.05}_{-0.04}$ | $>13.45^{+0.03}_{-0.21}$ | $>21.09^{+0.03}_{-0.21}$ |
| NGC 4388 | 5948.05 | 51 ± 17 | 125 ± 5 | $0.98^{+0.07}_{-0.07}$ | $0.32^{+0.02}_{-0.02}$ | $13.60^{+0.04}_{-0.04}$ | $21.24^{+0.04}_{-0.04}$ |
| NGC 5252 | 6034.47 | 39 ± 10 | 375 ± 23 | $0.10^{+0.02}_{-0.01}$ | $1.00^{+0.01}_{-0.01}$ | $13.14^{+0.15}_{-0.07}$ | $20.78^{+0.21}_{-0.13}$ |
| NGC 5728 | 5952.30 | -11 ± 1 | 262 ± 26 | $0.27^{+0.06}_{-0.03}$ | $0.37^{+0.08}_{-0.04}$ | $13.40^{+0.17}_{-0.13}$ | $21.04^{+0.23}_{-0.19}$ |
| NGC 7319 | 6026.74 | -133 ± 19 | 100 ± 1 | $3.00^{+0.24}_{-2.12}$ | $0.20^{+0.02}_{-0.14}$ | $13.34^{+0.04}_{-0.10}$ | $20.98^{+0.04}_{-0.10}$ |
| ... | 6026.82 | -130 ± 1 | 450 ± 1 | $0.46^{+0.06}_{-0.06}$ | $0.49^{+0.06}_{-0.06}$ | $13.81^{+0.05}_{-0.12}$ | $21.45^{+0.05}_{-0.12}$ |
| NGC 7672 | 5976.55 | -25 ± 24 | 98 ± 6 | $1.12^{+0.17}_{-0.07}$ | $0.24^{+0.04}_{-0.01}$ | $13.53^{+0.11}_{-0.06}$ | $21.17^{+0.18}_{-0.03}$ |
| NGC 7682 | 6000.21 | 99 ± 3 | 228 ± 21 | $0.49^{+0.09}_{-0.08}$ | $0.25^{+0.05}_{-0.04}$ | $13.59^{+0.08}_{-0.09}$ | $21.23^{+0.08}_{-0.09}$ |
| UGC 3995 | 5992.99 | 127 ± 2 | 268 ± 15 | $0.13^{+0.02}_{-0.01}$ | $1.00^{+0.01}_{-0.01}$ | $13.09^{+0.07}_{-0.03}$ | $20.73^{+0.07}_{-0.03}$ |

Col.(2): Redshifted heliocentric wavelength, in vacuum, of the Na I D₁ λ 5896 line. Col.(3): Velocity relative to systemic. Negative velocities are blueshifted, positive are redshifted. Components with $\Delta v < -50 \text{ km s}^{-1}$ and $|\Delta v| > 2\delta(\Delta v)$ are assumed to be outflowing; those with $\Delta v > 50 \text{ km s}^{-1}$ and $|\Delta v| > 2\delta(\Delta v)$ are assumed to be inflowing. Col.(4): Doppler parameter. Col. (5): Central optical depth of the Na I D₁ λ 5896 line; the optical depth of the D₂ line is twice this value. Col.(6): Covering fraction of the gas. Col.(7-8): Logarithm of column density of Na I and H, respectively.

Table 2.4: Properties of individual velocity components: Seyfert 1s.

| Name (1) | $\lambda_{1,c}$ (\AA) (2) | Δv (km s^{-1}) (3) | b (km s^{-1}) (4) | $\tau_{1,c}$ (5) | C_f (6) | $N(\text{Na I})$ (cm^{-2}) (7) | $N(\text{H})$ (cm^{-2}) (8) |
|-------------|--|---|--------------------------------------|------------------------|------------------------|---|--|
| Akn 202 | 6069.22 | 113 ± 11 | 129 ± 32 | $1.02^{+0.23}_{-0.05}$ | $0.05^{+0.01}_{-0.01}$ | $13.67^{+0.12}_{-0.13}$ | $21.31^{+0.12}_{-0.13}$ |
| Mrk 6 | 6008.03 | -229 ± 1 | 25 ± 1 | $1.46^{+0.03}_{-0.03}$ | $0.48^{+0.01}_{-0.01}$ | $13.12^{+0.17}_{-0.29}$ | $20.76^{+0.17}_{-0.29}$ |
| ... | 5992.12 | -1024 ± 1 | 16 ± 11 | $4.75^{+0.23}_{-0.89}$ | $0.06^{+0.01}_{-0.01}$ | $13.44^{+0.20}_{-0.31}$ | $21.08^{+0.20}_{-0.31}$ |
| Mrk 10 | 6070.59 | 26 ± 7 | 305 ± 34 | $0.17^{+0.06}_{-0.02}$ | $0.45^{+0.15}_{-0.04}$ | $13.28^{+0.23}_{-0.11}$ | $20.92^{+0.30}_{-0.17}$ |
| Mrk 79 | 6028.25 | -15 ± 7 | 112 ± 23 | $0.92^{+0.32}_{-0.31}$ | $0.06^{+0.06}_{-0.02}$ | $13.57^{+0.25}_{-0.24}$ | $21.21^{+0.31}_{-0.30}$ |
| Mrk 352 | 5986.09 | 45 ± 8 | 111 ± 25 | $0.16^{+0.04}_{-0.01}$ | $0.16^{+0.03}_{-0.01}$ | $12.82^{+0.07}_{-0.42}$ | $20.46^{+0.07}_{-0.42}$ |
| Mrk 359 | 5997.12 | -17 ± 11 | 147 ± 28 | $0.21^{+0.12}_{-0.03}$ | $0.20^{+0.12}_{-0.03}$ | $13.03^{+0.30}_{-0.17}$ | $20.67^{+0.36}_{-0.23}$ |
| Mrk 506 | 6154.09 | 135 ± 7 | 296 ± 32 | $0.17^{+0.05}_{-0.01}$ | $0.64^{+0.18}_{-0.05}$ | $13.26^{+0.12}_{-0.06}$ | $20.90^{+0.12}_{-0.06}$ |
| Mrk 595 | 6059.26 | 8 ± 5 | 230 ± 21 | $0.15^{+0.03}_{-0.01}$ | $0.44^{+0.08}_{-0.03}$ | $13.09^{+0.15}_{-0.05}$ | $20.73^{+0.22}_{-0.12}$ |
| Mrk 1018 | 6150.34 | 67 ± 5 | 379 ± 31 | $0.12^{+0.03}_{-0.01}$ | $0.36^{+0.09}_{-0.03}$ | $13.22^{+0.10}_{-0.05}$ | $20.86^{+0.10}_{-0.05}$ |
| Mrk 1126 | 5962.64 | 138 ± 3 | 204 ± 11 | $0.08^{+0.01}_{-0.01}$ | $1.00^{+0.01}_{-0.01}$ | $12.79^{+0.06}_{-0.03}$ | $20.43^{+0.06}_{-0.03}$ |
| NGC 788 | 5977.35 | 0 ± 3 | 253 ± 61 | $0.72^{+0.06}_{-0.08}$ | $0.28^{+0.02}_{-0.03}$ | $13.81^{+0.19}_{-0.19}$ | $21.45^{+0.25}_{-0.25}$ |
| NGC 1019 | 6044.02 | 68 ± 4 | 253 ± 23 | $0.31^{+0.05}_{-0.04}$ | $0.41^{+0.07}_{-0.05}$ | $13.44^{+0.07}_{-0.07}$ | $21.08^{+0.07}_{-0.07}$ |
| NGC 7603 | 6073.78 | 93 ± 11 | 497 ± 45 | $0.06^{+0.04}_{-0.05}$ | $0.14^{+0.10}_{-0.11}$ | $13.06^{+0.22}_{-0.70}$ | $20.70^{+0.22}_{-0.70}$ |
| UGC 3223 | 5989.19 | -39 ± 1 | 81 ± 10 | $5.00^{+0.77}_{-1.89}$ | $0.08^{+0.01}_{-0.03}$ | $14.16^{+0.17}_{-0.17}$ | $21.80^{+0.17}_{-0.17}$ |
| ... | 5991.73 | 88 ± 1 | 98 ± 22 | $0.92^{+0.39}_{-0.20}$ | $0.16^{+0.07}_{-0.04}$ | $13.50^{+0.12}_{-0.13}$ | $21.14^{+0.12}_{-0.13}$ |

See Table 2.8 for column descriptions.

Table 2.5: Outflow: individual objects (Seyfert 1s and 2s).

| Name (1) | Δv_{max} (km s ⁻¹) (2) | M (M_{\odot}) (3) | dM/dt (M_{\odot} yr ⁻¹) (4) | p (dyn s) (5) | dp/dt (dyn) (6) | E (ergs) (7) | dE/dt (ergs s ⁻¹) (8) |
|-------------------|--|-------------------------------|--|-----------------------|-------------------------|----------------------|---|
| Seyfert 2s | | | | | | | |
| Mrk 622 | -484 | 8.76 | 1.22 | 49.2 | 34.2 | 56.1 | 41.0 |
| NGC 3786 | -176 | 8.64 | 1.12 | 49.1 | 34.1 | 56.0 | 41.0 |
| NGC 7319 | -217 | 8.52 | 0.95 | 48.9 | 33.9 | 55.8 | 40.7 |
| ... | -504 | 9.39 | 1.85 | 49.8 | 34.8 | 56.7 | 41.7 |
| Seyfert 1s | | | | | | | |
| Mrk 6 | -250 | 8.69 | 1.36 | 49.4 | 34.5 | 56.4 | 41.6 |
| ... | -1037 | 8.08 | 1.40 | 49.4 | 35.2 | 57.1 | 42.9 |

Col.(2): Maximum velocity in the outflow, $\Delta v_{max} \equiv \Delta v - \text{FWHM}/2$. Col.(3): Log of total outflowing mass. Col.(4): Log of mass outflow rate. Col.(5): Log of total momentum of outflow. Col.(6): Log of momentum outflow rate. Col.(7): Log of total kinetic energy of outflow. Col.(8): Log of kinetic energy outflow rate. Note that all values are calculated using $\Omega \sim 0.1$.

Table 2.6: Outflow: average properties.

| Quantity (1) | IR-Faint Seyfert 2s (2) | IR-Faint Seyfert 1s (3) | IR-Lum. Seyfert 2s (4) | IR-Lum. Seyfert 1s (5) |
|--|----------------------------|----------------------------|---------------------------|---------------------------|
| Number of galaxies Detection rate (%) | 17 18 ± 9 | 18 6 ± 6 | 20 45 ± 11 | 6 50 ± 20 |
| Galaxy Properties | | | | |
| z | 0.018 ± 0.01 | 0.025 ± 0.01 | 0.148 ± 0.11 | 0.150 ± 0.09 |
| $\log(L_{\text{FIR}}/L_{\odot})$ | 10.02 ± 0.35 | 10.14 ± 0.23 | 11.86 ± 0.31 | 12.13 ± 0.1 |
| SFR ($M_{\odot} \text{ yr}^{-1}$) | 2.39 ± 1.92 | 2.99 ± 2.13 | 118 ± 109 | 164 ± 75 |
| Δv (km s^{-1}) | -137 ± 8 | -627 ± 562 | -322 ± 388 | -4942 ± 2831 |
| Δv_{max} (km s^{-1}) | -345 ± 173 | -643 ± 556 | -618 ± 422 | -5210 ± 4306 |
| $\log[N(\text{Na I D})/\text{cm s}^{-2}]$ | 13.51 ± 0.33 | 13.28 ± 0.23 | 13.5 ± 0.7 | 14.5 ± 0.8 |
| $\log[N(\text{H})/\text{cm s}^{-2}]$ | 21.15 ± 0.33 | 20.92 ± 0.23 | 20.9 ± 0.7 | 21.8 ± 0.8 |
| Velocity Component Properties | | | | |
| τ | $0.76^{+0.1}_{-0.7}$ | $1.01^{+0.5}_{-0.1}$ | $0.27^{+0.7}_{-0.2}$ | $0.69^{+1.6}_{-0.5}$ |
| b (km s^{-1}) | 250 ± 214 | 21 ± 6 | 232 ± 182 | 87 ± 130 |
| C_f | $0.34^{+0.1}_{-0.1}$ | $0.27^{+0.1}_{-0.1}$ | $0.42^{+0.5}_{-0.2}$ | $0.67^{+1.2}_{-0.4}$ |

“IR-Lum.” refers to the IR-luminous data of RVS05c. For most quantities we list the mean and 1σ dispersions, under the assumption of a Gaussian distribution in the log of the quantity. Statistics for all quantities except z , L_{FIR} , and SFR are computed only for outflowing velocity components. Note that the entries under IR-Faint Seyfert 2s (1s) corresponds to only three (one) objects.

Table 2.7: Inflow: individual objects.

| Name (1) | Δv_{max} (km s ⁻¹) (2) | M (M_{\odot}) (3) | dM/dt (M_{\odot} yr ⁻¹) (4) | p (dyn s) (5) | dp/dt (dyn) (6) | E (ergs) (7) | dE/dt (erg s ⁻¹) (8) |
|-------------------|--|-------------------------------|--|-----------------------|-------------------------|----------------------|--|
| Seyfert 2s | | | | | | | |
| Arp 107A | 323 | 7.39 | 0.15 | 48.4 | 32.7 | 53.9 | 39.2 |
| Mrk 348 | 282 | 7.22 | 0.04 | 47.3 | 32.7 | 53.8 | 39.2 |
| NGC 3362 | 352 | 7.32 | 0.27 | 47.6 | 33.0 | 54.2 | 39.6 |
| NGC 4388 | 155 | 7.59 | 0.31 | 47.6 | 32.8 | 54.0 | 39.2 |
| NGC 7682 | 289 | 7.48 | 0.49 | 47.8 | 33.3 | 54.5 | 40.0 |
| UGC 3995 | 350 | 7.58 | 0.69 | 48.0 | 33.6 | 54.8 | 40.4 |
| Seyfert 1s | | | | | | | |
| Akn 202 | 220 | 6.89 | -0.04 | 47.3 | 32.8 | 54.0 | 39.6 |
| Mrk 506 | 381 | 7.55 | 0.69 | 48.0 | 33.6 | 54.8 | 40.5 |
| Mrk 1018 | 382 | 7.27 | 0.10 | 47.4 | 32.7 | 53.9 | 39.3 |
| Mrk 1126 | 308 | 7.27 | 0.43 | 47.7 | 33.4 | 54.6 | 40.2 |
| NGC 1019 | 279 | 7.54 | 0.39 | 47.7 | 33.0 | 54.2 | 39.6 |
| NGC 7603 | 507 | 6.70 | -0.32 | 47.0 | 32.5 | 53.6 | 39.1 |
| UGC 3223 | 169 | 7.19 | 0.15 | 47.4 | 32.9 | 54.1 | 39.5 |

All inflow dynamics calculations assume an absorber radius of 1 kpc. Col.(2): Maximum velocity of the inflow, $\Delta v_{max} \equiv \Delta v + \text{FWHM}/2$. Col.(3): Log of total inflowing mass. Col.(4): Log of mass inflow rate. Col. (5): Log of total momentum of inflow. Col.(6): Log of momentum inflow rate. Col.(7): Log of total kinetic energy of inflow. Col.(8): Log of kinetic energy inflow rate.

Table 2.8: Inflow: average properties.

| Quantity (1) | IR-Faint Seyfert 2s (2) | IR-Faint Seyfert 1s (3) |
|--|----------------------------|----------------------------|
| Number of galaxies | 17 | 18 |
| Detection rate (%) | 35 ± 11 | 39 ± 12 |
| Galaxy Properties | | |
| z | 0.018 ± 0.01 | 0.025 ± 0.01 |
| $\log(L_{\text{FIR}}/L_{\odot})$ | 10.02 ± 0.35 | 10.14 ± 0.23 |
| SFR ($M_{\odot} \text{ yr}^{-1}$) | 2.39 ± 1.92 | 2.99 ± 2.13 |
| Δv (km s^{-1}) | 80 ± 29 | 100 ± 29 |
| Δv_{max} (km s^{-1}) | 291 ± 37 | 321 ± 29 |
| $\log[N(\text{Na I D})/\text{cm s}^{-2}]$ | 13.13 ± 0.38 | 13.28 ± 0.29 |
| $\log[N(\text{H})/\text{cm s}^{-2}]$ | 20.77 ± 0.38 | 20.92 ± 0.29 |
| Velocity Component Properties | | |
| τ | $0.3^{+0.13}_{-0.06}$ | $0.38^{+0.05}_{-0.03}$ |
| b (km s^{-1}) | 254 ± 74 | 265 ± 140 |
| C_f | $0.75^{+0.09}_{-0.05}$ | $0.39^{+0.02}_{-0.02}$ |

For most quantities we list the mean and 1σ dispersions, under the assumption of a Gaussian distribution in the log of the quantity. Statistics for all quantities except z , L_{FIR} , and SFR are computed only for inflowing velocity components.

Table 2.9: Statistical comparisons of kinematic parameters: IR-faint and IR-luminous Seyfert galaxies.

| Samples | $P(\text{null, K-S})$ | $P(\text{null, Kuiper})$ |
|---|-----------------------|--------------------------|
| Δv | | |
| IR-Faint Seyfert 1s vs IR-Faint Seyfert 2s | 0.76 | 0.69 |
| IR-Faint Seyfert 1s vs IR-Luminous Seyfert 1s | <0.01 | <0.01 |
| IR-Faint Seyfert 2s vs IR-Luminous Seyfert 2s | 0.04 | 0.07 |
| IR-Faint Seyferts vs IR-Luminous Seyferts | <0.01 | <0.01 |
| Δv_{max} | | |
| IR-Faint Seyfert 1s vs IR-Faint Seyfert 2s | 0.84 | 0.95 |
| IR-Faint Seyfert 1s vs IR-Luminous Seyfert 1s | <0.01 | <0.01 |
| IR-Faint Seyfert 2s vs IR-Luminous Seyfert 2s | <0.01 | 0.03 |
| IR-Faint Seyferts vs IR-Luminous Seyferts | <0.01 | <0.01 |
| Doppler Parameter | | |
| IR-Faint Seyfert 1s vs IR-Faint Seyfert 2s | 0.33 | 0.71 |
| IR-Faint Seyfert 1s vs IR-Luminous Seyfert 1s | 0.09 | 0.06 |
| IR-Faint Seyfert 2s vs IR-Luminous Seyfert 2s | 0.28 | 0.72 |
| IR-Faint Seyferts vs IR-Luminous Seyferts | 0.23 | 0.41 |

$P(\text{null})$ is the probability that the two listed distributions are taken from the same parent population. Categories which have $P(\text{null}) < 0.1$ for both tests are printed in bold. Values are based on all absorption features.

Table 2.10: Statistical comparisons of kinematic parameters: all galaxies.

| Samples | $P(\text{null, K-S})$ | $P(\text{null, Kuiper})$ |
|--|-----------------------|--------------------------|
| Δv | | |
| Seyfert 1s vs Starburst ULIRGs & LIRGs | < 0.01 | < 0.01 |
| Seyfert 2s vs Starburst ULIRGs & LIRGs | 0.03 | 0.09 |
| Seyfert 1s vs Seyfert 2s | < 0.01 | < 0.01 |
| Δv_{max} | | |
| Seyfert 1s vs Starburst ULIRGs & LIRGs | < 0.01 | < 0.01 |
| Seyfert 2s vs Starburst ULIRGs & LIRGs | 0.02 | 0.02 |
| Seyfert 1s vs Seyfert 2s | < 0.01 | < 0.01 |
| Doppler Parameter | | |
| Seyfert 1s vs Starburst ULIRGs & LIRGs | 0.21 | 0.03 |
| Seyfert 2s vs Starburst ULIRGs & LIRGs | < 0.01 | < 0.01 |
| Seyfert 1s vs Seyfert 2s | 0.02 | < 0.01 |

$P(\text{null})$ is the probability that the two listed distributions are taken from the same intrinsic distribution. Categories which have $P(\text{null}) < 0.1$ for both tests are printed in bold. Values are based on all absorption features, both inflowing and outflowing. Note that Seyfert 1 and Seyfert 2 galaxies include both IR-Faint Seyferts from the present study, as well as IR-Luminous Seyferts from RVS05c. Starburst data are taken from RVS05b.

Table 2.11: Statistical comparisons of kinematic parameters: galaxies with outflows.

| Samples | $P(\text{null, K-S})$ | $P(\text{null, Kuiper})$ |
|--|-----------------------|--------------------------|
| Δv | | |
| Seyfert 1s vs Starburst ULIRGs & LIRGs | <0.01 | <0.01 |
| Seyfert 2s vs Starburst ULIRGs & LIRGs | 0.96 | 0.84 |
| Seyfert 1s vs Seyfert 2s | <0.01 | <0.01 |
| Δv_{max} | | |
| Seyfert 1s vs Starburst ULIRGs & LIRGs | <0.01 | <0.01 |
| Seyfert 2s vs Starburst ULIRGs & LIRGs | 0.26 | 0.31 |
| Seyfert 1s vs Seyfert 2s | <0.01 | <0.01 |
| Doppler Parameter | | |
| Seyfert 1s vs Starburst ULIRGs & LIRGs | <0.01 | <0.01 |
| Seyfert 2s vs Starburst ULIRGs & LIRGs | 0.24 | 0.28 |
| Seyfert 1s vs Seyfert 2s | 0.02 | 0.01 |

$P(\text{null})$ is the probability that the two listed distributions are taken from the same parent population. Categories which have $P(\text{null}) < 0.1$ for both tests are printed in bold. Values are based on outflowing absorption only. Note that Seyfert 1 and Seyfert 2 galaxies include both IR-Faint Seyferts from the present study, as well as IR-Luminous Seyferts from RVS05c. Starburst data are taken from RVS05b.

Table 2.12: Statistical comparisons of kinematic parameters: Seyfert 1s vs Seyfert 2s with inflows.

| Samples | $P(\text{null, K-S})$ | $P(\text{null, Kuiper})$ |
|-------------------|-----------------------|--------------------------|
| Δv | 0.83 | 0.87 |
| Δv_{max} | 0.72 | 0.89 |
| Doppler Parameter | 0.68 | 0.99 |

$P(\text{null})$ is the probability that the two listed distributions are taken from the same parent population. Values are based on objects with inflowing absorption only, and include data for IR-faint galaxies from this survey and IR-bright galaxies from RVS05c.

Chapter 3

Neutral Gas Outflows and Inflows in PG QSOs and ULIRGs

3.1 INTRODUCTION

The study of galactic-scale outflows remains an exciting and ever-growing field, with significant numbers of often high-velocity outflows being discovered in ionized gas (e.g., Crenshaw et al. (2003b), Arav et al. (2008), Moe et al. (2009), Spoon & Holt (2009), Alexander et al. (2010), Bautista et al. (2010), Villar Martín et al. (2011)), neutral gas (e.g., Rupke et al. (2005b,05c), Morganti et al. (2007), Krug et al. (2010), Hardcastle et al. (2012)), and most recently, molecular gas (e.g., Veilleux et al. (2009b,13b), Feruglio et al. (2010), Sturm et al. (2011), Guillard et al. (2012), Contursi et al. (2013)). These galactic outflows are often attributed to either high star formation rates / starbursts, an active galactic nucleus, or a combination of the two, with the highest-velocity winds generally being driven by the AGN [Leitherer et al. (1992), Rupke et al. (2005c), Krug et al. (2010), Faucher-Giguère & Quataert (2012)]. Such high-velocity, AGN-driven winds are predicted to play a major role in AGN feedback, ejecting cold gas from the AGN host, thus quenching star formation and leading to a close-knit relationship between the mass of the black hole and the velocity dispersion of the galaxy (e.g., Silk & Rees (1998), Di Matteo et al. (2005), Veilleux et al. (2005), Feruglio et al. (2010), Hopkins & Elvis (2010)). These outflows can also be responsible for a

number of other observed phenomena, as outlined and cited in Section 2.1: the observed Milky Way baryon deficit, the mass-metallicity relation in external galaxies, metal enrichment of the IGM, AGN luminosity drop at low redshift, the cutoff of the overall extragalactic luminosity function at high luminosities, and the formation of disks with high specific angular momentum (see Chapter 2, Krug et al. (2010), and references therein).

Galactic outflows have also been suggested to play a major role in the process of galaxy mergers. The present picture of the merger sequence is as follows. Galactic mergers begin in gas-rich environments, triggering starbursts when the cold gas in the merging galaxies becomes destabilized, resulting in an obscured ULIRG [Feruglio et al. (2010), Sturm et al. (2011)]. An AGN is triggered once enough of that cold gas is accreted onto the supermassive black hole at the center of that ULIRG, leading to the generation of a QSO [Sanders et al. (1988), Hopkins et al. (2005), Hopkins et al. (2006a)]. As the black hole mass grows, winds from the AGN and the triggered starbursts can expel gas and dust from the QSO host, thus removing the obscuring material [Silk & Rees (1998), Fabian (1999), Feruglio et al. (2010), Sturm et al. (2011), Glikman et al. (2012)]. Star formation is quenched by the removal of that material, leaving behind a QSO, and the merger remnant eventually becomes a gas-poor elliptical galaxy [Toomre & Toomre (1972), Kormendy & Sanders (1992), Naab et al. (2006), Hopkins et al. (2009), Sturm et al. (2011)].

The Quasar and ULIRG Evolution Study (QUEST) (see Schweitzer et al. (2006), Netzer et al. (2007), Veilleux et al.(2009a,09c), Teng & Veilleux (2010))

was devised in an attempt to provide more observational tests for the above described merger sequence and to better understand the relationship between local ULIRGs and PG QSOs. It is a multi-wavelength study, incorporating both imaging and spectroscopy and probing merger morphology, kinematics, and evolution [Veilleux et al. (2009a)]. The full QUEST sample consists of 74 ULIRGs and 34 PG QSOs, chosen to be representative of samples in Kim et al. (1998) for the ULIRGs and Guyon (2002) & Guyon et al. (2006) for the PG QSOs, and is described in Section 3.2. Thus far, work on the QUEST sample has used PAH emission to probe the sources of the far-IR continuum and starburst-AGN connection in PG QSOs [Schweitzer et al. (2006)], the spectral energy distributions of QSOs, the morphologies and host properties of PG QSOs [Veilleux et al. (2009c)], the strength of the AGN in ULIRGs and PG QSOs [Veilleux et al. (2009a)], the X-ray properties of ULIRGs and PG QSOs [Teng & Veilleux (2010)], and small-scale molecular outflows (~ 100 pc) in PG QSOs and ULIRGs [Veilleux et al. (2013b)]. At this time, however, only some of the QUEST ULIRGs have been observed in terms of galactic-scale outflows [Rupke et al. (2005a,05b,05c), Rupke & Veilleux (2011,13)].

The following study has several goals: to use the QUEST ULIRGs to expand the sample of AGN-dominated ULIRGs of Rupke et al. (2005c) and determine the prevalence and properties of neutral gas outflows and inflows, as well as to cover the sample of QUEST QSOs; to look for trends with far-infrared luminosity, with AGN luminosity, and with spectral type, thus determining AGN versus starburst contribution to galactic-scale outflows; and to look for connections between merger phase and outflow properties, thereby informing the commonly held merger sequence pic-

ture. As in Chapter 2, we probe galactic outflows and inflows in these objects using the Na I D $\lambda\lambda 5890, 5896$ doublet absorption feature, which probes neutral gas in the ISM of these objects. Blueshifted velocities (outflowing gas) and redshifted velocities (inflowing gas) as measured in Na I D absorption are unambiguous indicators of gas outflow/inflow, as there must be a continuum source behind the absorber, and thus we are sure that we are measuring gas between us and the nucleus of each target.

The organization of this chapter is as follows. We describe the galaxies in the sample in Section 3.2, including luminosities, star formation rates, spectral types, and interaction classes. Section 3.3 describes the observations. Section 3.4 describes our analysis: line fitting, velocities, column densities, and stellar contributions. In Section 3.5, we detail the resulting outflow measurements for the PG QSOs and ULIRGs and then discuss the outflow detection, kinematic, and dynamic results for the PG QSOs and ULIRGs in combination with older studies. Section 3.6 is organized in the same fashion as Section 3.5, but for inflows rather than outflows. Finally, we summarize the results of this study in Section 3.7.

All calculations in this chapter assume present-day cosmological parameter values, with $H_0 = 70 \text{ km s}^{-1}$, $\Omega_m = 0.3$, and $\Omega_\Lambda = 0.7$, chosen to coincide with the values of the QUEST study. Luminosities from Chapter 2 have been modified accordingly. All wavelengths quoted are vacuum wavelengths.

3.2 SAMPLE

The objects in this sample were taken from the Quasar and ULIRG Evolution Study (QUEST) sample of galaxies Schweitzer et al. (2006), Veilleux et al. (2009a) and references therein); the sample focused on in this work is comprised of 28 Palomar-Green (PG) QSOs and 10 ULIRGs. The PG QSOs [Schmidt & Green (1983)] were chosen, as in Schweitzer et al. (2006), to encompass broad luminosity, radio loudness, and IR excess ranges, and thus be representative members of the sample of local PG QSOs. Our PG QSO sample spans a range of $\sim 10^{10.9}$ - $10^{12.6}$ in infrared luminosity and a range of ~ 0.03 - 0.3 in redshift. THE ULIRGs were taken from the 1 Jy sample deriving from the Kim & Sanders (1998) flux-limited, $60 \mu\text{m}$ -selected sample of the *IRAS* faint source catalog. This set, as described in Veilleux et al. (2009a), was chosen to be representative in terms of luminosity, redshift, and *IRAS* 25-to- $60 \mu\text{m}$ colors. Our ULIRG sample spans roughly the same IR-luminosity and redshift ranges of our PG QSO sample. Our specific targets were chosen because they are local, gas-rich mergers which were observed using *Herschel*, *HST*, and GBT, but they have not yet all been observed via long-slit spectroscopy. The purpose of this work is to provide those long-slit spectroscopic observations which are necessary to probe winds in these objects on the galactic scale. Details of our full sample of objects and their properties can be found in Tables 3.1. The last column in that table lists references used for the compilation of these properties.

3.2.1 Redshifts

In Chapter 2, we were able to use Nelson & Whittle (1995) to obtain redshifts for the bulk of our objects. No such all-encompassing resource exists for this sample, so we were forced to accumulate redshifts from a number of different sources. A full list can be seen in Table 3.1, but our highest priority source was the Sloan Digital Sky Survey (SDSS), which uses spectroscopic redshifts based on the positions of the emission lines. Uncertainties are a bit higher in these values (~ 0.001), but we find them to be quite reliable. The second-most used resource was the ASIAGO-ESO/RASS QSO Survey of 2000 [Grazian et al. (2000)], which measured redshifts via optical spectroscopy with fairly low uncertainty (~ 0.0001). We used redshift measurements in the literature to calculate an expected central wavelength for $H\alpha$, which we then compared to the actual measured wavelength of $H\alpha$ (see Figure 3.7). For those where the peak of $H\alpha$ was not located at $\Delta v = 0$, we delved into the literature in an attempt to find more accurate redshifts. For six of our objects, we found that redshifts derived from the H I measurements of Teng et al. (2013) were more accurate than all other values listed in the literature following that test. There were still several objects for which we could not obtain reliable redshifts, as seen in Figure 3.7, particularly PG 0838+770, PG 1435-067, PG 1440+356, F09111-1007, and F15130-1958. Of those, only the last two showed measurable Na I D absorption, and the uncertainty in velocity for each of these objects accounts for that redshift uncertainty.

3.2.2 Far-Infrared Luminosities and Star Formation Rates

As in Section 2.2.2, we use the far-infrared luminosities ($L_{\text{FIR}} = L(40\text{-}120 \mu\text{m})$) of these objects to estimate their star formation rates, again under the caveat that the AGN may be contributing $\sim 10\text{-}20\%$ of the L_{FIR} [Netzer et al. (2007)]. We once again use the prescription of Sanders & Mirabel (1996) to calculate L_{FIR} for each of these targets, using data from the *IRAS* Faint Source Catalog as well as the literature. We give preference to *ISO* fluxes over *IRAS* fluxes when available; *IRAS* data have larger effective beam sizes than *ISO* data, which can result in occasional cirrus contamination in the $100 \mu\text{m}$ measurements [Schweitzer et al. (2006)]. We also note the caveat as mentioned in Schweitzer et al. (2006) that the fluxes of our targets, particularly the PG QSOs, are similar to the detection limits of the references used for *IRAS* and *ISO* fluxes, and thus there may be substantial errors in our F_{FIR} calculations (up to $\sim 50\%$). Sanders & Mirabel (1996) give $F_{\text{FIR}} = 1.26(S_{100} + 2.58S_{60}) \times 10^{-18} \text{ W cm}^{-2}$, with flux densities S in Jy; in order to convert from there to L_{FIR} , we use the luminosity distance as calculated by NED, based on cosmological parameters listed in Section 3.1. To convert from L_{FIR} to SFR, we use the Kennicutt (1998) prescription as written in Section 2.2.2 to determine star formation rates in $M_{\odot} \text{ yr}^{-1}$. The far-infrared luminosities and star formation rates of the objects in our sample are listed in Table 3.1.

3.2.3 Bolometric and AGN Luminosities

The objects in this sample span a bolometric luminosity range of $10^{11.0}$ - $10^{12.6} L_{\odot}$. These luminosities were either taken from Veilleux et al. (2009a) or calculated using the prescription in that paper: $L_{\text{bol}} = 1.15L_{\text{IR}}$ for ULIRGs and $L_{\text{bol}} = 7L_{5100\text{\AA}} + L_{\text{IR}}$ for PG QSOs. We again use a Sanders & Mirabel (1996) prescription for calculating infrared luminosity based on IRAS 12, 25, 60, and 100 μm flux densities and use luminosity distances from NED to convert to L_{IR} .

To then determine AGN luminosity, we turn again to Veilleux et al. (2009a), which derived α_{AGN} , a fraction quantifying the contribution of the AGN to the bolometric luminosity, via a number of methods. We choose here to use the rest-frame f_{30}/f_{15} continuum ratio, as it is easy to use for a large sample, and, as described in Veilleux et al. (2009a), is well-correlated with a MIR/FIR ratio devoid of PAHs and silicates. This method is not the most accurate method of those used in Veilleux et al. (2009a), but we have chosen this method as, whereas most of our new sample is included in the Veilleux et al. (2009a) sample, the bulk of the IR-luminous starbursts and AGN in RVS05b and c are not. We are able to easily obtain either f_{30} and f_{15} values for those targets, or IRAS 25 and 60 μm flux densities, which can be converted to f_{30}/f_{15} (see below). Thus, for proper statistical comparison of a full sample, we choose the f_{30}/f_{15} ratio as our AGN fraction probe.

The fraction of the bolometric luminosity that is contributed by the AGN is calculated using this method in Veilleux et al. (2009a) for all targets which are included in the Veilleux et al. (2009a) sample. For the remaining targets, we

use CASSIS¹ [Higdon et al. (2004), Houck et al. (2004), Werner et al. (2004), Lebouteiller et al. (2010,11)] to calculate the f_{30}/f_{15} ratio, and then use the prescription outlined in Veilleux et al. (2009a) to calculate AGN contribution fraction. In those cases where neither Veilleux et al. (2009a) nor CASSIS measurements of the 30/15 ratio were available, we extrapolated from IRAS f_{25}/f_{60} ratios according to a regression function determined from existing data (Veilleux et al. (2009a), M. Meléndez, private communication):

$$\log_{10}(25/60) = -0.70716 * \log_{10}(30/15) - 0.17257 \quad (3.1)$$

AGN fraction is then calculated according to the Veilleux et al. (2009a) prescription, and L_{AGN} is calculated by multiplying that fractional value by the bolometric luminosity, as calculated above. Bolometric luminosities and AGN luminosities for our sample can be seen in Table 3.1.

3.2.4 Spectral Types

Optical spectral types were primarily taken from Veilleux et al. (1995), Veilleux et al. (1999a), and Gonçalves et al. (1999), and are listed in Table 3.1. PG QSOs and Seyfert 1 - 1.5 are classified as Type 1 AGN, and Seyfert 1.6 - 2.0 are classified as Type 2 AGN. LINERs and HII galaxies are classified as such in Table 3.1, but are grouped with IR-luminous starbursts for the purposes of plotting and statistical analysis. Data from Chapter 2 and RVS05c are split into Type 1 AGN (previously

¹The Cornell Atlas of Spitzer/IRS Sources (CASSIS) is a product of the Infrared Science Center at Cornell University, supported by NASA and JPL.

listed in Chapter 2 as Seyfert 1s) and Type 2 AGN (previously listed in Chapter 2 as Seyfert 2s) in plots and statistical tests as found in this chapter, in order to make proper comparisons. RVS05b data remain in the IR-luminous starbursts grouping. The IR-luminous starbursts grouping primarily includes HII galaxies and LINERs; these are galaxies which do have AGN, but of which the extreme starbursts are dominating the luminosity and energetics of the galaxy and therefore are the defining characteristics of these objects.

3.2.5 Interaction Classes

Interaction classes for these objects are listed in Table 3.1 and were taken from Veilleux et al. (2002), Veilleux et al. (2006), and Veilleux et al. (2009c). We follow the prescriptions of Veilleux et al. (2002), which splits merging systems into five major classes: I. first approach, II. first contact, III. pre-merger, IV. merger, and V. old merger. Classes III and IV are split into further categories. III is divided into a and b, which are dependent upon apparent separation of the two objects; all of our Class III objects fall into group b, which are close binaries with apparent separation ≤ 10 kpc, but some RVS05b and c objects fall under group a, wide binary (separation > 10 kpc). IV is also divided into a and b, dependent upon luminosity ratios; all of our Class IV objects are in group b, compact mergers, although some RVS05b and c objects fall under group a, diffuse mergers. See Section 1.3 for more detail. For statistical comparisons, we split our interaction class groupings into binaries (all Class III objects) and singles (all Class IV and V objects). This enables us to

compare outflow and inflow properties based on whether the galaxy in question is in the process of merging or has already completed its merger.

3.3 OBSERVATIONS

Observations of this data set were taken during two different runs on the Mayall 4-m telescope at KPNO: April 27-30 and December 11-13 2012. The data were taken using the Ritchey-Chrétien Spectrograph with a moderate-resolution grating, KPC-18c, in the first order, along with the OG-530 blocking filter, which, as in Section 2.3, combines for an average resolution of 85 km s^{-1} with a $1.25''$ slit. The wavelength range was 2300 \AA , allowing us to obtain measurements of both the Na I D absorption doublet and the $\text{H}\alpha + [\text{NII}]$ emission complex in the same exposure. Observing dates and exposure times can be found in Table 3.1. The median signal-to-noise ratio (SNR) near Na I D for the April observing run was 126 per \AA , ranging from 24 to 218 per \AA . The signal-to-noise ratio values for the December run are significantly lower, as it was discovered after the fact that the telescope was improperly focused during this run, and larger extraction apertures were required (see Section 3.4.1). The median SNR value for the December run was 73.0 per \AA and ranged from 16 to 147 per \AA . As such, we give preference to data from the April run for those objects which were observed during both runs. The average seeing for these runs was 1.2-1.5''.

3.4 ANALYSIS

3.4.1 Line Fitting

Fitting procedures were performed as described in Section 2.4.1, using a curve of growth analysis but explicitly fitting line profiles. One difference in this study from Chapter 2 is the generally larger extraction apertures used to fit these objects. We attempted to keep a constant physical aperture radius of ~ 1.5 kpc to match that of Chapter 2 and the seeing, but in many cases were unable to do so. This stemmed from the fact that many of our targets in this sample were at higher redshift; additionally, the telescope focus problems of the December run (see Section 3.3) forced us to use significantly larger apertures. The extraction radius used for each of our targets can be found in Table 3.2. The median physical extraction radius used for the April run was 2.5 kpc; for the December run, it was 7.8 kpc. Extraction and calibration were performed using standard IRAF reduction packages. HeNeAr lamps were used for wavelength calibration; flux standards used were Feige 34, BD+28 4211, and G191-B2B. See Section 2.4.1 for specific fitting details regarding He I and Na I D fitting parameters.

As in Section 2.4.1, initial guesses for the fitting parameters (amplitude, A , Doppler parameter, b , and central wavelength, λ_0 , for He I emission; covering fraction, C_f , central optical depth and wavelength of the red line, τ_1 and $\lambda_{0,1}$, and b for Na I D absorption) were supplied to the fitting program and best fits were returned. Most He I emission lines were fit with two components, and unless multiple components (corresponding to multiple velocity components for each line of the Na I

doublet) were considerably better than a fit with one component, only one velocity component (one Na I doublet) was used to fit the Na I D absorption features. Three PG QSOs – PG 1119+120, PG 1501+106, and PG 1613+658 – showed absorption which could be fit, all with only one Na I D component. Ten ULIRGs showed absorption (including two galaxies with data from both observing runs) – F04103-2838, F09111-1007, F12112+0305, F15130-1958, F15250+3608, F22491-1808, IRAS 08572+3915, and Mrk 231 – and of those, only one (Mrk 231) was fit with multiple (three) velocity components in absorption. See Figure 2.1 in Chapter 2 for examples of how the fitting program deblends Na I D features. After fitting, we again iterated a Monte Carlo simulation 1000 times in order to determine parameter errors. The resulting fits can be seen in Figures 3.1-3.2. Note that the He I line in the fit for PG 2349-014 seems to be extremely blueshifted; we believe this to be due to the effect of O₂ telluric absorption eating away at the He I emission, as we are confident in this redshift value. See Table 3.3 for the fit parameters and properties of absorption components of the PG QSOs and ULIRGs.

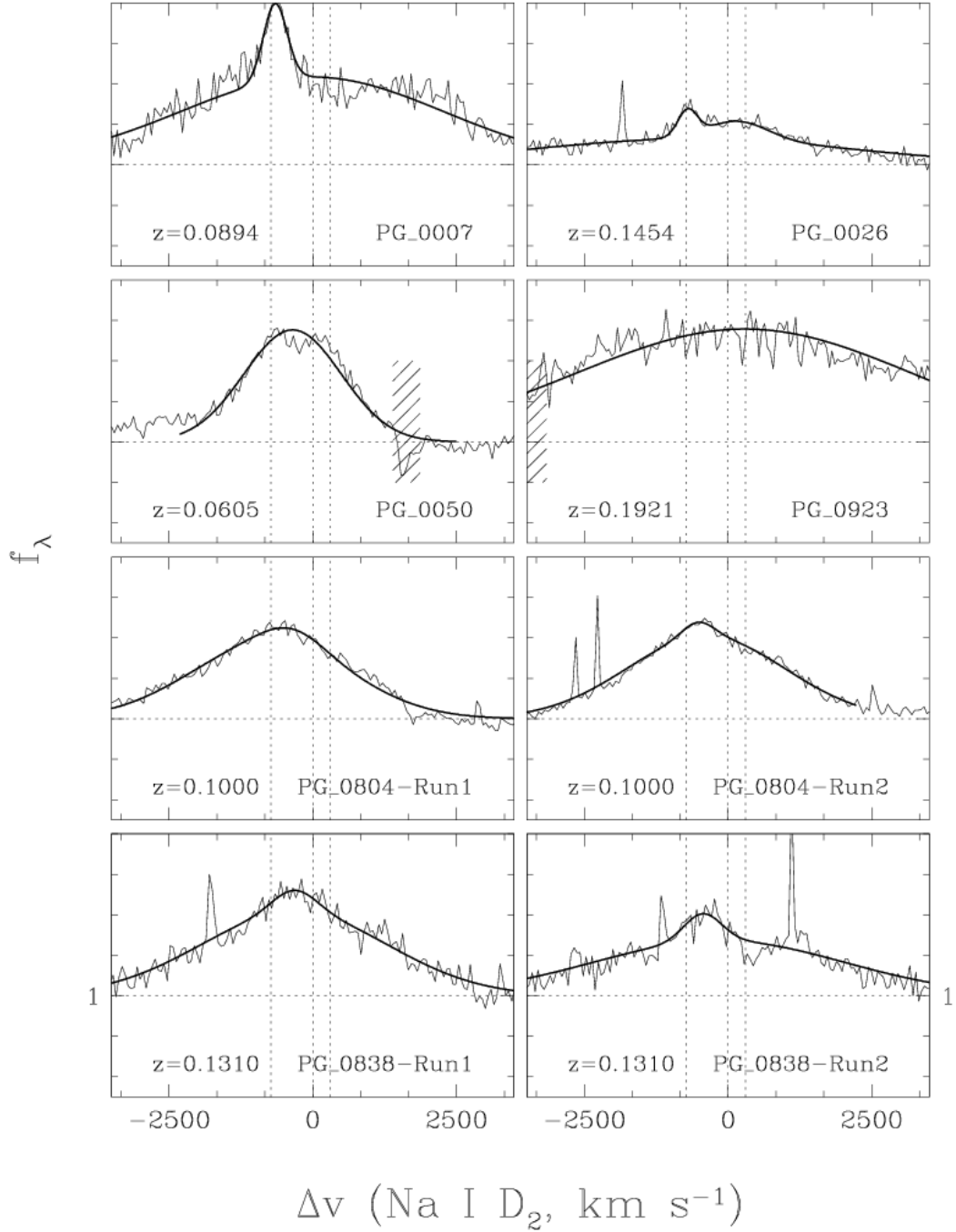
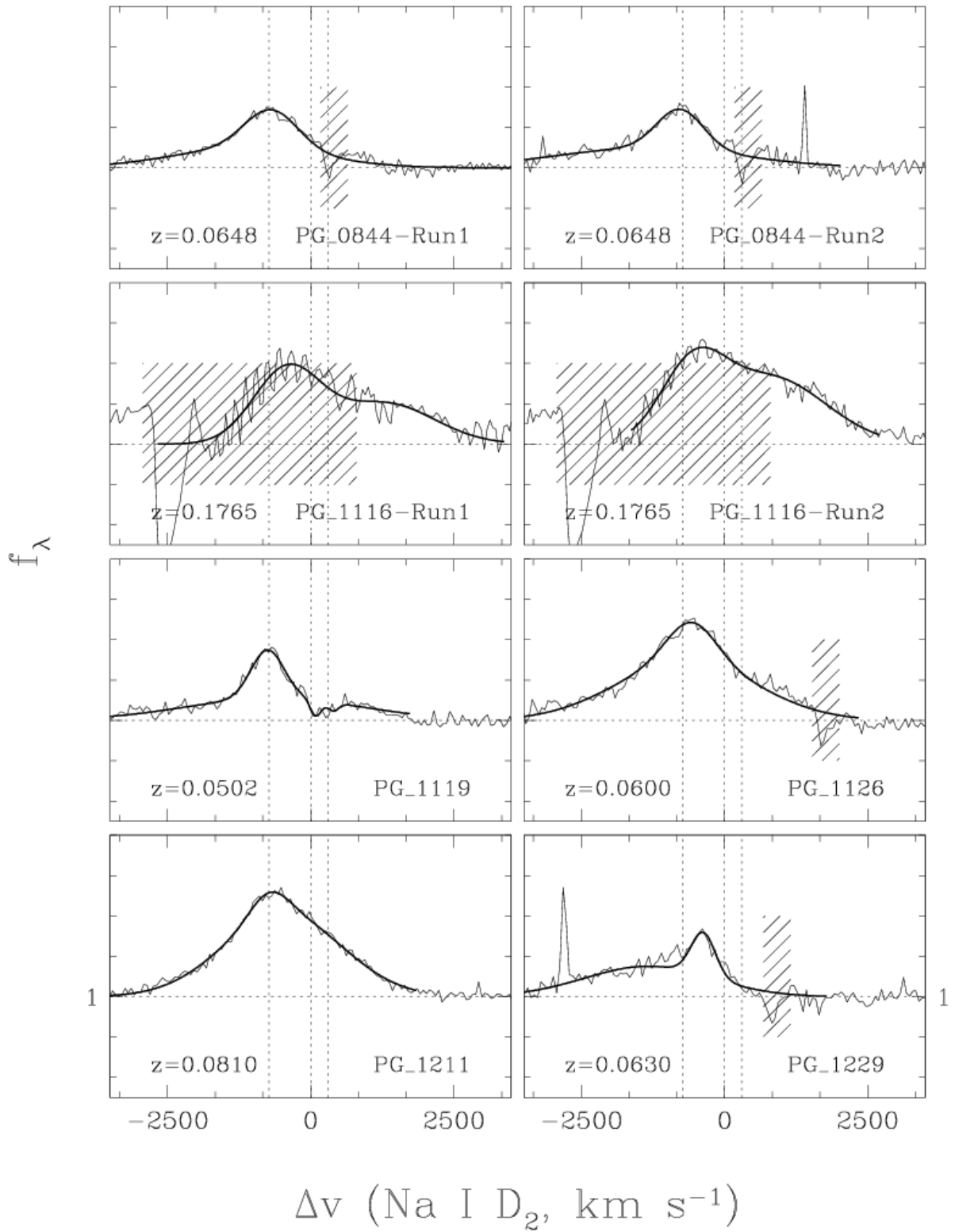
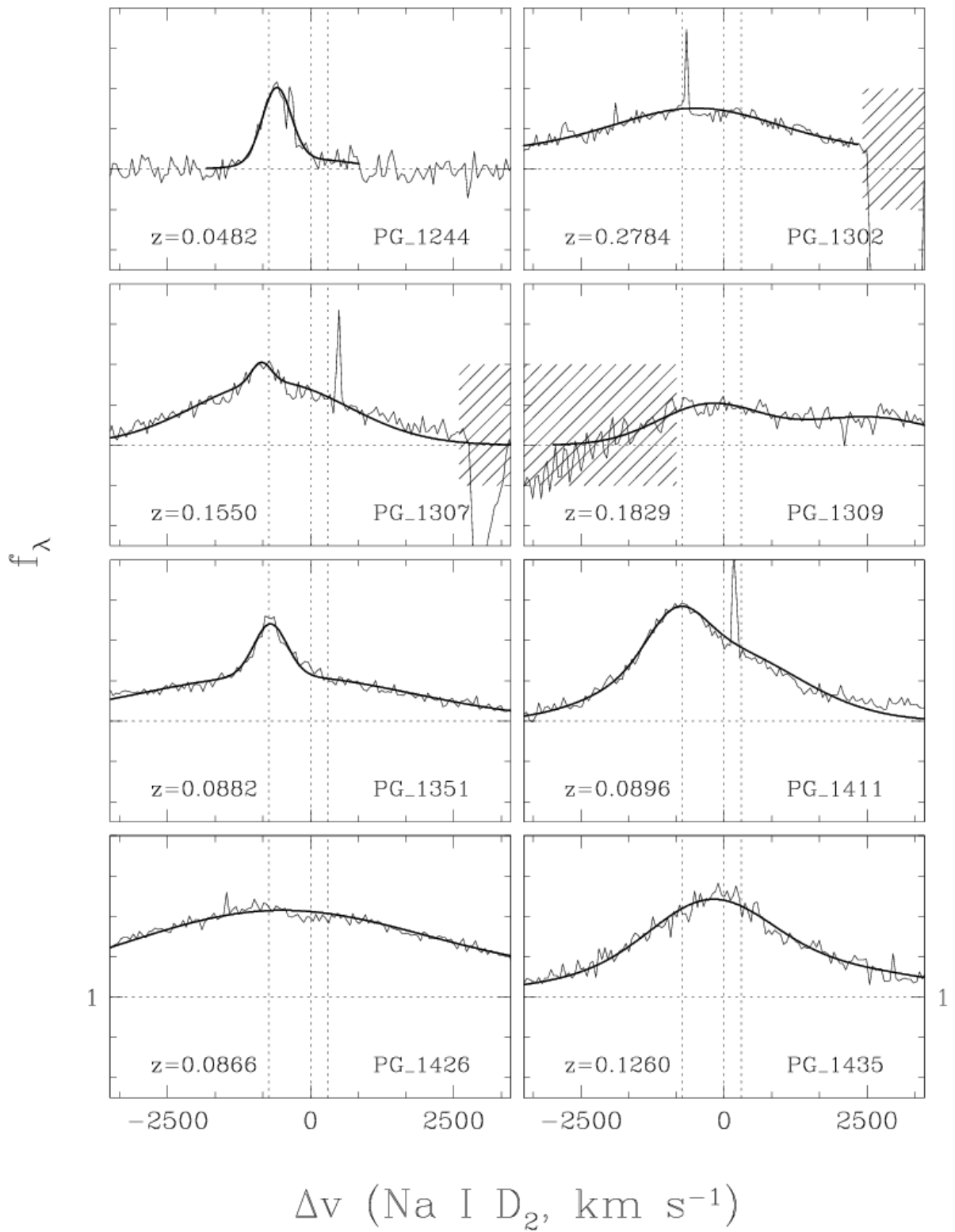
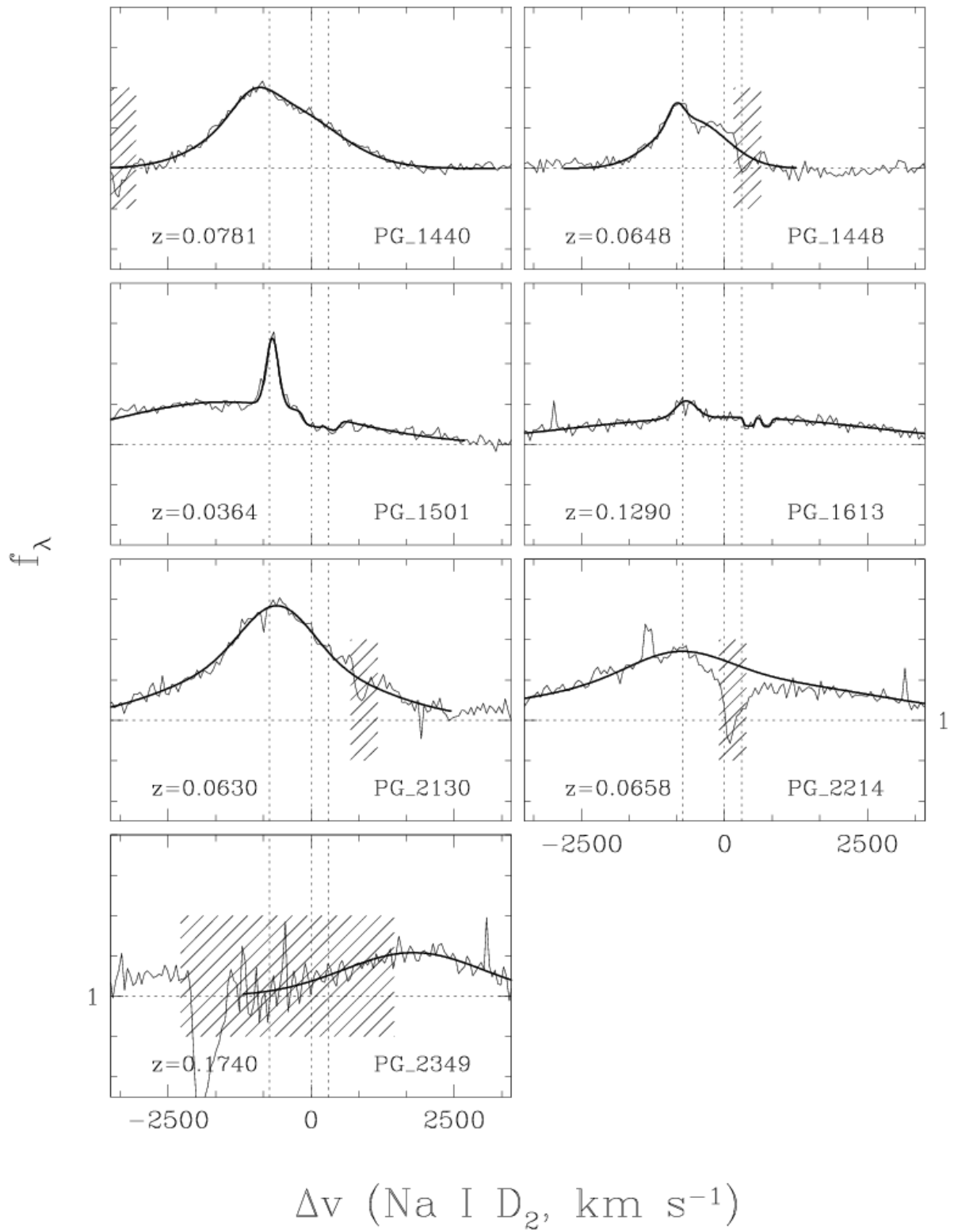


Figure 3.1: Spectra of the He I emission + Na I D absorption region in PG QSOs (Fit 1). These spectra are plotted on a velocity scale based on the systemic Na I D $\lambda 5890$ velocity. The thin lines are smoothed original spectra, and thick lines are fits to the data. The vertical dotted lines show the locations of the Na I D $\lambda\lambda 5890, 5896$ doublet and He I $\lambda 5876$ emission line in the object’s rest frame. Hatched lines indicate O_2 telluric absorption, when present; this absorption prevented us from being able to properly fit several of the objects.







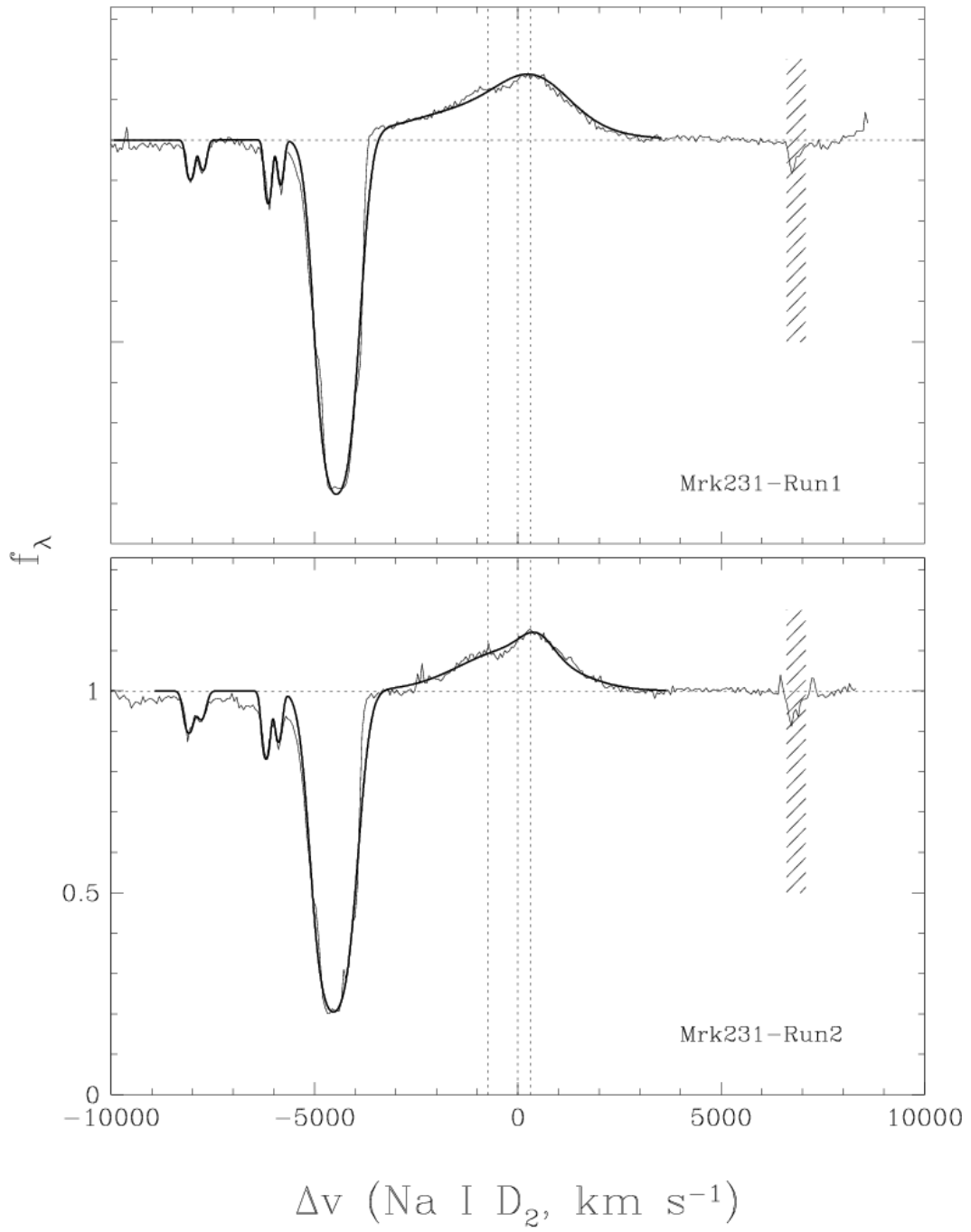
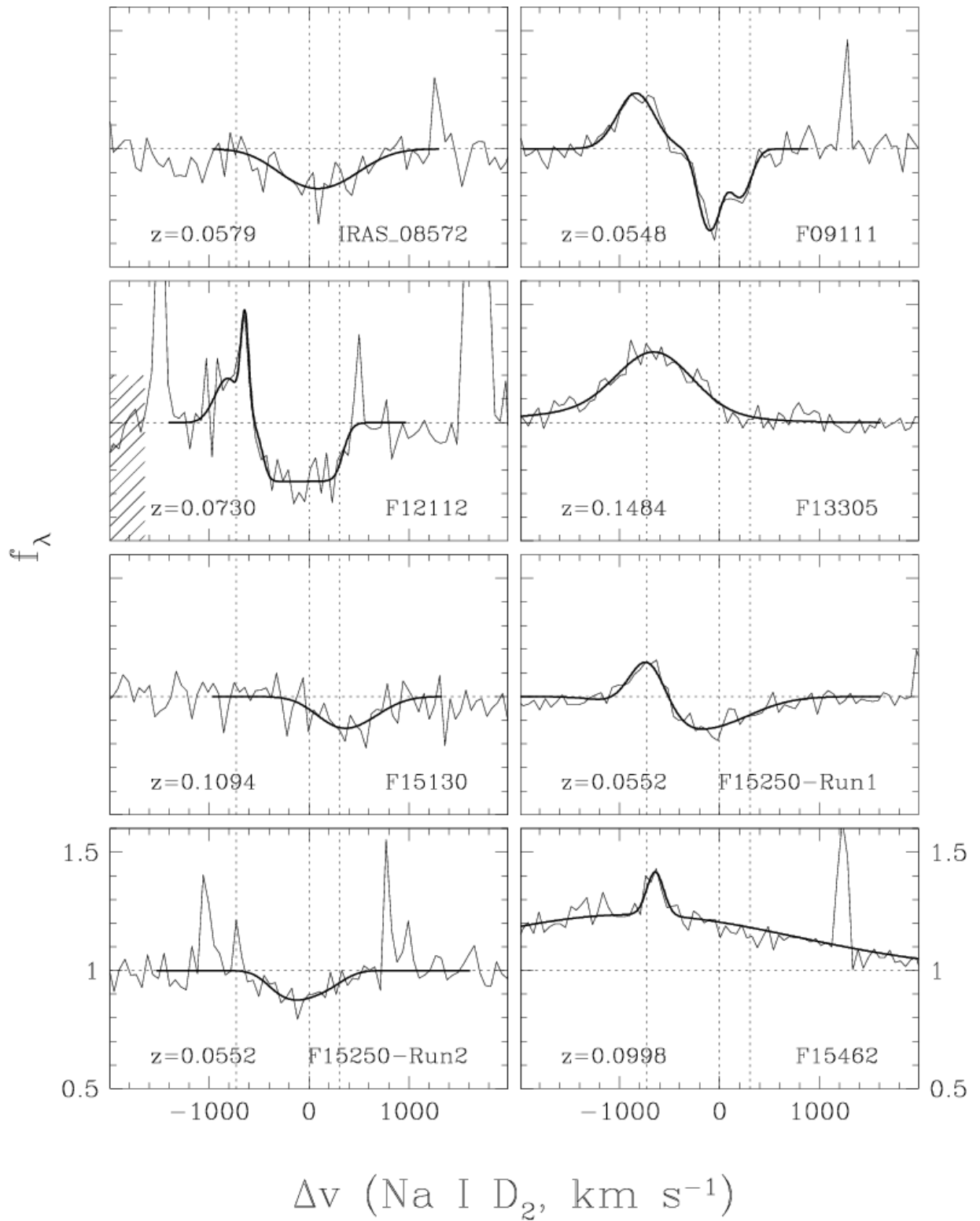
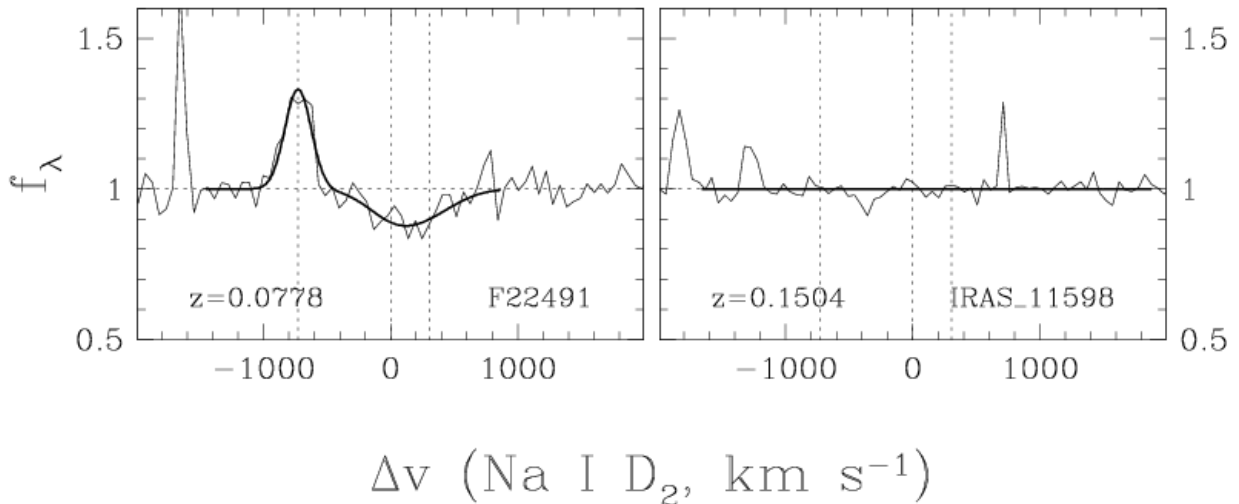


Figure 3.2: Spectra of the He I emission + Na I D absorption region in ULIRGs (Fit 1). See Figure 3.1 for description.





For the initial fits, as described and plotted above, all He I and Na I D parameters were allowed to float. This free-floating fit is hereafter known as Fit 1. It is of utmost importance to fit the He I emission properly, as improperly fit emission can have a large effect on both the properties of Na I D absorption lines and also whether an absorption line is deemed to be present. In order to try to properly fit the He I emission lines, we turn to the H α emission line, fitting H α emission (using 1-2 Gaussians) in the same way as the He I emission, then using those parameters to constrain the He I fits. For objects whose H α emission is blended with that of the [N II] $\lambda\lambda$ 6548, 6583 emission, we must remove the [N II] emission before fitting. In most of these cases, we can use the basic IDL interpolation script as used to fit the H α lines in Chapter 2, however, the H α flux is so strong in many of our IR-luminous targets that the simple script was unusable. For these objects, we wrote a new IDL script to roughly fit the [N II] emission lines, subtract those [N II] emission lines from the H α + [N II] complex, and then convolve that region with a Gaussian. While not a perfect [N II] subtraction, this still gives us a reasonably good fit to

H α . Parameters used to fit the H α lines for each object are listed in Table 3.4. Once the H α line was fit, we put the [N II] lines back in before making our figures. Fits to the H α lines in these objects can be seen in Figures 3.3-3.4 (note that we do not show H α fits for objects without measurable He I emission).

We then fit the He I + Na I D complex three more times. For Fit 2, we take the central wavelength of the H α fit and convert it to velocity space based on the expected H α central wavelength for that redshift. We then use that velocity difference to calculate a central wavelength for He I based on the H α fit. When two components are used in the H α fit, we fix He I parameters for both components (narrow matched to narrow, broad matched to broad). For Fit 3, the central wavelength is fixed as in Fit 2, and the Doppler parameter, b , of the He I line is set to the Doppler parameter of the H α line. For Fit 4, the central wavelength and Doppler parameter are fixed as in Fit 3; additionally, the ratio of the amplitudes of the He I emission line components is fixed to the ratio of the amplitudes of the H α emission line components (within the constraints of the fitting program). For objects with only one He I emission component, Fit 4 is the same as Fit 3. Parameters used to fit the He I line in these objects are tabulated in Table 3.5. The resulting fully fixed fits – Fit 4 – can be seen in Figures 3.5-3.6.

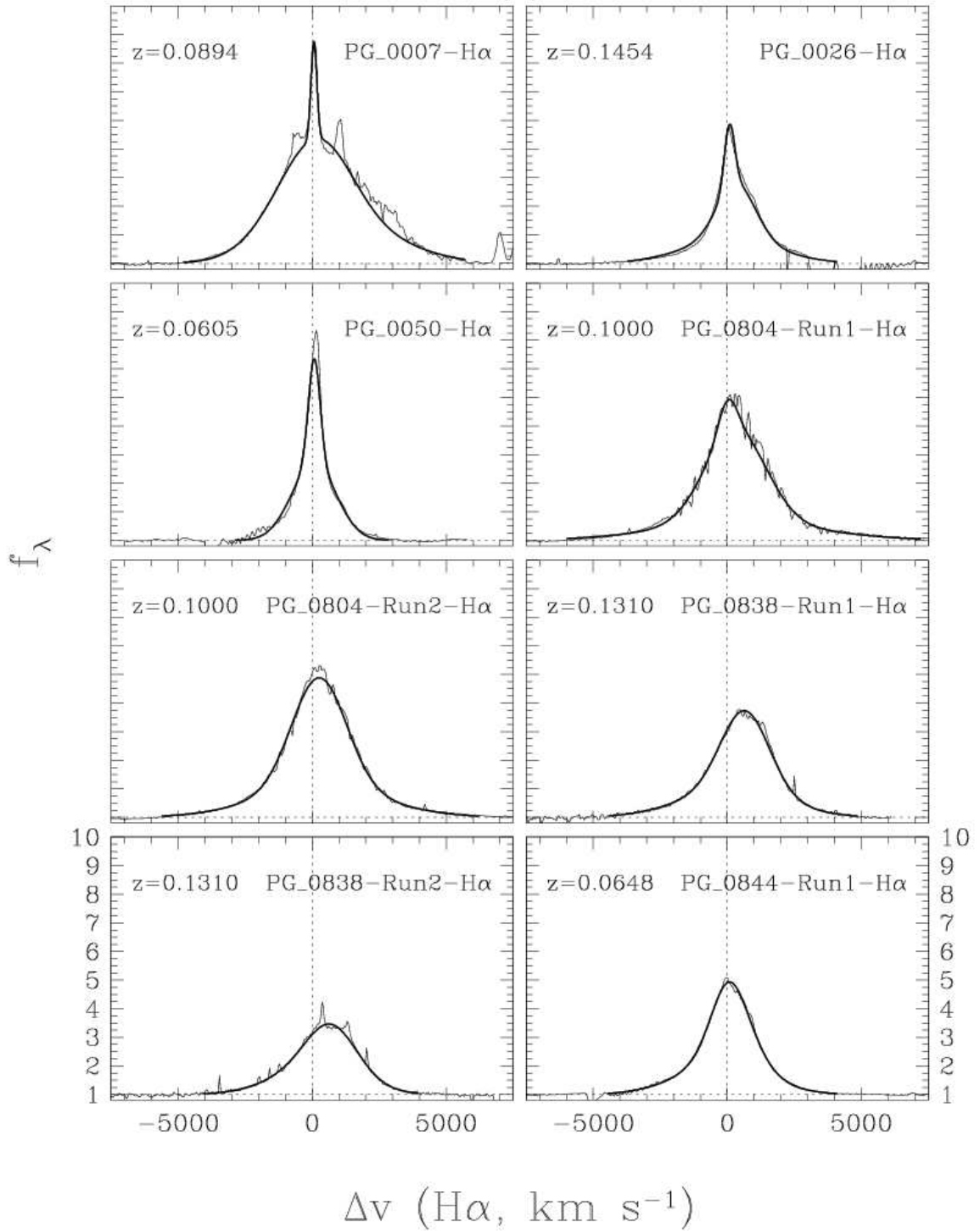
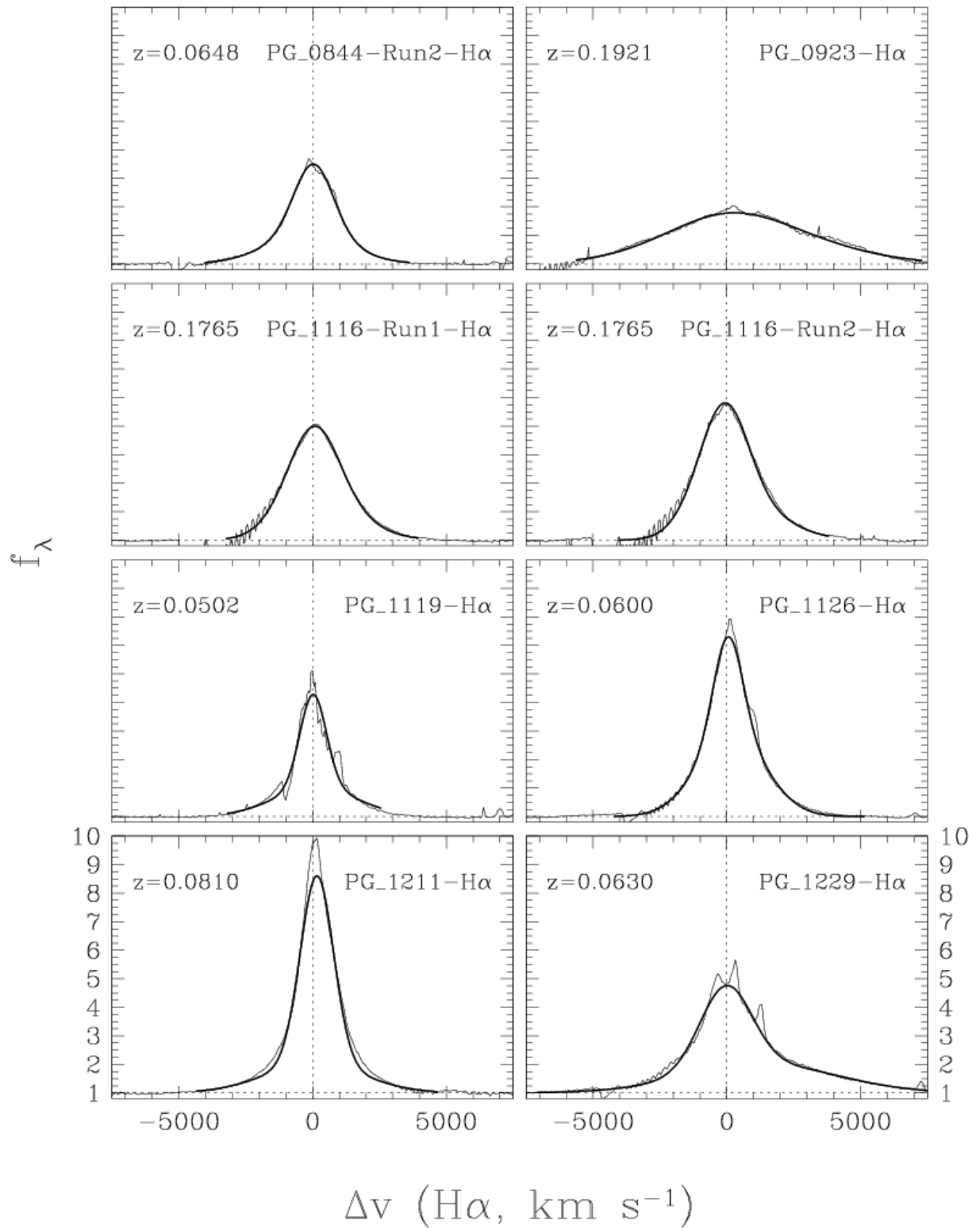
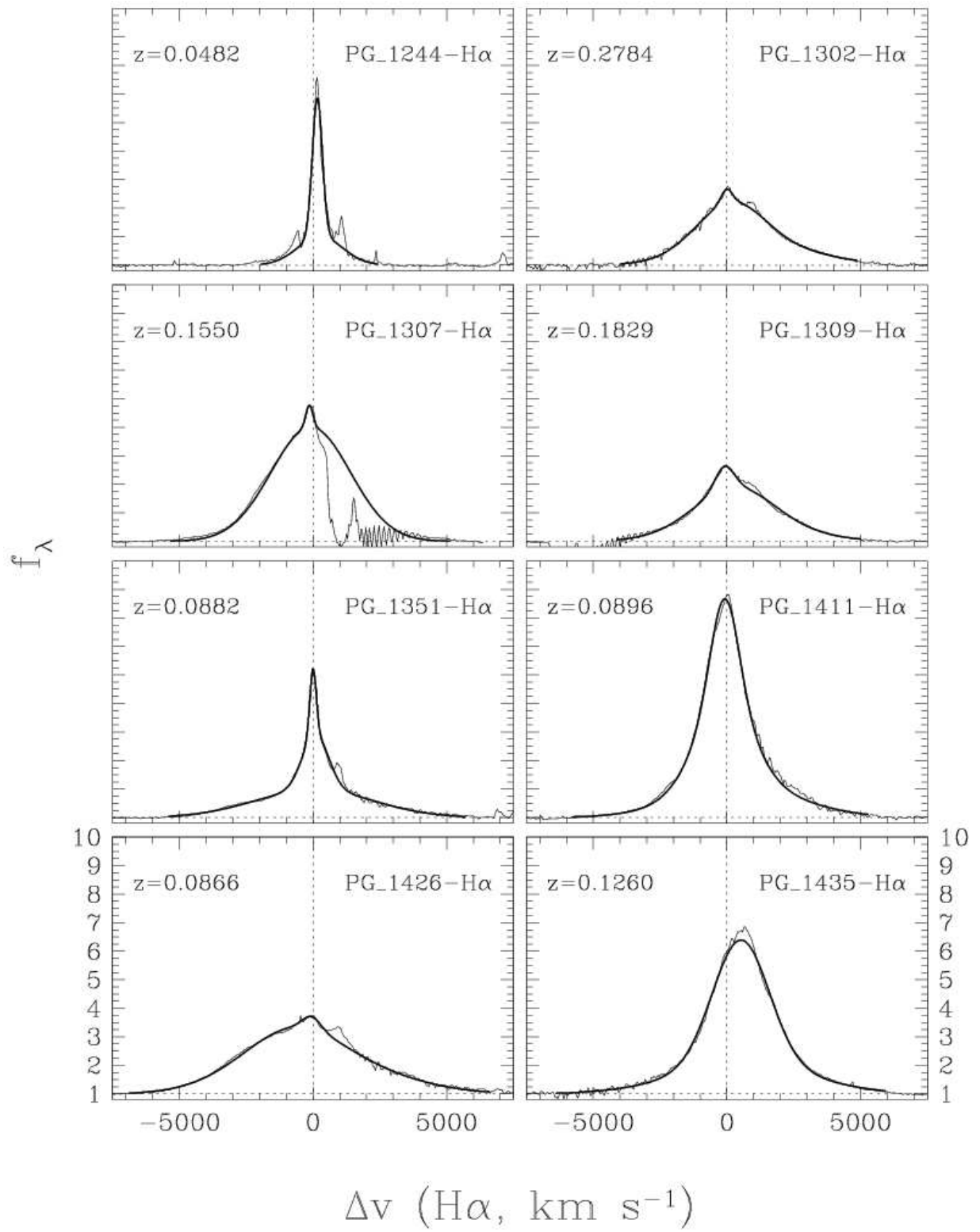
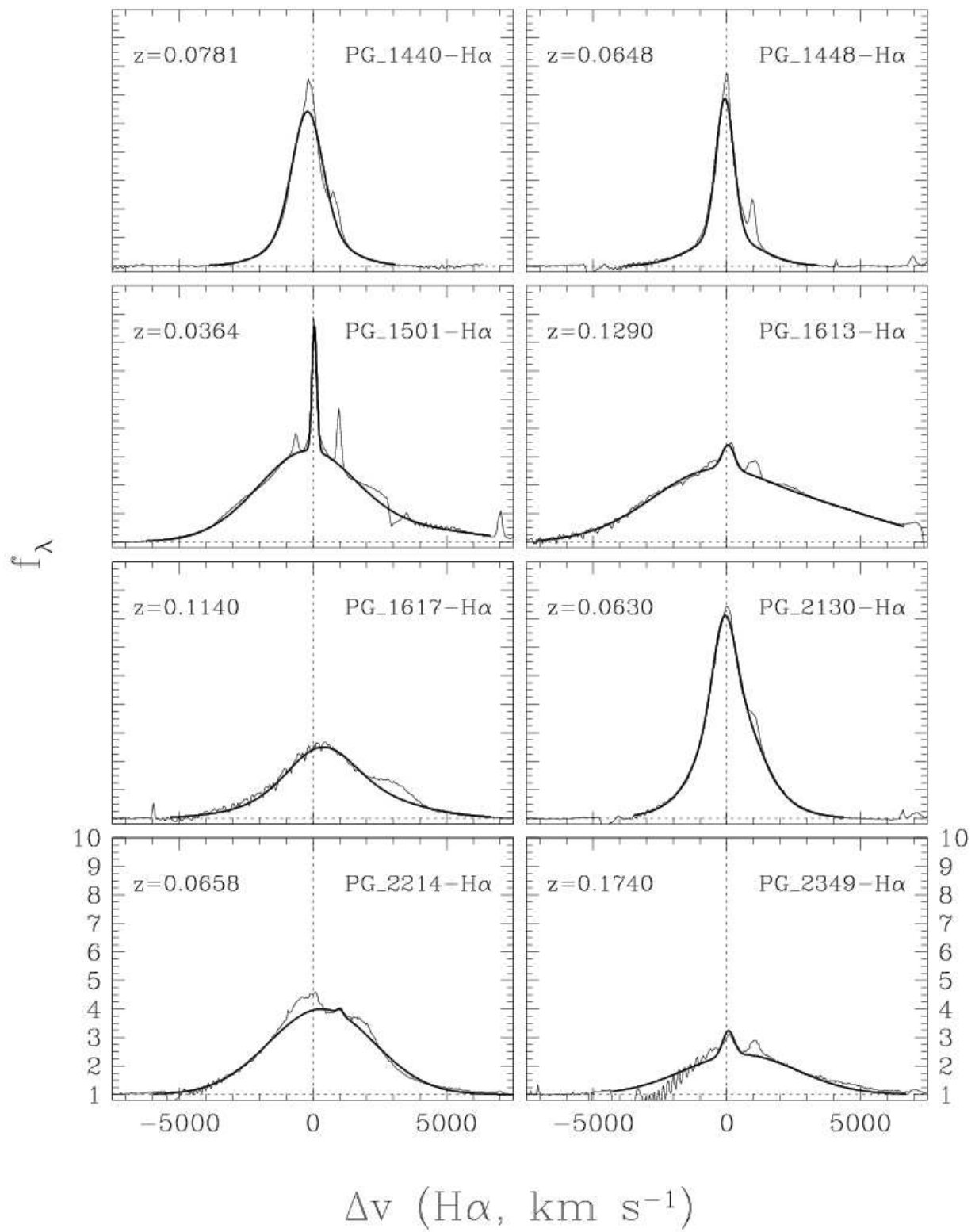


Figure 3.3: Spectra of the $H\alpha + [N II] \lambda\lambda 6548, 6583$ complexes in PG QSOs. The two $[N II]$ emission lines were removed prior to fitting according to the procedure described in Section 3.4.1, but are included here. These spectra are plotted on a velocity scale based on the systemic $H\alpha \lambda 6563$ velocity. The thin lines are smoothed original spectra, and thick lines are fits to the data. The vertical dotted lines show the location of the $H\alpha \lambda 6563$ emission line in the object's rest frame.







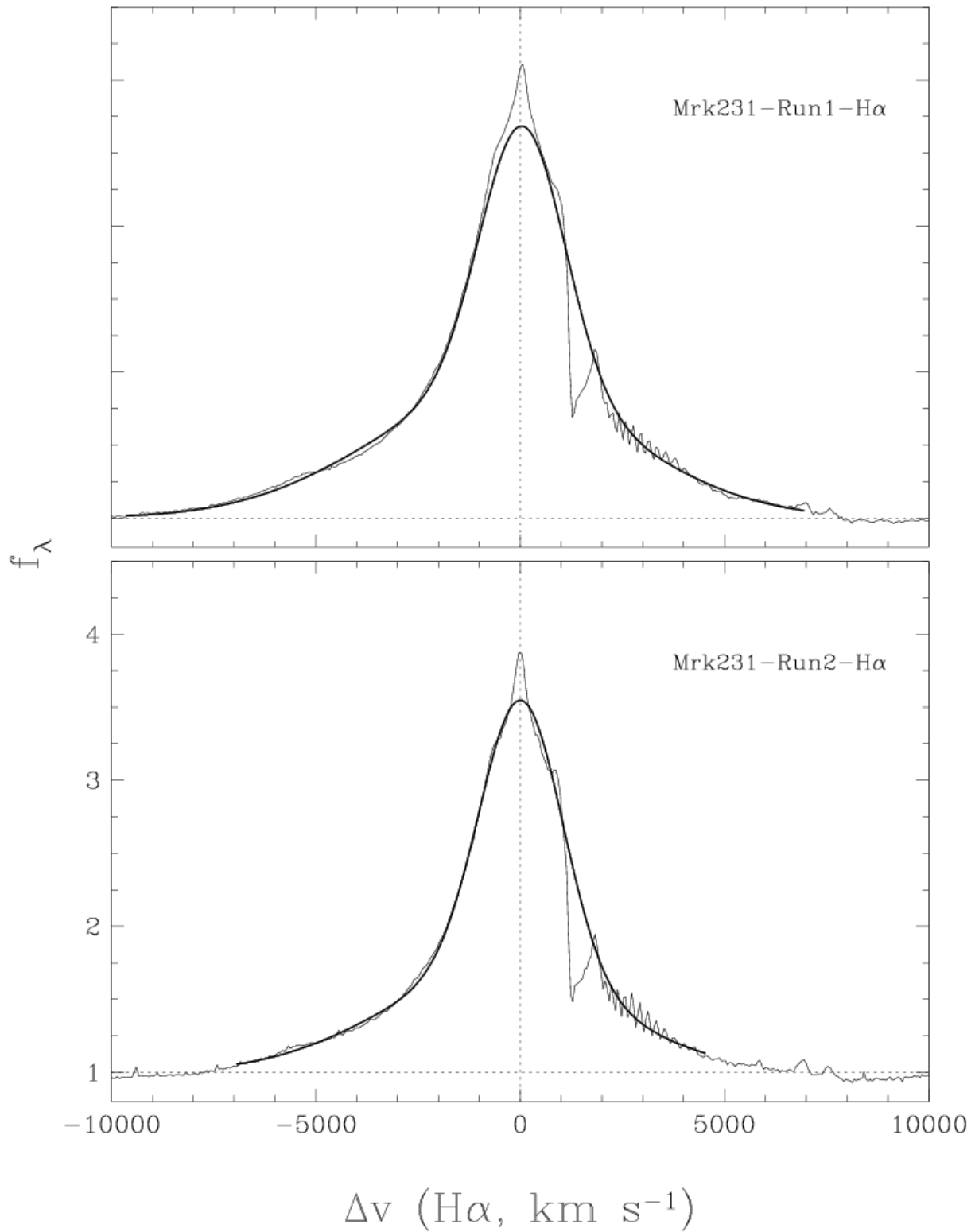
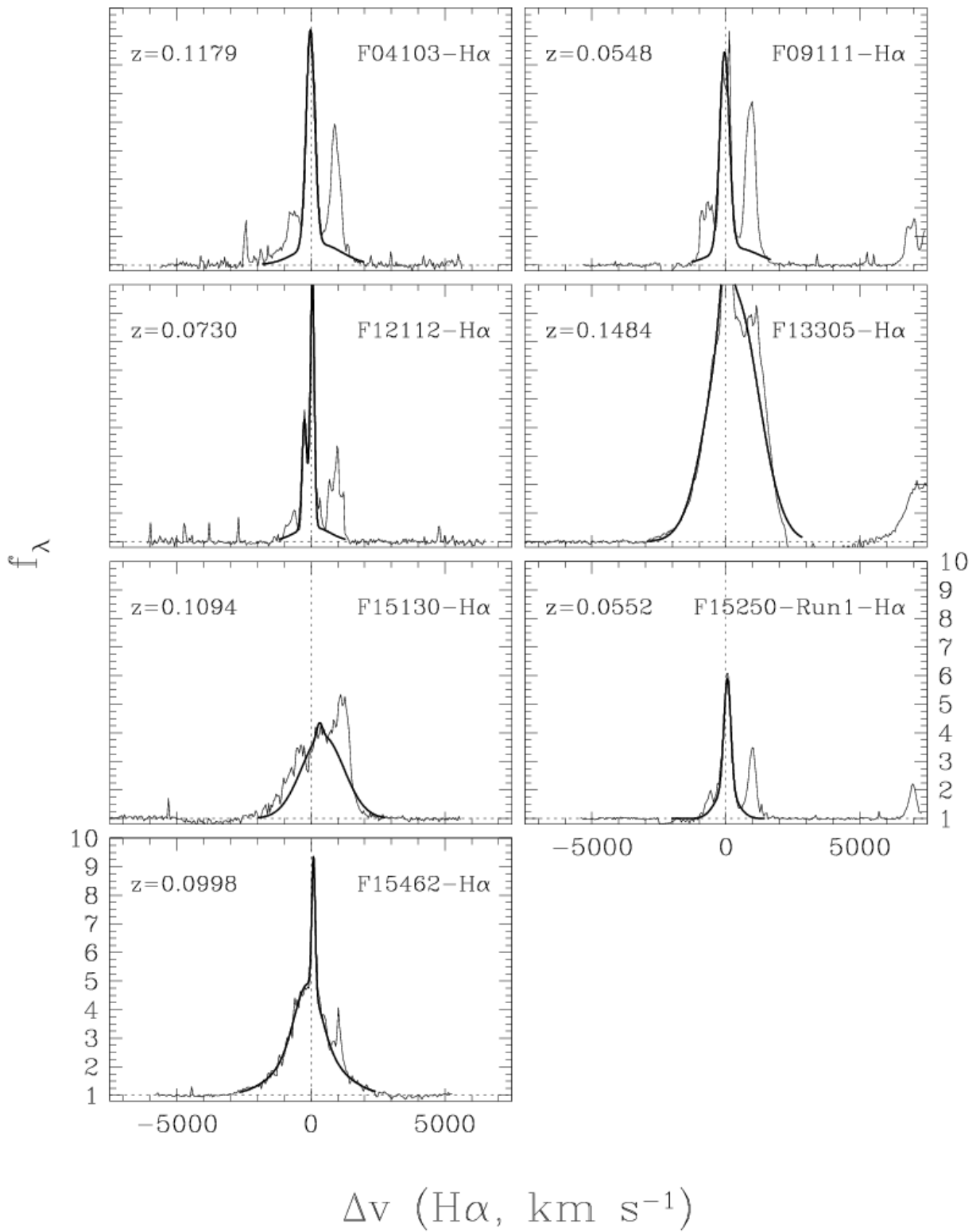


Figure 3.4: Spectra of the H α + [N II] $\lambda\lambda$ 6548, 6583 complexes in ULIRGs. See Figure 3.3 for details.



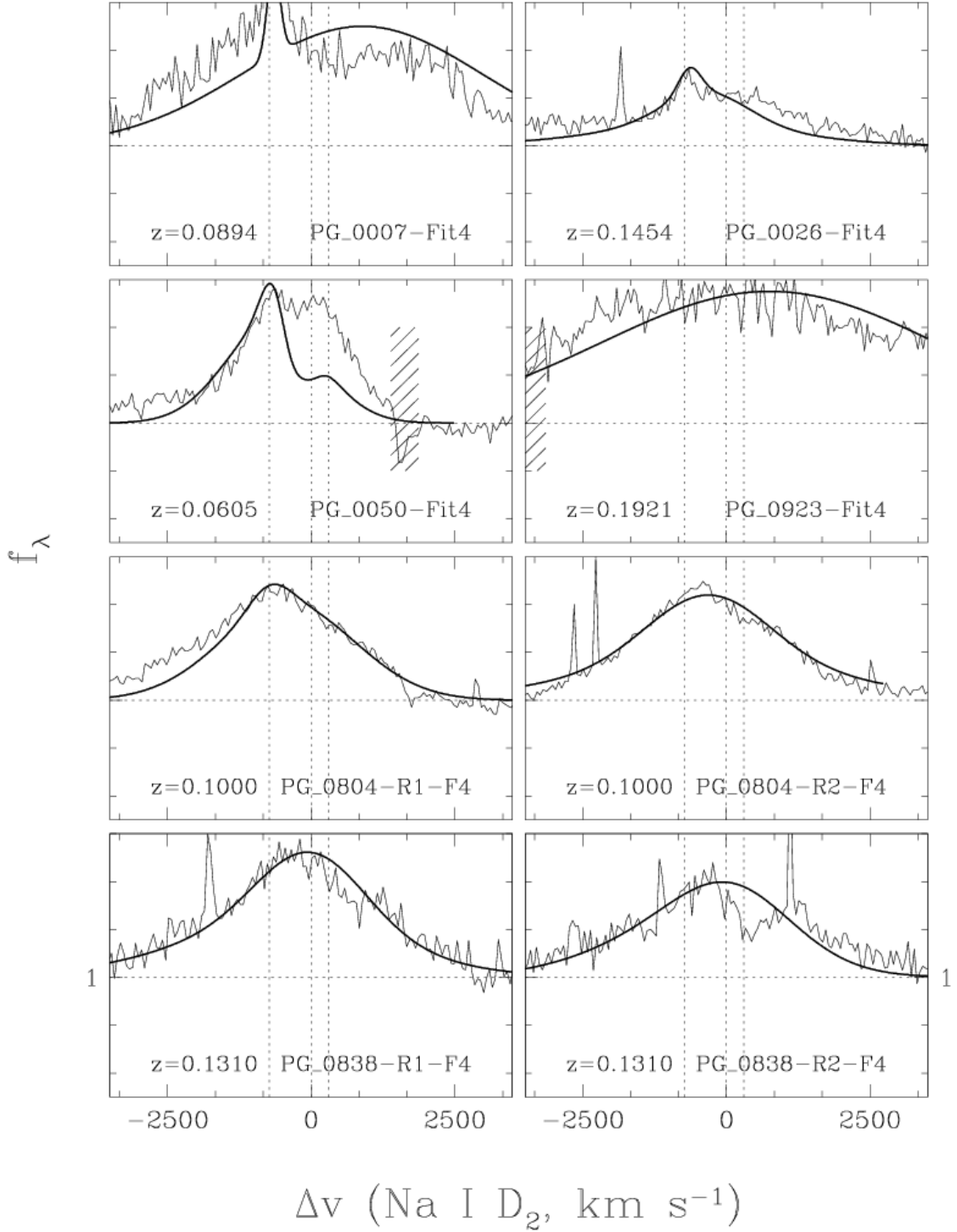
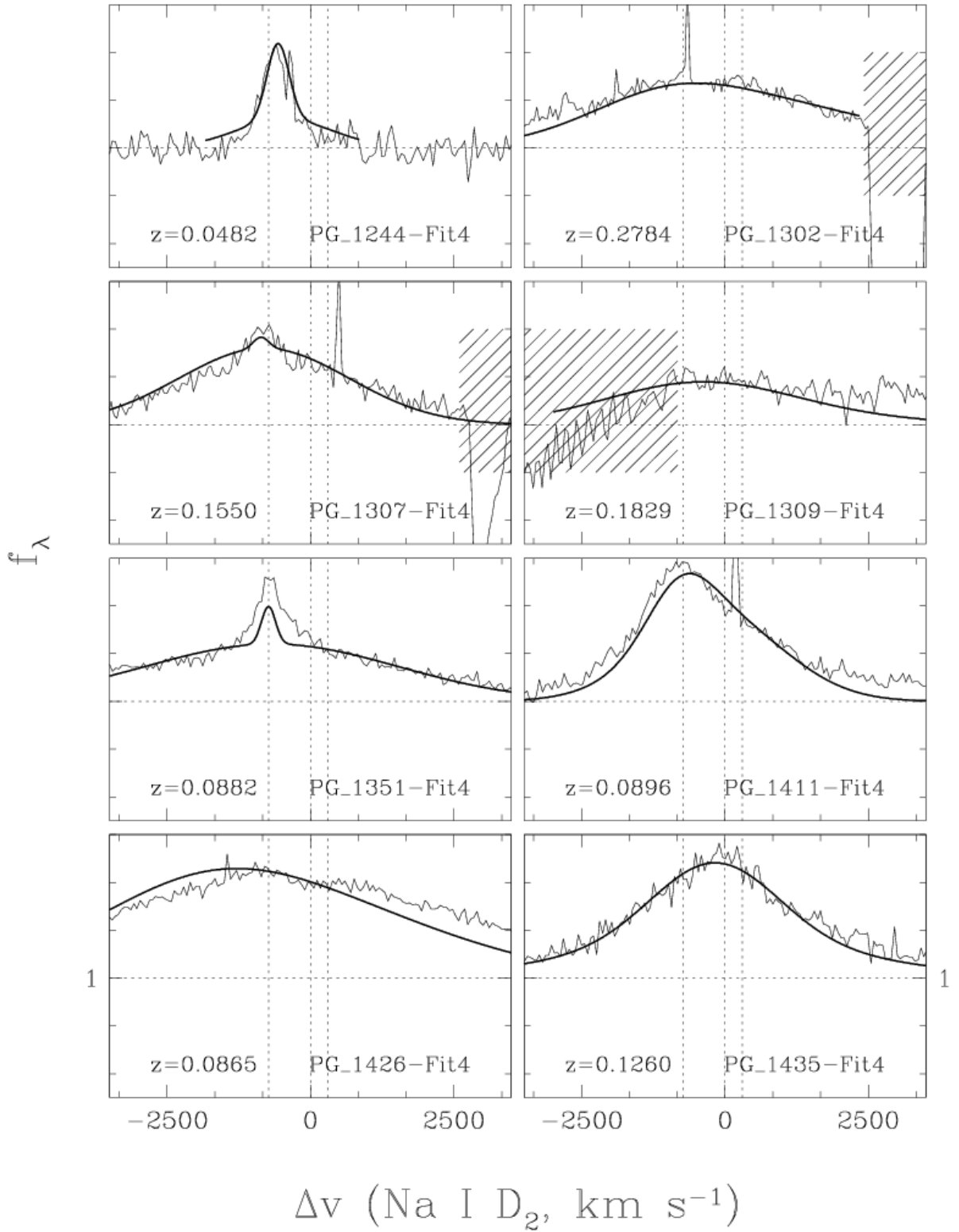
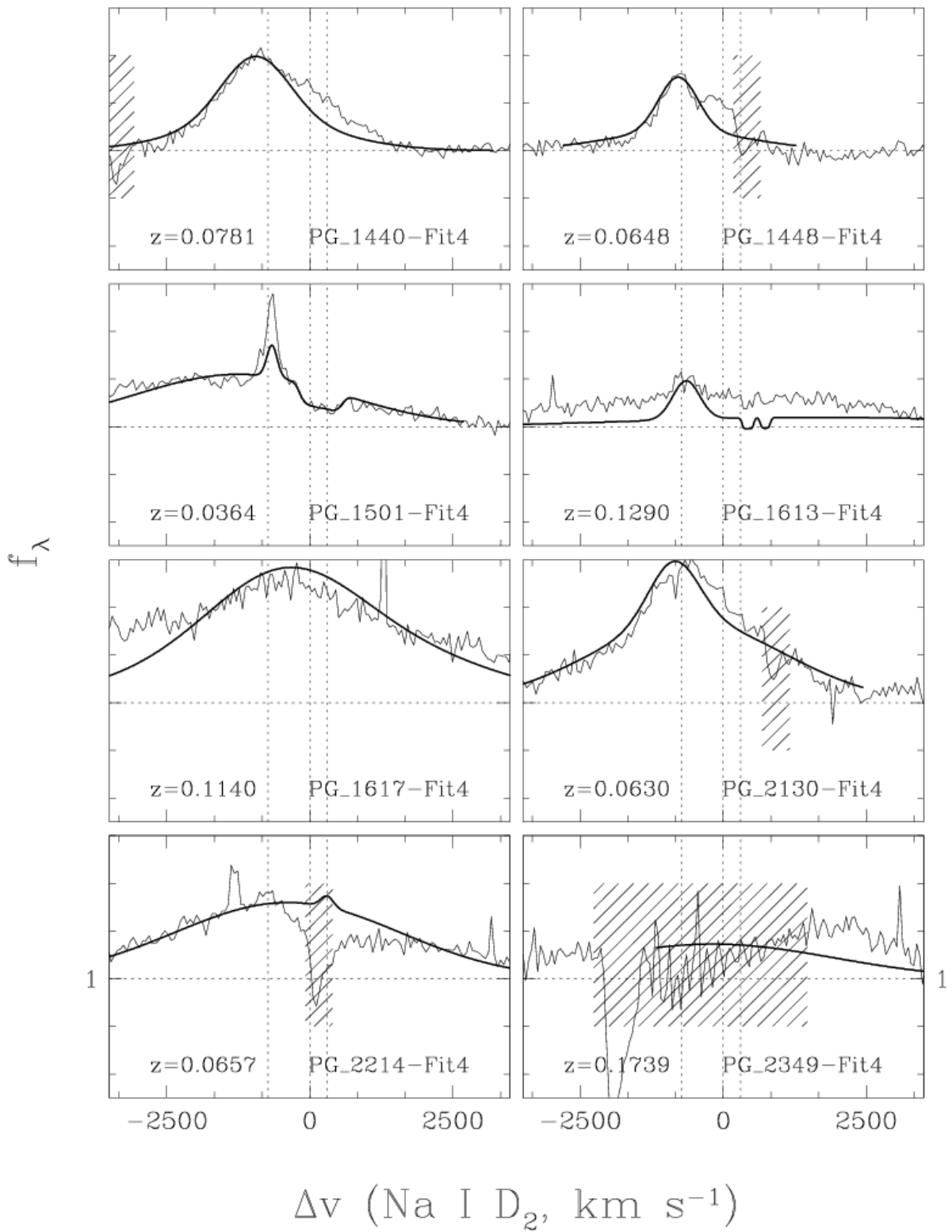


Figure 3.5: Spectra of the He I emission + Na I D absorption region in PG QSOs fitted using method #4: the central velocity(ies), Doppler width parameter(s) (b), and intensity ratio of narrow to broad components of the He I line(s) are fixed to match those of the H α fits as seen in Figure 3.3 Only galaxies with He I emission are plotted here. See Figure 3.1 for further details.





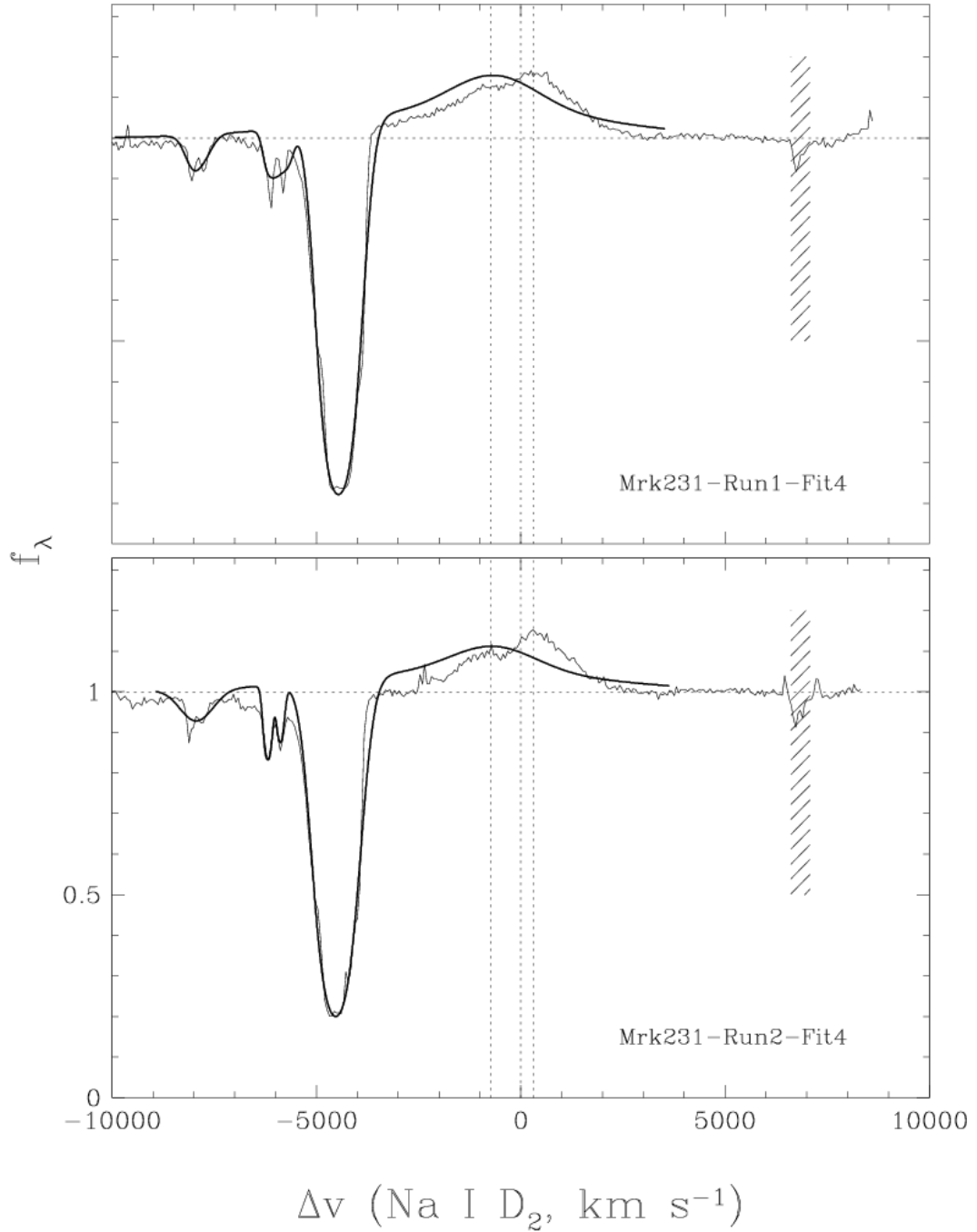
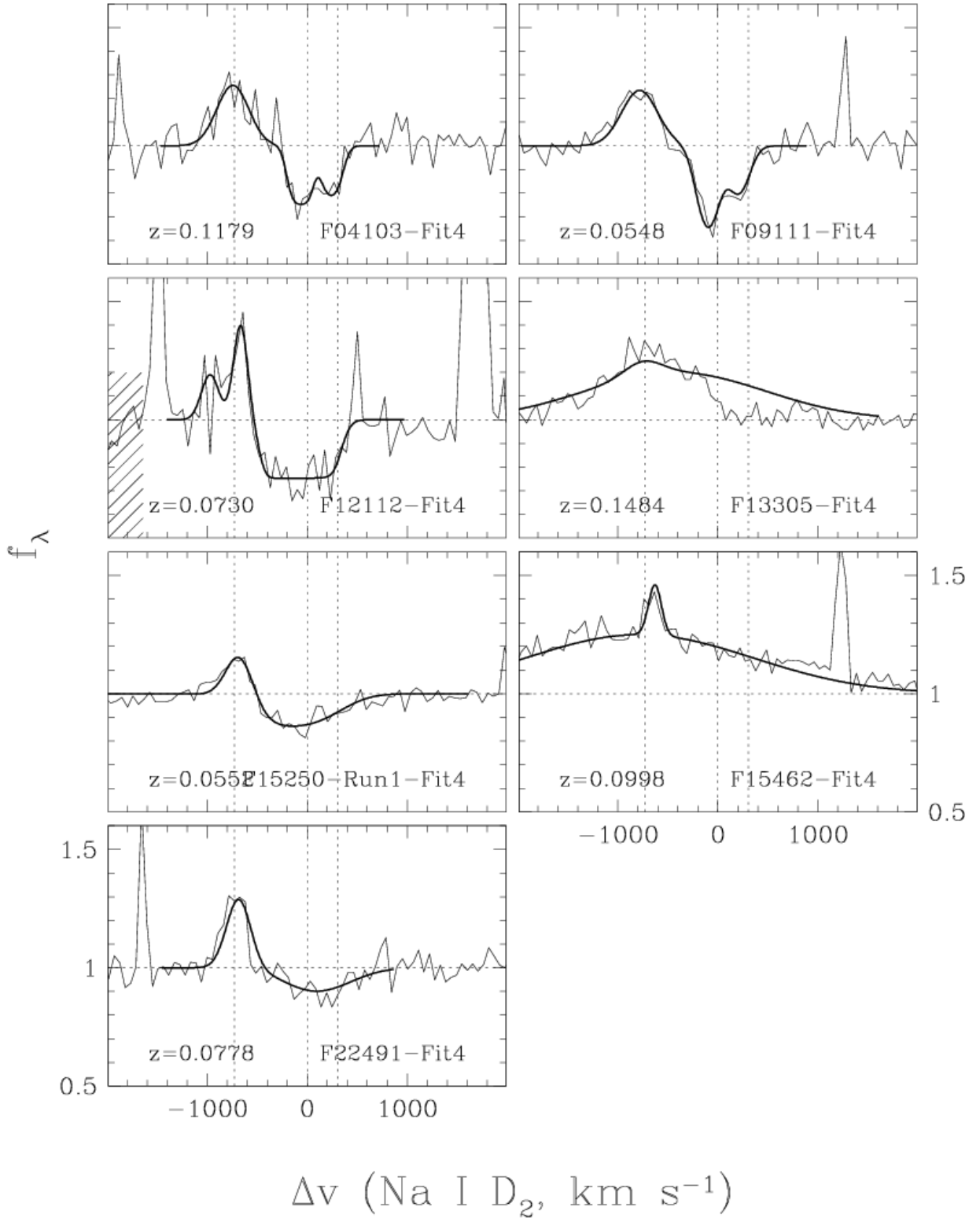


Figure 3.6: Fully-fixed spectra of the He I emission + Na I D absorption region in ULIRGs fitted using method #4: the central velocity(ies), Doppler width parameter(s) (b), and intensity ratio of narrow to broad components of the He I line(s) are fixed to match those of the H α fits as seen in Figure 3.4. Only galaxies with He I emission are plotted here. See Figure 3.2 for description.



We then compared the results of the free-floating fits (Fit 1, “free”) to the results of the fully-fixed fits (Fit 4, “fixed”). For two-thirds of the objects, agreement

between the two is within 10%. For the remaining one-third, discrepancies in Na I D $\lambda_{0,1}$ start at 25% and, in two cases, are over 100%. In the cases of F15250+3608 (25% difference in central wavelength) and F22491-1808 (75%), the difference between Fits 1 and 4 appears to be due to redshift uncertainties; it can be seen in Figure 3.4 that the central peaks of the H α fits for these two objects are slightly redshifted from the expected H α central wavelength, which would affect the central wavelength of the He I line and in turn the measured central wavelength of Na I D. For PG 1613+658 (140%), the discrepancy appears to result from difficulties fitting the H α emission and continuum for the two objects, respectively, due to O₂ telluric absorption. The discrepancy in PG 1501+106 (36%) stems from the He I narrow emission line having a much larger amplitude than predicted by H α ; this, however, could be an artifact of the fitting program, which limits how finely the amplitude can be tuned. The only object whose discrepancy cannot be readily explained is PG 1119+120 (102%); the He I in Fit 4 looks far too broad than the observed He I profile, yet the H α is well fit. As a Type 1 object, however, our Fit 1 may still be correct, as collisional and radiative transfer effects in the broad line region may affect the He I and H α lines differently.

Figure 3.7 shows comparisons between reduced χ^2 for all of our objects. Given that reduced χ^2 values are much closer to unity for the free-floating fits than for their fully-fixed counterparts, and the fact that we can explain all but one of the objects without major Fit 1 vs Fit 4 discrepancies, we choose to use the free-floating fits in our analysis. This is further discussed in the following section, and also allows for better comparison to the data from Chapter 2. The uncertainties on the

measurements, and the following discussion of these measurements, will take into account the discrepancies between Fit 1 and Fit 4 in the few cases where they are significant.

3.4.2 Velocities

Following fitting, velocities of the Na I D absorption complexes could be calculated using the same procedure as in Section 2.4.2. Once again, Δv is the velocity difference between measured Na I D velocity centroid and the systemic Na I D velocity, as determined by the redshift (see Table 3.1 for redshift values). The “maximum” velocity, Δv_{max} , using the width of the absorption line, was again calculated as in Section 2.4.2, although maximum velocities were also calculated for inflowing, positive Δv , using $\Delta v_{max} \equiv \Delta v + \text{FWHM}/2$. A comparison of values for Δv and Δv_{max} based on Fit 1 to those based on Fit 4 can be seen in Figure 3.8. We see very good agreement here, with the exception of the cases mentioned in the previous section. This further justifies our decision to use the free-floating, Fit 1 results in our analysis.

We use the same detection criterion of $\Delta v < -50 \text{ km s}^{-1}$ for an outflow and $\Delta v > 50 \text{ km s}^{-1}$ for an inflow as in Section 2.4.2 for the reasons listed there. We also require a 2σ threshold in measurement uncertainty, corresponding to $|\Delta v| > 2\delta(\Delta v)$, where $\delta(\Delta v)$ is the error in velocity; if twice the error in Δv is greater than Δv itself, we exclude that object. Velocities of the Na I D components of individual objects can be found in Table 3.3. We find no PG QSOs with outflow and only one

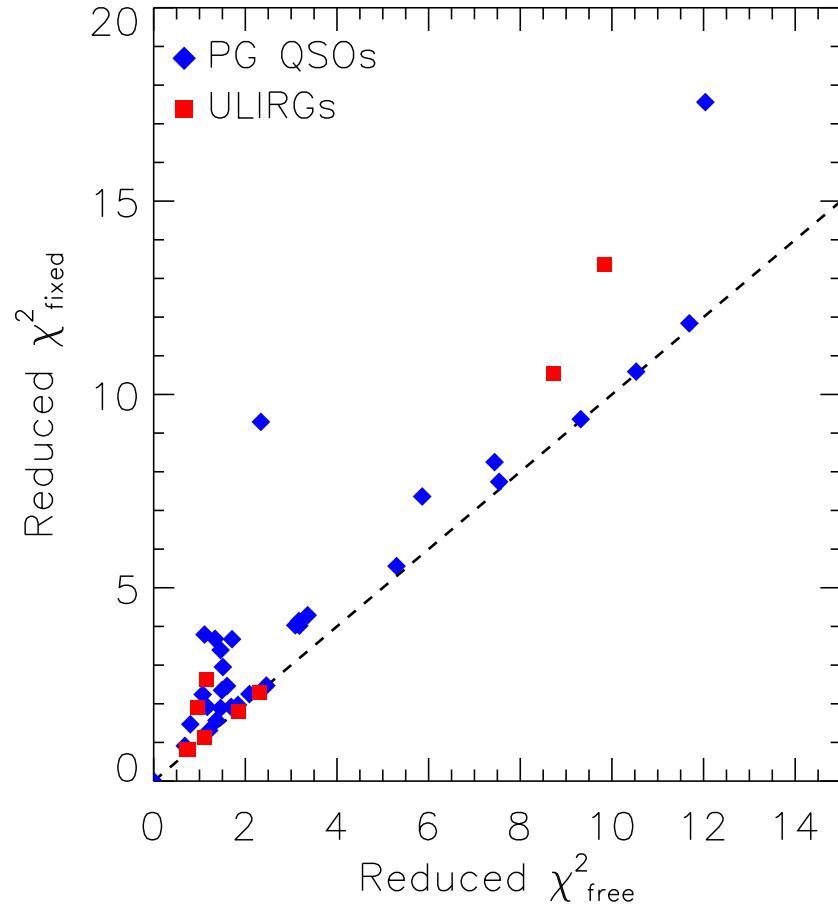


Figure 3.7: Reduced χ^2 values for free-floating and H α -fixed He I parameter fits. See Section 3.4.1 for an explanation of these fits. The dashed black line corresponds to equal χ^2 values. The free fits generally give lower χ^2 , and thus the results from these fits were adopted in the present work.

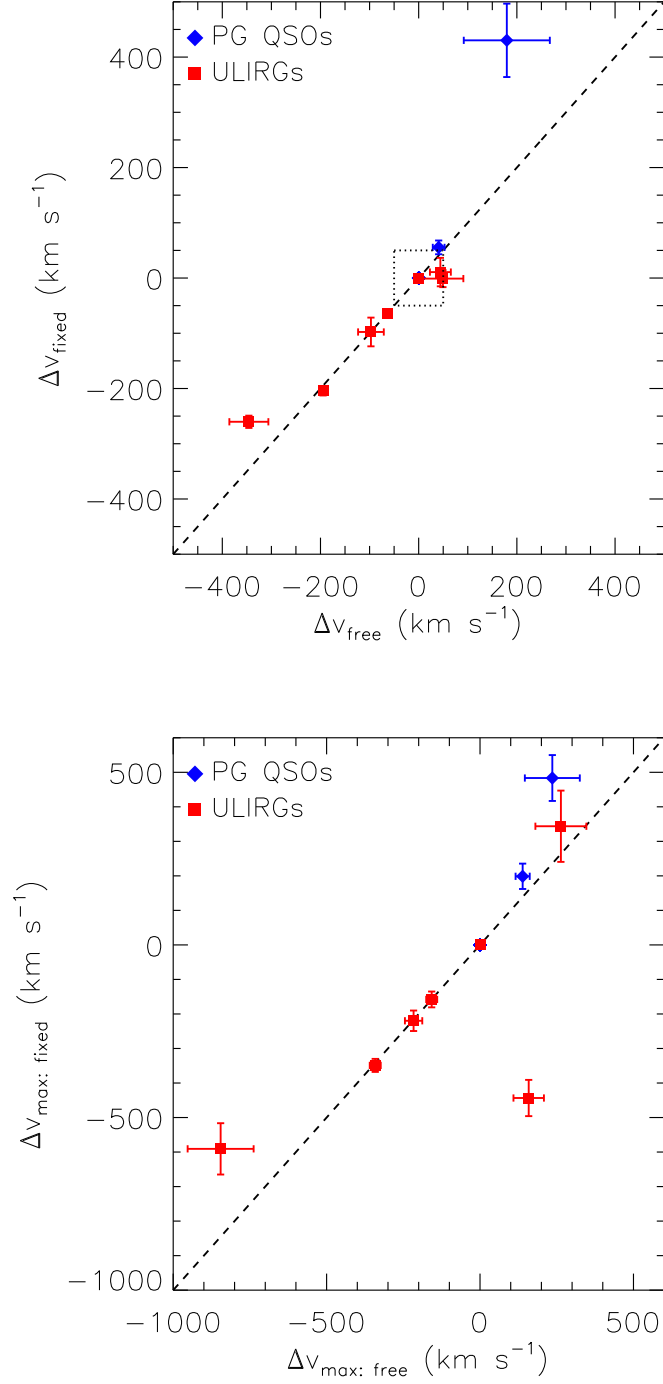


Figure 3.8: *Top:* Δv for $\text{H}\alpha$ -fixed He I fit versus Δv for free-floating He I fit. Dashed black line through center corresponds to equal fixed and free values, and all points outside dashed black box have $|\Delta v| > 50 \text{ km s}^{-1}$. *Bottom:* Same, but for Δv_{max} . With one exception, F15250+3608, the two types of fits give very similar results.

with inflow; the ULIRGs five different objects with outflow and one with inflow. These results will be discussed further in Sections 3.5-3.6.

3.4.3 Column Densities

The formulas used to calculate column densities of Na I D and H along the line of sight are the same as in Section 2.4.3. We again correct for effects of dust depletion and ionization using empirical results that assume Galactic depletion and a 0.9 ionization fraction. For proper comparison with the results of Chapter 2, we again assume solar Na abundance. Calculated Na I D and H column densities are listed in Table 3.3.

3.4.4 Stellar Na I D Contribution

In order to attempt to determine whether the absorption measured in these objects is stellar or interstellar, we turn again to the stellar population synthesis models as described in Section 2.4.4. The preferred method, a scaling relation between Na I D and Mg I *b* equivalent width, is not possible here given that the spectral range of our data does not include the Mg I *b* triplet. We again use the Sed@.0 code (see Section 2.4.4 for references and description): one model is composed of 10% young, instantaneous burst stars(40 Myr), and 90% old stars (10 Gyr), the other model is 1% young stars and 99% old stars. We again emission subtract our spectra, removing He I emission via an IDL code using Fit 1 parameters; we then boxcar smooth the resulting Na I D absorption spectra by 150 km s^{-1} and convolve them

with a $\sigma = 200 \text{ km s}^{-1}$ Gaussian. The emission-subtracted spectra were overlaid with the stellar population synthesis models; if the measured, emission-subtracted Na I D line depth is significantly greater than the Na I D line depth of the models, then we can confidently say that the outflow or inflow is interstellar.

Comparison of our emission-subtracted spectra with the models shows that all but one of our ULIRGs show convincing evidence for interstellar absorption. The Na I D features in PG QSOs, however, are consistent with stellar absorption and thus we cannot determine unambiguously the origin of these features. PG 1613+658 presents an interesting case, however, as the high inflowing velocities measured for this object ($\Delta v = 180 \text{ km s}^{-1}$, $\Delta v_{max} = 236 \text{ km s}^{-1}$) are significantly stronger than would be expected for a stellar feature. The uncertainty in redshift for this object is only 0.0001, which contributes only $\sim 25 \text{ km s}^{-1}$ to the velocity error, so redshift uncertainty is likely not to blame for such high measured velocity. In Figure 3.9, we show the results for PG 1119+120, a case in which the measured Na I D line (or at least a significant fraction of it) is likely due to stellar absorption, as well as the results for F09111-1007, which is clearly representative of interstellar absorption. This criterion is very conservative, however, since the AGN continuum emission reduces the equivalent width of the Na I D profile.

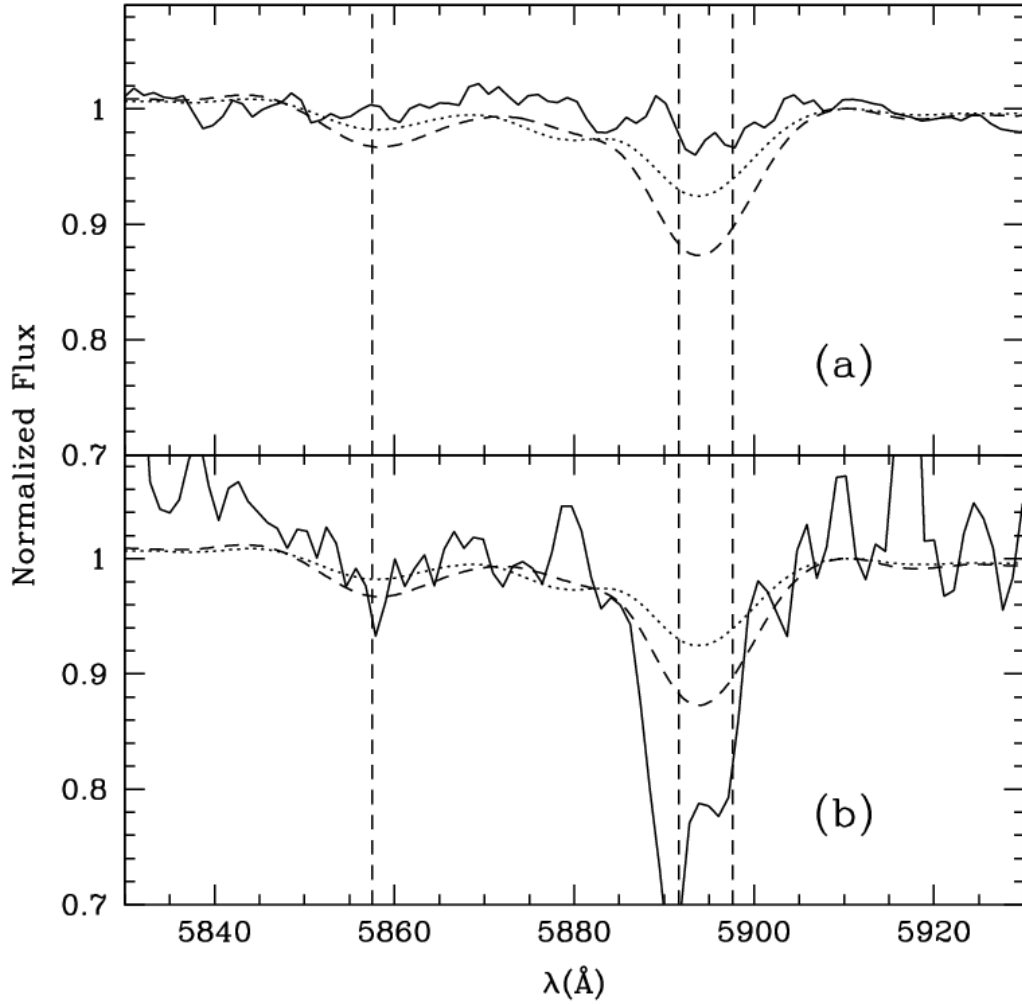


Figure 3.9: Spectra of a PG QSO, (a) PG 1119+120, and a ULIRG, (b) F09111-1007, in the Na I D region. These spectra were He I emission line subtracted, boxcar smoothed, and normalized to unity at 5910 Å. The dotted line shows the model corresponding to 10% young 40 Myr instantaneous burst population and 90% old 10 Gyr population, as outlined in Section 3.4.4. The dashed line shows the model corresponding to 1% young and 99% old. Strong stellar features are marked with vertical lines. The spectrum for PG 1119+120 shows weak absorption in comparison to the stellar models, which indicates that the absorption may be stellar in origin (see caveat at the end of Section 3.4.4). The spectrum for F09111-1007, however, shows very strong absorption compared to the stellar models, consistent with absorption that is most likely of an interstellar origin.

3.5 RESULTS AND DISCUSSION: OUTFLOWS

3.5.1 Detection Rates

As described previously, Figure 3.1 shows the He I and Na I D complexes for the 28 PG QSOs in our sample, plus 4 additional spectra for those objects which were observed in the first run as well as the second. These spectra are plotted on a velocity scale based on Na I D $\lambda 5890$ systemic. Out of a total of 28 PG QSOs, we failed to detect any blueshifted Na I D absorption. The dearth of PG QSO outflow detections could be explained by two physical causes: one, the extreme brightness of the QSO optical nucleus may dilute the equivalent width of the Na I D lines in outflows, making them too faint to detect unambiguously, and two, if these PG QSOs have already reached the blowout phase in their merger evolution (see Chapter 1), there may simply be not enough neutral gas remaining to become entrained in outflows.

The He I and Na I D complexes for the 10 ULIRGs in our sample, plus 2 additional spectra for those objects observed in the first run as well as the second, can be seen in Figure 3.2. The measured properties for each individual Na I D outflow, as well as the overall outflow averages, are listed in Tables 3.6 (see Section 3.5.3 for descriptions of dynamical quantities) and 3.7, respectively.

Out of a total of 10 ULIRGs, we detected blueshifted Na I D absorption with $\Delta v < -50 \text{ km s}^{-1}$ in five objects – F04103-2838, F09111-1007, F12112+0305, F15250+3608, and Mrk 231 – for an outflow detection rate of $50 \pm 14\%$. None was ruled out by the $2\text{-}\sigma$ criterion. For the ULIRGs with outflows, Mrk 231 was the only

object with multiple (three) absorption components. Velocities for these objects ranged from -64 to -7980 km s^{-1} , with Δv_{max} spanning a similar range of -158 to -8098 km s^{-1} . These ranges in Δv and Δv_{max} are also very similar to that found for the IR-luminous AGN in Rupke et al. (2005c), and -67 to -9608 km s^{-1} and -240 to -11244 km s^{-1} , respectively.

In order to properly address the scientific goals of this study, we must not only examine this data set individually but also compare it with results of previous studies in order to draw accurate conclusions. We hereafter refer to the combination of this sample, the Krug et al. (2010) data (Chapter 2), and the RVS05b and c data as the “combined sample.” We can group the data in three ways for the most thorough analysis: detection of outflows and outflow strength as a function of far-infrared luminosity, as a function of spectral type, and as a function of interaction class. To create this combined sample with these groupings, we do as follows: PG QSOs, Seyferts from Krug et al. (2010) (Chapter 2), and Seyferts from RVS05c are grouped in with IR-luminous AGN or IR-faint AGN depending upon their far-infrared luminosity (IR-luminous AGN have $L_{\text{FIR}} > 10^{11} L_{\odot}$, IR-faint AGN have $L_{\text{FIR}} < 10^{11} L_{\odot}$) – we use far-IR luminosity in order to keep the data from Chapter 2 separate. Objects from each of those data sets are also grouped with Type 1 AGN or Type 2 AGN depending upon their optical spectral type: Seyfert 1s and PG QSOs are classified as Type 1 AGN, and Seyfert 2s are classified as Type 2 AGN. The IR-luminous starbursts category comprises ULIRGs from this sample with optical spectral types of HII or LINER, as well as data from RVS05b. The singles and binaries groupings are performed as described in Section 3.2.5.

The most basic property we can examine is whether there is a correlation between outflow detection rate (in this case, as in Chapter 2, this is defined by taking the number of outflows in a given luminosity bin and dividing that by the number of absorption components in the combined sample) and far-infrared luminosity in our sample. Several previous studies have indicated that outflow detection rate increases with infrared and far-infrared luminosity [Rupke et al. (2005b), Sato et al. (2009)]. This trend was again found in our previous study, Chapter 2 [Krug et al. (2010)], as outflow detection rate increased with far-infrared luminosity. For IR-faint AGN and IR-luminous starbursts, this trend indicates that as star formation rates increase, so too does the likelihood of finding an outflow in a given object, as L_{FIR} is a tracer of SFR [Kennicutt (1998)]; this becomes different for IR-luminous AGN, as will be described below.

A simple look at the percentages indicates that we find that trend in our data set, as ULIRGs, by definition infrared-bright, show a 50% outflow detection rate, whereas no PG QSO outflows were found. We are dealing here with small numbers of galaxies, however, and so we would like to include other data in this comparison. Panel *a* of Figure 3.10 shows that the combined sample reveals the same trend. Here, the trend is even stronger here once we include additional data: higher far-infrared luminosity gives a higher likelihood of detecting an outflow. For starbursting objects, this would imply that higher star formation increases likelihood of detection. However, this may be a secondary correlation, as IR-brightness is proportional to dust and gas content in AGN. In the AGN with lower IR-luminosities, the gas content is lower, and thus there is less neutral gas that can become entrained in

outflows. We note, though, that the detection rate for IR-luminous AGN is nearly double the detection rate for IR-luminous starbursts in the highest luminosity bin, possibly implying that it is not the starburst but rather the AGN which is primarily driving the IR-luminous AGN outflows.

Panel *b* of Figure 3.10 shows the same outflow detection rate calculation, but this time for the spectral type grouping. Again we note an increasing outflow detection rate with L_{FIR} , particularly in Type 2 AGN. We note also extreme jumps in Type 1 and Type 2 AGN detection above $L_{\text{FIR}} = 10^{12} L_{\odot}$, also referenced for IR-luminous AGN in the previous section. The detection rate for Type 1 AGN is significantly higher than the detection rate for IR-luminous starbursts in the highest luminosity bin, potentially implying that outflows in Type 1 AGN, like those in IR-luminous AGN, are driven by the AGN. The detection rates of outflows in Type 2 AGN are equal to the detection rates of outflows in IR-luminous starbursts in all bins within 1σ .

Panel *c* of Figure 3.10 shows the outflow detection percentages in binaries and singles versus L_{FIR} . We once again see an increase in outflow detection rate with L_{FIR} , markedly increasing above $L_{\text{FIR}} = 10^{12} L_{\odot}$. When we look at the binary and single galaxy samples as a whole, as tabulated in Table 3.8, we note that overall, binaries show a slightly higher outflow detection percentage than singles, although we believe that this is due to the significantly smaller number of binaries.

As noted above, there is a marked jump in outflow detection rate for IR-luminous starbursts at $L_{\text{FIR}} > 10^{11} L_{\odot}$ and for IR-luminous AGN and Type 1 AGN at $L_{\text{FIR}} > 10^{12} L_{\odot}$. A recent study probing molecular gas has shown increasing

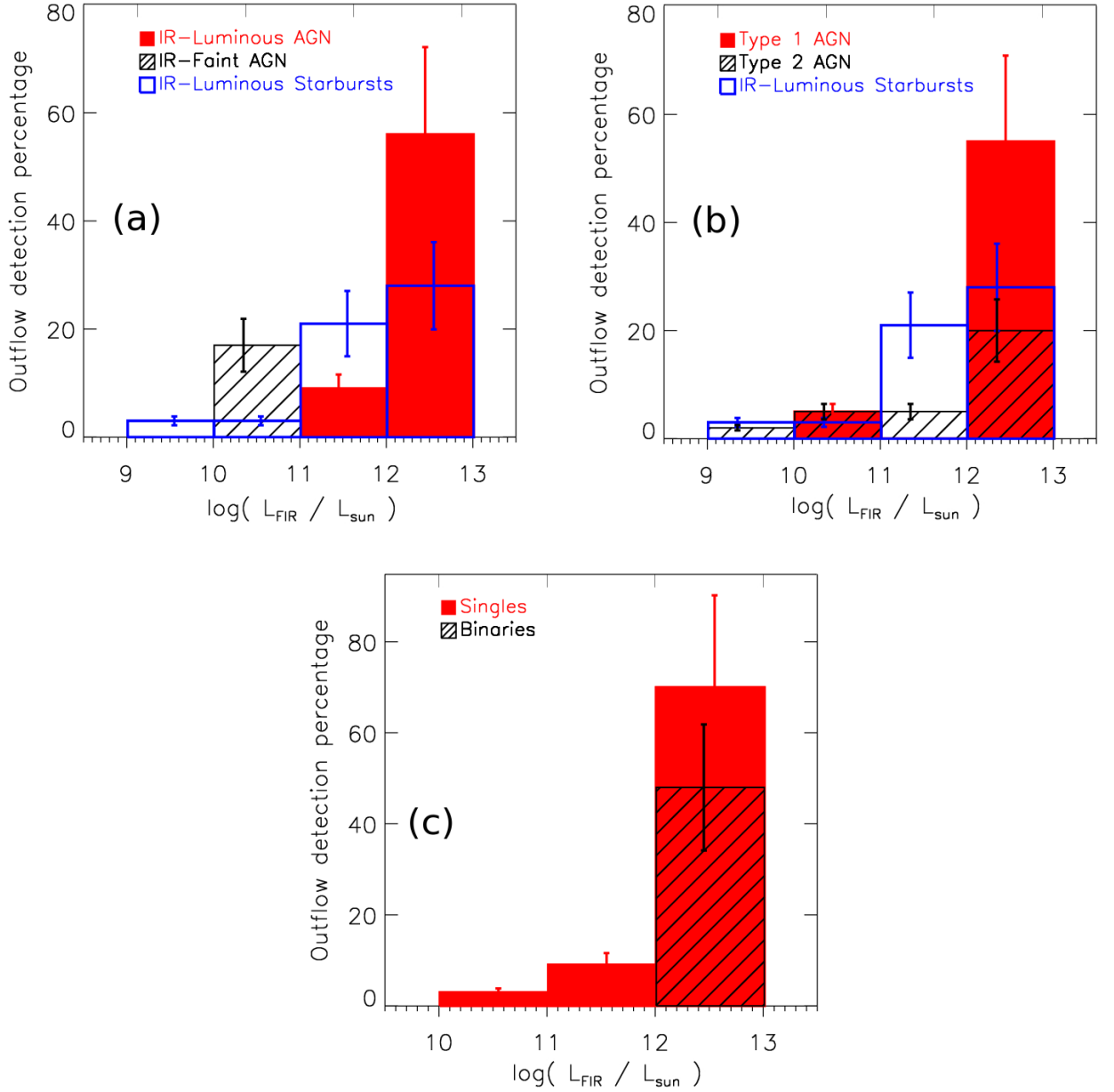


Figure 3.10: *a*: Histogram showing the fraction of IR-luminous AGN, IR-faint AGN, and IR-luminous starbursts with outflows as a function of L_{FIR} for the combined sample. Errors are 1σ , assuming a binomial distribution. Note a general trend of increasing detection percentage with increasing L_{FIR} . *b*: Same, but for the Type 1 AGN, Type 2 AGN, and IR-luminous starbursts in the combined sample. There is a steady increase in detection rate with L_{FIR} . IR-luminous starbursts show a jump in detection rate at $L_{\text{FIR}} \geq 10^{11} L_{\odot}$, and both types of AGN show significant jumps at $L_{\text{FIR}} \geq 10^{12} L_{\odot}$. *c*: Same, but for singles and binaries in the combined sample. The data are split into singles and binaries as described in Section 3.2.5. Singles show a very strong increase in outflow detection above $L_{\text{FIR}} \geq 10^{12} L_{\odot}$; binary outflows are only detected in this luminosity bin.

outflow rates for $L_{\text{AGN}} > 10^{12} L_{\odot}$ [Veilleux et al. (2013b)], and it is worthwhile to examine the effect of AGN luminosity on outflow detection rate here as well. We have calculated the AGN luminosity for the PG QSOs and ULIRGs, as well as for the RVS05b and c data, via the methods of Veilleux et al. (2009a) (see Section 3.2.3). The resulting detection percentages per bin versus L_{AGN} for our luminosity grouping are plotted in Figure 3.11. In the top panel, we note an increase in detection percentage with $L_{\text{AGN}} > 10^{11} L_{\odot}$ for IR-luminous starbursts; detection percentages for both IR-luminous AGN remain somewhat constant above $10^{11} L_{\odot}$. When we split the IR-luminous AGN into types, as seen in the bottom panel of Figure 3.11, we find that, whereas Type 2 AGN detections remain fairly constant above $10^{11} L_{\odot}$, Type 1 AGN are not detected until $L_{\text{AGN}} > 10^{12} L_{\odot}$. There were too few outflowing binaries in our sample which had L_{AGN} measurements for us to plot outflow detection rate versus L_{AGN} for singles and binaries.

3.5.2 Kinematics

Beyond simple detection rates, examining the kinematics of these outflows is of utmost importance. Figure 3.12 shows the percentage of total absorption components in a given velocity bin for each of the groupings described in Section 3.5.1. We note here that IR-luminous starbursts fall in a limited range of velocities, whereas the AGN, particularly IR-luminous AGN, tend toward more extreme velocities. Roughly one-third of the total IR-luminous AGN absorption components show velocities of -1000 km s^{-1} or below, and IR-luminous AGN also show

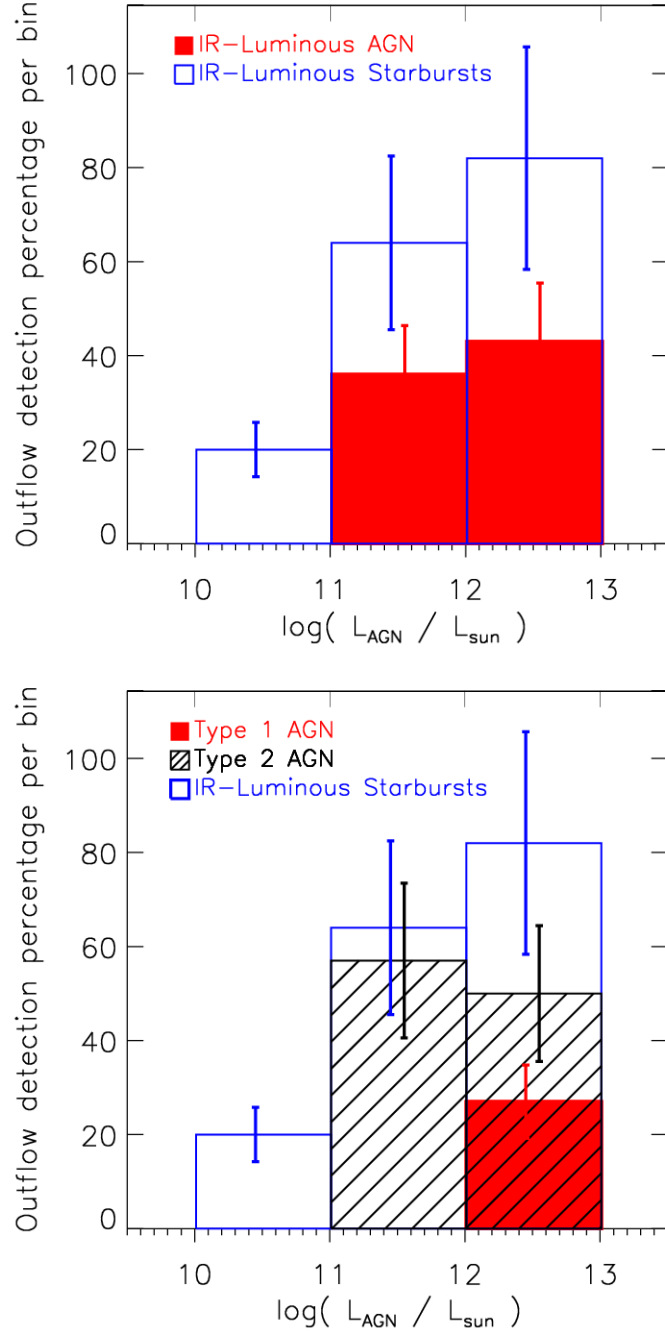


Figure 3.11: Top: Histogram showing the percentage of IR-luminous AGN and IR-luminous starbursts in each AGN luminosity bin which have an outflow (see Section 3.2.3 for L_{AGN} calculation). The error bars are 1σ , assuming a binomial distribution. Note the increasing trend in detection percentage with L_{AGN} , as well as the jump in detection at $L_{\text{AGN}} \geq 10^{11} L_{\odot}$. Bottom: Same, but for Type 1 AGN, Type 2 AGN, and IR-luminous starbursts. Detections for Type 2 AGN begin at $L_{\text{AGN}} \geq 10^{11} L_{\odot}$ and remain fairly constant, whereas Type 1 AGN do not show outflow detections until $L_{\text{AGN}} \geq 10^{12} L_{\odot}$.

the most positive velocities (which will be discussed more in Section 3.6). We can thus conclude, as in Section 3.5.1, that IR-luminous AGN outflows are likely driven primarily by the AGN, as their velocities tend to be so much greater than those of IR-luminous starbursts and of IR-faint AGN. In the spectral type histogram, we note that Type 1 AGN show the strongest negative velocities, with over 50% of their components having velocities below -1000 km s^{-1} . Very few Type 1 AGN have small negative velocities, with the next-largest fraction of Type 1 components having positive velocities. Type 2 AGN are primarily concentrated around $\Delta v = 0$. The extreme velocities of Type 1 AGN again validate our claim that Type 1 AGN outflows are powered primarily by AGN; the lower-velocity Type 2 AGN outflows are likely, as in Chapter 2, powered by starbursts. In the interaction class velocity histogram, we see that binaries are fairly closely distributed about zero velocity, whereas singles show a wide range of velocities, both positive and highly negative. Over one-third of the Na I D velocity components in singles have velocities below -1000 km s^{-1} . The wide range of Na I D absorption velocities, particularly the number that are extremely negative, could be indicative of strong outflows being triggered by the merger process, whether by triggered star formation or triggered AGN [Sanders et al. (1988), Feruglio et al. (2010), Sturm et al. (2011)].

Another important conclusion of these figures is that these outflows that we are measuring are really outflows, and that we are not simply seeing galactic rotation. As described in Section 2.7.1, were these blue- and redshifted Na I D lines solely due to rotation, we should see a symmetric distribution about $\Delta v = 0$, but none of our groupings shows that symmetric distribution. The IR-faint AGN are closely

clustered around $\Delta v = 0$ simply because they less frequently are found to have outflows (see Table 3.8); this effect is not due to rotation as the distribution is asymmetric. IR-luminous starbursts are also somewhat clustered about $\Delta v = 0$, but have a tail toward the negative velocity end.

Looking at the average properties in Table 3.8 again bolsters the claims that we have made: IR-luminous AGN and Type 1 AGN show by far the fastest outflowing velocities, implying that the AGN is playing the largest role in powering those winds; Type 2 AGN velocities are very similar to those of starbursts, implying that they may be fundamentally similar; and that whereas binary detection rates are higher than singles (likely due to small sample size), the outflow velocities in singles are typically much faster.

Additionally, we can look at plots showing Δv_{max} as a function of L_{FIR} (typically correlated with star formation rate) and of galactic circular velocity (correlated with galactic mass) for these groupings, as seen in Figure 3.13. References for v_{circ} are listed in Table 3.1, but values are primarily taken from Dasyra et al. (2006a, 06b, 07, 08) and Ho et al. (2007, 08). We find again that IR-luminous starbursts are closely clustered at low Δv_{max} values, that IR-faint AGN show some high-velocity outflows but are mostly low-velocity, and that IR-luminous AGN show the highest values for Δv_{max} . Looking in particular at the IR-luminous starbursts, we note a rough trend of faster outflows with L_{FIR} . Δv_{max} for Type 2 AGN seem to closely follow the trends of IR-luminous starbursts with L_{FIR} and v_{circ} , increasing only slightly with L_{FIR} and keeping fairly constant with v_{circ} . The Type 1 AGN at low far-IR luminosity have substantially slower velocities than those at high far-IR luminosity,

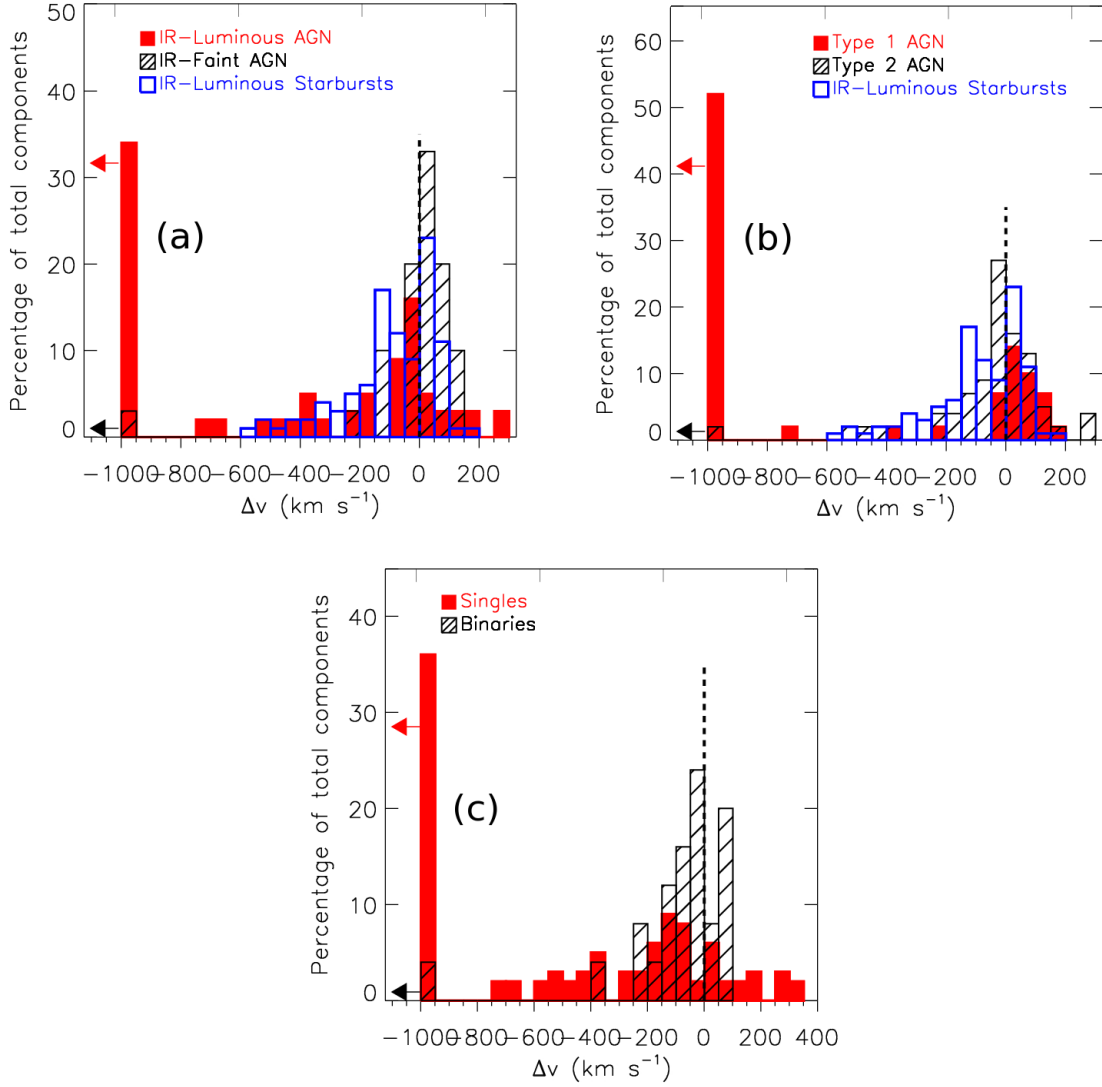


Figure 3.12: *a*: Histogram showing the percentage of total components of IR-luminous AGN, IR-faint AGN, and IR-luminous starbursts in the combined sample in a given velocity bin. IR-luminous AGN show the widest spread in velocities, with by far the highest percentage of highly negative velocities. IR-faint AGN are fairly well-concentrated around zero velocity, but with the highest overall percentage of positive components. IR-luminous starbursts are also somewhat concentrated about zero velocity, but with a tail toward negative velocities. *b*: Same, but for Type 1 AGN, Type 2 AGN, and IR-luminous starbursts of the combined sample. Over half of the Type 1 AGN components have outflowing velocities faster than -1000 km s^{-1} , whereas Type 2 AGN velocities are more closely concentrated about zero velocity. *c*: Same, but for singles and binaries in the combined sample. Binary outflow velocities are primarily concentrated about $\Delta v = 0$. Single outflow velocities are highly spread out between $-800 < \Delta v < 400 \text{ km s}^{-1}$ but show a significant number of highly negative components.

but there are only two Type 1 AGN outflow components at $L_{\text{FIR}} < 10^{12.0} L_{\odot}$, and we cannot draw conclusions from such small numbers. The plots for binaries and singles do not reveal much in the way of trends with L_{FIR} or v_{circ} . The most notable feature of these plots is that, like Δv , singles span a much larger range in Δv_{max} than binaries. We cannot draw any firm conclusions here regarding Δv_{max} versus v_{circ} for any of these groupings due to small number statistics (many galaxies in our sample do not have circular velocity measurements).

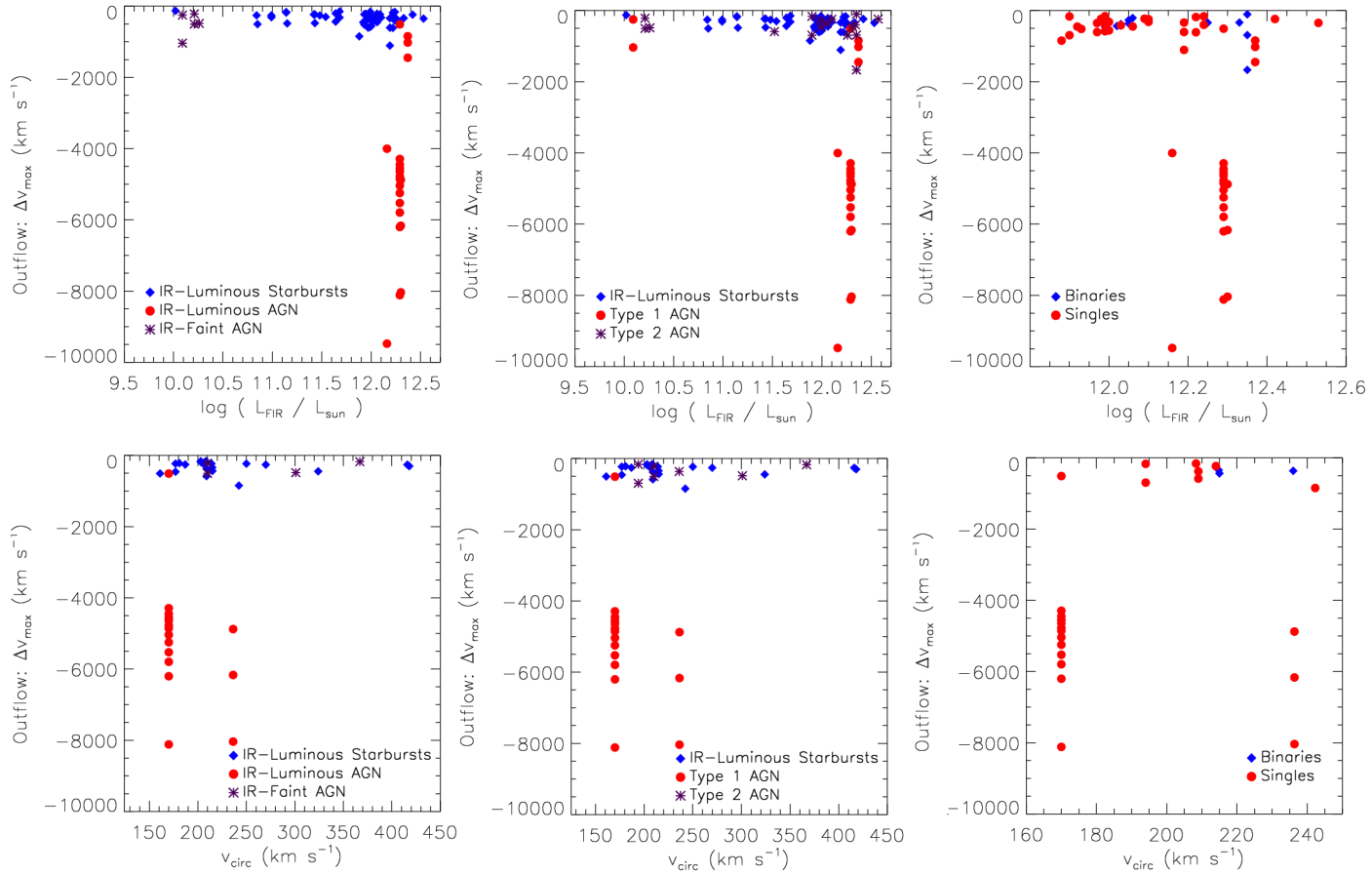


Figure 3.13: *Left*: Plots showing outflow Δv_{max} as a function of L_{FIR} for IR-luminous starbursts, IR-luminous AGN, and IR-faint AGN for the combined sample (*top*), and for Δv_{max} vs the circular velocity of the galaxy (*bottom*). The Δv_{max} for IR-luminous starbursts may show a slight increase with L_{FIR} , but no discernible trend can be seen with v_{circ} . *Middle*: Same, but for IR-luminous starbursts, Type 1 AGN, and Type 2 AGN in the combined sample. There appears to be an increasing trend in Δv_{max} with L_{FIR} , but Δv_{max} values are fairly constant with respect to v_{circ} . *Right*: Same, but for binaries and singles in the combined sample. No discernible trends can be seen in either plot.

Looking now at velocity trends with AGN luminosity, Veilleux et al. (2013) have also reported finding increases in outflow velocities above an AGN luminosity of $10^{12} L_{\odot}$, so we will explore that for the IR-luminous AGN and IR-luminous starbursts as well. The upper left panel of Figure 3.14 shows the outflowing velocities for IR-luminous AGN and IR-luminous starbursts as a function of their AGN luminosities. We find here that, remarkably consistent with both a recent neutral gas (Na I D) study [Rupke & Veilleux (2013)] and a recent molecular gas (OH) study [Veilleux et al. (2013b)], objects with $L_{\text{AGN}} > 10^{11.7} L_{\odot}$ have high-velocity outflows ($\Delta v < -1000 \text{ km s}^{-1}$) more frequently than objects with $L_{\text{AGN}} < 10^{11.7} L_{\odot}$. We can examine again the influence of AGN luminosity on outflow maximum velocity. The upper right panel of Figure 3.14 uses the same sample as the upper left panel, but this time we splits those IR-luminous AGN into Type 1 and Type 2 AGN. We note that, of those outflows which showed high velocities at $L_{\text{AGN}} > 10^{11.7} L_{\odot}$, all but one is a Type 1 AGN. In the lower panels of Figure 3.14, we plot in terms of maximum outflowing velocity, and we find that all objects shift downward, and that one starbursting galaxy has crossed the -1000 km s^{-1} line.

Finally, we have also performed rigorous statistical analyses to confirm our conclusions regarding the differences in each of these groupings. As in Chapter 2, we have used both the Kolmogorov-Smirnov (K-S) and Kuiper tests; the K-S test is inherently biased in terms of differences about the mean and thus we use both tests for proper comparison. These tests are performed on two different quantities (Δv and Δv_{max}) for all objects in a given sample and for objects with outflows only. The results of these tests are tabulated in Table 3.11, divided up by grouping. Overall,

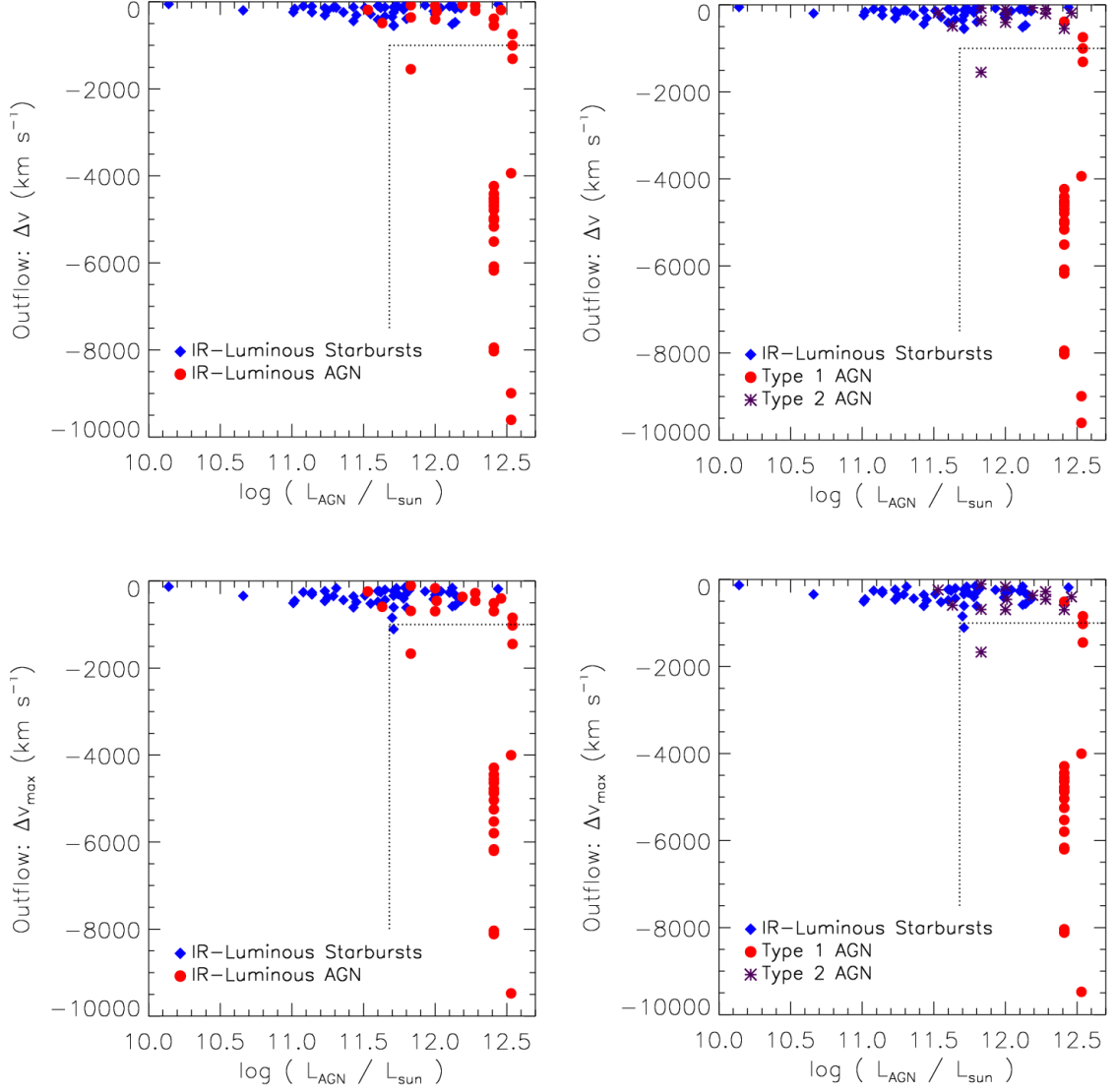


Figure 3.14: *Upper panels:* At left, outflow velocities for IR-luminous AGN and IR-luminous starbursts in the combined sample, as plotted versus AGN luminosity. The dotted lines help to highlight our finding that objects with $L_{\text{AGN}} > 10^{11.7} L_{\odot}$ tend to more frequently have high velocity outflows ($\Delta v_{\text{max}} < -1000 \text{ km s}^{-1}$). At right, same, but for Type 1 AGN, Type 2 AGN, and IR-luminous starbursts in the combined sample. We note that all but one of the high-velocity outflows located in the dotted line box are Type 1 AGN. *Lower panels:* The left and right panels are the same groupings as the upper panels, but this time are plotted in terms of maximum outflow velocity. Note that the upper points outside the box have all shifted downward, particularly the IR-luminous starbursts, and one non-AGN has crossed the -1000 km s^{-1} line.

we find that Type 1 AGN and IR-luminous starbursts have, for both Δv and Δv_{max} , the lowest likelihood of originating from the same parent distribution, and thus are most physically distinct from one another, in terms of outflows only, as well as the full sample. The other two comparisons with the next lowest overall probabilities are Type 1 AGN versus Type 2 AGN, which is in good agreement with the results of Chapter 2, and IR-luminous AGN versus IR-luminous starbursts. Binaries and singles are shown to be fundamentally distinct in the full sample, but just barely failed our $P(null) < 0.1$ for both tests criterion in outflows; this may be due to small number statistics in binary outflows in our sample. One other important comparison to note is that Type 2 AGN and IR-luminous starbursts show a strong likelihood of arising from the *same* parent population, which again is in good agreement with the results of Chapter 2.

These statistical analyses of kinematic properties shore up the claims which we have made in both Chapter 2 and heretofore in this chapter: 1, that outflows in IR-luminous AGN and IR-luminous starbursts are driven by fundamentally different processes, those in IR-luminous AGN being driven primarily by the AGN, those in IR-luminous starbursts being driven primarily by star formation; 2, that outflows in Type 1 AGN and Type 2 AGN are fundamentally distinct, those in Type 1 AGN being powered by the AGN and those in Type 2 AGN being primarily powered by starbursts; and 3, that kinematic properties of outflows in binaries and singles are fundamentally different, but that merger phase is not necessarily the primary driver of those outflows. The AGN unification model could explain some of these connections [Antonucci (1993), Urry & Padovani (1995)]. Obscuration from a dusty

torus could prevent high-velocity outflows in Type 2 AGN from being observed, particularly if such high-velocity outflows originate from sub-parsec scales in the broad line region. The unification model could also explain why we see more high-velocity outflows in absorption in Type 1 AGN; if our line of sight is towards the nucleus and avoids the torus, we not only miss that obscuration but we also have a brighter optical continuum source against which to measure Na I D absorption. The earlier described merger picture could also provide an obscuring patchy dust screen to prevent the observation of high-velocity outflows in Type 2 AGN; this would not affect Type 1 AGN to the same extent given the aforementioned brighter continuum.

3.5.3 Dynamics

We wish to examine the dynamical properties of these outflows, in addition to their kinematics, for full comparisons between our sets of data. Using the covering fraction, as determined by the fitting function, as well as column density and velocities, as calculated according to the prescriptions in Sections 3.4.2 and 3.4.3, we can estimate the mass, momentum, and total energy of the neutral gas phase of the ISM that these winds are probing, as well as the outflow rates of each of those quantities. As in Chapter 2, Section 2.7.1.2, we follow the method outlined in the original study, RVS05b. This method assumes that the Na I D outflows which we are probing here are spherically symmetric, mass-conserving, free winds. Velocity and instantaneous mass outflow rate are both independent of radius and fall to zero

outside of the wind, where the wind is assumed to be a thin shell with a uniform radius of 5 kpc. The radii, like in Chapter 2, have been scaled up to 5 kpc in order to facilitate comparisons across the samples. Numerous unproven assumptions are being used here to calculate these dynamical quantities, and thus we treat these dynamic results as order-of-magnitude estimates. As a caveat, we thus note that these dynamical estimates should be considered to be illustrative examples rather than hard data.

In order to estimate the global covering factor for the ULIRGs in our sample, thereby estimating the degree of collimation of these winds, we use the average value of covering fraction, $\langle C_f \rangle$. This value is based on the C_f values returned by the fitting program and is listed in Table 3.7. The covering fraction is used to parameterize wind clumpiness, and can also reflect the global solid angle that the wind subtends if the wind were to be viewed from the galactic center. For the large-scale covering factor, which is dependent upon the opening angle of the wind, we assume $C_\Omega = 0.8$ for ULIRGs, as chosen in RVS05b. Putting these together, we obtain $\Omega \sim 0.3$ for the ULIRGs. The ULIRG Ω is consistent with that of RVS05b for IR-luminous ULIRGs.

Figures 3.15-3.20 show the resulting values for these quantities as functions of L_{FIR} and v_{circ} for each grouping (see Section 3.5.1). In general, for the luminosity grouping and the spectral type grouping, dynamical quantities increase as L_{FIR} increases and appear to roughly decrease as v_{circ} increases. The L_{FIR} trend is in good agreement with the results of RVS05b, RVS05c, and Chapter 2 [Krug et al. (2010)], and agrees with our conclusion from the kinematics that IR-luminous AGN and

Type 1 AGN have significantly stronger outflows than IR-faint AGN / Type 2 AGN and IR-luminous starbursts, owing to being powered by the AGN.

One quantity which was not discussed in Chapter 2 but was calculated in RVS05b and c is the mass entrainment efficiency, η . This value takes the entrained mass outflow rate of the wind and divides it by the star formation rate. This value was not very applicable to the Chapter 2 data, as those objects were IR-faint and had significantly lower star formation rates, but is useful to look at here, given that it quantifies the relationship between the wind and those starbursts which are likely driving the wind. We find that η ranges from ~ 0.2 -60 in ULIRGs, the upper ends due to one case of extremely high velocity winds (Mrk 231). These values are again dependent upon the assumptions made in global covering fraction and radius. Each of these values, SFR, dM/dt , and η , is averaged over the life of the wind (the starburst, in the case of SFR) in our model [Rupke et al. (2005b)]. The lifetimes of these winds, which we calculate as $t_{\text{wind}} = r_2/v$ as in RVS05b, range from 0.6-73 Myr for the ULIRGs. Leitherer et al. (1992) suggest that stellar winds and supernovae can power winds on timescales of ~ 10 Myr, which is consistent with our calculated wind timescales.

The role that these outflows can play in galactic feedback has been discussed in RVS05b and c and in Chapter 2 [Krug et al. (2010)] for the older data sets, but we can still examine it here for the ULIRGs. Dynamical quantities as calculated for the ULIRGs are tabulated in Table 3.6. For the seven ULIRG outflows (we are here only including the results for the April 2012 run for F15250+3608 and Mrk 231, not the December run), we get an average energy outflow rate of $\sim 10^{43.9}$

$(\frac{\Omega}{0.3}) (\frac{r}{5 \text{ kpc}}) \text{ erg s}^{-1}$, or $\sim 10^{11} (\frac{\Omega}{0.3}) (\frac{r}{5 \text{ kpc}}) L_{\odot}$. The average bolometric luminosity of these targets is $L_{\text{bol}} = 10^{12.3} L_{\odot}$ [Veilleux et al. (2009a)]; the average energy outflow rate of the ULIRGs in our sample is $\sim 5\%$ that of the average bolometric luminosity. This indicates that the ULIRG Na I D outflows could not really play a significant role in galactic feedback. If we look solely at our strongest outflowing target, Mrk 231, we get an average energy outflow rate of $\sim 10^{46.5} (\frac{\Omega}{0.3}) (\frac{r}{5 \text{ kpc}}) \text{ erg s}^{-1}$, or $\sim 10^{13} (\frac{\Omega}{0.3}) (\frac{r}{5 \text{ kpc}}) L_{\odot}$. This calculation would seem to show that the outflowing Na I D in Mrk 231 contributes over 100% of its bolometric luminosity, which is obviously incorrect and indicates that we are over-estimating these dynamical values due to over-simplified assumptions (particularly the calculated value of Ω and the chosen radius). It has been shown via integral field spectroscopy that the slowest of the Mrk 231 outflows originates from roughly 2-3 kpc from the nucleus [Rupke & Veilleux (2011), Veilleux et al. (2013b)]; the extreme-velocity, broad absorption line outflows in Mrk 231, however, are likely originating on the same scale at the broad line region (sub-pc), in which case the highest-velocity outflows may be originating from within a parsec of the nucleus. If we adjust the calculations above for that change in radius, we find that the highest-velocity Na I D component for Mrk 231 contributes on the order of 1% of the bolometric luminosity. It is likely that the lower velocity outflows in Mrk 231 could be playing some role in galactic feedback, but again note that our dynamical estimates are rather uncertain.

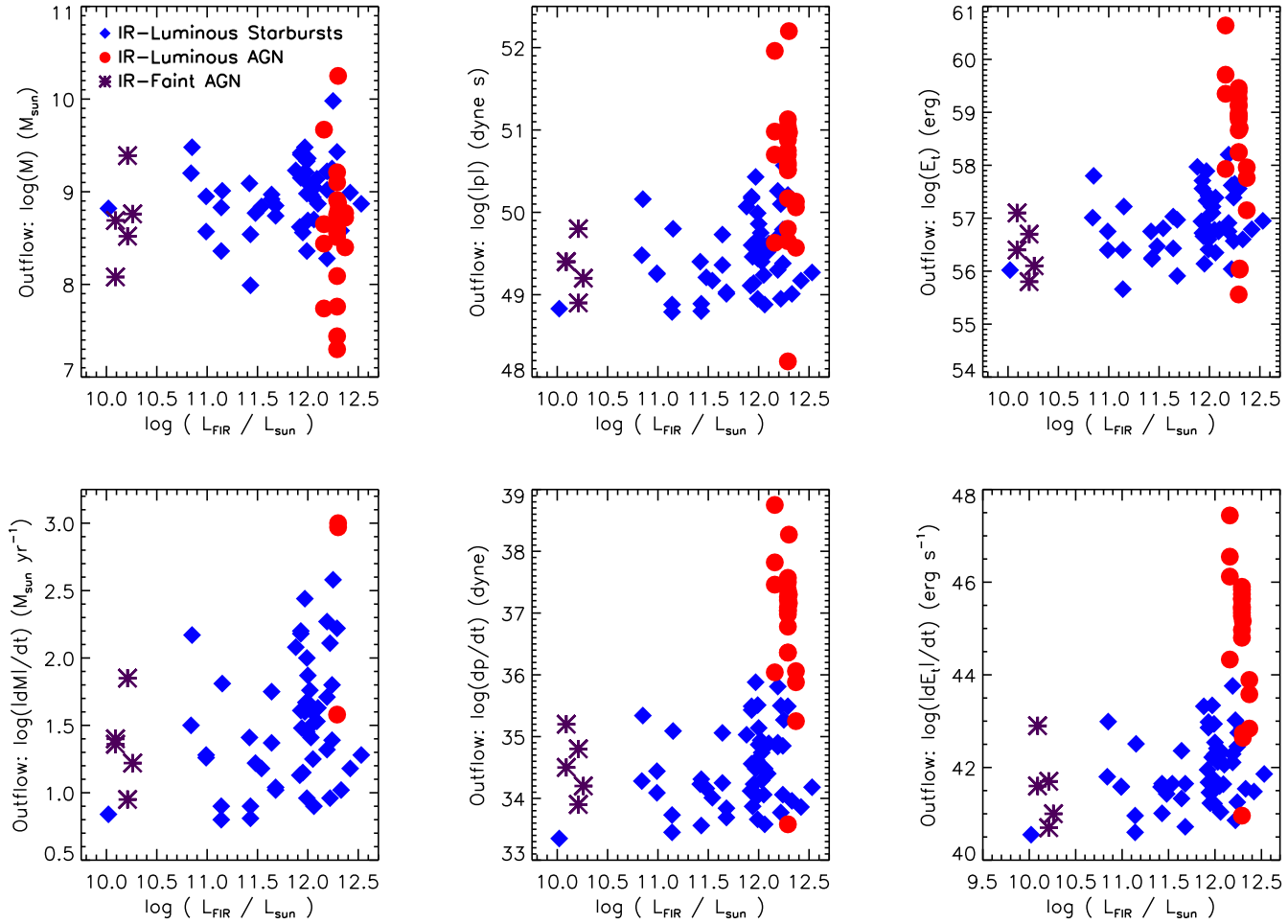


Figure 3.15: Plots showing outflow mass, momentum, energy, mass rate, momentum rate, and energy rate as a function of L_{FIR} for IR-luminous starbursts, IR-luminous AGN, and IR-faint AGN. See Section 3.5.3 for details. Note that values tend to increase with L_{FIR} .

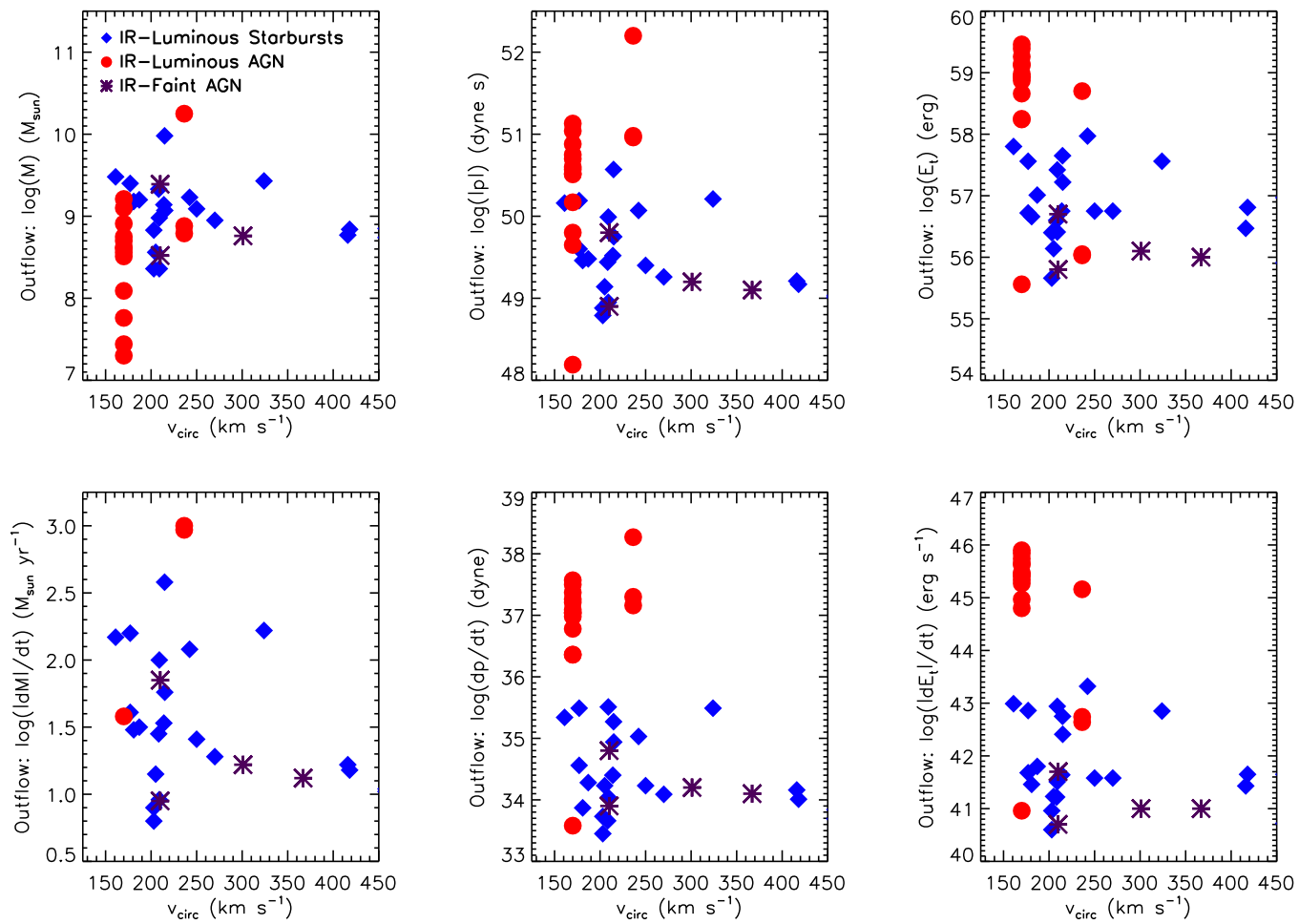


Figure 3.16: Same as Figure 3.15, but versus circular velocity of the galaxy. Note the values tend to decrease with v_{circ} .

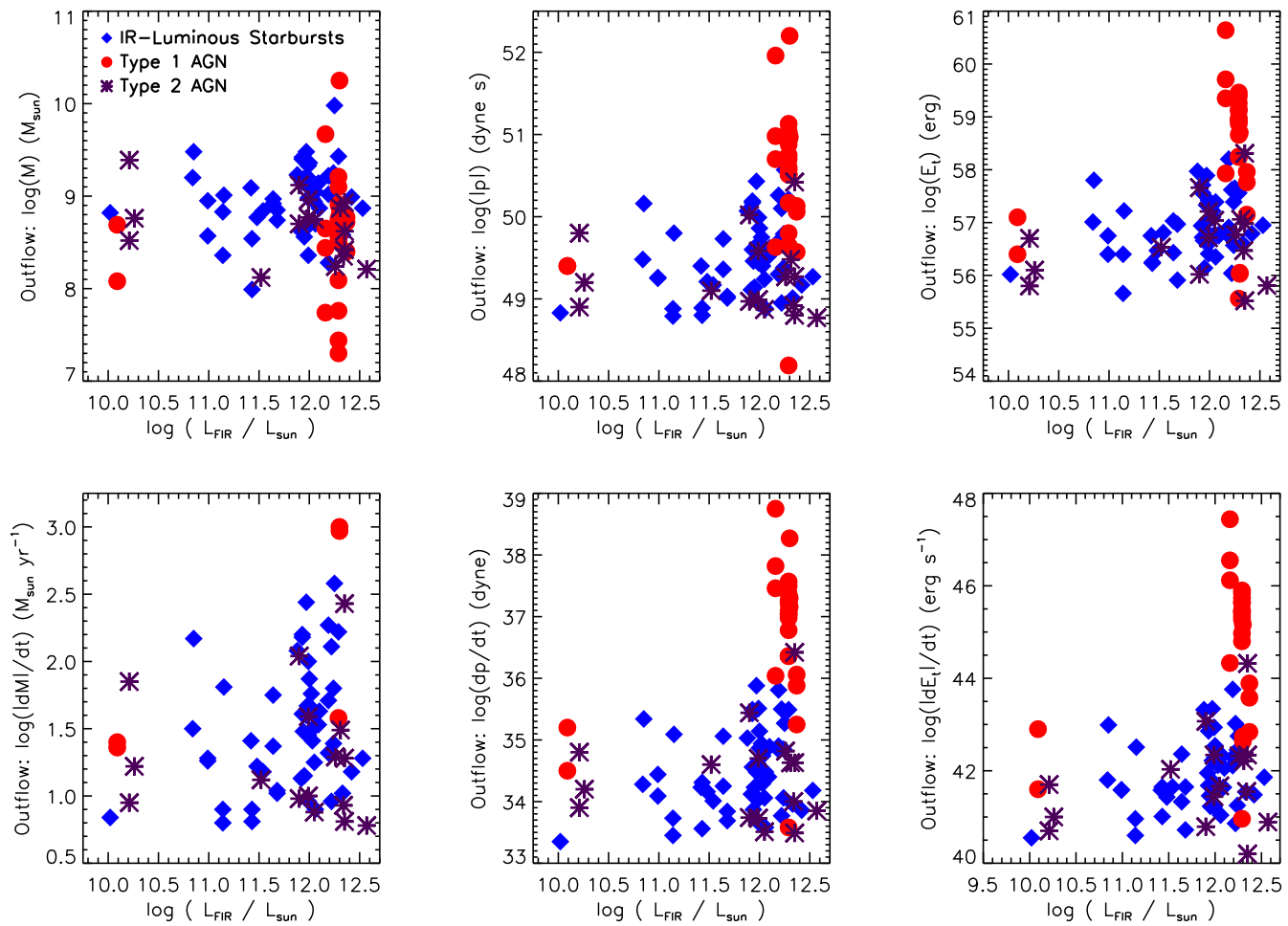


Figure 3.17: Plots showing outflow mass, momentum, energy, mass rate, momentum rate, and energy rate as a function of L_{FIR} for IR-luminous starbursts, Type 1 AGN, and Type 2 AGN. See Section 3.5.3 for details. Note that values tend to increase with L_{FIR} .

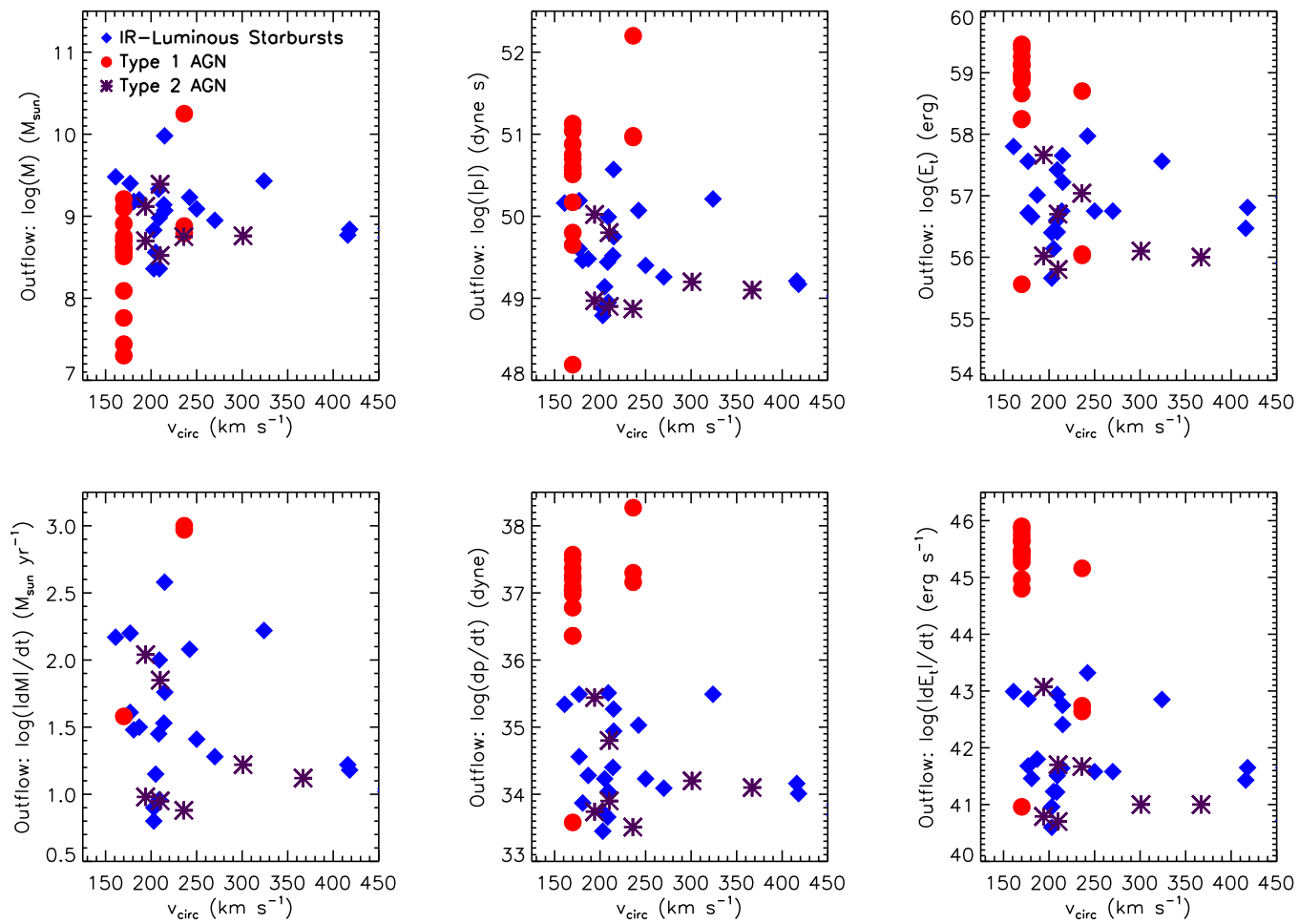


Figure 3.18: Same as Figure 3.17, but versus circular velocity of the galaxy. Note the values tend to decrease with v_{circ} .

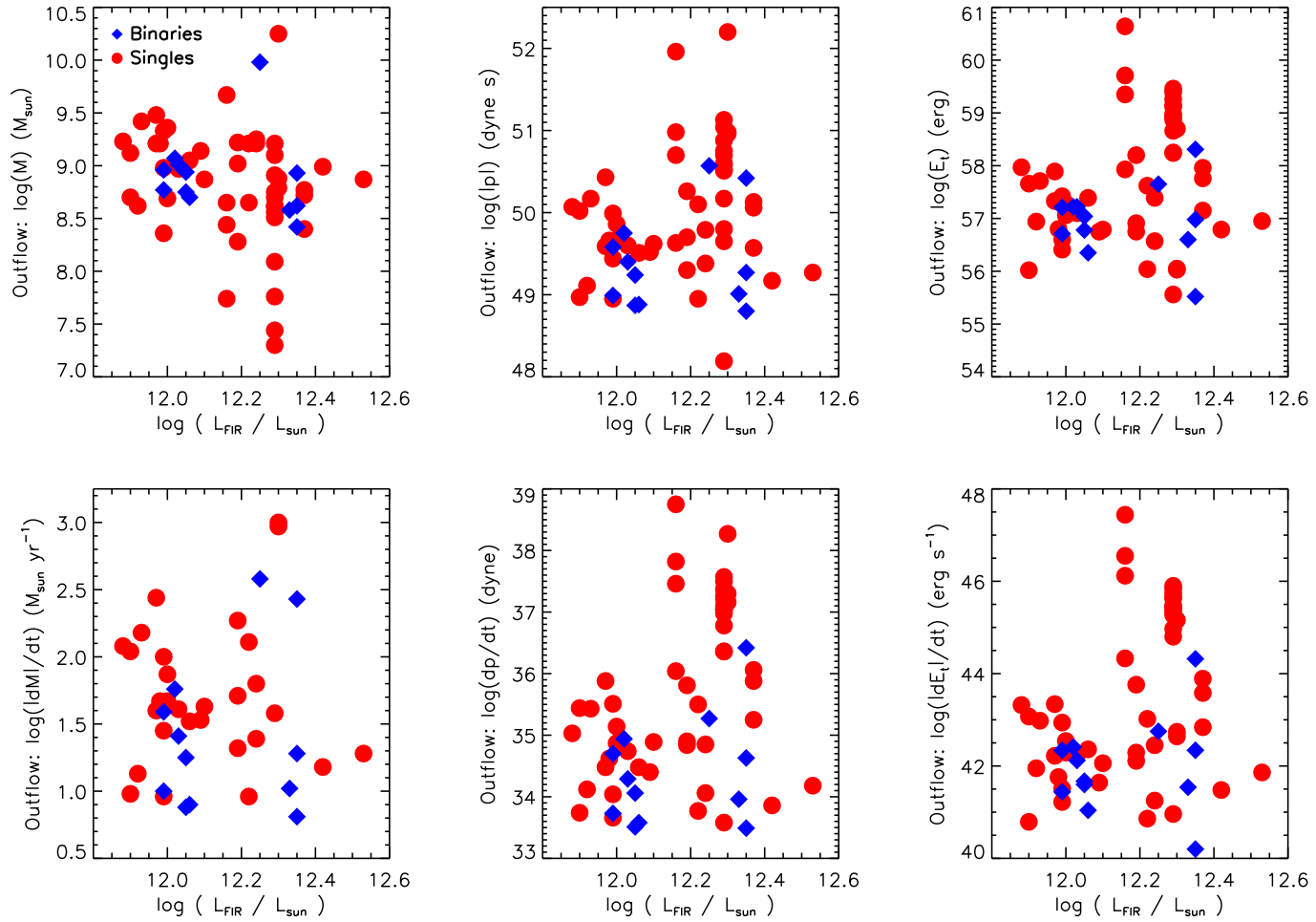


Figure 3.19: Plots showing outflow mass, momentum, energy, mass rate, momentum rate, and energy rate as a function of L_{FIR} for binaries and singles. See Section 3.5.3 for details. Note that singles tend to have larger dynamics values on average.

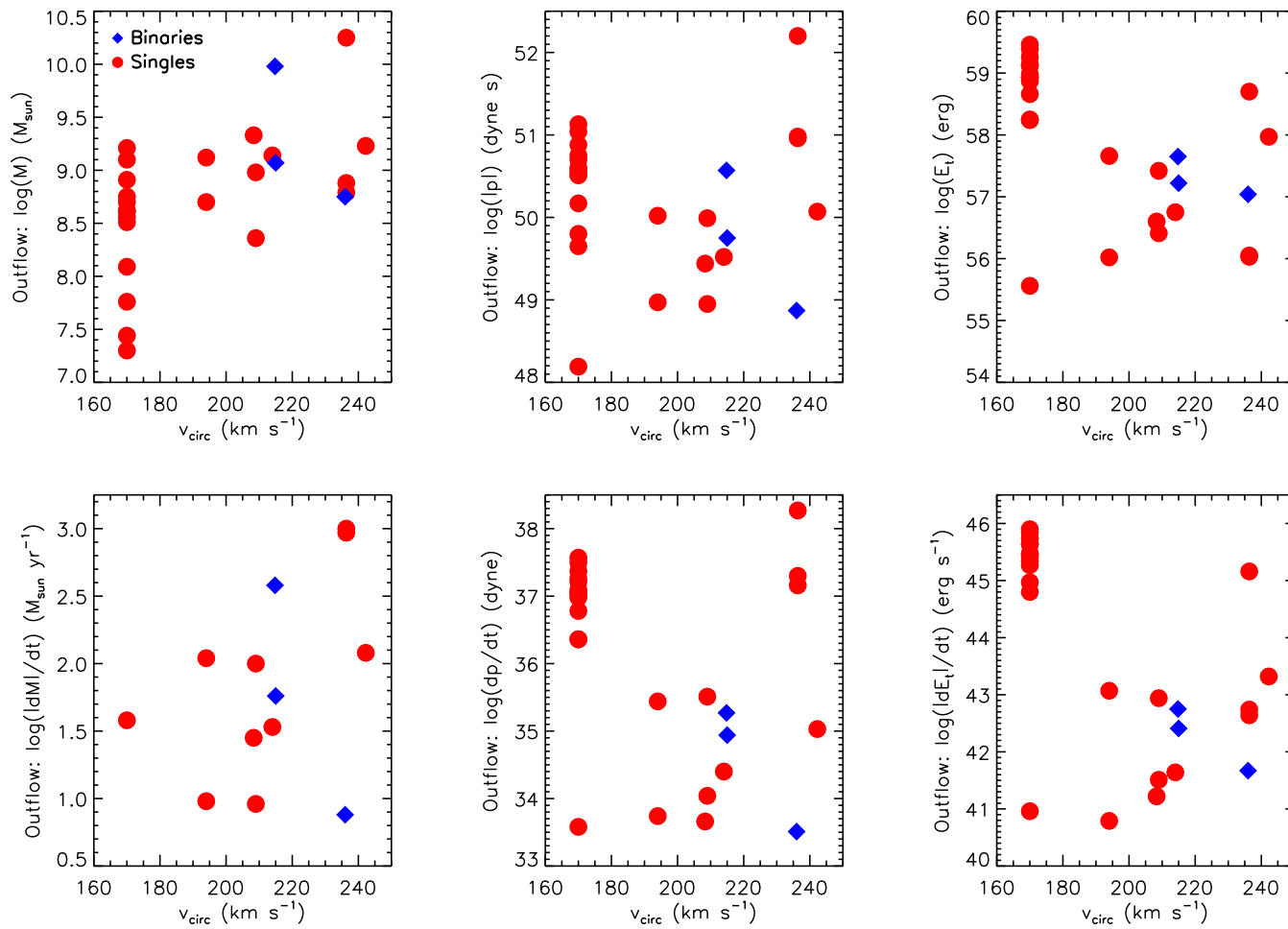


Figure 3.20: Same as Figure 3.19, but versus circular velocity of the galaxy. Note the lack of discernible trend.

We also can compare our measurements of momentum flux to predictions of recent theoretical work on momentum-conserving winds [Faucher-Giguère & Quataert (2012)]. This work predicts that, in the momentum-conserving phase, the rate of momentum flux, \dot{p} , when divided by L_{AGN}/c , should show a decreasing trend with peak outflow velocity; work by Novak et al. (2012) concurs, implying that only rarely does $\dot{p}/(L_{\text{AGN}}/c) > 1$ in the momentum-driven phase. The authors suggest that high values of $\dot{p}/(L_{\text{AGN}}/c)$ for high-velocity outflows could be explained by AGN-driven winds in an energy-conserving phase. We thus plot $\dot{p}/(L_{\text{AGN}}/c)$ versus Δv_{max} in Figure 3.21 in order to compare our data with the results of Faucher-Giguère & Quataert (2012). The values of $\dot{p}/(L_{\text{AGN}}/c)$ versus Δv_{max} for IR-luminous starbursts concur with the ULIRG values referenced by Faucher-Giguère & Quataert (2012) and fit within their theoretical framework, but the IR-luminous AGN values are much higher than that work would predict (although we acknowledge that the uncertainties are fairly large; see Figure 3.21 caption). This would suggest that the IR-luminous AGN winds which we are probing here may actually be AGN-driven winds in the energy-conserving phase.

3.6 RESULTS AND DISCUSSION: INFLOWS

3.6.1 Detection Rates

The same general detection criteria apply for inflows as well as outflows, albeit with $\Delta v > 50 \text{ km s}^{-1}$. Of the 28 PG QSOs, only one, PG 1613+658, showed inflow, for a detection rate of $4 \pm 1\%$. This Na I D inflow was measured with a Δv of 180

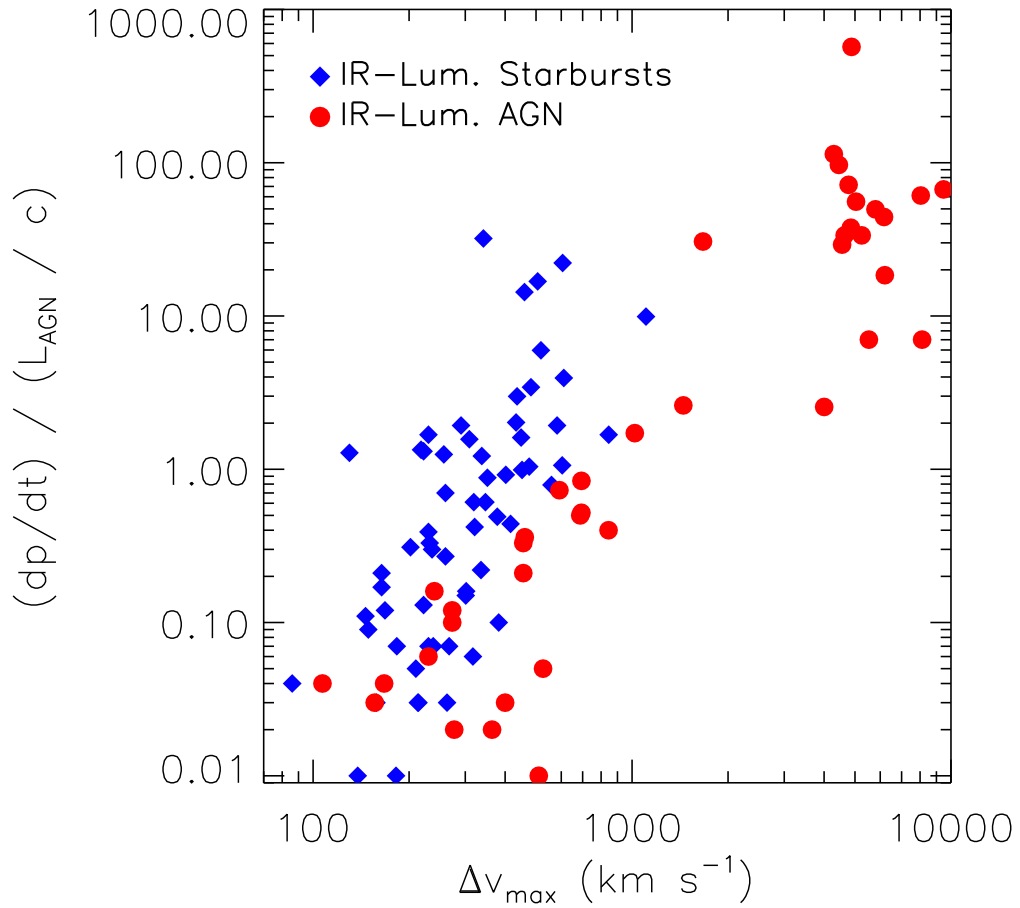


Figure 3.21: Plot of $\dot{p}/(L_{AGN}/c)$ versus Δv_{max} for IR-Luminous Starbursts and IR-Luminous AGN. Faucher-Giguère & Quataert (2012) predict a downward sloping trend for winds in the momentum-conserving phase. The IR-luminous starburst data roughly agree with Figure 5 of Faucher-Giguère & Quataert (2012) but the IR-luminous AGN data show much higher $\dot{p}/(L_{AGN}/c)$ values. Faucher-Giguère & Quataert predict that such high values can be explained by AGN-driven winds in the energy-conserving phase. Note: uncertainties for these points range from ~ 0.5 -5 in log space; to include them in the figure would have made the plot difficult to read.

km s⁻¹ and a Δv_{max} of 236 km s⁻¹. The redshift uncertainty in PG 1613+658 is only 0.0001, which contributes only ~ 25 km s⁻¹ to the ± 88 km s⁻¹ uncertainty in Δv . Properties of this object can be seen in Table 3.9.

Of the 10 ULIRGs, only 1 showed inflow, for an inflow detection rate of $10 \pm 3\%$. This object, F15130-1958, had an inflow velocity of 290 km s⁻¹ and a significantly higher Δv_{max} , 526 km s⁻¹, owing to its large Doppler parameter. Again, properties for this object can be found in Table 3.9.

The detection rates found in this study were consistent with those of RVS05b and RVS05c for IR-luminous objects ($\sim 15\%$), with detection rates of $4\% \pm 1\%$ and $10\% \pm 3\%$ for PG QSOs and ULIRGs, respectively (properties of the individual objects are listed in Table 3.9). The inflows detected in this sample were of quite high velocity, as noted in Section 3.6, but the detection rates were significantly lower than those for the IR-faint Seyferts of Chapter 2. Here, we again use the combined sample to look for trends among the three grouping types. We caution, however, that the detection percentages overall for inflows are significantly lower than the detection percentages for outflows, and thus, while we look for trends in the way we did for outflows, we cannot draw any statistically significant conclusions in this section.

As in Section 3.5.1, we have divided the combined sample into IR-faint AGN, IR-luminous AGN, and IR-luminous starbursts to look for correlations between IR-luminosity and inflow detection. We found similar detection percentages for PG QSOs and ULIRGs in our new data set, however the statistics are small: only one of each was detected with an inflow. When we combine the data with the previous

data sets (see Table 3.10), we find that, overall, the detection percentage of inflows is significantly higher on the whole for lower luminosity AGN than any other group. This can be seen in Figure 3.22, particularly in the $L_{\text{FIR}}=10^{10} - 10^{11} L_{\odot}$ bin.

Plots of inflow detection rate and Δv_{max} for the spectral type grouping were not particularly informative, so we do not show them here, but we can discuss the average properties of these inflows as listed in Table 3.10. Type 2 AGN show the highest detection rate and IR-luminous starbursts again show the lowest. We found a concurrence between IR-faint AGN and Type 2 AGN in terms of outflow trends; IR-faint AGN and Type 2 AGN each showing the highest inflow detection percentage implies a similar relationship in terms of inflows, though this may be partially due to overlap in the samples. Given the particularly small sample sizes for binary and single inflows, we are unable to comment on trends of neutral gas inflows with interaction class.

3.6.2 Kinematics

In terms of general inflow velocities, we can see in Figure 3.12 that IR-faint AGN have the highest overall percentage of inflowing components of the three groupings, but that IR-luminous AGN inflows, much like their outflowing counterparts, have the highest velocities of the three groupings.

We next examine the relationship between Δv_{max} and L_{FIR} , as well as between Δv_{max} and galactic circular velocity; both of these plots can be seen in Figure 3.23. Unlike for outflows, we find no obvious trends with L_{FIR} (and thus SFR) or with

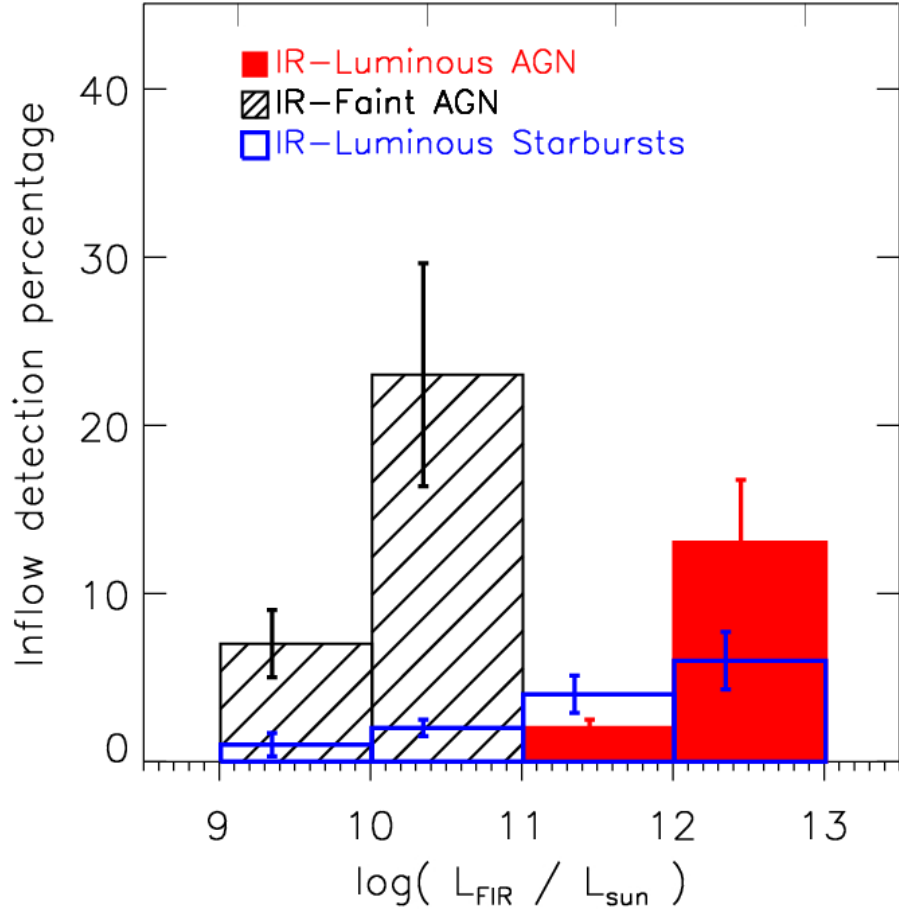


Figure 3.22: Histogram showing the fraction of IR-luminous AGN, IR-faint AGN, and IR-luminous starbursts with inflows as a function of L_{FIR} . Errors are again 1σ , assuming a binomial distribution. IR-faint AGN show the highest percentages of inflows. Each grouping shows an increase with L_{FIR} , but the numbers are small enough – particularly for IR-luminous starbursts – that we cannot make any statistically significant conclusions about inflow detection trends.

v_{circ} (and thus galactic mass). The only notable distinction that can be made is that the highest velocity inflows occur at lower L_{FIR} . Again, statistics are such that we notice no real trends for spectral type and interaction class groupings, and ask the reader to turn to Chapter 2 for more on inflow properties versus spectral type. The sample sizes are too small to perform an informative K-S or Kuiper statistical calculation, and thus we cannot draw concrete conclusions here but can only point out the aforementioned detection and velocity trends.

3.6.3 Dynamics

As in Section 3.5.3, we can use the same method to calculate mass, momentum, and kinetic energy for outflows as in order to calculate inflows, under the same caveat that these are simply illustrative examples. Here we drop the characteristic absorber radius to 1 kpc; this radius was chosen because the typical structures responsible for fueling inflows, such as nuclear bars or dust spirals, are often at a rough upper limit of one 1 kpc [Martini et al. (2003a)]. It is unclear whether the PG QSOs and ULIRGs with inflows possess those structures, but 1 kpc is still a reasonable radius to use, as these dynamical quantities are uncertain regardless. We still would like to examine how these rough inflow quantities compare with the mass accretion rates required to obtain the bolometric luminosities of these systems. The mass, momentum, and kinetic energies calculated for the objects with measured inflows, as well as their respective rates, can be found in Table 3.11. The mass accretion rates for these inflows ranges from roughly $2 \left(\frac{r}{1 \text{ kpc}}\right) M_{\odot} \text{ yr}^{-1}$ to $8 \left(\frac{r}{1 \text{ kpc}}\right) M_{\odot} \text{ yr}^{-1}$.

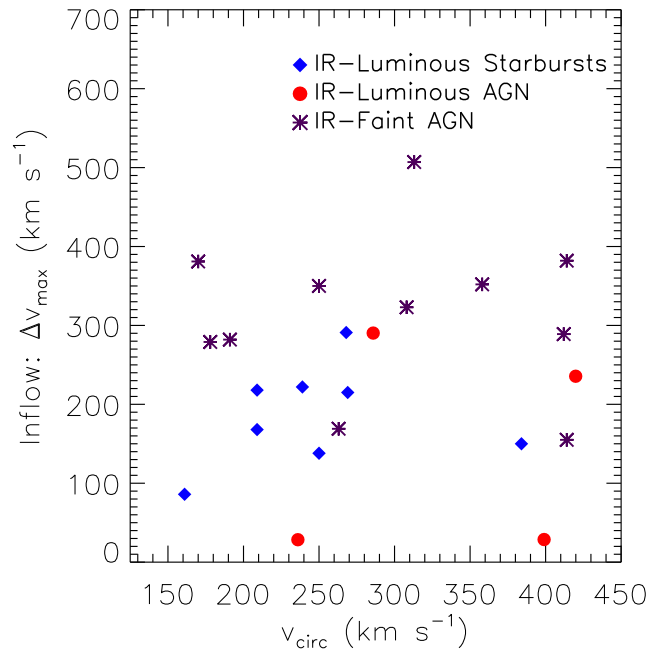
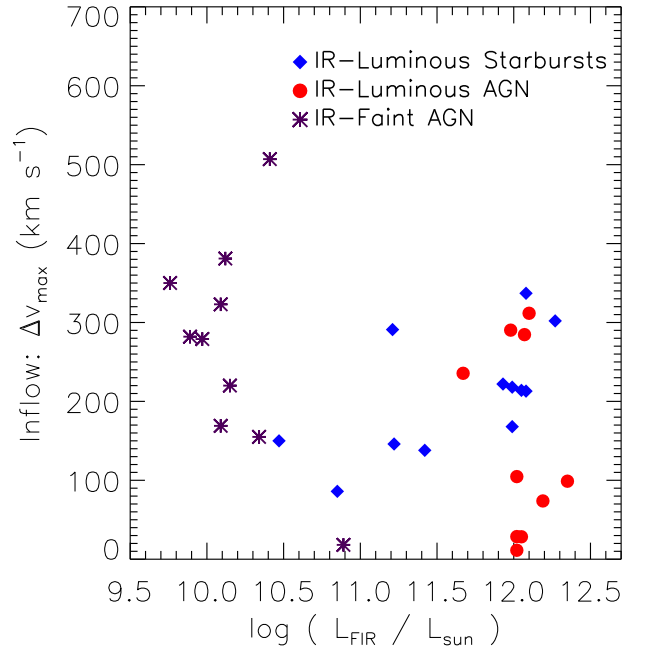


Figure 3.23: Top: Plot showing inflow Δv_{max} as a function of L_{FIR} for IR-luminous starbursts, IR-luminous AGN, and IR-faint AGN. Bottom: Same, but for Δv_{max} vs the circular velocity of the galaxy. Note the general lack of discernible trend in each plot.

In order to power an AGN, a mass accretion rate of $\dot{M} = L_{\text{bol}}/c^2\eta$ is required. Here we assume an efficiency, η , of 0.25 for the PG QSO, as was found to be an average efficiency for PG QSOs in a CO absorption study [Dasyra et al. (2007)]. For the ULIRG with inflow, we assume an efficiency of $\eta \approx 0.5$, as found in Dasyra et al. (2006b). The bolometric luminosities for these targets range from $10^{12.23}$ to $10^{12.29} L_{\odot}$ [Veilleux et al. (2009a)]. We find that the mass accretion rates required to power these objects are $\dot{M} \sim 0.5$ and $0.2 M_{\odot} \text{ yr}^{-1}$, respectively, for the objects in the order listed in Table 3.11. The rough order of magnitude estimates of \dot{M} for these objects, as found in that same table, are well above the amount required to fuel the AGN, even if less than $\sim 1\%$ of the material reaches the AGN. And, just as in Chapter 2, the total infalling masses of $\sim 10^7 \left(\frac{r}{1 \text{ kpc}}\right) M_{\odot}$ that we have estimated for these objects would be more than enough to sustain nuclear activity over the course of the typical 10^7 - 10^8 year AGN lifetimes [Mouri & Taniguchi (2002), Croom et al. (2004)].

3.7 SUMMARY

The main results from our study of Na I D absorption in PG QSOs, ULIRGs, and the combined sample can be summarized as follows:

- *Outflow Detection Rates:* We failed to detect any outflows in PG QSOs but found that 50% of our ULIRG sample showed the presence of an outflow. We believe that the lack of outflow detection in PG QSOs is due to either dilution of Na I D equivalent width due to the extremely bright optical nucleus, or the fact that much of the neutral gas may already have been removed from

the object during the merger process. In the combined sample, we find that high L_{FIR} (and thus high SFR) increases the likelihood of outflow detection in IR-luminous starbursts, IR-faint AGN, and Type 2 AGN. Whereas IR-luminous AGN and Type 1 AGN detections increase with L_{FIR} , we believe this to be a secondary correlation, as increased L_{FIR} implies increased dust and gas content in IR-luminous AGN; with more dust and gas comes more material to be entrained in outflows. AGN luminosity also seems to increase likelihood of detection. We also note a possible bias in outflow detection due to AGN type; if high-velocity AGN-driven outflows primarily originate near the nucleus, they could be obscured from view in Type 2 AGN due to the dusty torus.

- *Outflow Kinematics:* Based on analysis, both visual and statistical, of outflow kinematics, we come to three major conclusions. First, that outflows in IR-luminous AGN and IR-luminous starbursts are driven by fundamentally different processes: the AGN and star formation, respectively. Second, that outflows in Type 1 and Type 2 AGN are fundamentally distinct, powered by the AGN and star formation respectively. Third, that the kinematic properties of outflows in binaries and singles are fundamentally different, but that we cannot necessarily say that outflows in these objects are primarily driven by merger phase. As noted above, the differences in Type 1 and Type 2 outflows may be driven at least in part by an orientation effect, with the dusty torus potentially obscuring high-velocity outflows from view in Type 2 AGN.

- *Outflow Dynamical Estimates:* Rough estimates of mass, momentum, kinetic energy, and fluxes of those three quantities show that, for both the luminosity and spectral type groupings, these quantities tend to increase with the L_{FIR} of the galaxy and decrease with the circular velocity of the galaxy. No clear trends are present for the dynamical quantities of binaries versus singles, although the dynamical quantities of galaxies which are in the process of merging or have completed their mergers are on average larger than those for galaxies which are still pre-merger. We also find that, with the possible exception of the extreme outflows in Mrk 231, the ULIRGs in our sample likely do not play much of a role in galactic feedback.
- *Inflow Detection Rates:* The detection rates of inflows in PG QSOs and ULIRGs are significantly lower than those of the IR-faint Seyferts of Chapter 2 (4% and 10% for PG QSOs and ULIRGs, respectively, versus 39% and 35% for Seyfert 2s and 1s). No clear trends could be found amongst the groupings, although IR-faint AGN and Type 2 AGN show the highest inflow detection percentages among these small sample sizes.
- *Inflow Kinematics:* Much like their outflowing counterparts, IR-luminous AGN inflows show the highest velocities among the far-infrared luminosity grouping, and singles show significantly higher inflowing velocities than binaries. The statistics for inflows are quite poor, however, so no firm conclusions can be drawn.
- *Inflow Dynamical Estimates:* We use the same method to roughly estimate

mass, momentum, kinetic energy, and fluxes of those quantities as we did for outflows. We find that the accretion rates for the two PG QSOs and ULIRGs with inflows are more than sufficient to power the AGN in these objects, as well as that the total masses in the inflows are sufficient to last for typical AGN lifetimes, noting, however, that these are highly uncertain estimates.

Table 3.1: Galaxy properties

| Name (1) | z (2) | L_{IR} (3) | L_{FIR} (4) | SFR (5) | f_{30}/f_{15} (6) | α_{AGN} (7) | L_{Bol} (8) | L_{AGN} (9) | v_{circ} (10) | Sp.Type (11) | IC (12) | Refs (13) |
|-------------|----------------------|------------------------|-------------------------|------------|------------------------|------------------------------|-------------------------|-------------------------|---------------------------|-----------------|------------|--------------------|
| PG 0007+106 | 0.08943 ^g | 11.32 | 10.77 | 8.1 | 2.12 | 94.8 | 12.23 | 12.21 | 325 | 1 | IVb | 3, 4, 8, 12, 16 |
| PG 0026+129 | 0.14540 ⁿ | 11.72 | 11.25 | 24.5 | 2.10 | 95.9 | 12.07 | 12.05 | 470 | 1 | V | 6, 8, 17 |
| PG 0050+124 | 0.06048 ^m | 11.91 | 11.49 | 42.7 | 2.31 | 94.3 | 12.07 | 12.04 | 352 | 1 | IVb | 1, 8, 12-13, 16 |
| PG 0804+761 | 0.10000 ^c | 11.62 | 10.86 | 9.9 | 1.38 | 100.0 | 12.08 | 12.08 | 665 | 1 | ... | 4, 13 |
| PG 0838+770 | 0.13100 ^c | 11.50 | 11.11 | 17.9 | 2.50 | 92.7 | 11.76 | 11.73 | 70 | 1 | IVb | 4, 8, 13 |
| PG 0844+349 | 0.06481 ^m | 11.22 | 10.52 | 4.5 | 1.49 | 100.0 | 11.44 | 11.44 | 451 | 1 | IVb | 3, 8, 12 |
| PG 0923+201 | 0.19214 ^a | 12.27 | 11.88 | 105.5 | 1.71 | 99.0 | 12.45 | 12.45 | ... | 1 | V | 3, 5, 8 |
| PG 1116+215 | 0.17650 ^e | 12.21 | 11.54 | 48.2 | 1.45 | 100.0 | 12.54 | 12.54 | ... | 1 | V | 4, 8 |
| PG 1119+120 | 0.05020 ^g | 11.17 | 10.68 | 6.6 | 2.20 | 95.1 | 11.33 | 11.31 | 189 | 1 | V | 1, 5, 8, 12-13, 16 |
| PG 1126−041 | 0.06000 ^j | 11.42 | 10.98 | 13.2 | 3.04 | 88.7 | 11.52 | 11.47 | 313 | 1 | V | 5, 8, 16 |
| PG 1211+143 | 0.08100 ^c | 11.59 | 10.98 | 13.0 | 1.40 | 100.0 | 11.96 | 11.96 | 338 | 1 | ... | 4, 5, 16 |
| PG 1229+204 | 0.06301 ^b | 11.10 | 10.63 | 2.2 | 2.15 | 95.5 | 11.56 | 11.54 | 262 | 1 | V | 4, 8, 12, 16 |
| PG 1244+026 | 0.04818 ^a | 10.99 | 10.54 | 4.8 | 2.83 | 90.2 | 11.02 | 10.98 | 276 | 1 | ... | 4, 12 |
| PG 1302−102 | 0.27840 ^e | 12.59 | 11.98 | 132.5 | 2.28 | 94.5 | 12.74 | 12.72 | 559 | 1 | V | 3, 8, 18 |
| PG 1307+085 | 0.15500 ^c | 11.93 | 11.16 | 19.9 | 1.96 | 97.0 | 12.34 | 12.33 | 354 | 1 | V | 3, 5, 8, 17 |

Col.(2): Heliocentric redshift. *a*: SDSS, *b*: [Falco et al. (1999)], *c*: [Grazian et al. (2000)], *d*: [Jones et al. (2009)], *e*: [Marziani et al. (1996)], *f*: [Ho & Kim (2009)], *g*: [de Vaucouleurs et al. (1995)], *h*: [Murphy et al. (2001)], *i*: [Wisotzki (2000)], *j*: [Petrosian et al. (2007)], *k*: [Huchra et al. (1999)], *l*: [Strauss et al. (1992)], *m*: [Teng et al. (2013)], *n*: [Veilleux et al. (2013a)]. Col.(3): Infrared luminosity, in logarithmic units of L_{\odot} . Col.(4): Far-infrared luminosity, in logarithmic units of L_{\odot} (see Section 3.2.2). Col.(5): Star formation rate, computed from the far-infrared luminosity (Section 3.2.2). Col.(6): f_{30}/f_{15} flux density ratio (see Section 3.2.3). Col.(7): Fraction of bolometric luminosity contributed by the AGN (see 3.2.3). Col.(8): Bolometric luminosity (see 3.2.3). Col.(9): AGN luminosity (see 3.2.3). Col.(10): Circular velocity, equal to $\sqrt{2}\sigma$, v_{rot} , or the quadratic combination of both are available. Col.(11): Optical spectral types (1: Type 1 AGN, 2: Type 2 AGN, H: HII galaxy, L: LINER), taken from [Gonçalves et al. (1999), Veilleux et al. (1995), Veilleux et al. (1999a), Véron-Cetty & Véron (2010)]. Col.(12): Interaction class (see Section 3.2.5). Col.(13): Reference. (continued on next table)

| Name (1) | z (2) | L_{IR} (3) | L_{FIR} (4) | SFR (5) | f_{30}/f_{15} (6) | α_{AGN} (7) | L_{Bol} (8) | L_{AGN} (9) | v_{circ} (10) | Sp.Type (11) | IC (12) | Refs (13) |
|-----------------|----------------------|------------------------|-------------------------|------------|------------------------|------------------------------|-------------------------|-------------------------|---------------------------|-----------------|------------|--------------|
| PG 1309+355 | 0.18292 ^a | 11.94 | 11.42 | 36.6 | 1.53 | 100.0 | 12.31 | 12.31 | 381 | 1 | V | 4, 8, 18 |
| PG 1351+640 | 0.08820 ^e | 11.82 | 11.33 | 29.7 | 2.57 | 92.2 | 12.04 | 12.00 | 273 | 1 | ... | 4, 13 |
| PG 1411+442 | 0.08960 ^e | 11.46 | 10.71 | 7.2 | 1.44 | 100.0 | 11.78 | 11.78 | 283 | 1 | IVb | 3, 5, 8, 17 |
| PG 1426+015 | 0.08675 ^f | 11.57 | 11.01 | 14.3 | 1.83 | 98.0 | 11.92 | 11.92 | 299 | 1 | IVb | 3-5, 8, 12 |
| PG 1435-067 | 0.12600 ⁱ | 11.69 | 11.33 | 29.7 | 2.39 | 93.6 | 11.91 | 11.88 | ... | 1 | V | 4, 8 |
| PG 1440+356 | 0.07807 ^m | 11.58 | 11.22 | 23.1 | 2.77 | 90.7 | 11.80 | 11.76 | 422 | 1 | V | 4, 8, 13 |
| PG 1448+273 | 0.06484 ^m | 11.02 | 10.43 | 3.7 | 1.70 | 99.0 | 11.43 | 11.43 | 542 | 1 | ... | 3, 19 |
| PG 1501+106 | 0.03642 ^b | 10.94 | 10.47 | 4.1 | 1.55 | 100.0 | 11.33 | 11.33 | 462 | 1 | ... | 3-5, 20 |
| PG 1613+658 | 0.12900 ^j | 11.98 | 11.71 | 70.4 | 2.51 | 92.6 | 12.29 | 12.26 | 420 | 1 | IVb | 3, 6, 8, 13 |
| PG 1617+175 | 0.11400 ^c | 11.34 | 10.43 | 3.7 | 1.37 | 100.0 | 11.33 | 11.33 | 296 | 1 | V | 3, 5, 8, 17 |
| PG 2130+099 | 0.06298 ^k | 11.46 | 10.89 | 10.7 | 1.77 | 98.5 | 11.76 | 11.77 | 278 | 1 | IVb | 4, 8, 12 |
| PG 2214+139 | 0.06576 ^b | 11.07 | 10.73 | 7.4 | 1.05 | 100.0 | 11.77 | 11.77 | 331 | 1 | V | 3, 8, 12-13 |
| PG 2349-014 | 0.17396 ^a | 12.14 | 11.58 | 52.1 | 2.69 | 91.3 | 12.58 | 12.54 | 362 | 1 | IVb | 3, 8, 18 |
| F04103-2838 | 0.11790 ^m | 12.19 | 12.02 | 145.6 | 14.41 | 66.20 | 12.30 | 12.12 | 208 | L | IVb | 1, 8, 9, 15 |
| F09111-1007 | 0.05483 ^l | 12.01 | 11.97 | 129.6 | 5.91 | 77.0 | 12.04 | 11.92 | 287 | H | ... | 2, 15 |
| F12112+0305 | 0.07298 ^a | 12.36 | 12.28 | 264.6 | 22.98 | 1.9 | 12.38 | 10.66 | 181 | L | IIIb | 2, 10, 13-14 |
| F13305-1739 | 0.14836 ^d | 12.31 | 12.05 | 155.0 | 2.65 | 92.3 | 12.34 | 12.31 | 215 | 2 | V | 1, 10 |
| F15130-1958 | 0.10938 ^l | 12.20 | 12.01 | 141.6 | 7.33 | 55.6 | 12.23 | 11.98 | 286 | 2 | IVb | 1, 9, 15 |
| F15250+3608 | 0.05525 ^a | 12.06 | 11.92 | 113.7 | 12.00 | 37.6 | 12.12 | 11.70 | 242 | L | ... | 2, 11, 15 |
| F15462-0450 | 0.09979 ^h | 12.21 | 12.08 | 166.0 | 6.91 | 43.9 | 12.28 | 11.92 | 273 | 1 | IVb | 1, 7, 9, 15 |
| F22491-1808 | 0.07776 ^m | 12.19 | 12.10 | 173.8 | 17.45 | 10.8 | 12.25 | 11.28 | 236 | H | IIIb | 2, 10, 13-14 |
| IRAS 08572+3915 | 0.05794 ^a | 12.16 | 11.96 | 125.4 | 5.82 | 69.5 | 12.22 | 12.06 | 287 | L | IIIb | 2, 10, 13 |
| Mrk 231 | 0.04220 ^j | 12.56 | 12.33 | 297.3 | 4.62 | 64.2 | 12.60 | 12.41 | 236 | 1 | IVb | 2, 8, 13 |

(1) IRAS Faint Source Catalog; (2) [Sanders et al. (2003)]; (3) [Sanders et al. (1989)]; (4) [Haas et al. (2003)]; (5) [Serjeant & Hatziminaoglou (2009)]; (6) [Haas et al. (2000)]; (7) [Klaas et al. (2001)]; (8) [Veilleux et al. (2009c)]; (9) [Veilleux et al. (2006)]; (10) [Veilleux et al. (2002)]; (11) [Scoville et al. (2000)]; (12) [Ho et al. (2008)]; (13) [Ho (2007)]; (14) [Dasyra et al. (2006a)]; (15) [Dasyra et al. (2006b)]; (16) [Dasyra et al. (2007)]; (17) [Dasyra et al. (2008)]; (18) [Wolf & Sheinis (2008)]; (19) [Hutchings et al. (1987)]; (20) [Wandel & Mushotzky (1986)]

Table 3.2: Observing logs

| Name (1) | Run (2) | t_{exp} (3) | r_{ext} (4) |
|-------------|-------------|------------------|------------------|
| PG 0007+106 | 11 Dec 2012 | 3600 | 6.7 |
| PG 0026+129 | 12 Dec 2012 | 3600 | 11.73 |
| PG 0050+124 | 11 Dec 2012 | 3600 | 5.36 |
| PG 0804+761 | 29 Apr 2012 | 3600 | 2.47 |
| PG 0804+761 | 12 Dec 2012 | 4800 | 9.90 |
| PG 0838+770 | 29 Apr 2012 | 3600 | 3.13 |
| PG 0838+770 | 12 Dec 2012 | 3600 | 10.96 |
| PG 0844+349 | 27 Apr 2012 | 3600 | 1.65 |
| PG 0844+349 | 13 Dec 2012 | 3600 | 6.61 |
| PG 0923+201 | 30 Apr 2012 | 3600 | 4.29 |
| PG 1116+215 | 30 Apr 2012 | 3600 | 4.01 |
| PG 1116+215 | 12 Dec 2012 | 3600 | 14.03 |
| PG 1119+120 | 28 Apr 2012 | 3600 | 1.98 |
| PG 1126-041 | 27 Apr 2012 | 3600 | 1.61 |
| PG 1211+143 | 27 Apr 2012 | 3600 | 2.05 |
| PG 1229+204 | 28 Apr 2012 | 3600 | 1.63 |
| PG 1244+026 | 28 Apr 2012 | 3600 | 1.90 |
| PG 1302-102 | 30 Apr 2012 | 3600 | 5.67 |
| PG 1307+085 | 29 Apr 2012 | 3600 | 3.61 |
| PG 1309+355 | 30 Apr 2012 | 3600 | 4.13 |
| PG 1351+640 | 27 Apr 2012 | 3600 | 2.21 |
| PG 1411+442 | 27 Apr 2012 | 3600 | 2.24 |
| PG 1426+015 | 27 Apr 2012 | 3600 | 2.17 |
| PG 1435-067 | 29 Apr 2012 | 3600 | 3.02 |
| PG 1440+356 | 28 Apr 2012 | 3600 | 2.01 |
| PG 1448+273 | 28 Apr 2012 | 3600 | 1.67 |
| PG 1501+106 | 28 Apr 2012 | 3600 | 1.94 |
| PG 1613+658 | 30 Apr 2012 | 2400 | 3.09 |
| PG 1617+175 | 29 Apr 2012 | 2400 | 2.74 |
| PG 2130+099 | 13 Dec 2012 | 3600 | 5.69 |
| PG 2214+139 | 11 Dec 2012 | 3600 | 5.08 |
| PG 2349-014 | 12 Dec 2012 | 4800 | 9.90 |
| F04103-2838 | 13 Dec 2012 | 6000 | 9.98 |
| F09111-1007 | 11 Dec 2012 | 3600 | 4.94 |
| F12112+0305 | 11 Dec 2012 | 4800 | 8.43 |

Col.(2): Observing dates (Section 3.3). Instrument used was the R-C Spectrograph on the KPNO 4m. Col.(3): Total exposure time in seconds. Col.(4): Extraction radius in kpc.

| Name (1) | Run (2) | t_{exp} (3) | r_{ext} (4) |
|-----------------|-------------|------------------|------------------|
| F13305–1739 | 29 Apr 2012 | 3600 | 3.48 |
| F15130–1958 | 29 Apr 2012 | 3600 | 2.66 |
| F15250+3608 | 28 Apr 2012 | 3600 | 2.16 |
| F15250+3608 | 13 Dec 2012 | 3600 | 4.32 |
| F15462–0450 | 29 Apr 2012 | 3600 | 2.47 |
| F22491–1808 | 13 Dec 2012 | 3600 | 7.89 |
| IRAS 08572+3915 | 13 Dec 2012 | 7200 | 6.83 |
| Mrk 231 | 27 Apr 2012 | 4800 | 1.68 |
| Mrk 231 | 13 Dec 2012 | 3600 | 4.47 |

Table 3.3: Properties of individual velocity components (fit 1)

| Name (1) | $\lambda_{1,c}$ (\AA) (2) | Δv (km s^{-1}) (3) | b (km s^{-1}) (4) | $\tau_{1,c}$ (5) | C_f (6) | W_{eq} (7) | $N(\text{Na I})$ (cm^{-2}) (8) | $N(\text{H})$ (cm^{-2}) (9) |
|--------------------------|--|---|--------------------------------------|---------------------|-----------------|-----------------|---|--|
| PG 1119+120 | 6194.6 | 49 ± 42 | 131 ± 27 | 0.06 ± 0.18 | 0.36 ± 0.29 | 0.28 | 12.41 ± 0.51 | 20.05 ± 0.51 |
| PG 1501+106 | 6113.2 | 41 ± 12 | 118 ± 20 | 3.23 ± 3.98 | 0.03 ± 0.01 | 0.36 | 14.13 ± 0.10 | 21.77 ± 0.10 |
| PG 1613+658 | 6662.3 | 180 ± 88 | 67 ± 18 | 5.00 ± 10.28 | 0.02 ± 0.01 | 0.20 | 14.08 ± 0.32 | 21.72 ± 0.32 |
| F04103-2838 | 6591.4 | -64 ± 4 | 112 ± 17 | 1.70 ± 1.34 | 0.26 ± 0.06 | 2.65 | 13.83 ± 0.09 | 21.47 ± 0.09 |
| F09111-1007 | 6128.9 | -97 ± 46 | 143 ± 31 | 0.36 ± 0.32 | 0.67 ± 0.44 | 3.07 | 13.26 ± 0.05 | 20.90 ± 0.05 |
| F12112+0305 | 6323.8 | -195 ± 6 | 176 ± 17 | 5.00 ± 6.53 | 0.25 ± 0.02 | 4.43 | 14.50 ± 0.12 | 22.14 ± 0.12 |
| F15130-1958 | 6549.0 | 290 ± 50 | 283 ± 113 | 0.057 ± 0.40 | 1.00 ± 0.88 | 1.79 | 12.76 ± 0.85 | 20.40 ± 0.85 |
| F15250+3608 ^a | 6216.2 | -346 ± 40 | 600 ± 100 | 0.20 ± 0.86 | 0.32 ± 0.17 | 3.57 | 13.64 ± 0.63 | 21.28 ± 0.64 |
| F15250+3608 ^b | 6219.2 | -205 ± 14 | 238 ± 80 | 0.46 ± 1.31 | 0.19 ± 0.14 | 1.66 | 13.59 ± 0.46 | 21.23 ± 0.45 |
| F22491-1808 | 6357.1 | 44 ± 21 | 263 ± 80 | 0.05 ± 0.40 | 0.99 ± 0.93 | 1.50 | 12.70 ± 0.87 | 20.34 ± 0.85 |
| IRAS 08572+3915 | 6239.2 | -3 ± 213 | 442 ± 139 | 0.20 ± 1.30 | 0.41 ± 0.33 | 3.26 | 13.49 ± 0.82 | 21.13 ± 0.82 |
| Mrk 231 ^c | 5983.5 | -7948 ± 25 | 108 ± 4 | 1.18 ± 0.28 | 0.11 ± 0.01 | 0.83 | 13.66 ± 0.61 | 21.30 ± 0.58 |
| | 6021.7 | -6083 ± 26 | 100 ± 3 | 0.91 ± 0.15 | 0.19 ± 0.02 | 1.16 | 13.51 ± 0.78 | 21.15 ± 0.78 |
| | 6053.9 | -4515 ± 28 | 436 ± 2 | 0.98 ± 0.02 | 0.95 ± 0.01 | 20.74 | 14.18 ± 1.79 | 21.82 ± 1.79 |
| Mrk 231 ^b | 5982.8 | -7980 ± 22 | 141 ± 9 | 0.74 ± 0.31 | 0.14 ± 0.03 | 0.99 | 13.57 ± 0.37 | 21.21 ± 0.37 |
| | 6020.8 | -6126 ± 25 | 111 ± 4 | 1.10 ± 0.22 | 0.19 ± 0.02 | 1.43 | 13.64 ± 0.70 | 21.28 ± 0.68 |
| | 6052.4 | -4587 ± 27 | 459 ± 3 | 0.93 ± 0.03 | 0.86 ± 0.01 | 19.44 | 14.18 ± 1.54 | 21.82 ± 1.54 |

(a): data from 28 Apr 2012; (b): data from 13 Dec 2012; (c): data from 27 Apr 2012. Col.(2): Redshifted heliocentric wavelength, in vacuum, of the Na I D₁ λ 5896 line. Col.(3): Velocity relative to systemic. Negative velocities are blueshifted, positive are redshifted. Components with $\Delta v < -50 \text{ km s}^{-1}$ and $|\Delta v| > 2\delta(\Delta v)$ are assumed to be outflowing; those with $\Delta v > 50 \text{ km s}^{-1}$ and $|\Delta v| > 2\delta(\Delta v)$ are assumed to be inflowing. Col.(4): Doppler parameter. Col. (5): Central optical depth of the Na I D₁ λ 5896 line; the optical depth of the D₂ line is twice this value. Col.(6): Covering fraction of the gas. Col.(7): Rest-frame equivalent width of Na I D as computed from our model fits. Col.(8-9): Logarithm of column density of Na I and H, respectively. Note that Mrk 231 has multiple Na I D absorption components.

Table 3.4: H α fit parameters

| Name (1) | $\lambda_{\text{H}\alpha,\text{n}}$ (\AA) (2) | $b_{\text{H}\alpha,\text{n}}$ (km s^{-1}) (3) | Flux $_{\text{H}\alpha,\text{n}}$ (4) | $\lambda_{\text{H}\alpha,\text{b}}$ (\AA) (5) | $b_{\text{H}\alpha,\text{b}}$ (km s^{-1}) (6) | Flux $_{\text{H}\alpha,\text{b}}$ (7) |
|--------------------------|--|--|--|--|--|--|
| PG 0007+106 | 7153.1 | 155 | 10.17 | 7190.0 | 2933 | 14.84 |
| PG 0026+129 | 7521.0 | 275 | 19.86 | 7522.0 | 2500 | 22.68 |
| PG 0050+124 | 6963.4 | 325 | 22.16 | 6963.1 | 1171 | 39.67 |
| PG 0804+761 ^a | 7220.9 | 503 | 59.35 | 7229.0 | 1654 | 84.81 |
| PG 0804+761 ^b | 7227.2 | 1504 | 78.33 | 7228.7 | 3406 | 81.33 |
| PG 0838+770 ^a | 7442.2 | 1338 | 10.42 | 7429.4 | 2732 | 11.20 |
| PG 0838+770 ^a | 7446.1 | 142. | 8.95 | 7425.9 | 2160 | 10.06 |
| PG 0844+349 ^c | 6988.8 | 921 | 41.23 | 6985.1 | 2341 | 57.87 |
| PG 0844+349 ^d | 6991.7 | 1096 | 28.22 | 6986.0 | 2212 | 32.14 |
| PG 0923+201 | 7705.0 | 3429 | 31.65 | 7860.1 | 4150 | 40.28 |
| PG 1116+215 ^e | 7720.0 | 1498 | 50.53 | 7739.9 | 2085 | 45.38 |
| PG 1116+215 ^b | 7715.0 | 1400 | 35.36 | 7742.9 | 2441 | 31.38 |
| PG 1119+120 | 6894.4 | 716 | 24.57 | 6896.8 | 2213 | 29.41 |
| PG 1126-041 | 6959.1 | 827 | 37.04 | 6962.4 | 1803 | 63.20 |
| PG 1211+143 | 7100.8 | 900 | 66.04 | 7097.8 | 2622 | 62.80 |
| PG 1229+204 | 6975.6 | 1400 | 34.51 | 7009.6 | 3980 | 40.08 |
| PG 1244+026 | 6884.4 | 272 | 6.03 | 6887.0 | 11867 | 7.01 |
| PG 1302-102 | 8380.5 | 1864 | 24.55 | 8430.0 | 3008 | 25.15 |
| PG 1307+085 | 7578.6 | 187 | 14.90 | 7580.0 | 2101 | 42.23 |
| PG 1309+355 | 7767.5 | 2210 | 31.03 | 7790.5 | 2941 | 28.05 |
| PG 1351+640 | 7145.8 | 700 | 45.67 | 7144.8 | 3128 | 66.47 |
| PG 1411+442 | 7150.8 | 799 | 34.46 | 7148.4 | 1663 | 44.20 |
| PG 1426+015 | 7098.0 | 2739 | 101.3 | 7153.6 | 3490 | 111.5 |
| PG 1435-067 | 7404.4 | 1555 | 20.60 | 7407.0 | 3570 | 20.61 |
| PG 1440+356 | 7072.1 | 842 | 47.92 | 7073.7 | 1872 | 47.87 |
| PG 1448+273 | 6988.6 | 480 | 25.05 | 6989.1 | 1783 | 27.93 |
| PG 1501+106 | 6805.0 | 129 | 58.66 | 6791.9 | 2584 | 95.19 |
| PG 1613+658 | 7412.8 | 332 | 53.83 | 7469.9 | 4387 | 93.14 |
| PG 1617+175 | 7318.8 | 1800 | 34.41 | 7334.0 | 3420 | 42.81 |

(a): data from 29 Apr 2012; (b): data from 12 Dec 2012; (c): data from 27 Apr 2012; (d): data from 13 Dec 2012; (e): data from 30 Apr 2012; (f): data from 28 Apr 12. Col.(2): Central wavelength used to fit narrow component of H α . Col.(3): Doppler parameter b used to fit narrow component of H α . Col.(4): Flux of narrow H α line, in units of 10^{-14} erg s $^{-1}$ cm $^{-2}$. Col.(5)-Col.(7): same as Col.(2)-Col.(4), but for broad component of H α . Note that F15130-1958, F15250+3608 (run 2), and IRAS 08572+3915 do not have measurable He I emission and thus are not included here.

| Name (1) | $\lambda_{\text{H}\alpha,\text{n}}$ (\AA) (2) | $b_{\text{H}\alpha,\text{n}}$ (km s^{-1}) (3) | $\text{Flux}_{\text{H}\alpha,\text{n}}$ (4) | $\lambda_{\text{H}\alpha,\text{b}}$ (\AA) (5) | $b_{\text{H}\alpha,\text{b}}$ (km s^{-1}) (6) | $\text{Flux}_{\text{H}\alpha,\text{b}}$ (7) |
|--------------------------|--|--|--|--|--|--|
| PG 2130+099 | 6975.0 | 615 | 20.97 | 6980.9 | 2374 | 29.50 |
| PG 2214+139 | 7020.0 | 156 | 48.72 | 7003.9 | 2788 | 101.8 |
| PG 2349-014 | 7708.0 | 300 | 13.85 | 7720.0 | 3000 | 22.70 |
| F04103-2838 | 7338.0 | 227 | 12.36 | 7346.2 | 1194 | 11.66 |
| F09111-1007 | 6923.2 | 254 | 30.59 | 6932.5 | 1242 | 25.40 |
| F12112+0305 | 7045.0 | 100 | 9.96 | 7037.9 | 124 | 8.71 |
| F13305-1739 | 7537.8 | 264 | 25.52 | 7546.0 | 1276 | 11.05 |
| F15250+3608 ^f | 6928.1 | 194 | 2.417 | 6927.1 | 561 | 9.83 |
| F15462-0450 | 7222.0 | 92 | 24.19 | 7218.3 | 1609 | 42.08 |
| F22491-1808 | 7076.5 | 171 | 10.90 | 7077.0 | 248 | 6.81 |
| Mrk 231 ^c | 6843.6 | 1501 | 229.2 | 6831.1 | 4490 | 277.5 |
| Mrk 231 ^d | 6842.9 | 1459 | 123.9 | 6829.1 | 3998 | 138.0 |

Table 3.5: He I fit parameters.

| Name (1) | Fit (2) | $\lambda_{\text{He I,n}}$ (\AA) (3) | $b_{\text{He I,n}}$ (km s^{-1}) (4) | $\text{Flux}_{\text{He I,n}}$ (5) | $\lambda_{\text{He I,b}}$ (\AA) (6) | $b_{\text{He I,b}}$ (km s^{-1}) (7) | $\text{Flux}_{\text{He I,b}}$ (8) |
|--------------------------|------------|--|--|--------------------------------------|--|--|--------------------------------------|
| PG 0007+106 | 1 | 6404.4 | 289 | 8.15 | 6418.4 | 3220 | 9.00 |
| | 2 | 6404.3 | 400 | 8.20 | 6437.4 | 3489 | 8.92 |
| | 3 | 6404.3 | 155 | 8.14 | 6437.4 | 2933 | 8.81 |
| | 4 | 6404.3 | 155 | 8.14 | 6437.4 | 2933 | 9.05 |
| PG 0026+129 | 1 | 6732.4 | 240 | 182.4 | 6752.5 | 701 | 182.9 |
| | 2 | 6733.8 | 192 | 182.2 | 6740.1 | 975 | 183.2 |
| | 3 | 6733.8 | 275 | 182.2 | 6740.1 | 1050 | 183.3 |
| | 4 | 6733.8 | 275 | 182.4 | 6740.1 | 1050 | 184.2 |
| PG 0050+124 | 1 | 6241.1 | 1196 | 15.14 | ... | ... | ... |
| | 2 | 6234.1 | 1346 | 15.14 | ... | ... | ... |
| | 3 | 6234.1 | 1172 | 15.12 | ... | ... | ... |
| | 4 | 6234.1 | 1172 | 13.69 | ... | ... | ... |
| PG 0804+761 ^a | 1 | 6473.4 | 750 | 23.01 | 6464.8 | 1941 | 24.41 |
| | 2 | 6465.0 | 750 | 23.04 | 6472.1 | 1897 | 24.31 |
| | 3 | 6465.0 | 503 | 22.95 | 6472.1 | 1654 | 24.36 |
| | 4 | 6465.0 | 503 | 22.99 | 6472.1 | 1654 | 24.26 |
| PG 0804+761 ^b | 1 | 6469.4 | 372 | 30.66 | 6472.4 | 1955 | 33.56 |
| | 2 | 6473.8 | 395 | 32.86 | 6475.1 | 1985 | 35.84 |
| | 3 | 6473.8 | 1504 | 33.04 | 6475.1 | 3406 | 37.39 |
| | 4 | 6473.8 | 1504 | 34.42 | 6475.1 | 3406 | 34.38 |
| PG 0838+770 ^a | 1 | 6656.5 | 508 | 7.71 | 6656.3 | 2299 | 8.24 |
| | 2 | 6663.5 | 1500 | 7.80 | 6652.0 | 2450 | 8.12 |
| | 3 | 6663.5 | 1338 | 7.79 | 6652.0 | 2732 | 8.17 |
| | 4 | 6663.5 | 1338 | 7.92 | 6652.0 | 2732 | 8.00 |

(a): data from 29 Apr 2012; (b): 12 Dec 2012; (c): 27 Apr 2012; (d): 13 Dec 2012; (e): 30 Apr 2012; (f): 28 Apr 2012. Col.(2): Fit type. Fit #1: no constraints (“free-floating”); #2: He I narrow and broad components constrained to match H α narrow and broad systemic velocities; #3: same as #2, with the narrow and broad Doppler parameters matched to those of the H α ; #4: same as #3, but with the ratio of broad-to-narrow component intensities matched to that of H α (see Section 3.4.1 for details). Col.(3): Central wavelength used to fit narrow component of He I. Col.(4): Doppler parameter b used to fit narrow component of He I. Col.(5): Flux of narrow He I line, in units of 10^{-14} erg s $^{-1}$ cm $^{-2}$. Col.(6)-Col.(8): same as Col.(3)-Col.(5), but for broad component of He I. Note that F15130-1958, F15250+3608 (run 2), and IRAS 08572+3915 do not have measurable He I emission and thus are not included here. Note also that objects with no listed values for the broad component of He I have only one He I component.

| Name (1) | Fit (2) | $\lambda_{\text{He I,n}}$ (\AA) (3) | $b_{\text{He I,n}}$ (km s^{-1}) (4) | $\text{Flux}_{\text{He I,n}}$ (5) | $\lambda_{\text{He I,b}}$ (\AA) (6) | $b_{\text{He I,b}}$ (km s^{-1}) (7) | $\text{Flux}_{\text{He I,b}}$ (8) |
|--------------------------|------------|--|--|--------------------------------------|--|--|--------------------------------------|
| PG 0838+770 ^b | 1 | 6653.5 | 418 | 9.33 | 6660.0 | 3604 | 9.88 |
| | 2 | 6667.0 | 447 | 9.33 | 6648.9 | 3076 | 9.88 |
| | 3 | 6667.0 | 1422 | 9.39 | 6648.9 | 2160 | 9.71 |
| | 4 | 6667.0 | 1422 | 9.50 | 6648.9 | 2160 | 9.60 |
| PG 0844+349 ^c | 1 | 6259.2 | 663 | 42.76 | 6249.8 | 1820 | 42.96 |
| | 2 | 6257.2 | 673 | 42.76 | 6254.0 | 1861 | 42.97 |
| | 3 | 6257.2 | 921 | 42.90 | 6254.0 | 2341 | 43.12 |
| | 4 | 6257.2 | 921 | 42.54 | 6254.0 | 2341 | 43.96 |
| PG 0844+349 ^d | 1 | 6257.2 | 575 | 17.43 | 6245.6 | 2274 | 17.68 |
| | 2 | 6259.9 | 480 | 17.34 | 6254.8 | 1943 | 17.74 |
| | 3 | 6254.8 | 1096 | 17.51 | 6259.9 | 2204 | 17.86 |
| | 4 | 6254.8 | 1096 | 17.48 | 6259.9 | 2204 | 17.76 |
| PG 0923+201 | 1 | 7030.4 | 4136 | 27.19 | ... | ... | ... |
| | 2 | 7040.9 | 4161 | 27.17 | ... | ... | ... |
| | 3 | 7040.9 | 4150 | 27.16 | ... | ... | ... |
| | 4 | 7040.9 | 4150 | 27.16 | ... | ... | ... |
| PG 1116+215 ^e | 1 | 6921.2 | 816 | 22.14 | 6960.9 | 1246 | 22.00 |
| | 2 | 6912.1 | 361 | 21.30 | 6929.9 | 1213 | 22.68 |
| | 3 | 6912.1 | 1498 | 21.44 | 6929.9 | 2085 | 23.59 |
| | 4 | 6912.1 | 1498 | 22.41 | 6929.9 | 2085 | 22.12 |
| PG 1116+215 ^b | 1 | 6917.4 | 800 | 9.99 | 6949.6 | 1371 | 10.41 |
| | 2 | 6907.7 | 361 | 9.56 | 6932.6 | 1710 | 10.88 |
| | 3 | 6907.7 | 1400 | 9.60 | 6932.6 | 2441 | 11.18 |
| | 4 | 6907.7 | 1400 | 10.26 | 6932.6 | 2441 | 10.13 |
| PG 1119+120 | 1 | 6172.9 | 414 | 14.39 | 6174.3 | 2184 | 14.69 |
| | 2 | 6172.6 | 423 | 14.39 | 6174.7 | 2221 | 14.69 |
| | 3 | 6172.6 | 716 | 14.54 | 6174.7 | 2213 | 15.69 |
| | 4 | 6172.6 | 716 | 14.45 | 6174.7 | 2213 | 15.04 |
| PG 1126-041 | 1 | 6233.1 | 604 | 20.63 | 6231.2 | 1716 | 21.65 |
| | 2 | 6230.5 | 603 | 20.60 | 6233.5 | 1637 | 21.67 |
| | 3 | 6230.5 | 827 | 20.67 | 6233.5 | 1803 | 21.79 |
| | 4 | 6230.5 | 827 | 20.61 | 6233.5 | 1803 | 21.83 |
| PG 1211+143 | 1 | 6353.3 | 469 | 25.66 | 6358.4 | 1463 | 27.62 |
| | 2 | 6357.6 | 1000 | 26.42 | 6354.9 | 1835 | 26.75 |
| | 3 | 6357.6 | 900 | 26.33 | 6354.9 | 2622 | 27.13 |
| | 4 | 6357.6 | 900 | 26.79 | 6354.9 | 2622 | 26.51 |

| Name (1) | Fit (2) | $\lambda_{\text{He I},n}$ (\AA) (3) | $b_{\text{He I},n}$ (km s^{-1}) (4) | $\text{Flux}_{\text{He I},n}$ (5) | $\lambda_{\text{He I},b}$ (\AA) (6) | $b_{\text{He I},b}$ (km s^{-1}) (7) | $\text{Flux}_{\text{He I},b}$ (8) |
|-------------|------------|--|--|--------------------------------------|--|--|--------------------------------------|
| PG 1229+204 | 1 | 6255.1 | 295 | 10.71 | 6235.8 | 1569 | 10.97 |
| | 2 | 6245.3 | 1172 | 13.88 | 6275.8 | 3000 | 13.68 |
| | 3 | 6245.3 | 1400 | 13.90 | 6275.8 | 3979 | 13.80 |
| | 4 | 6245.3 | 1400 | 13.74 | 6275.8 | 3979 | 13.80 |
| PG 1244+026 | 1 | 6163.2 | 353 | 2.77 | 6171.8 | 1012 | 2.71 |
| | 2 | 6163.3 | 367 | 3.41 | 6166.2 | 1500 | 3.30 |
| | 3 | 6163.3 | 272 | 3.38 | 6166.2 | 1187 | 3.37 |
| | 4 | 6163.3 | 272 | 3.37 | 6166.2 | 1187 | 3.41 |
| PG 1302-102 | 1 | 7520.0 | 1800 | 17.31 | 7519.5 | 4557 | 18.01 |
| | 2 | 7503.7 | 1762 | 17.29 | 7548.0 | 4945 | 18.01 |
| | 3 | 7503.7 | 1864 | 17.31 | 7548.0 | 3008 | 17.74 |
| | 4 | 7503.7 | 1864 | 17.34 | 7548.0 | 3008 | 17.76 |
| PG 1307+085 | 1 | 6785.3 | 243 | 17.03 | 6789.2 | 1899 | 17.69 |
| | 2 | 6785.2 | 247 | 17.04 | 6786.5 | 1940 | 17.69 |
| | 3 | 6785.2 | 187 | 17.04 | 6786.5 | 2101 | 17.72 |
| | 4 | 6785.2 | 187 | 17.02 | 6786.5 | 2101 | 17.78 |
| PG 1309+355 | 1 | 6963.0 | 1268 | 18.86 | 7027.8 | 1712 | 18.85 |
| | 2 | 6955.9 | 935 | 18.49 | 6976.6 | 2659 | 19.23 |
| | 3 | 6955.9 | 2210 | 18.56 | 6976.6 | 2941 | 19.30 |
| | 4 | 6955.9 | 2210 | 18.86 | 6976.6 | 2941 | 18.72 |
| PG 1351+640 | 1 | 6396.2 | 407 | 46.50 | 6398.5 | 3368 | 48.74 |
| | 2 | 6395.6 | 394 | 46.49 | 6396.6 | 3344 | 48.75 |
| | 3 | 6395.6 | 173 | 46.34 | 6396.6 | 3128 | 48.59 |
| | 4 | 6395.6 | 173 | 46.30 | 6396.6 | 3128 | 48.72 |
| PG 1411+442 | 1 | 6401.1 | 700 | 29.79 | 6415.1 | 2000 | 31.36 |
| | 2 | 6402.3 | 700 | 29.81 | 6415.7 | 2000 | 31.31 |
| | 3 | 6402.3 | 799 | 29.85 | 6415.7 | 1663 | 31.01 |
| | 4 | 6402.3 | 799 | 29.86 | 6415.7 | 1663 | 30.99 |
| PG 1426+015 | 1 | 6385.1 | 3710 | 101.1 | 6508.6 | 8595 | 99.17 |
| | 2 | 6354.9 | 1846 | 96.19 | 6404.7 | 5296 | 104.0 |
| | 3 | 6354.9 | 2739 | 96.43 | 6404.7 | 3490 | 101.2 |
| | 4 | 6354.9 | 2739 | 98.56 | 6404.7 | 3490 | 99.68 |
| PG 1435-067 | 1 | 6628.1 | 1473 | 11.72 | 6644.8 | 3665 | 11.96 |
| | 2 | 6629.9 | 1079 | 11.58 | 6632.3 | 3164 | 12.11 |
| | 3 | 6629.9 | 1555 | 11.64 | 6632.3 | 3570 | 12.19 |
| | 4 | 6629.9 | 1555 | 11.82 | 6632.3 | 3570 | 11.81 |
| PG 1440+356 | 1 | 6330.4 | 485 | 29.82 | 6338.8 | 1361 | 31.26 |
| | 2 | 6331.7 | 247 | 29.72 | 6333.2 | 1314 | 31.37 |
| | 3 | 6331.7 | 842 | 29.81 | 6333.2 | 1872 | 32.06 |
| | 4 | 6331.7 | 842 | 30.48 | 6333.2 | 1872 | 30.49 |

| Name (1) | Fit (2) | $\lambda_{\text{He I},n}$ (\AA) (3) | $b_{\text{He I},n}$ (km s^{-1}) (4) | $\text{Flux}_{\text{He I},n}$ (5) | $\lambda_{\text{He I},b}$ (\AA) (6) | $b_{\text{He I},b}$ (km s^{-1}) (7) | $\text{Flux}_{\text{He I},b}$ (8) |
|-------------|------------|--|--|--------------------------------------|--|--|--------------------------------------|
| PG 1448+273 | 1 | 6255.8 | 193 | 10.12 | 6261.1 | 862 | 10.55 |
| | 2 | 6256.9 | 166 | 10.12 | 6257.3 | 924 | 10.56 |
| | 3 | 6256.9 | 480 | 10.17 | 6257.3 | 1784 | 10.91 |
| | 4 | 6256.9 | 480 | 10.32 | 6257.3 | 1784 | 10.37 |
| PG 1501+106 | 1 | 6092.4 | 149 | 33.48 | 6075.7 | 2709 | 35.31 |
| | 2 | 6092.6 | 138 | 33.47 | 6080.8 | 2756 | 35.41 |
| | 3 | 6092.6 | 129 | 33.46 | 6080.8 | 2584 | 35.30 |
| | 4 | 6092.6 | 129 | 33.39 | 6080.8 | 2584 | 35.32 |
| PG 1613+658 | 1 | 6636.5 | 266 | 33.54 | 6657.3 | 2781 | 34.42 |
| | 2 | 6637.2 | 500 | 33.65 | 6688.4 | 2800 | 34.14 |
| | 3 | 6637.2 | 486 | 33.66 | 6688.4 | 2712 | 34.16 |
| | 4 | 6637.2 | 486 | 33.74 | 6688.4 | 2712 | 33.82 |
| PG 1617+175 | 1 | 6561.8 | 3000 | 25.65 | ... | ... | ... |
| | 2 | 6552.8 | 2954 | 37.28 | 6566.3 | 3562 | 36.77 |
| | 3 | 6552.8 | 1800 | 36.73 | 6566.3 | 3420 | 36.73 |
| | 4 | 6552.8 | 1800 | 36.64 | 6566.3 | 3420 | 37.68 |
| PG 2130+099 | 1 | 6250.4 | 871 | 15.79 | 6248.5 | 2292 | 16.62 |
| | 2 | 6244.8 | 649 | 15.58 | 6250.0 | 1917 | 16.84 |
| | 3 | 6244.8 | 615 | 15.57 | 6250.0 | 2374 | 17.13 |
| | 4 | 6244.8 | 615 | 15.70 | 6250.0 | 2374 | 16.85 |
| PG 2214+139 | 1 | 6262.7 | 1309 | 39.77 | 6274.0 | 3971 | 41.61 |
| | 2 | 6285.0 | 113 | 39.33 | 6270.6 | 3000 | 41.45 |
| | 3 | 6285.0 | 156 | 39.35 | 6270.6 | 2788 | 41.31 |
| | 4 | 6285.0 | 156 | 39.31 | 6270.6 | 2788 | 41.92 |
| PG 2349-014 | 1 | 6957.8 | 1723 | 6.59 | ... | ... | ... |
| | 2 | 6911.9 | 2969 | 6.38 | ... | ... | ... |
| | 3 | 6911.9 | 3000 | 6.43 | ... | ... | ... |
| | 4 | 6911.9 | 3000 | 6.43 | ... | ... | ... |
| F04103-2838 | 1 | 6569.9 | 240 | 0.441 | ... | ... | ... |
| | 2 | 6569.8 | 240 | 0.441 | ... | ... | ... |
| | 3 | 6569.8 | 227 | 0.441 | ... | ... | ... |
| | 4 | 6569.8 | 227 | 0.441 | ... | ... | ... |
| F09111-1007 | 1 | 6197.3 | 259 | 1.630 | ... | ... | ... |
| | 2 | 6198.4 | 255 | 1.629 | ... | ... | ... |
| | 3 | 6198.4 | 254 | 1.628 | ... | ... | ... |
| | 4 | 6198.4 | 254 | 1.628 | ... | ... | ... |

| Name (1) | Fit (2) | $\lambda_{\text{He I,n}}$ (\AA) (3) | $b_{\text{He I,n}}$ (km s^{-1}) (4) | $\text{Flux}_{\text{He I,n}}$ (5) | $\lambda_{\text{He I,b}}$ (\AA) (6) | $b_{\text{He I,b}}$ (km s^{-1}) (7) | $\text{Flux}_{\text{He I,b}}$ (8) |
|--------------------------|------------|--|--|--------------------------------------|--|--|--------------------------------------|
| F12112+0305 | 1 | 6308.0 | 57 | 0.610 | 6304.0 | 133 | 0.612 |
| | 2 | 6307.5 | 104 | 0.617 | 6301.1 | 112 | 0.607 |
| | 3 | 6307.5 | 101 | 0.617 | 6301.1 | 124 | 0.607 |
| | 4 | 6307.5 | 101 | 0.617 | 6301.1 | 124 | 0.610 |
| F13305–1739 | 1 | 6751.2 | 517 | 1.560 | 6746.2 | 1183 | 1.505 |
| | 2 | 6748.7 | 636 | 1.576 | 6756.1 | 453 | 1.491 |
| | 3 | 6748.7 | 264 | 1.509 | 6756.1 | 1276 | 1.568 |
| | 3 | 6748.7 | 264 | 1.566 | 6756.1 | 1276 | 1.645 |
| F15250+3608 ^f | 1 | 6201.8 | 249 | 2.789 | ... | ... | ... |
| | 2 | 6202.7 | 239 | 2.777 | ... | ... | ... |
| | 3 | 6202.7 | 194 | 2.765 | ... | ... | ... |
| | 4 | 6202.7 | 194 | 2.765 | ... | ... | ... |
| F15462–0450 | 1 | 6465.6 | 117 | 2.477 | 6460.7 | 2283 | 2.750 |
| | 2 | 6465.9 | 123 | 2.480 | 6462.6 | 2285 | 2.751 |
| | 3 | 6465.9 | 92 | 2.477 | 6462.6 | 1609 | 2.708 |
| | 4 | 6465.9 | 92 | 2.477 | 6462.6 | 1609 | 2.682 |
| F22491–1808 | 1 | 6334.3 | 145 | 1.430 | ... | ... | ... |
| | 2 | 6335.2 | 161 | 1.433 | ... | ... | ... |
| | 3 | 6335.2 | 172 | 1.432 | ... | ... | ... |
| | 4 | 6335.2 | 172 | 1.432 | ... | ... | ... |
| Mrk 231 ^b | 1 | 6149.3 | 1205 | 16.33 | 6126.7 | 2554 | 16.57 |
| | 2 | 6127.1 | 2398 | 16.76 | 6115.9 | 1076 | 16.14 |
| | 3 | 6127.1 | 1501 | 16.52 | 6115.9 | 4490 | 16.23 |
| | 4 | 6127.1 | 1501 | 16.37 | 6115.9 | 4490 | 16.80 |
| Mrk 231 ^c | 1 | 6150.0 | 571 | 9.137 | 6137.4 | 1801 | 9.344 |
| | 2 | 6126.5 | 1499 | 9.301 | 6114.1 | 3836 | 9.171 |
| | 3 | 6126.5 | 1459 | 9.295 | 6114.1 | 4490 | 9.179 |
| | 4 | 6126.5 | 1459 | 9.218 | 6114.1 | 4490 | 9.374 |

Table 3.6: Outflow: individual objects.

| Name (1) | Δv_{max} (km s ⁻¹) (2) | M (M_{\odot}) (3) | dM/dt (M_{\odot} yr ⁻¹) (4) | p (dyn s) (5) | dp/dt (dyn) (6) | E (ergs) (7) | dE/dt (ergs s ⁻¹) (8) | η (9) |
|--------------------------|--|-------------------------------|--|-----------------------|-------------------------|----------------------|---|---------------|
| F04103–2838 | -158 | 9.3 | 28.1 | 49.4 | 33.7 | 55.9 | 40.6 | 0.2 |
| F09111–1007 | -217 | 9.2 | 30.0 | 49.5 | 33.9 | 56.2 | 41.0 | 0.2 |
| F12112+0305 | -342 | 10.0 | 382 | 50.6 | 35.3 | 57.6 | 42.7 | 1.6 |
| F15250+3608 ^a | -845 | 9.2 | 122 | 50.1 | 35.0 | 57.3 | 42.7 | 1.2 |
| F15250+3608 ^b | -403 | 9.0 | 38.4 | 49.6 | 34.3 | 56.6 | 41.7 | 0.4 |
| Mrk 231 ^c | -8038 | 8.8 | 992 | 51.0 | 37.3 | 59.6 | 46.3 | 3.6 |
| | -6166 | 8.9 | 934 | 51.0 | 37.2 | 59.4 | 46.0 | 3.4 |
| | -4877 | 10.3 | 16200 | 52.2 | 38.3 | 60.6 | 47.0 | 59.6 |
| Mrk 231 ^b | -8098 | 8.8 | 1010 | 51.0 | 37.3 | 59.6 | 46.3 | 3.7 |
| | -6219 | 9.0 | 1270 | 51.1 | 37.3 | 59.6 | 46.2 | 4.7 |
| | -4969 | 10.2 | 15200 | 52.2 | 38.2 | 60.5 | 47.0 | 55.6 |

(a), (b), and (c) correspond to those found in Table 3.5. Col.(2): Maximum velocity in the outflow, $\Delta v_{max} \equiv \Delta v - \text{FWHM}/2$. Col.(3): Log of total outflowing mass. Col.(4): Mass outflow rate. Col.(5): Log of total momentum of outflow. Col.(6): Log of momentum outflow rate. Col.(7): Log of total kinetic energy of outflow. Col.(8): Log of kinetic energy outflow rate. Col.(9): Mass entrainment efficiency, $\eta \equiv dM/dt / \text{SFR}$. Note that Mrk 231 has multiple Na I D absorption components.

Table 3.7: Outflow: average properties.

| Quantity (1) | ULIRGs (2) |
|--|------------------|
| Number of galaxies | 10 |
| Detection rate (%) | 50 ± 14 |
| Galaxy Properties | |
| z | 0.084 ± 0.03 |
| $\log(L_{\text{FIR}}/L_{\odot})$ | 12.08 ± 0.14 |
| SFR ($M_{\odot} \text{ yr}^{-1}$) | 171 ± 556 |
| α_{AGN} | 51.9 ± 28.7 |
| $\log(L_{\text{AGN}}/L_{\odot})$ | 11.84 ± 0.52 |
| Δv (km s^{-1}) | -2750 ± 22 |
| Δv_{max} (km s^{-1}) | -2949 ± 36 |
| $\log[N(\text{Na I})/\text{cm s}^{-2}]$ | 13.8 ± 0.6 |
| $\log[N(\text{H})/\text{cm s}^{-2}]$ | 21.4 ± 0.58 |
| Velocity Component Properties | |
| τ | 1.47 ± 1.36 |
| b (km s^{-1}) | 239 ± 22 |
| C_f | 0.39 ± 0.10 |

For most quantities we list the mean and 1σ dispersions, under the assumption of a Gaussian distribution in the log of the quantity. Statistics for all quantities except z , L_{FIR} , SFR, α_{AGN} , and L_{AGN} are computed only for outflowing velocity components.

Table 3.8: Outflow: average properties (combined sample).

| Quantity (1) | IR-Faint AGN (2) | IR-Lum. AGN (3) | Starbursts (4) | Type 1 AGN (5) | Type 2 AGN (6) | Binaries (7) | Singles (8) |
|-------------------------|---------------------|--------------------|-------------------|-------------------|-------------------|-------------------|------------------|
| # of galaxies | 43 | 47 | 71 | 41 | 38 | 15 | 48 |
| Det. rate (%) | 9 ± 3 | 30 ± 9 | 61 ± 18 | 12 ± 3 | 34 ± 9 | 60 ± 17 | 48 ± 14 |
| Gal. Prop. | | | | | | | |
| z | 0.067 ± 0.15 | 0.141 ± 0.10 | 0.100 ± 0.09 | 0.098 ± 0.13 | 0.126 ± 0.11 | 0.150 ± 0.10 | 0.121 ± 0.10 |
| $\log(L_{\text{FIR}})$ | 10.34 ± 0.41 | 12.08 ± 0.36 | 11.71 ± 0.56 | 11.34 ± 0.87 | 11.54 ± 0.98 | 12.14 ± 0.16 | 11.91 ± 0.53 |
| SFR | 3 ± 4 | 108 ± 60 | 126 ± 91 | 60 ± 66 | 80 ± 67 | 159 ± 64 | 125 ± 85 |
| α_{AGN} | ... | 71.7 ± 23.8 | 49.6 ± 32.1 | 83.6 ± 15.9 | 65.0 ± 29.1 | 39.92 ± 30.58 | 62.1 ± 30.1 |
| $\log(L_{\text{AGN}})$ | ... | 12.19 ± 0.29 | 11.47 ± 0.49 | 12.11 ± 0.51 | 12.03 ± 0.24 | 11.69 ± 0.54 | 12.01 ± 0.42 |
| Δv | -1142 ± 1878 | -3294 ± 3176 | -202 ± 133 | -4746 ± 2882 | -281 ± 348 | -267 ± 412 | -2477 ± 3053 |
| Δv_{max} | -1276 ± 1848 | -3477 ± 3244 | -361 ± 180 | -4915 ± 3012 | -468 ± 354 | -461 ± 406 | -2662 ± 3105 |
| $\log[N(\text{Na I})]$ | 13.08 ± 0.70 | 13.39 ± 0.59 | 13.69 ± 0.42 | 13.41 ± 0.59 | 13.38 ± 0.52 | 13.61 ± 0.44 | 13.54 ± 0.57 |
| $\log[N(\text{H})]$ | 20.72 ± 0.70 | 20.73 ± 0.62 | 21.08 ± 0.44 | 20.78 ± 0.63 | 20.78 ± 0.54 | 20.96 ± 0.49 | 20.91 ± 0.59 |
| Vel. Comp. | | | | | | | |
| τ | 1.85 ± 2.12 | 0.94 ± 0.99 | 1.56 ± 1.73 | 1.25 ± 1.26 | 1.03 ± 1.36 | 1.12 ± 1.42 | 1.33 ± 1.60 |
| b | 160 ± 175 | 219 ± 239 | 191 ± 118 | 203 ± 286 | 225 ± 135 | 233 ± 99 | 222 ± 225 |
| C_f | 0.65 ± 0.79 | 0.46 ± 0.40 | 0.42 ± 0.26 | 0.59 ± 0.53 | 0.50 ± 0.34 | 0.44 ± 0.29 | 0.48 ± 0.34 |

“Gal. Prop.”: Galaxy Properties; “Vel. Comp.”: Velocity Component Properties; “Starbursts”: IR-Luminous Starbursts. Units for all quantities are the same as in Table 3.7. For most quantities we list the mean and 1σ dispersions, under the assumption of a Gaussian distribution in the log of the quantity. Statistics for all quantities except z , L_{FIR} , SFR, α_{AGN} , and L_{AGN} are computed only for outflowing velocity components.

Table 3.9: Inflow: individual objects.

| Name (1) | Δv_{max} (km s ⁻¹) (2) | M (M_{\odot}) (3) | dM/dt (M_{\odot} yr ⁻¹) (4) | p (dyn s) (5) | dp/dt (dyn) (6) | E (ergs) (7) | dE/dt (ergs s ⁻¹) (8) |
|-------------|--|-------------------------------|--|-----------------------|-------------------------|----------------------|---|
| PG 1613+658 | 236 | 7.1 | 2.4 | 47.7 | 33.0 | 54.6 | 40.4 |
| F15130-1958 | 526 | 7.5 | 8.4 | 48.2 | 33.8 | 55.4 | 41.4 |

(a), (b), and (c) correspond to those found in Table 3.5. Col.(2): Maximum velocity in the inflow, $\Delta v_{max} \equiv \Delta v + \text{FWHM}/2$. Col.(3): Log of total inflowing mass. Col.(4): Log of mass inflow rate. Col.(5): Log of total momentum of inflow. Col.(6): Log of momentum inflow rate. Col.(7): Log of total kinetic energy of inflow. Col.(8): Log of kinetic energy inflow rate.

Table 3.10: Inflow: average properties (combined sample).

| Quantity (1) | IR-Faint AGN (2) | IR-Lum. AGN (3) | Starbursts (4) | Type 1 AGN (5) | Type 2 AGN (6) | Binaries (7) | Singles (8) |
|--------------------------------|---------------------|--------------------|-------------------|-------------------|-------------------|-------------------|------------------|
| # of galaxies Det. rate (%) | 43 28 ± 8 | 47 21 ± 6 | 71 17 ± 5 | 41 20 ± 6 | 38 37 ± 11 | 15 33 ± 10 | 48 13 ± 4 |
| Gal. Prop. | | | | | | | |
| z | 0.067 ± 0.15 | 0.141 ± 0.10 | 0.100 ± 0.09 | 0.098 ± 0.13 | 0.126 ± 0.11 | 0.150 ± 0.10 | 0.121 ± 0.10 |
| $\log(L_{\text{FIR}})$ | 10.34 ± 0.41 | 12.08 ± 0.36 | 11.71 ± 0.56 | 11.34 ± 0.87 | 11.54 ± 0.98 | 12.14 ± 0.16 | 11.91 ± 0.53 |
| SFR | 3 ± 4 | 108 ± 60 | 126 ± 91 | 60 ± 66 | 80 ± 67 | 159 ± 64 | 125 ± 85 |
| Δv | 90 ± 30 | 177 ± 90 | 83 ± 39 | 110 ± 39 | 141 ± 92 | 70 ± 18 | 210 ± 89 |
| Δv_{max} | 309 ± 90 | 314 ± 113 | 208 ± 72 | 310 ± 109 | 312 ± 103 | 264 ± 50 | 329 ± 134 |
| $\log[N(\text{Na I})]$ | 13.18 ± 0.31 | 13.51 ± 0.42 | 13.38 ± 0.39 | 13.38 ± 0.39 | 13.30 ± 0.41 | 13.14 ± 0.47 | 13.43 ± 0.53 |
| $\log[N(\text{H})]$ | 20.82 ± 0.31 | 20.91 ± 0.51 | 20.76 ± 0.42 | 21.02 ± 0.39 | 20.77 ± 0.41 | 20.44 ± 0.46 | 20.87 ± 0.63 |
| Vel. Comp. | | | | | | | |
| τ | 0.38 ± 0.36 | 1.77 ± 2.25 | 0.94 ± 0.94 | 0.96 ± 1.68 | 1.03 ± 1.71 | 0.29 ± 0.39 | 1.16 ± 1.73 |
| b | 263 ± 111 | 164 ± 94 | 150 ± 91 | 240 ± 147 | 205 ± 95 | 234 ± 59 | 143 ± 84 |
| C_f | 0.58 ± 0.39 | 0.46 ± 0.40 | 0.51 ± 0.29 | 0.35 ± 0.34 | 0.63 ± 0.39 | 0.70 ± 0.26 | 0.41 ± 0.40 |

“Gal. Prop.”: Galaxy Properties; “Vel. Comp.”: Velocity Component Properties; “Starbursts”: IR-Luminous Starbursts. Units for all quantities are the same as in Table 3.7. For most quantities we list the mean and 1σ dispersions, under the assumption of a Gaussian distribution in the log of the quantity. Statistics for all quantities except z , L_{FIR} , SFR, α_{AGN} , and L_{AGN} are computed only for inflowing velocity components.

Table 3.11: Statistical comparisons of kinematic parameters (combined sample).

| Samples | All Galaxies $P(\text{null, K-S})$ | $P(\text{null, Ku})$ | Outflows Only $P(\text{null, K-S})$ | $P(\text{null, Ku})$ |
|--|---------------------------------------|------------------------|--|------------------------|
| Δv | | | | |
| IR-Faint AGN (30, 5) vs IR-Luminous AGN (64, 42) | 4.26×10^{-6} | 4.20×10^{-6} | 0.10 | 0.50 |
| IR-Faint AGN (30, 5) vs IR-Luminous Starbursts (100, 55) | 1.02×10^{-3} | 3.73×10^{-3} | 0.31 | 0.94 |
| IR-Luminous AGN (64, 42) vs IR-Luminous Starbursts (100, 55) | 6.23×10^{-6} | 8.37×10^{-8} | 1.01×10^{-7} | 8.52×10^{-7} |
| Type 1 AGN (42, 25) vs Type 2 AGN (56, 18) | 1.27×10^{-6} | 1.37×10^{-5} | 7.02×10^{-8} | 5.20×10^{-6} |
| Type 1 AGN (42, 25) vs IR-Luminous Starbursts (100, 55) | 1.56×10^{-8} | 5.31×10^{-11} | 5.70×10^{-14} | 1.93×10^{-11} |
| Type 2 AGN (56, 18) vs IR-Luminous Starbursts (100, 55) | 0.02 | 0.03 | 0.93 | 0.83 |
| Binaries (25, 12) vs Singles (61, 50) | 6.26×10^{-4} | 5.69×10^{-4} | 4.29×10^{-3} | 0.06 |
| Δv_{max} | | | | |
| IR-Faint AGN (30, 5) vs IR-Luminous AGN (64, 42) | 8.87×10^{-6} | 1.68×10^{-4} | 0.10 | 0.50 |
| IR-Faint AGN (30, 5) vs IR-Luminous Starbursts (100, 55) | 3.56×10^{-4} | 1.95×10^{-3} | 0.26 | 0.50 |
| IR-Luminous AGN (64, 42) vs IR-Luminous Starbursts (100, 55) | 1.35×10^{-6} | 2.65×10^{-8} | 3.95×10^{-9} | 6.79×10^{-8} |
| Type 1 AGN (42, 25) vs Type 2 AGN (56, 18) | 1.27×10^{-6} | 3.78×10^{-6} | 7.02×10^{-8} | 5.20×10^{-6} |
| Type 1 AGN (42, 25) vs IR-Luminous Starbursts (100, 55) | 5.97×10^{-8} | 4.20×10^{-11} | 6.39×10^{-13} | 1.91×10^{-10} |
| Type 2 AGN (49, 30) vs IR-Luminous Starbursts (100, 55) | 0.02 | 0.03 | 0.26 | 0.36 |
| Binaries (25, 12) vs Singles (61, 50) | 1.89×10^{-3} | 1.57×10^{-2} | 0.02 | 0.13 |

$P(\text{null})$ is the probability that the two listed distributions are taken from the same intrinsic distribution. Categories which have $P(\text{null}) < 0.1$ for both tests (for either all galaxies or outflows only) are printed in bold. “K-S” refers to the Kolmogorov-Smirnov test, “Ku” to the Kuiper test. The numbers in parentheses refer to the total number of objects in that particular sample: the first value for all galaxies, the second for outflows only. Values for “all galaxies” are based on all absorption features, both inflowing and outflowing, whereas values for “outflows only” are based only on outflowing components.

Chapter 4

Searching for $z=7.7$ Ly α -Emitters in the COSMOS Field with NEWFIRM

4.1 INTRODUCTION

Direct observations of distant galaxies remain the most straightforward way to probe the fundamental nature of the high-redshift universe. Such observations can provide some much-needed constraints on numerical simulations, which may provide better answers to the question of how large scale structure forms and how star formation begins in dark matter halos. Star formation in early galaxies is dependent upon the mechanism by which gas cools; that mechanism itself is dependent upon the ionization state and metal enrichment of that gas which are not well constrained at high redshift. The Ly α emission line is a very useful tool for the detection of high-redshift galaxies, as the earliest stars in the universe should ionize surrounding hydrogen gas, which will then recombine to produce Ly α emission (see Willis et al. (2008)). This Ly α line can be probed quite effectively at high redshifts via the use of narrowband filters, which focus on regions with low sky background and that are free of strong OH lines (e.g., Cuby et al. (2007)). High-redshift objects should have essentially no flux blueward of rest-frame Ly α and none blueward of rest-frame 912 Å; this is a result of the Ly α forest effect at high redshift, due to strong

absorption by intervening clouds (e.g., Bahcall & Salpeter (1965), Gunn & Peterson (1965), Lynds (1971), Rees (1986), Miralda-Escudé (1996), Schaye (2001)). Such narrowband surveys have proved quite successful so far (e.g., Cowie & Hu (1998), Hu et al. (1999,2002,04), Rhoads et al. (2000,03,04), Fynbo et al. (2001), Ouchi et al. (2001,03,08), Malhotra & Rhoads (2002,04), Taniguchi et al. (2005), Kashikawa et al. (2006), Shimasaku et al. (2006), Nilsson et al. (2007), Finkelstein et al. (2009)) and have resulted in samples of galaxies over a range of redshifts, including the spectroscopic confirmation of a Ly α emitting galaxy at $z = 6.96$ [Iye et al. (2006)]. Even when these narrowband surveys do not successfully detect high- z objects, such null results can be used to constrain the Ly α luminosity function (e.g., Cuby et al. (2007), Willis et al. (2008), Sobral et al. (2009)).

The early universe is expected to be metal poor, but metals have been detected in the intergalactic medium (IGM) at $z = 5.7$ [Ryan-Weber et al. (2006)], and so the IGM must have been enriched in metals by $z \sim 6$ at the latest, with recent results tentatively indicating a metallicity downturn between $z \sim 5.7$ and $z \sim 5$ [Simcoe et al. (2011)]. Additionally, the Ly α line is sensitive to IGM obscuration at neutral hydrogen fractions ranging from low to high (e.g., $10\% \sim < x_{HI} < 100\%$; Haiman (2002), Santos (2004)), and thus observations of Ly α -emitting galaxies serve as a powerful probe of the reionization history of the universe; the Gunn-Peterson test, for example, is only useful when the neutral gas fraction is $< 1\%$ [Cuby et al. (2007)]. Increasing the neutral hydrogen fraction in the IGM increases the attenuation of Ly α emission from those galaxies [Sobral et al. (2009)]. As this neutral fraction increases, the Ly α luminosity function will vary according to the

amount of light being attenuated by the IGM. Previous estimates of the redshift of the epoch of reionization using constraints from studies of Ly α emitters do not concur with constraints derived from polarization observations of the CMB. The latter suggests that the redshift of reionization is $z_{\text{re}} = 10.5 \pm 1.2$, should reionization be an instantaneous process [Komatsu et al. (2011)], whereas the former have indicated a significantly later end to the epoch. Constraints on the Ly α luminosity function (LF) can assist in determination of the redshift at which reionization has been completed, owing to the resonant scattering of Ly α photons in a neutral IGM. If the intrinsic number density of young galaxies remains constant over redshift, then a significant decline in the observed Ly α LF at a given redshift could indicate a change in IGM phase. On the lower redshift end, Malhotra & Rhoads (2004) found no significant evolution of Ly α LF between $5.7 < z < 6.6$; whereas at higher redshifts, an evolution of Ly α LF between $6.5 < z < 7$ is suggested based on single detections [Iye et al. (2006), Ota et al. (2008)]. Ouchi et al. (2008) found little evolution between $z \sim 3$ and $z \sim 6$ in the observed LFs, although they suggest a real evolution, with increase in intrinsic Ly α luminosity being canceled out by increase in IGM absorption. Curtis-Lake et al. (2011) have recently identified Ly α emitters at a high rate over $6 < z < 6.5$ in UKIDSS. Ono et al. (2012) have measured a decrease in Ly α emission line detection fraction over $6 < z < 7$, as have Schenker et al. (2012) over $6 < z < 8$ and Pentericci et al. (2011; following up work by Fontana et al. (2010)) over $6 < z < 7$; these studies are UV-continuum-selected galaxies (i.e., Lyman break galaxies) rather than selected via Ly α emission line but share the same goal, and all conclude that the neutral hydrogen fraction of the IGM

is increasing over those epochs. The seven Ly α candidates found by Hibon et al. (2010) at $z = 7.7$ would indicate no evolution of the Ly α LF if they are found to be spectroscopically confirmed (although soon to be published work suggests that at least five are not confirmed; see Clément et al. (2011)); the four Ly α candidates found by Tilvi et al. (2010) could either indicate mild or no evolution between $6.5 < z < 7.7$ depending on the number of candidates which are confirmed. Two Lyman break galaxies at $z > \sim 7.0$ were recently spectroscopically confirmed by Vanzella et al. (2011), their luminosities fairly consistent with that of the well-known confirmed $z = 6.96$ Iye et al. (2006) Ly α emitter. At present, small number statistics severely affect our ability to draw definite conclusions on the Ly α luminosity function and properties of the IGM. It is therefore essential to expand the sample of high-redshift candidates at epochs when the IGM became metal-enriched and reionized, and thus shed light on the nature of the early universe.

As redshift increases, galaxy sizes and luminosities decrease, and cosmological dimming must also be taken into account. Because of this, detection of galaxies at $z > 7$ can be quite difficult [Ferguson et al. (2004), Bouwens et al. (2006), Capak et al. (2011)]. Thus it is essential to have a large survey volume in order to detect a sufficient number of high- z objects. This conclusion is bolstered by the biased nature of galaxy formation and the non-uniformity of large-scale structure at high- z [Steidel et al. (1999), Malhotra et al. (2005), Wang et al. (2005), Ouchi et al. (2005), Tilvi et al. (2009)]. Presently, most studies searching for high- z galaxies have significant depth but small area (e.g., Bouwens et al. (2010), Oesch et al. (2010)) or have small volume but high magnification by virtue of cluster lensing

[Richard et al. (2007), Richard et al. (2008), Stark et al. (2007)], so all results are affected by cosmic variance. There is a need for surveys which probe both a deep and wide region in order to best constrain global properties of high- z galaxies; the present paper reports on a survey that tries to fill that role.

In this chapter, we present the results from a search for Ly α emitting galaxies at $z = 7.7$ in the COSMOS field, utilizing custom-made ultra-narrowband filters which are tuned to avoid the OH sky lines and thus reach extremely low infrared sky backgrounds. The organization of this chapter is as follows. In Section 4.2, we discuss our observations and reduction of the data that we obtained, as well as photometric calibration. In Section 4.3, we describe our method of candidate Ly α emitter selection and the basic properties of the resulting candidate Ly α emitters. In Section 4.4, we discuss possible sources of contamination in our samples. In Section 4.5, we estimate the number of Ly α emitting galaxies that we should expect to find in our survey through the use of a detailed Monte Carlo simulation. In Section 4.6, we present the Ly α luminosity function derived from our candidates and compare to previously derived Ly α LFs. Finally, in Section 4.7, we summarize our conclusions. This work shares authors, instrument, and technique with the work of Tilvi et al. (2010), and can thus be viewed as part of a series with that paper. Throughout this work, we assume a standard flat Λ CDM cosmology with $\Omega_m = 0.3$, $\Omega_\Lambda = 0.7$, and $h = 0.71$, where Ω_m , Ω_Λ , and h are the matter density, dark energy density, and Hubble parameter (in units of $100 \text{ km s}^{-1} \text{ Mpc}^{-1}$), respectively. All magnitudes listed are in the AB magnitude system.

4.2 OBSERVATIONS AND DATA

4.2.1 Observations with NEWFIRM

Our observations were centered on the Cosmological Evolution Survey (COSMOS) field (RA 10:00:28.6, Dec. +02:12:21.0), taking advantage of the large amount of ancillary data available on this field¹. We used the NOAO Extremely Wide-Field Infrared Mosaic (NEWFIRM) camera on the Mayall 4m telescope at Kitt Peak National Observatory (KPNO) on three different observing runs over the course of two years (2008 February 28 - March 14; 2009 January 29 - February 1; 2009 February 17 - March 2) for a total of roughly 100 hours over 32 nights. Average seeing over the course of these exposures was $\sim 1.2''$.

The NEWFIRM camera, sensitive to 1-2.4 μm wavelengths, is a wide-field imager consisting of four mosaiced 2048 x 2048 pixel ALADDIN InSb arrays, $0.4''$ pixel⁻¹, for a cumulative field of view of 27.6' x 27.6' (cumulative area ~ 760 arcmin²). Our observing time was split evenly between two University of Maryland custom-made ultra-narrowband (UNB) filters ($R \sim 1000$) centered at 1.056 and 1.063 μm , with FWHM of 7.4 and 8.1 \AA , respectively. These UNB filters were designed in order to isolate Ly α emitters at $z \sim 7.7$, while simultaneously avoiding the bright OH lines near these wavelengths (Figure 4.1 shows UNB filter profiles). The transmitted wavelength varies across the field according to roughly $m\lambda = \mu d \cos \theta$ (here the order, m , index of refraction, μ , and thickness of the filter, d , are constant; θ is the angle of incidence of light onto the detector); the path length increases as

¹<http://cosmos.astro.caltech.edu>

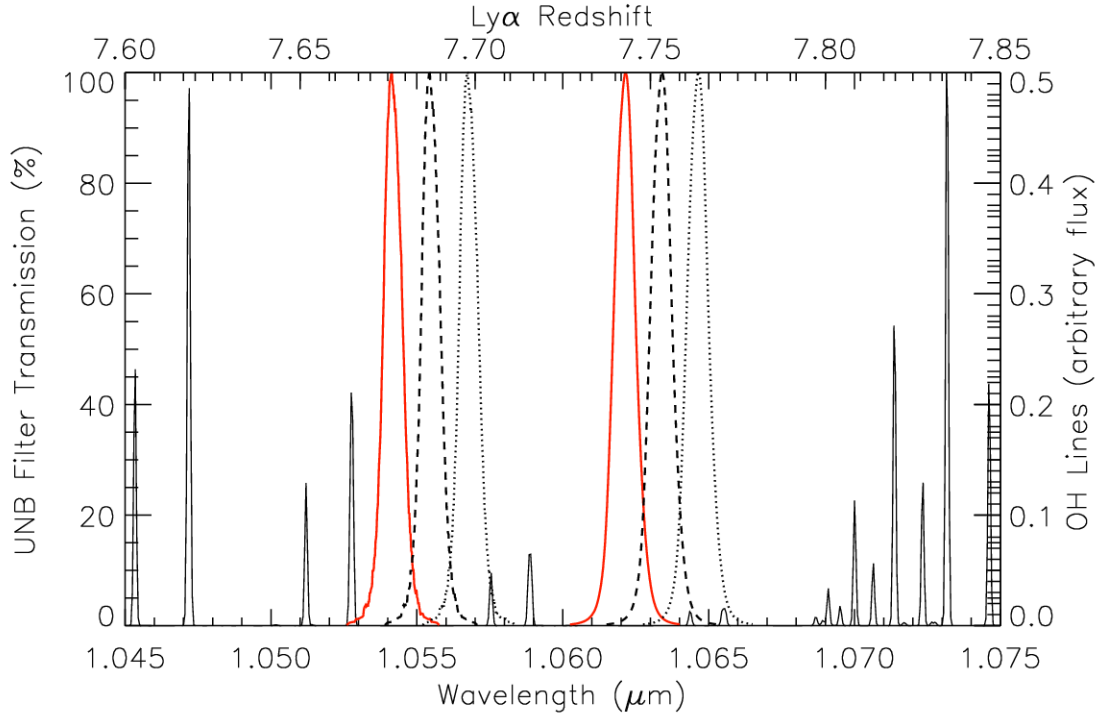


Figure 4.1: NEWFIRM ultra-narrowband filter profiles, centered at 1.056 and 1.063 μm . The solid red, dashed, and dotted lines show the range of profile from center (solid red) to $\sim 40\%$ (dashed) and 80% center-to-corner distance (dotted) of the field of view. The Rousselot et al. (2000) OH sky spectrum is also plotted.

one gets further off-axis and the wavelength of transmitted light is correspondingly shorter. This effect is more apparent for a UNB filter in a wide field imager, since the bandpass is narrow and the range of angle of incidence is large (see Figure 4.1). Atmospheric absorption (primarily due to O_2 and H_2O in the IR) is irrelevant in these bandpasses. Each 1200s exposure science frame was taken using Fowler 8 sampling and we utilized random dithering within a $45''$ box after each exposure.

Additional ancillary data in broadband filters were required for $\text{Ly}\alpha$ candidate

selection. We made use of publicly-available data from the COSMOS archive² for this purpose: B , r , and i band data from Subaru and J band data from UKIRT.

4.2.2 Data Reduction

The reduction of our data was done by the NEWFIRM Science Pipeline (see Dickinson and Valdes 2009; Swaters et al. 2011). Frames with seeing of $> 1.5''$ were rejected outright. The pipeline flagged pixels affected by detector blemishes, saturation, and persistence, and then subtracted the dark current, linearized the data, and applied the dome flat. Image gradients remaining after the flat fielding were subtracted out. The astrometric solution was determined from 2MASS stars in the field; these same stars were also used to determine an initial photometric calibration of the data. In the pipeline, the sky was subtracted in a two-pass approach. First, the sky was subtracted using a running-median window, and then the data were combined by taking the median over all the exposures. This so-called harsh stack was then used to identify and mask sources. The mask was then applied to the original images, and the sky-subtraction was repeated. Cosmic ray hits and other transient phenomena were detected by comparing individual images against the first-pass stack, and outliers were flagged.

Starting with these pipeline products, custom IDL4 scripts designed by Krug & Swaters were used to eliminate artifacts such as OH rings and striping due to data readout from the science frames. For OH ring elimination, pixel values were separated into 1000 radial bins across one NEWFIRM chip at a time. Owing to

²<http://irsa.ipac.caltech.edu/Missions/cosmos.html>

the unevenness of the NEWFIRM chip gaps, the pixel center of the OH ring varied from chip to chip; the ring centers were determined for each chip through a combination of visual inspection and fitting rings to the values at each pixel. Data within the radial bins were then median smoothed, and these smoothed bins were then subtracted from the original image data. Stripe removal was also performed on individual NEWFIRM chips at one time. Each chip was divided into horizontal or vertical strips, depending on data readout direction. Pixels across each strip were summed and averaged, and the original data pixels in each strip were subtracted by the average pixel value in that strip. A comparison of stacks made from frames before and after ring and stripe removal showed that the signal-to-noise ratio (SNR) increased by 1.2 times on average across the frames, with SNR increasing by as much as 4-7 times in regions where the OH rings were strong prior to algorithm implementation. The SNR in the most extreme rings, however (namely those areas as seen in Figure 4.1 where the OH lines cross the outer edge filters, particularly the strongest OH ring in the 1.063 μm filter), was not quite high enough for candidate detection (see Section 4.3).

Following removal of artifacts and sky subtraction, the world coordinate system of each individual frame was assigned using the IRAF task *nfwcs*, which matches as many sources as possible to those of the 2MASS point source catalog, searching within a 450" radius. The *mscimage* task was used to reproject all four chips onto a single image with the same pixel grid. Finally, images were combined into two yearly stacks (weighted by seeing) as well as one full data stack for each filter via *imcombine*; these were median combined using noise values from *mscstat*

and zeropoint magnitudes as calculated based on the 2MASS catalog during the prior *nfwcs* task. This resulted in two full UNB stacks - one each for the 1.056 and 1.063 μm filters - as well as stacks from year one and year two for each filter (in order to properly check for transients). Broadband data mosaics supplied by the COSMOS team were already reduced.

4.2.3 Photometric Calibration

Photometric calibration was performed by making use of the 2MASS point source catalog. SExtractor (SE; Bertin & Arnouts (1996)) was run on each NEWFIRM UNB stack using a magnitude zero point set to zero. The resulting catalogs were matched with the 2MASS point source catalog; in order to avoid saturated sources or objects that are too faint, all stars with 2MASS J band magnitudes (AB) of less than 13.0 or greater than 16.5 were discarded. Plots were made comparing the SE UNB magnitudes with 2MASS J magnitudes in order to determine an appropriate zeropoint. Before SE could be run with the proper magnitude zeropoint, it was necessary to determine a color correction between the 2MASS J magnitude and the NEWFIRM UNB magnitudes, as they do not share the same central wavelength. 2MASS J , H , and K band magnitudes for overlapping stars were converted to flux and used to calculate the flux expected at 1.056 and 1.063 μm , the central wavelengths of the NEWFIRM UNB filters. The difference between 2MASS J flux and extrapolated NEWFIRM UNB flux corresponds to a magnitude difference of $\sim +0.1$ mag in J . This correction was then applied to the previously determined

magnitude zeropoint.

4.2.4 Limiting Magnitude

In order to determine which of our detections can be considered real, we must obtain some estimate of the limiting magnitude of our science frames. We have chosen to define our limiting magnitude as the 50% completeness limit in our frames. To determine this, we inject artificial sources into our frames. These sources are randomly distributed throughout each frame, although care is taken to avoid locations within 4" of any existing bright star. Two hundred artificial point sources are generated in each of 0.1 magnitude bins, ranging between 20 and 24 mag for UNB frames, 21 and 25 for J band, and 24 and 28 mag for the broadband optical frames. Once these sources were generated, SE was run and the resultant SE catalog was matched with the catalog of artificial sources to determine a recovery fraction. This procedure was then iterated 25 times for each band. Once all iterations were completed, histograms of recovery fraction of artificial sources were plotted for each band in order to determine the magnitude at which 50% of all artificial sources were detected by SE (Figure 4.2 for UNB recovery fraction histograms). We define the limiting magnitude for each band as the 50% completeness limit for that filter, as this is the magnitude brighter than which sources can be reliably detected in these fields via our methods. Limiting magnitudes for the two NEWFIRM UNB bands were determined to be 22.4 and 22.5 (AB) for 1.056 μm and 1.063 μm , respectively. Shifts in central wavelength of the UNB filters with distance from the field center

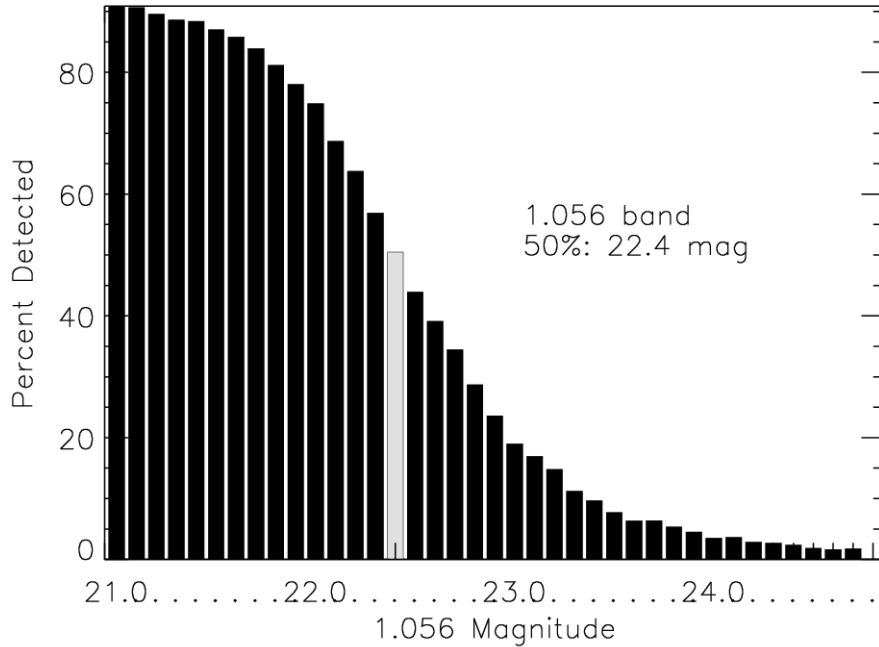


Figure 4.2: SExtractor detection percentages for randomly generated false sources in 0.1 magnitude bins in a given UNB band. The light gray bar marks 50% completeness. That value is used as the limiting magnitude (AB) for our survey. Our 1.063 μm band data is 0.1 mag deeper than our 1.056 μm band data.

were not found to significantly affect these limiting magnitudes. For the broadband data, limiting magnitudes were found to be 27.3, 26.6, 26.3, and 24.0 for B , r , i , and J , respectively.

4.3 CANDIDATE $\text{Ly}\alpha$ EMITTERS

4.3.1 Selection Criteria

To select potential candidate $\text{Ly}\alpha$ emitters, we initially ran SE on the NEW-FIRM UNB frames individually, with minimum detection area of 5 pixels and de-

tection threshold of 1.2 sigmas. We then used dual-image mode in SE, which takes the coordinates of objects detected in the NEWFIRM UNB frames but measures fluxes at those coordinates in the UKIRT J band image. Thus we obtained J band fluxes at the exact locations of NEWFIRM UNB targets. For all of our dual-image mode detections, we made use of the SExtractor auto aperture size scaling. We also needed to obtain optical fluxes at those coordinates, so in order to do so, we created a chi-squared image of a combination of B , r , and i band data from Subaru using the program *Sswarp* [Bertin et al. (2002)]. The chi-squared image is created by deriving the distribution of the pixels that are dominated by object flux rather than those dominated by sky noise [Szalay et al. (1999)]. This is an optimal combination of images which enhances real objects in the resultant frame rather than a simple stack. We then ran SE in dual-image mode on this combined optical image in the same vein as the J images. We also ran dual-image mode on the two NEWFIRM UNB frames together - first using the coordinates for 1.056 μm detections but getting 1.063 μm flux, and vice versa - as any potential candidate Ly α emitter should appear in one of the UNB frames but not both. We likely miss highly extended Ly α blobs with this technique, especially following sky subtraction, but such highly extended sources would be difficult to isolate in any case.

Once the SE catalogs were created, we ran a custom python script to comb through those catalogs and identify potential candidates. There were five main initial criteria that had to be met in order for an object to be considered a candidate (J data refers to the UKIRT band, centered at 1.2 μm and outside the UNB filter range):

1. UNB signal-to-noise ratio (SNR) of at least 5.
2. UNB excess $f_\nu(\text{UNB}) - f_\nu(J)$ of at least 3σ .
3. Flux ratio $f_\nu(\text{UNB}) / f_\nu(J)$ of at least 2.
4. UNB SNR in the other UNB filter of no more than 2 (e.g. if detected in 1.056 μm , must not have a 1.063 μm SNR of more than 2).
5. Optical SNR in the chi-squared broadband image of no more than 2.

These selection criteria have been utilized in lower redshift ($z = 4.5, 5.7$) searches for Ly α emitters and have detected those emitters at a 70-80% success rate after spectroscopic confirmation, and we are confident that these criteria will translate to higher redshift, as the fundamental physics of the Ly α forest should not change, and similar criteria have been used in a successful spectroscopic search at $z = 6.96$ (see, e.g., Rhoads & Malhotra (2001), Rhoads et al. (2003), Dawson et al. (2004,07), Iye et al. (2006), Wang et al. (2009)). These criteria are also the same as those used in the work of Tilvi et al. (2010). The first three criteria are used to isolate emission line sources. The remaining two are used to eliminate as many low-redshift sources as possible; as detailed in Section 4.1, Ly α emitters should have no flux blueward of their Ly α emission line, and the Ly α line should be narrow enough that it is only detected in one NEWFIRM UNB filter and not both.

Following execution of the selection script, we were left with 65 potential candidates out of 31254 initial detections for the 1.056 μm band, and 110 potential candidates out of 32382 initial detections for the 1.063 μm band. We then matched

our target lists to the existing COSMOS source catalogs (obtained from Peter Capak of the COSMOS team; personal communication). All targets which met our selection criteria but which were also in the COSMOS catalog with a measured photometric redshift were set aside (Section 4.4.1 for further information on these low-redshift interlopers). Once the low- z interlopers were removed, target lists were then narrowed down further through a variety of methods: eliminating all targets on the edges of the chip which lie in or outside the main OH-line ring; eliminating all targets that lie within two arcseconds of the chip gap (5 pixels); eliminating all targets within two arcseconds from a very bright star. Roughly 90% of the initial non-interloper candidates were removed this way. Basic visual inspection was then performed as a sanity check. Our targets were also compared with the yearly stacks for each filter (both via SE and visual inspection) in order to ensure that these targets were not transients (Section 4.4). As a final sanity check, we did not consider any candidates with magnitudes fainter than the limiting magnitudes for each filter (Section 4.2.4).

4.3.2 Results

After all these tests were completed, we were left with a total of 4 candidates brighter than the 50% completeness limit - 3 candidates in 1.056 μm , 1 in 1.063 μm . Three of these candidates lie at the survey line flux limit. The coordinates and basic properties of these four luminous candidates - AB magnitude, line flux, and luminosity - are listed in Table 4.2. Line flux was calculated from the SExtractor

magnitude using:

$$F = 10^{-0.4*(\text{mag}_{\text{AB}}+48.60)} \frac{c}{\lambda^2} W \text{ ergs}^{-1}\text{cm}^{-2}\text{s}^{-1}, \quad (4.1)$$

where mag_{AB} is the magnitude from the isophotal fit as reported by SExtractor, c is the speed of light, λ is the central wavelength of the given filter, and W is the filter width ($6.95 \times 10^{-4} \mu\text{m}$ for the $1.056 \mu\text{m}$ filter, $7.49 \times 10^{-4} \mu\text{m}$ for 1.063). Whereas we used the SE auto fit for initial dual-image mode detection, we use isophotal fit for flux calculation to avoid losing signal and gaining noise. We can also estimate the star formation rates for these objects, assuming that there is little attenuation of the Ly α line by the neutral IGM and that the dust content along the line of sight is low. We use the following prescription from Ota et al. (2010), which uses the Kennicutt law [Kennicutt (1998)] and assumes case B recombination:

$$\text{SFR}(\text{Ly}\alpha) = 9.1 \times 10^{-43} L(\text{Ly}\alpha) M_{\odot} \text{ yr}^{-1}. \quad (4.2)$$

Using this calculation, we find that star formation rates for our four Ly α candidates range from 5 to $7.6 M_{\odot} \text{ yr}^{-1}$. Postage-stamp images of these candidates are shown in Figure 4.3. Note that each candidate is visible in one particular NEWFIRM UNB stamp but is not visible in the other NEWFIRM UNB stamp. Additionally, no candidate is visible either in the chi-squared broadband optical stamp nor the UKIRT J band stamp. As stated in Section 4.3, in order to eliminate most foreground galaxies, it is required that none of the candidates are detected in the broadband image; non-detection in the J band image is simply due to the faint continuum of

the Ly α candidates. As can be seen in Figure 4.3, the PSF is considerably better in the Subaru band stack than in our UNB data. To try to determine whether this could affect our candidate selection, we have attempted a modified aperture correction using a comparison between total SE auto flux in the Subaru field and flux derived from isophotal fits; this correction allows us to account for faint sources in the optical image. Following this correction, we re-ran our selection criteria. Three of our four high- z Ly α candidates still passed the selection criteria, but candidate #3 failed selection following this aperture correction (optical SNR > 2). We still include candidate #3 in the following analysis but flag it in Table 4.2 as more uncertain than the other candidates.

4.3.3 Ly α Equivalent Widths

As we have a sample of four strong candidate Ly α emitters, it is worthwhile to compare the equivalent widths (EWs) of their Ly α emission lines to those already noted in the literature. Several published studies have spectroscopically identified Ly α emitters with rest-frame equivalent widths of $\text{EW}_{\text{rest}} > 240\text{\AA}$ at $z = 4.5$ and 5.7, significantly higher than predicted by theoretical simulations of star-forming galaxies [Malhotra & Rhoads (2002), Shimasaku et al. (2006), Dawson et al. (2007), Gronwall et al. (2007), Ouchi et al. (2008)].

The calculation for rest-frame EW for our Ly α emitters makes use of the fluxes measured in both the NEWFIRM UNB filters and the broadband UKIRT J data, as the Ly α line does not appear in the J band (again, the J band data is centered

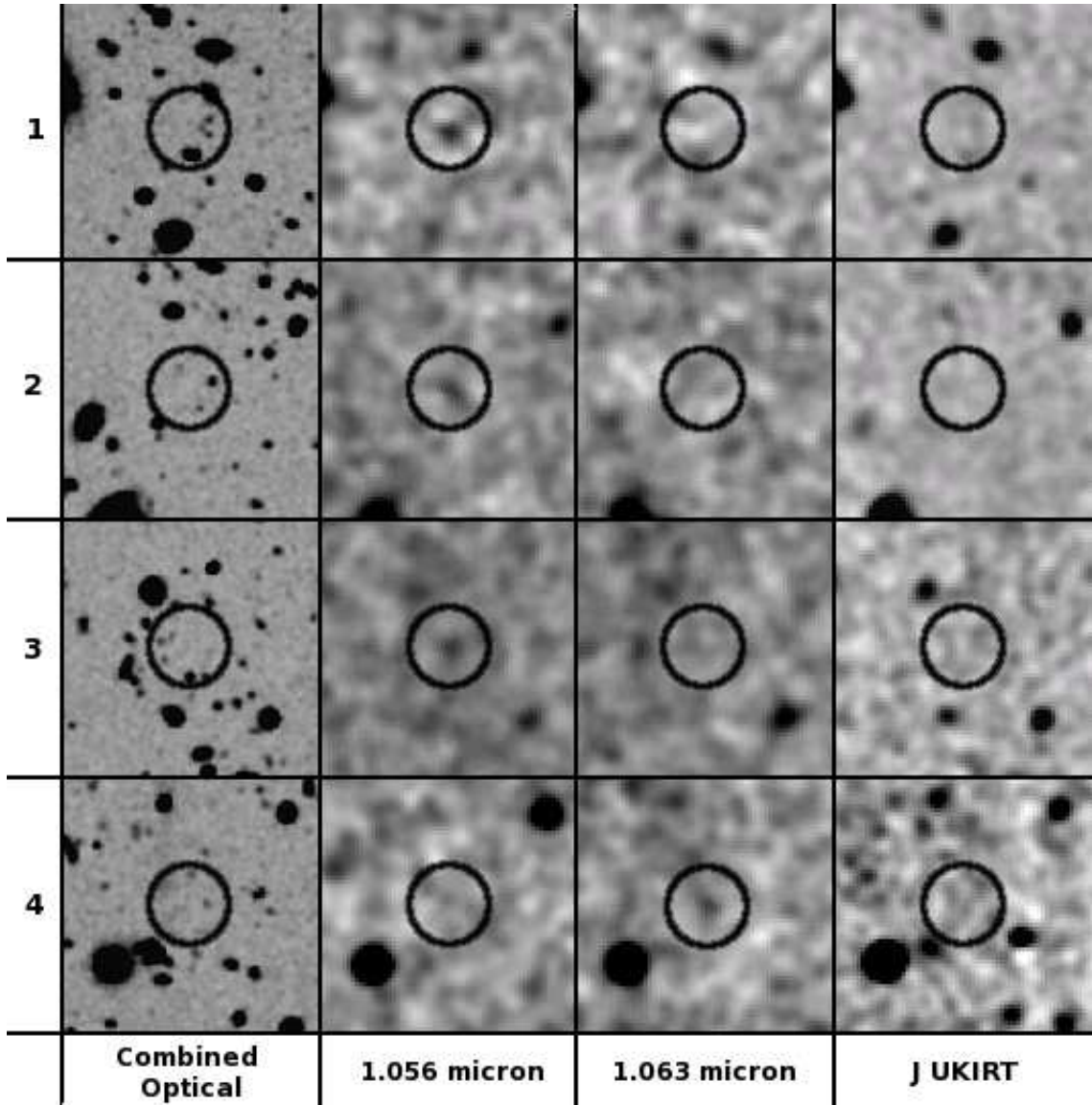


Figure 4.3: Image cutouts for our four Ly α emitter candidates. UNB cutout images have been Gaussian smoothed according to the average seeing of the 1.056 and 1.063 μm data. Cutouts are 50'' on each side, and the circles are 16'' in diameter (corresponding to ~ 400 kpc at $z = 7.7$). Each row represents one candidate. The optical column shows a weighted chi-squared combination of B , r , and i band images from Subaru. The middle two columns show our UNB NEWFIRM data. The J band column represents data from UKIRT. Candidates #1-3 are detected in 1.056 μm but not in any other band; candidate #4 is only detected in 1.063 μm . All other objects present only in one UNB band are either transients (detected in only one yearly UNB stack) or fail to meet the Ly α selection criteria.

at $1.2\mu\text{m}$, with no overlap with our UNB filters). However, none of our candidates were detected in the J band, and thus we must use the J band limiting magnitude (Section 4.2.4) to calculate an upper limit on J band flux. In this case, given the limiting magnitude of 24.0 in the UKIRT J band, the upper limit on the J band continuum flux $f_{\lambda,J} = 1.9 \times 10^{-19} \text{ erg s}^{-1} \text{ cm}^{-2} \text{ \AA}^{-1}$. This value is used to calculate a lower limit on the rest-frame Ly α EW for our candidates:

$$\text{EW}_{\text{rest}} = \frac{f_{\text{UNB}}}{f_{\lambda,J}} \times \frac{1}{1+z}, \quad (4.3)$$

where f_{UNB} is the UNB line flux in $\text{erg s}^{-1} \text{ cm}^{-2}$. This calculation assumes that the Ly α line falls entirely within the transmission profile of our UNB filters. In reality, the UNB filters may not enclose all of the Ly α emission. Moreover, we are using upper limits on the J band fluxes. The EWs measured in this way should thus be viewed as $1\text{-}\sigma$ lower limits. This calculation also assumes an exact redshift of $z = 7.7$.

The resultant lower limits on the rest-frame EW (Ly α) are 7.32, 5.17, 4.89, and 4.84 \AA for candidates 1-4, respectively. Thus our lower limit on EW for our candidates is $\text{EW}_{\text{rest}} > \sim 4.8 \text{ \AA}$, much more consistent with theoretical predictions than the numbers quoted above for lower redshift surveys. Our lower limit EW is smaller than that of Hibon et al. (2010) by several angstroms, primarily owing to the difference in bandwidths of UNB filters used by these two surveys. This line width is also larger by $\sim 2 \text{ \AA}$ than the results of the Tilvi et al. (2010) survey,

although this difference can be accounted for by the increase in depth of our J band data (limiting magnitude of 24.0 for our data versus 23.5 for their data). As future surveys obtain deeper J band data, we should be able to better constrain the lower limits of Ly α EWs for these emitters.

4.4 POSSIBLE SAMPLE CONTAMINATION

There are several possible sources of contamination in our sample of candidate Ly α emitters. These include such real sources as foreground emitters, transients, and cool L & T dwarfs, as well as false sources such as detector noise spikes and general false detections. We discuss each class of contaminants below.

4.4.1 Foreground Emission Line Sources

There are three main species of foreground emission line objects which are most likely to contaminate our sample, as each species should have a strong emission line that falls within our UNB filter window and, assuming faint continuum emission, negligible flux in nearby blue- and redward bands. These species are H α λ 6563 emitters at $z = 0.62$, [OIII] λ 5007 emitters at $z = 1.12$, and [OII] λ 3727 emitters at $z = 1.85$. Given the extensive amount of ancillary data available for the COSMOS field, we were able to first check our catalog with the main COSMOS catalog and eliminate any low- z interlopers from our Ly α candidate list, as mentioned in Section 4.3. A total of 3 interlopers fulfilled the five main Ly α emitter selection criteria (Section 4.3), all in the 1.063 μ m filter – one brighter than the

limiting magnitude of the field – which were removed from the sample of Ly α candidates. These faint objects, however, are not at the exact redshifts listed above: the COSMOS photometric redshifts are $z \sim 1.5 \pm 0.2$ (1σ ; possibly corresponding to redshifted H γ), $z \sim 1.7 \pm 0.2$ (possibly [OII] $\lambda 3727$), $z \sim 2.5 \pm 0.2$ (possibly broad Mg II $\lambda 2798$), but the errors may be even larger. It is possible that there remain some foreground emission line objects in our Ly α candidate sample that do not have tabulated photometric redshifts. Our survey benefits greatly from the multi-wavelength coverage and accurate photometric redshifts of the COSMOS data catalog; the presence in our sample of interlopers with photo- z s different from the three expected species listed above may imply that surveys in other fields without such comprehensive ancillary data coverage suffer from greater low- z contamination than estimated.

To estimate the number of additional possible emission line source interlopers that could remain among our candidates, we must estimate the minimum equivalent width required for these emission lines to contaminate our sample. We must also use the depth of our UNB image in order to calculate the minimum luminosities of these emission lines. As described in Section 4.2.4, the limiting magnitude of our 1.056 μm stack is 22.4, which is equivalent to a 50% completeness limit in flux of 7.4×10^{-18} erg s $^{-1}$ cm $^{-2}$. Given the redshifts of the aforementioned emission lines and using *CosmoCalc*³ to calculate luminosity distances, we find that the minimum luminosities required to detect these emitters are 1.15×10^{40} erg s $^{-1}$, 4.96×10^{40} erg s $^{-1}$, and 1.72×10^{41} erg s $^{-1}$ for H α , [OIII], and [OII] respectively. To calculate

³<http://www.astro.ucla.edu/~wright/CosmoCalc.html>

the necessary minimum equivalent width (observer-frame), we use the prescription from Rhoads & Malhotra (2001):

$$\text{EW}_{\min} \equiv \left[\frac{f_{\text{nb}}}{f_{\text{bb}}} - 1 \right] \Delta\lambda_{\text{nb}} = \left[\frac{5\sigma_{\text{nb}}}{2\sigma_{\text{bb}}} - 1 \right] \Delta\lambda_{\text{nb}}, \quad (4.4)$$

where f_{nb} and f_{bb} refer to the flux densities of the UNB and the chi-squared optical image, respectively, σ_{nb} and σ_{bb} refer to the flux measurement uncertainties in the two frames, and $\Delta\lambda_{\text{nb}}$ is the width of the UNB filter. For these calculations, we have simply used the 1.056 μm UNB filter. It is safe to assume that the continuum contribution to the overall flux in the UNB filter is negligible, since the overall width (effective FWHM) of the transmission profile of the 1.056 μm filter is only 9 \AA (6.95 \AA). For our filters, $\sigma_{\text{nb}} = 1.06 \times 10^{-29} \text{ erg cm}^{-2} \text{ s}^{-1} \text{ Hz}^{-1}$ and $\sigma_{\text{bb}} = 2.1 \times 10^{-31} \text{ erg cm}^{-2} \text{ s}^{-1} \text{ Hz}^{-1}$. This results in a minimum equivalent width for the foreground emission line contaminants of $\text{EW}_{\min} > \sim 870 \text{\AA}$.

Although the distribution of equivalent widths of these three species of emitters has not been probed at the high redshifts of our observations, we can scale the published results under the assumption that the luminosity functions of these species have not evolved significantly between the relevant redshifts. One particular recent study has probed emission line sources of $\text{H}\alpha$ at $z = 0.27$, $[\text{OIII}]$ at $z = 0.51$, and $[\text{OII}]$ at $z = 1.0$ in the GOODS-South field [Straughn et al. (2009)]. The minimum EW calculated above was scaled appropriately in each instance to the EW one would expect at the redshifts probed by the Straughn et al. (2009) survey. Using

that value and the required minimum luminosity listed above, we determined how many emission line objects we should expect in our field, after scaling appropriately by the ratio of survey volumes. We find that we expect fewer than one additional interloper for each species (0.1 each for $H\alpha$ and [OII], 0.3 for [OIII]). If we relax the minimum equivalent width criterion to 500 \AA prior to scaling EWs to what would be expected at $z = 7.7$, the expectation increases to 1 additional interloper each for $H\alpha$ and [OII], and 2 additional interlopers for [OIII].

4.4.2 Other Possible Contaminants

The utilization of individual yearly stacks, as well as nightly stacks, which were produced by the data reduction pipeline, allowed us to eliminate both possible detections due to noise spikes as well as real sources such as transient objects. We required during our candidate selection process that potential candidate $Ly\alpha$ emitters be detected in all stacks as well as the overall stack, though the detection requirements for individual nightly/yearly stacks were less stringent. This eliminates contamination by noise spikes from the detector, as such noise spikes should not be present at the same coordinates across multiple nights over a span of years. Transients will also be eliminated by this yearly stack check, as supernovae should only be visible for a few weeks, not years. We were able to eliminate upward of twenty contaminants via this requirement.

In order to determine whether any false detections were contaminating our candidate list, we checked to see whether taking the negative of our UNB stacks

would result in a detection. We used IRAF to multiply each UNB stack by -1 and then ran SExtractor on the resultant negative images. The SE negative stack catalogs were then run through the exact same selection process as the positive stack catalogs, but no candidates were identified this way. We are thus confident that the probability of false detections contaminating our Ly α sample is insignificant.

The final source of potential contaminants consists of cool stars - namely, L and T dwarfs - passing our selection process. We use previously observed relationships between spectral type and absolute magnitude [Tinney et al. (2003)] to determine in what J band magnitude range L and T dwarfs fall, and then we use our calculated J band limiting magnitude to determine distance ranges at which we should be able to see these objects. We find that L dwarfs could be detected between roughly 550 and 1700 pc, and T dwarfs could be detected between roughly 200 and 750 pc. These L and T dwarfs are most likely found within a Galactic disk scale height of 350 pc, however [Ryan et al. (2005)] – the number density drops significantly above the scale height of the disk – and thus knowing that these dwarfs typically have a volume density of no more than $\sim 3 \times 10^{-3} \text{ pc}^{-3}$, we thus can conclude that we should expect at most one L or T dwarf in our survey. If we then take our selection criteria into account, we can determine if any L and T dwarfs would satisfy our narrowband excess criterion. Tilvi et al. (2010) used existing observed spectra of L and T dwarfs and a calculation of expected flux through our NEWFIRM filters. They determined that the flux which would be transmitted through the NEWFIRM UNB filters, in comparison to that which would be transmitted through the NEWFIRM J filter, would not be sufficient to pass our narrowband excess criterion. Thus, we should

expect that no L nor T dwarfs would pass our selection criteria and contaminate our sample.

4.5 MONTE CARLO SIMULATIONS

As discussed in Section 4.4, we do not expect all of our four candidate Ly α emitters to be real, as it is possible that further low- z emission line source interlopers may pass our selection criteria. In order to determine how many of our Ly α candidates we should expect to be real, we run Monte Carlo statistical simulations using previously known Ly α luminosity functions at lower redshift. In this work, we make use of the Kashikawa et al. (2006) Ly α luminosity function at $z = 6.5$ and assume that there has been no significant evolution between $z = 6.5$ and $z = 7.7$. These simulations also make use of the fact that the NEWFIRM UNB filter transmission curves may not encompass the full width of the expected Ly α emission lines in these objects, and thus our measurements may in fact be underestimating the Ly α line flux produced by our Ly α candidates. The transmission curves of our two UNB filters were obtained from the NEWFIRM website^{4,5}.

To begin our Monte Carlo simulations, we utilized the aforementioned Kashikawa et al. (2006) luminosity function to generate one million random galaxies. These galaxies were distributed with both a random Ly α luminosity in the range of 10^{42} erg s⁻¹ to 1.5×10^{43} erg s⁻¹, as well as a random redshift in the range probed by our filters. In the case of the 1.056 μ m band, this range is $7.66 < z < 7.71$; for the

⁴<http://www.noao.edu/ets/newfirm/documents/1056%20nm%20data%20pack.xls>

⁵<http://www.noao.edu/ets/newfirm/documents/1063%20nm%20data%20pack.xls>

1.063 μm band, this range is $7.72 < z < 7.76$; we chose these ranges to correspond to the full width of the transmission profile at which the transmission falls to 5%.

From these luminosities and redshifts, we were then able to assign a flux to each of our randomly generated galaxies. We made use of an asymmetric Ly α line flux profile based on spectra of $z = 5.7$ Ly α emitters taken by Rhoads et al. (2003). We were able to then use the detailed NEWFIRM UNB filter transmission curve profiles to derive the flux that would pass through the filter via a convolution of filter profile and line flux according to $f_{\text{trans}} = \int f_{\lambda} T_{\lambda} d\lambda$, where T_{λ} is the NEWFIRM UNB filter transmission curve and f_{λ} is the flux density of the emission line based on the Rhoads et al. (2003) spectra. This takes the likely underestimation of Ly α line flux into account. Following this, we were able to convert the convolved line flux into a magnitude by the use of the formula:

$$\text{mag}_{\text{AB}} = -2.5 \log_{10} \left(\frac{f_{\text{trans}}}{f_0} \right), \quad (4.5)$$

where

$$f_0 = \frac{3.6 \text{kJy} \times c}{(1.06 \mu\text{m})^2} \times \int T_{\lambda} d\lambda \text{ ergs}^{-1} \text{cm}^{-2}, \quad (4.6)$$

and c is the speed of light. In order to ensure that all instrumental effects were taken into account, the last step in this process was to incorporate the detection fraction at each magnitude bin (Section 4.2.4; Figure 4.2). This detection fraction was

multiplied by the number of galaxies in each magnitude bin before we converted those magnitudes to Ly α luminosities. The number of detected galaxies in each Ly α luminosity bin was then used to estimate how many Ly α emitters we should expect from our survey.

This Monte Carlo simulation was run for each individual NEWFIRM UNB filter and then iterated 10 times for each filter. We then averaged the results of those ten iterations, and the expected number of sources per filter at each magnitude bin is shown in Figure 4.4. Looking at the limiting magnitudes for each filter and integrating out to that point, we find that we expect ~ 1 source per filter to be a true $z = 7.7$ Ly α emitter. This result should be viewed with some caution, however, as we have assumed that the Ly α luminosity function does not undergo significant evolution between redshifts of 6.5 and 7.7, and that the emission line profiles of all Ly α emitters at $z = 7.7$ are the same as that of a Ly α emission line profile at $z = 5.7$. Moreover, this simulation makes use of the Kashikawa et al. (2006) luminosity function, which is based upon detections in only one field, the Subaru Deep Field. We expect that there will be field-to-field variations among Ly α emitters, and thus the expected number of sources may be different for the COSMOS field. Various methods can be taken to estimate the cosmic variance between fields of these Ly α emitters; for large survey volumes ($\sim 2 \times 10^5 \text{ Mpc}^3$), Tilvi et al. (2009) estimated this variance to be $> \sim 30\%$. We can also utilize the method of Trenti & Stiavelli (2008) to calculate the cosmic variance expected assuming 2 intrinsic Ly α sources as reported by our Monte Carlo simulations. Using the redshift interval of 0.1 for our two filters and

a Press-Schechter bias, the Trenti & Stiavelli cosmic variance calculator⁶ returns an expected cosmic variance of $\sim 58\%$ (this number drops by $\sim 10\%$ with Sheth-Tormen bias). In addition to cosmic variance, we note here that the most recent $z=5.7$ and 6.5 Ly α LF results [Hu et al. (2010), Ouchi et al. (2010), Kashikawa et al. (2011)] indicate that the predictions for the number densities of $z=7.7$ emitters based on the results of Kashikawa et al. (2006) may be up to a factor of 3 too large. The uncertainty that remains in the lower- z Ly α LFs, taken in concert with the significant role that cosmic variance can play, requires the Monte Carlo simulations to be viewed with caution rather than interpreted at face value.

4.6 $z = 7.7$ Ly α LUMINOSITY FUNCTION

The primary goal of this work is to constrain the observed luminosity function (LF) of Ly α emitters at $z = 7.7$. As described in the Introduction, our survey has the advantage of being both wide and deep, leading to our volume and limiting flux being better than or comparable to most other surveys at this redshift or higher (Table 4.1). To construct our $z = 7.7$ Ly α LF, we have used our four targets, which have Ly α line fluxes of 12.1, 8.6, 8.1, and 8.0×10^{-18} erg s $^{-1}$ cm $^{-2}$, all higher than our survey's limiting flux of 8×10^{-18} erg s $^{-1}$ cm $^{-2}$. Using our survey volume of $\sim 1.4 \times 10^4$ Mpc 3 per filter, we have constructed a cumulative Ly α LF which is shown in Figure 4.5. In order to calculate the errors, we have used Poissonian statistics with Bayesian likelihood (where the likelihood is equivalent to the probability), assuming

⁶<http://casa.colorado.edu/~trenti/CosmicVariance.html>

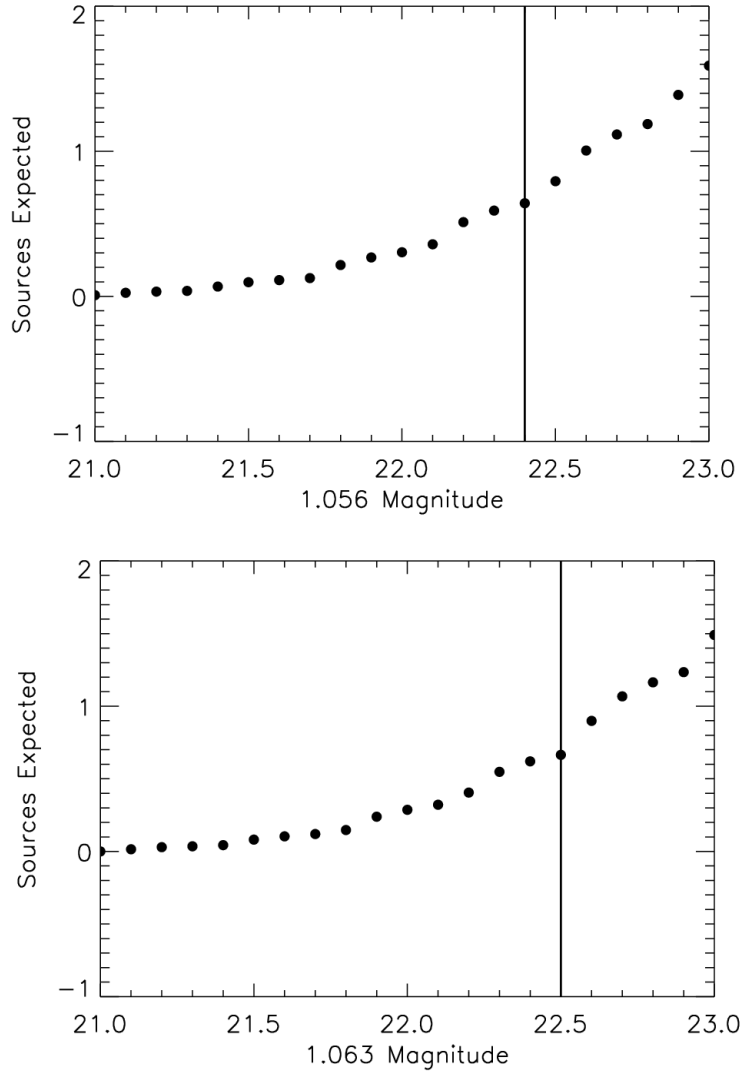


Figure 4.4: Average results of the ten Monte Carlo simulation iterations, showing the number of $\text{Ly}\alpha$ emitter sources we should expect at each magnitude bin. Integrating out to our limiting magnitudes for each field (Section 4.2.4), indicated by the vertical line, we expect roughly 1 source per filter to be a real $z = 7.7$ $\text{Ly}\alpha$ emitter if there is no evolution in the luminosity function between $z = 6.5$ and $z = 7.7$. Top: $1.056 \mu\text{m}$ band. Bottom: $1.063 \mu\text{m}$ band.

each target is in a separate luminosity bin. The assumption in this error model is that the luminosity distribution is uncorrelated - one galaxy having a certain luminosity has no effect on the luminosity of another - and thus it is safe to divide our luminosity bins this finely. As we have a prior probability distribution that is uniform in the expected number m (from Poisson), then the lower and upper limits on our errors are both finite. We have plotted our LF along with the results of several other major surveys. Two of these, Tilvi et al. (2010) and Hibon et al. (2010), focus on the same redshift as our work but have made use of alternate fields (CETUS and CFHT-LS D1, respectively) and thus cosmic variance may come into play. Neither survey has published spectroscopic confirmation at this time, although Clément et al. (2011) note that VLT spectroscopy failed to detect Ly α emission from the five most luminous Hibon et al. (2010) candidates, a result which will be published soon; we plot the Clément et al. (2011) upper limits for $z = 7.7$ Ly α LFs as well. We also plot the spectroscopically confirmed Iye et al. (2006) $z = 6.96$ Ly α emitter. In addition to individual data points, we also plot three curves from previous, slightly lower redshift surveys, which are based on best-fit functions to spectroscopically confirmed data. These include the Ouchi et al. (2008) $z = 5.7$ LF, as well as the well-cited Kashikawa et al. (2006) $z = 6.5$ LF data. We have also included a new data set, the $z = 6.6$ LF from Ouchi et al. (2010), which samples a different field from the Kashikawa $z = 6.5$ LF but agrees well with that data set.

Our data points agree quite well with the findings of Tilvi et al. (2010), despite our surveys probing different fields, but only the most luminous target matches with the Clément et al. (2011) upper limits for $z = 7.7$ within the error; our

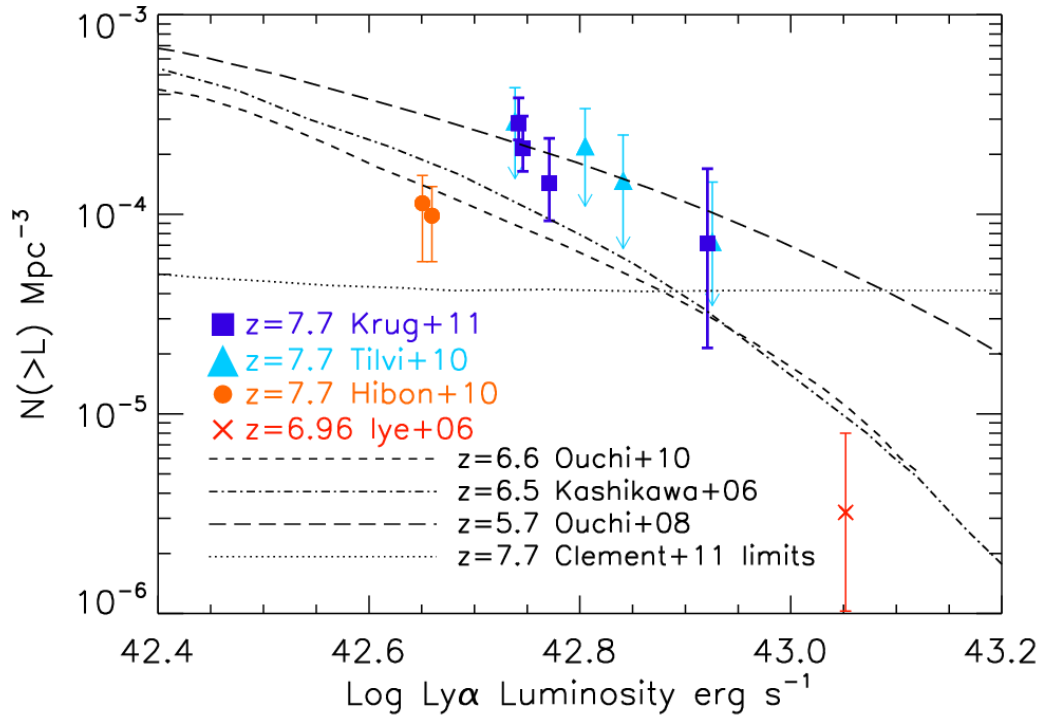


Figure 4.5: Ly α luminosity function compiled from data from this work (dark blue squares) and those previously published. Errors are calculated using Poissonian statistics with Bayesian likelihood. The light blue triangles [Tilvi et al. (2010)] and orange circles [Hibon et al. (2010)] represent candidates at $z=7.7$ that have not been spectroscopically confirmed. Recent follow-up spectroscopy by Cl  ment et al. (2011) did not detect Ly α emission from the five most luminous candidates of Hibon et al. (2010), so we have excluded these objects from the present figure. The black dotted curve represents upper limits on the $z=7.7$ luminosity function from Cl  ment et al. (2011). The red X [Iye et al. (2006)] represents a spectroscopically confirmed $z=6.96$ Ly α emitter. The three black dashed and dashed-dotted curves represent best fit luminosity functions to spectroscopically confirmed Ly α emitters at redshifts $z=5.7 - 6.6$. Note that our Ly α luminosity function agrees well with that of Tilvi et al. (2011). Our two most luminous candidates are consistent within the error with either the $z=5.7$ or $z=6.5$ luminosity function, and thus we do not see any evidence for significant evolution of the Ly α luminosity function or neutral hydrogen fraction of the IGM between $z=5.7$ and $z=7.7$.

data points also may seem inconsistent with recent Lyman break surveys (e.g., [Pentericci et al. (2011), Schenker et al. (2012)]). Assuming that all four of our data points are real Ly α emitters at $z = 7.7$, we find good agreement with the $z = 5.7$ Ouchi et al. (2008) function, yet our fainter luminosity objects do not agree with the $z = 6.5$ LF [Kashikawa et al. (2006)] nor the $z = 6.6$ LF [Ouchi et al. (2010)]. This could imply moderate evolution between $z = 7.7$ and $z = 6.6$, yet it is interesting that in such a case, the LFs at $z = 7.7$ and $z = 5.7$ would be in agreement. If we instead take the more conservative approach indicated by our Monte Carlo simulation results and assume only the two most luminous of our targets to be real Ly α emitters, then our results are consistent within error with both the $z = 5.7$ Ouchi et al. (2008) function and the $z = 6.5$ Kashikawa et al. (2006) function. Given that it is more probable statistically that only these two candidates are real, we must take this case as the more likely outcome until we have the ability to spectroscopically verify our sources. Thus, given the agreement of our two most luminous emitters with the LFs at both lower redshifts, there is no conclusive evidence for evolution of the Ly α LF over the redshift range $5.7 < z < 7.7$.

4.7 SUMMARY

We have utilized two custom-made UNB filters, at wavelengths 1.056 and 1.063 μm (FWHM 7.4 and 8.1 \AA , respectively) on the NEWFIRM camera at the KPNO 4m Mayall telescope to perform a deep and wide search for $z = 7.7$ Ly α emitters in the COSMOS field. Our study comprised a co-moving volume of $2.8 \times 10^4 \text{ Mpc}^3$

(survey area ~ 760 arcmin²) and probed down to a limiting flux of $\sim 8 \times 10^{-18}$ erg s⁻¹ cm⁻² (50% completeness limit), which is comparable to or better than previous Ly α searches at similar redshifts.

We used a very detailed selection procedure, making use of five different quantitative parameters as well as qualitative methods to ensure narrow-line detection and elimination of contaminants (including 3 low- z interlopers already known in the COSMOS catalog). We were left with a total of four candidates (three detected in the 1.056 μ m filter, one in the 1.063 μ m filter), each detected at 5 sigmas or higher, down to line fluxes of 8×10^{-18} erg s⁻¹ cm⁻². Detailed Monte Carlo simulations would suggest that up to two of these candidates are real. If we assume only two real candidates, comparison of the resultant Ly α LF to the $z = 5.7$ Ouchi et al. (2008) and $z = 6.5$ Kashikawa et al. (2006) Ly α LFs would indicate that there has been no significant evolution of the Ly α LF between $5.7 < z < 7.7$. This result is consistent with the findings of Tilvi et al. (2010) – that work used the same instrument, equivalent field of view, reached similar flux limits, but was half the volume of our work, owing to our extra filter.

To pin down the neutral hydrogen fraction at $z = 7.7$ and thus the stage of the reionization process at that epoch, we will need more detailed Ly α LFs in order to accurately determine the characteristic luminosity, L^* , of these objects. This will require a) spectroscopic confirmations of these candidate high-redshift Ly α emitters, and b) surveys encompassing more fields, as cosmic variance is likely to affect the number of emitters found in each region. The success of previous narrowband surveys at identifying Ly α emitters at lower redshift and the robustness of our current

set of candidates mean that the future of such high- z studies is quite promising. It is also encouraging to note that our results match well with surveys in different fields. The pursuit of surveys such as these, along with the advances that should be brought to the field by JWST and other new instruments, should provide a bright future for the study of the Dark Ages.

Table 4.1: Comparison to previous high- z searches.

| z (1) | Survey Vol. (Mpc ³) (2) | Detec. Limits (erg s ⁻¹ cm ⁻²) (3) | # of LAE Detec. (4) | Refs (5) |
|------------|--|--|------------------------|-------------|
| 7.7 | 6.3×10^4 | 8.3×10^{-18} | 7 | Hibon+ 2010 |
| 7.7 | 1.4×10^4 | 7×10^{-18} | 4 | Tilvi+ 2010 |
| 7.7 | 2.8×10^4 | 8×10^{-18} | 4 | This work |
| 8-10 | 35 | 2×10^{-17} | 6 | Stark+2007 |
| 8.8 | 6.3×10^4 | 1.3×10^{-17} | 0 | Cuby+2007 |
| 8.96 | 1.12×10^6 | 6×10^{-17} | 0 | Sobral+2009 |

Col.(1): Ly α redshift probed. Col.(2): Survey volume. The volume of our study is 2x deeper than Tilvi et al. 2010 owing to our use of a second filter for candidate selection (each filter probes a volume of 1.4×10^4 Mpc³). Col.(3): Survey flux detection limit. Col.(4): Number of candidate Ly α emitters detected. Col.(5): Survey reference.

Table 4.2: Properties of four candidate Ly α emitters.

| Cand. # (1) | RA (2) | Dec (3) | Mag _(AB) (4) | Line Flux (erg s ⁻¹ cm ⁻²) (5) | L _{Lyα} (erg s ⁻¹) (6) | EW _{Lyα} (Å) (7) |
|------------------|-------------|--------------|----------------------------|--|--|--|
| 1 | 10:00:46.94 | +02:08:48.84 | 21.87 | 1.21×10^{-17} | 8.34×10^{42} | 7.32 |
| 2 | 10:00:20.52 | +02:18:50.04 | 22.25 | 8.55×10^{-18} | 5.90×10^{42} | 5.17 |
| 3 ^(a) | 09:59:56.21 | +02:10:09.84 | 22.31 | 8.09×10^{-18} | 5.58×10^{42} | 4.89 |
| 4 | 10:00:48.79 | +02:09:21.24 | 22.39 | 8.00×10^{-18} | 5.52×10^{42} | 4.84 |

(a) Candidate #3 fails the optical selection criterion following an aperture correction of the Subaru data; it is thus considered more uncertain than the others. Col.(2): RA in J2000. Col.(3): Dec in J2000. Col.(4): AB magnitude, calculated using isophotal flux in SExtractor. Col.(5): Line flux, in the 1.056 μ m band for candidates 1-3 and in the 1.063 μ m band for candidate 4. Col.(6): Ly α luminosity, calculated assuming a redshift of $z=7.7$. Col.(7): Lower limit rest-frame equivalent width of Ly α emission, calculated as described in Section 4.3.3 equivalent widths.

Chapter 5

$z=7.7$ Ly α Emitter Candidates: Imaging and Spectroscopic

Follow-up

5.1 INTRODUCTION

The Ly α luminosity function (and thus the UV luminosity function) at redshifts greater than 6.5, as described in Chapter 4, remains highly uncertain since the publication of our paper [Krug et al. (2012)], as not enough Ly α nor Lyman-break galaxies have been spectroscopically confirmed at high-redshift. The discovery of significant numbers of $z \sim > 8$ Ly α emitter and Lyman-break candidates has continued, allowing some constraints to be put on luminosity functions (e.g., Bowler et al. (2012), Bradley et al. (2012), Oesch et al. (2012,13), Lorenzoni et al. (2013), Tilvi et al. (2013)), but the highest-redshift Ly α emitter that has been spectroscopically confirmed so far is at $z = 7.2$ [Shibuya et al. (2012)] (see Section 5.4 for further discussion on this topic). Numerical simulations are also being performed, based on new data from those galaxies at $z \sim 6 - 7$ which have been spectroscopically confirmed, to attempt to make predictions regarding reionization and attenuation of Ly α emission at high-redshift (e.g., Jensen et al. (2012,13), Treu et al. (2012), Bolton & Haehnelt (2013)); these simulations seem to agree that, based on current data, reionization of the universe was still underway at $z \sim 6$. The paucity of spec-

troscopic confirmations at $z \sim 8$ and higher, in addition to results of simulations, would imply that the IGM was significantly more opaque at $z \sim 8$ than $z \leq 7$ [Hu et al. (2010), Schenker et al. (2012), Ono et al. (2011), Clément et al. (2012), Shibuya et al. (2012), Treu et al. (2012), Bolton & Haehnelt (2013)]. In order to help make constraints on these results, we must attempt to confirm, via a combination of imaging and spectroscopy, our four LAE candidates [Krug et al. (2012)].

The $z = 7.7$ Ly α emitter search which we began in Chapter 4 depends on three main components. The first is the careful selection of Ly α emitter candidates from a very deep near-IR imaging survey in the COSMOS field with NEWFIRM, covered in Chapter 4 and published in Krug et al. (2012). The second is the use of deep optical and infrared broadband images, obtained from the publicly available COSMOS data archive and other sources, to eliminate foreground emission line galaxies at $z \lesssim 2$ and to potentially detect the continuum of $z = 7.7$ Ly α sources. This was partially undergone in Chapter 4, but more imaging follow-up will be described in this chapter. The third is spectroscopic follow-up to confirm the presence of emission lines (at $1.06 \mu\text{m}$, as well as additional lines in the wavelength range), measure equivalent widths, and look for the characteristic red asymmetry that distinguishes high- z Ly α lines. The attempt to obtain spectroscopic confirmation of these targets will be detailed in this chapter.

The organization of this chapter is as follows. In Section 5.2, we detail three separate attempts to follow-up our data via broadband imaging, using *HST* ACS, CFHT, and UltraVISTA data. In Section 5.3, we describe our attempt to confirm our $z = 7.7$ Ly α emitter candidates via spectroscopy on Gemini-N using GNIRS, as well

as via two other instruments in studies led by our collaborators. In Section 5.4, we discuss the implications of our follow-up endeavors, and in Section 5.5, we summarize our results. As in Chapter 4, we assume a standard flat Λ CDM cosmology with $\Omega_m = 0.3$, $\Omega_\Lambda = 0.7$, and $h = 0.71$, where Ω_m , Ω_Λ , and h are the matter density, dark energy density, and Hubble parameter (in units of $100 \text{ km s}^{-1} \text{ Mpc}^{-1}$), respectively.

5.2 IMAGING FOLLOW-UP

Three major broadband imaging data sets were made available to us after the publication of our paper (Chapter 4, Krug et al. (2012)), which we analyzed to determine if any of our candidates were present. As detailed in Chapter 4, should any of our candidates be detected in optical bands, that would immediately rule them out as $z = 7.7 \text{ Ly}\alpha$ emitters. Should any of our candidates be detected in an infrared band, including $1.06 \mu\text{m}$ or longer wavelengths, then that could potentially be a detection of the continuum of these targets and would further reinforce our claim that these candidates are actual galaxies and not artifacts nor noise spikes.

5.2.1 *Hubble* ACS *I*-Band Data

The Cosmic Assembly Near-Infrared Deep Extragalactic Legacy Survey, CANDELS¹, P.I. Sandra Faber, is a *Hubble Space Telescope* treasury project, using WFC3 and ACS on Hubble in order to do deep probes of the GOODS-S, GOODS-N, UDS, EGS, and COSMOS fields. While COSMOS is not the deepest of the fields being

¹<http://candels.ucolick.org/>

probed, the data provided by the CANDELS team are of great use to us in terms of attempting to follow-up our high-redshift candidates. We used the *HST* ACS *I*-band (F814W filter) mosaic, released publicly in summer 2012 but made available to us in January 2012 via the COSMOS team servers [Koekemoer et al. (2007), Massey et al. (2010)]. This data set has a depth of 25.94 in AB magnitudes, comparable to broadband data used in Chapter 4. Tentatively, we find that candidate #3 (see Table 4.2 in the previous chapter) is detected in the CANDELS ACS *I*-band mosaic, with a signal-to-noise ratio of 2.69. We say tentatively, as the ACS signal-to-noise ratio is high enough that this candidate fails our optical $\text{SNR} < 2$ criterion (Section 4.3), but the signal-to-noise is too low to be considered an actual optical detection. This candidate, however, also failed the optical selection criterion following aperture correction of Subaru data, as detailed in Section 4.3.2, and thus it may be likely that candidate #3 is not a $z = 7.7$ Ly α -emitter, as there should be no flux blueward of Ly α . This implies that this target is likely a low- z H α , [O III], H β , or [Mg II] emitter (see Section 5.3.1 for details).

5.2.2 CFHT *H*-Band Data

The COSMOS survey team performed imaging studies in *H*-band ($1.631 \mu\text{m}$) on CFHT in 2007 and 2009, which were made public on the COSMOS servers after our paper went to press [McCracken et al. (2010)]. The CFHT *H*-band mosaic has a depth of 30.09 AB magnitudes, substantially deeper than any of the data used in our published paper [Krug et al. (2012)]. Of our 4 candidates, only one (#4)

was detected in CFHT, with a moderate SNR of 2.06. This value is far too low to consider it an actual detection, as we have used a SNR cutoff of 5 in our detection criteria, but it is promising; this signal could possibly be the faint continuum of a $z = 7.7$ LAE. The remaining three candidates were not detected at all in the CFHT imaging data.

5.2.3 UltraVISTA Y -, J -, H -, and K -Band Data

The Ultra Deep Survey with the VISTA Telescope, UltraVISTA², is a near-infrared survey under the aegis of ESO which will be imaging the COSMOS field in five different bands over the course of five years. We were given early access to the initial data set prior to public release by Peter Capak, thanks to our collaboration with the COSMOS team [McCracken et al. (2012)]. We analyzed the Y -, J -, H -, and K -band data, with central wavelengths of 1.02, 1.25, 1.64, and 2.12 μm , respectively. The depths of the data in the respective bands were 30.75, 30.55, 30.03, and 29.57 AB magnitudes, determined from 2MASS comparison and extrapolation. These data are again significantly deeper than any of the broadband data sets used in Chapter 4. Detection in any of these bands would likely be due to the continuum of our targets, although the Y -band, which encompasses 1.06 μm , could likely include $\text{Ly}\alpha$ line flux as well as continuum. Candidate #4 had a moderate detection in the Y -band, with a SNR of just under 3. Very faint fluxes were measured for candidate #1 in the H -band (SNR 1.33) and candidate #4 in the K band (SNR 1.46), but these SNRs were so low that we cannot consider them real at this time. All other

²<http://ultravista.org/>

candidates had non-detections in every band.

5.3 SPECTROSCOPIC FOLLOW-UP

While imaging is useful for selection of candidates and can be helpful either for verification that a target is not an artifact or to rule out a target as being a $z = 7.7$ LAE, the only true way to verify that our candidates are indeed $z = 7.7$ Ly α emitters is to obtain a spectrum for each target and prove that spectroscopically (e.g., Iye et al. (2006)). We obtained time on Gemini to perform spectroscopic follow-up of our candidates, and the results are detailed here.

5.3.1 Gemini GNIRS Spectroscopy

We were awarded one night on the Gemini-North telescope in March 2012 to observe our two highest priority targets (candidates #1 and #2 from Table 4.2) with the GNIRS instrument. GNIRS is a near-infrared spectrograph built to be used on the Gemini telescopes. It is a spectrograph which can operate in cross-dispersed mode with a spectral range of 0.9-2.5 μm ; we selected a combination of the 31.7 lines/mm grating, the short blue camera, and the short camera's cross-dispersing prism to gain full wavelength coverage. We chose the 0.45" slit in order to obtain a resolution of ~ 1070 -1130, which allowed us to effectively match the resolution of the NEWFIRM UNB filters ($R \approx 1000$), avoid major OH sky line blending issues, and which would allow for the [O II] doublet to be resolved (see below). This slit width also allowed us sufficient positional accuracy for the proposed target, as the

NEWFIRM data showed a 3σ astrometric accuracy of $\sim 0.25\text{-}0.3''$.

In order to determine whether a line is Ly α , one can use the spectroscopic confirmation technique found in Rhoads et al. (2004). Ly α lines at high- z have been found to show characteristic red asymmetries due to intrinsic absorption and the intergalactic medium. Additionally, the wavelength coverage of GNIRS would allow us to observe both the potential Ly α line, measured at $1.06\ \mu\text{m}$, and a number of other lines which could rule out, rather than confirm, these targets being at $z = 7.7$. There are a number of other emitters at lower redshifts which could mimic $z = 7.7$ Ly α in imaging, such as H α at $z = 0.62$, [O III] at $z = 1.12$, H β at $z = 1.17$, and Mg II at $z = 2.85$. The GNIRS wavelength coverage would allow us to measure and identify such nearby lines as [S II] $\lambda\lambda 6716, 6731$ at $z = 0.62$, H β and [O II] $\lambda 7325$ at $z = 1.12$, [O III] $\lambda 5007$ and [O II] $\lambda 7325$ at $z = 1.17$, H γ and [O III] $\lambda 4363$ at $z = 1.85$, and H γ at $z = 2.85$. The wavelength range of GNIRS makes it one of the few instruments which could allow us to perform such identifications. Along with the presence of other lines, should the target not be a $z = 7.7$ Ly α emitter, the equivalent width of the line could help indicate its redshift: [O III] emitters have been measured with rest-frame equivalent widths on the order of $1000\ \text{\AA}$, whereas [O II] equivalent widths have been found to peak in ranges of $40\text{-}140\ \text{\AA}$ in rest-frame [Rhoads et al. (2000), Kornei et al. (2012), Lee et al. (2012), Ly et al. (2012)]. The coverage is less critical should our targets in fact be $z = 7.7$ Ly α emitters – there are other emission lines which would fall in the GNIRS wavelength range in that case, but those lines are high-ionization and significantly fainter than Ly α , and thus likely not detectable in our one night of time – but the

lack of other strong emission lines in that case would be indicative of high- z Ly α , regardless of equivalent width considerations.

Owing to the requirement of GNIRS target acquisition of a suitably bright, nearby offset star, we were unable to observe candidate #1, as there were no bright stars close enough to the target to ensure sufficient positional accuracy in blind observing. We thus focused our efforts on candidate #2. An unfortunate series of events involving telescope malfunctions and other circumstances beyond our control led to our only obtaining 2.5 hours of observation on our target. In this time, we reached a SNR at 1.06 μm of ~ 2 , and a corresponding 5σ sensitivity of $\sim 5 \times 10^{-17}$ erg s^{-1} cm^{-2} . Our calculated line flux for candidate #2, a sensitivity of which we would require for detection, is 8.6×10^{-18} erg cm^{-2} s^{-1} , as listed in Table 4.2. Our initial estimate was that we would reach a SNR in the line of $\sim > 7$ after 4 hours of integration, which is significantly higher than our observations would predict for that integration. Our observing conditions, however, were marginal, with seeing of primarily 0.8" and air mass above 1.2.

We reduced these GNIRS cross-dispersed spectra data using the Gemini IRAF Package³, using telluric standard HIP 49198, an A1V star. The continuum-subtracted spectrum we obtained after 2.5 hours of integration can be seen in Figure 5.1, in addition to an arbitrarily scaled raw sky emission spectrum for Mauna Kea [Lord (1992)]. This spectrum shows the GNIRS order #6 data and is flux-normalized to a line sensitivity of $\sim 5 \times 10^{-17}$ erg s^{-1} cm^{-2} . We have marked the expected position of a $z = 7.7$ Ly α emission line on our spectrum. Given the low signal-to-noise in the

³<http://www.gemini.edu/sciops/queue-and-schedules?q=node/10795>

vicinity of the expected Ly α emission line ($\sim < 2$), we cannot confirm the presence of a line at $1.06 \mu\text{m}$, nor the presence of lines longward of $1.06 \mu\text{m}$ were this not a $z = 7.7$ LAE. A recently published study of $z > 7$ candidates of fluxes similar to those of our target resulted in no detection after 2 hours of integration with GNIRS, down to a slightly better sensitivity than we reached and in much better conditions ($0.5''$ and lower air mass), which is consistent with our non-detection [Caruana et al. (2012)]. We attempted to request more time on GNIRS to obtain a better sensitivity but were denied, as the time allocation committee suggested that we should see some evidence of the line at this sensitivity, with which we cannot argue. We are forced to consider LAE candidate #2 a non-detection at this time.

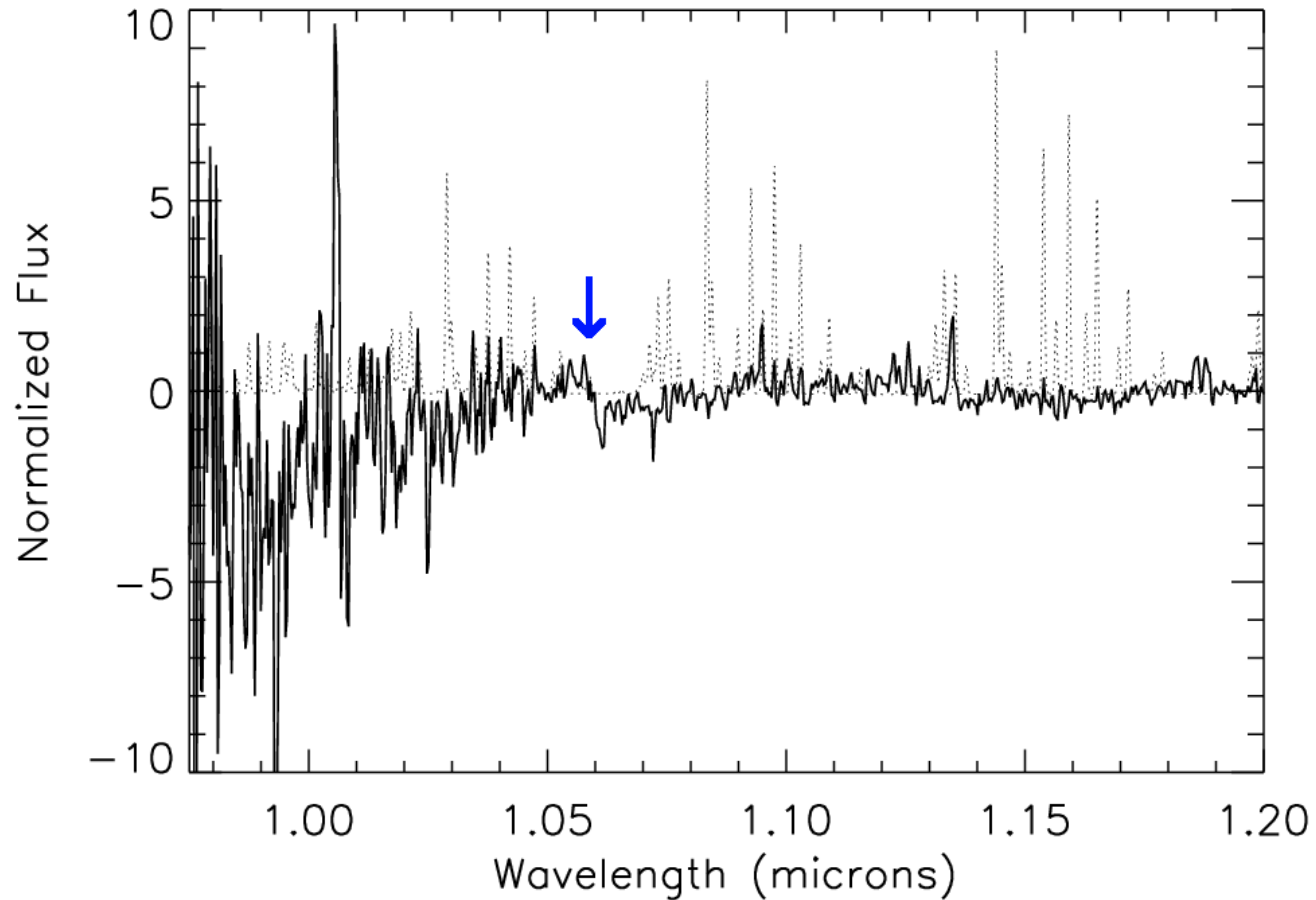


Figure 5.1: Continuum-subtracted spectrum obtained from ~ 2.5 hours of GNIRS data for LAE #2 (solid line). Overlaid on this spectrum are raw sky emission data (dotted line) for Mauna Kea, scaled arbitrarily [Lord (1992)]. Our spectrum is flux-normalized to a line sensitivity of $\sim 5 \times 10^{-17}$ erg s $^{-1}$ cm $^{-2}$. The increased noise on the blue end is due to that being the edge of the GNIRS order. The blue arrow marks the expected position of a $z = 7.7$ Ly α emission line. After 2.5 hours of observation in marginally good conditions, the SNR in the range of the expected Ly α line of this spectrum is $\sim < 2$. We therefore cannot confirm the presence of a line at this wavelength.

5.3.2 Additional Spectroscopic Follow-up

In addition to our GNIRS spectroscopy on LAE candidate #2, we have obtained additional spectroscopic follow-up via some of our collaborators. Candidate #1 was observed for 7.5 hours on the Large Binocular Telescope (LBT) using the infrared spectrograph LUCI [Jiang et al. (2013)]. The observations were centered at $1.1 \mu\text{m}$ with a $\sim 4000 \text{ \AA}$ wavelength range. The resulting spectrum was deep enough to have detected LAE candidate #1 at $3\text{-}5\sigma$, assuming a line flux of $1.21 \times 10^{-17} \text{ erg s}^{-1} \text{ cm}^{-2}$, as listed in Table 4.2, but no detection was found. This lack of detection came despite the fact that a very faint galaxy (22.6 Vega magnitudes in the J band) was detected in the same slit. That and the excellent positional accuracy of LUCI, using the faint galaxy and a reference star for offsetting, is enough for the authors to conclude that this candidate is not a $z = 7.7 \text{ Ly}\alpha$ emitter.

Another of our collaborators recently observed our first two candidates using the Multi-Object Spectrometer for Infra-Red Exploration, MOSFIRE, on the Keck telescope. This instrument covers the entire Y band ($0.91\text{-}1.12 \mu\text{m}$) with a minimum resolution of 2290⁴. As MOSFIRE uses a multi-object slit mask, we were able to piggyback on observations by Peter Capak and Nick Scoville, who were observing a combination of $z > 7$ LAEs and Lyman-break galaxies in the COSMOS field. These observations were taken on January 14-16 2013, and they included our LAE candidates #1 and #2. While we have not been provided with exact details of the run, the depth of the observations should have provided $>10\sigma$ detections of each

⁴<http://irlab.astro.ucla.edu/mosfire/>

of our candidates, but no signal was detected [Capak, P., private communication (2013)]. The lack of detection of candidate #2 is consistent with our lack of detection via GNIRS, and the lack of detection of candidate #1 is consistent with our collaborators' lack of detection of candidate #1 with LUCI.

5.4 DISCUSSION

The combination of lack of detection with GNIRS, LUCI, and MOSFIRE, each with increasing signal-to-noise yet each showing no $1.06 \mu\text{m}$ emission line, leads us to conclude that our candidates #1 and #2 from Chapter 4 are in fact not high- z Ly α emitters. What these candidates are, exactly, if not $z = 7.7$ Ly α emitters, is impossible to say at present without further follow-up. The presence of signal, albeit faint, of candidate #1 in the UltraVISTA H -band data reassures us that this object is real. Whether it may be one of the low- z emitters as detailed in Section 5.3.1 remains to be seen. As for candidate #2, the lack of detection in all broadband imaging studies, in combination with the lack of spectroscopy detection, is troubling. This object should be neither a transient nor an artifact, as it was detected in both yearly stacks (which were constructed using random dither patterns) as detailed in Section 4.3.1. It is potentially possible that this could be some longer-term transient (e.g., supernova remnants frequently show near-IR emission; Gerardy & Fesen (2001)) which has faded dramatically in the time between imaging and spectroscopy. Were that the case, however, there should have been some emission present in the CFHT imaging data, which was taken around the same time

as our NEWFIRM imaging data. We thus cannot make any firm conclusions about candidate #2 at this time, other than it not being a $z = 7.7$ Ly α emitter.

We cannot make any claims about candidates #3 and #4, as they have not been observed spectroscopically. Faint detections of candidate #3 in Subaru broad-band imaging data and ACS I -band data and of candidate #4 in CFHT H -band and UltraVISTA Y - and K -bands imply that these two targets are line emitters, but we cannot yet say what species; candidate #3 is likely a low- z emitter, as described in Section 5.3.1, owing to its flux blueward of Ly α . It would be premature to attempt to make any conclusions about candidate #4 at this time without spectroscopic confirmations, although it remains as our most promising $z = 7.7$ LAE candidate. Unfortunately, given the lack of success thus far with detections of our brightest candidates, and given that detecting objects at sensitivities below 10^{-17} erg s $^{-1}$ cm $^{-2}$ is really pushing the limits of many current ground-based spectrographs, it is nearly impossible to secure observing time to pursue this project further without piggybacking on another project.

Our inability to detect these candidates spectroscopically is consistent with several other recent undertakings at these redshifts. Ly α emitters and Lyman-break galaxies have been spectroscopically confirmed at redshifts of $z \sim 7$, such as the initial Iye et al. (2006) $z = 6.96$ detection, Ly α emitters of $z = 6.844$ and $z = 7.213$ from Ono et al. (2012), a $z = 6.944$ LAE in COSMOS [Rhoads et al. (2012)], a $z = 7.045$ Lyman-break galaxy [Schenker et al. (2012)], and the highest-confirmed LAE thus far, at $z = 7.215$ [Shibuya et al. (2012)]. For the most part, however, surveys attempting to spectroscopically confirm Ly α emitting galaxies above $z > 7$

have been unsuccessful. The previously mentioned Caruana et al. (2012) survey using GNIRS found no Ly α emission from four $z > 7$ candidates. An initial claim of a $z = 8.55$ Ly α emitter [Lehnert et al. (2010)], which was by far the highest redshift of any confirmed Ly α or Lyman-break galaxy, has recently been debunked by Bunker et al. (2013) using two different spectroscopic instruments on two different telescopes, VLT and Subaru. Brammer et al. (2013) claim tentative Ly α flux detection in what would be a $z = 12.12$ emitter, but note that the most plausible explanation is that this is a low-redshift emitter, potentially emitting [O III] $\lambda\lambda 4959, 5007$ at $z = 2.19$. While Lyman-break and Ly α emitter candidates are still being found at redshifts $z \sim 7 - 8$ and even higher (e.g., Bowler et al. (2012), Bradley et al. (2012), Oesch et al. (2012,13), Lorenzoni et al. (2013), Tilvi et al. (2013)), confirmations are still lacking, and the number of candidates found above these redshifts is still below the number found at lower z [Fontana et al. (2010), Stark et al. (2010), Curtis-Lake et al. (2012), Pentericci et al. (2011)]. This is likely due to two factors: one, that initial detections of these objects generally come from very narrow-band imaging searches which discover rather faint sources, which are very hard to follow-up from the ground [Treu et al. (2012)]; two: that the drop in numbers of candidates above $z \sim 7$, as well as inability to make spectroscopic confirmations is potentially a signal that the IGM becomes much more opaque at $z \sim 7-8$ [Hu et al. (2010), Clément et al. (2012), Ono et al. (2011), Schenker et al. (2012), Shibuya et al. (2012), Bolton & Haehnelt (2013)]. Thus our non-detections are not exceptional a posteriori, but rather they are symptomatic of the difficulty in detecting Ly α flux at $z > 7$.

5.5 SUMMARY

We have utilized two main types of follow-up on our four Ly α emitter candidates, as detailed in Chapter 4. The main results can be summarized as follows:

- *Broadband Imaging:* We searched for our candidates using *HST* ACS *I*-band (F814W) at a depth of 25.94 AB magnitudes, CFHT *H*-band (1.631 μm) at a depth of 30.09 AB magnitudes, and UltraVISTA *Y*-, *J*-, *H*-, and *K*-band (1.02, 1.25, 1.64, 2.12 μm) at depths of 30.75, 30.55, 30.03, and 29.57 AB magnitudes, respectively. Candidate #3 had a tentative detection (SNR of 2.69) in the ACS *I*-band, which would indicate that it is not a $z = 7.7$ Ly α emitter, as there should be no flux blueward of Ly α . Candidate #4 had a tentative detection (SNR 2.06) in the CFHT *H*-band, as well as a moderate detection in the UltraVISTA *Y*-band (SNR ~ 3) and some flux in the UltraVISTA *K*-band (SNR 1.46), which could potentially be measurements of the faint continuum of a $z = 7.7$ LAE, or even some LAE flux in *Y*. Candidate #1 had a very faint flux detection in the UltraVISTA *H*-band (SNR 1.33) but was not detected in any other band, and candidate #2 was not detected in imaging at all.
- *Spectroscopy:* We used GNIRS on Gemini-North in long-slit, cross-dispersed mode at $R \sim 1000$ over 0.9-2.5 μm to attempt to spectroscopically confirm LAE candidate #2. After 2.5 hours of observation, we reached a 5σ sensitivity of $\sim 5 \times 10^{17}$ erg s $^{-1}$ cm $^{-2}$, while the Ly α line flux calculated for this candidate was 8.6×10^{-18} erg s $^{-1}$ cm $^{-2}$. We found no detection of any Ly α line. Candidate #1 was observed for 7.5 hours using LUCI on the LBT by one of our collaborators.

The depth should have provided a $3\text{-}5\sigma$ detection, but no detection was found. Other collaborators observed candidates #1 and #2 using MOSFIRE on Keck for long enough to provide a 10σ detection, but again, no signal was detected.

- *Ly α Emitter Candidates:* Candidates #1 and #2 have effectively been ruled out as $z = 7.7$ Ly α emitters by spectroscopy. Candidate #3 has been detected in broadband optical imaging via Subaru and ACS, which likely rules it out as well. Candidate #4 has been tentatively detected in broadband infrared, but has not been detected in broadband optical. It remains our last viable $z = 7.7$ Ly α candidate, but its redshift cannot be determined without further spectroscopy.

Chapter 6

Summary

6.1 OBJECTIVES

This thesis focused on two topics which are of major interest right now in astronomy: one, galactic-scale outflows in local AGN and starbursts and their potential role in both galactic feedback and the merger process; two, Lyman- α emitting galaxies in the high-redshift universe and their role as both probes of and contributors to the reionization of the intergalactic medium. We attempted to answer several important questions on each topic, and we outline those thesis objectives here.

- What role does far-infrared luminosity play in the detection of galactic-scale outflows in local AGN? What role does it play in the velocities of those outflows?
- Does star formation rate or host galaxy mass have a bigger impact on the kinematics and dynamics of galactic outflows?
- What is the primary mechanism powering galactic outflows: starbursts, AGN, or some combination thereof?
- Does AGN type influence the detection of galactic-scale outflows? Does it influence the velocities of those outflows?

- What role does AGN luminosity play in outflow detection rate and outflow velocity?
- Is there any correlation between merger stage and outflow detection rate or outflow velocity?
- Can any trends be identified between host galaxy properties and the presence of strong inflows in AGN? Are such inflows strong enough to be powering the AGN?
- Can ultra-narrowband imaging surveys prove as effective at detecting $z \sim 8$ Ly α emitters as they have at detecting $z \sim 5 - 7$ Ly α emitters? Is present ground-based technology sufficient to detect such high-redshift objects?
- Has the Ly α luminosity function evolved over the course of $5.7 < z < 7.7$? What can this tell us about the state of the intergalactic medium, and thus of the progress of the reionization epoch, at these high redshifts?
- Can we spectroscopically confirm any of these high-redshift targets? Is present ground-based technology sufficient for confirmation of such faint high-redshift objects?

To attempt to answer these questions, we have embarked on two major studies. For the questions regarding galactic outflows, we have utilized the R-C spectrograph on the KPNO 4-m telescope and studied two samples of galaxies, detailed in Chapters 2 and 3. The first was an infrared-faint sample of Seyfert galaxies, the second an infrared-luminous sample of PG QSOs and ULIRGs drawn from the QUEST

sample of gas-rich mergers. In both cases, we measured the Na I D absorption, which, if blueshifted or redshifted, is an unambiguous indicator of outflowing or inflowing absorption. We combine these data sets with previously published data on infrared-luminous Seyferts and infrared-luminous starbursts, taken using the same instrument and analyzed with the same methodology, to look for patterns among the larger sample [Rupke et al. (2005a), Rupke et al. (2005b), Rupke et al. (2005c)].

For the questions regarding high-redshift Ly α emitters, we primarily made use of the NEWFIRM camera, a new, extremely wide-field near-infrared imager on the KPNO 4-m telescope. We used roughly 100 hours of ultra-narrowband filter data, centered around the 1.06 μm line, to look for $z = 7.7$ Ly α emission; the combination of an extremely wide-field (~ 760 arcmin²) imager and over thirty nights of observing time made this one of the deepest Ly α searches ever conducted. We combined this data with publicly-available broadband optical (Subaru) and infrared (UKIRT) imaging data to make use of rigorous high-redshift selection criteria, dependent upon ultra-narrowband infrared excess and lack of optical detection, to select our $z = 7.7$ Ly α candidates, as described in Chapter 4. We then followed this data up with near-infrared spectroscopy, using GNIRS on Gemini-North, as well as using LUCI on the LBT and MOSFIRE on Keck via our collaborators, to attempt to spectroscopically confirm our candidates, as detailed in Chapter 5.

6.2 RESULTS

Here we summarize the major results found in each chapter, attempting to answer the questions outlined in Section 6.1.

In **Chapter 2**, we examined neutral gas outflows and inflows in infrared-faint Seyferts:

1. Unlike infrared-luminous Seyferts or infrared-luminous starbursts, the majority of infrared-faint Seyferts do not possess outflows.
2. Among infrared-faint Seyferts which do show evidence of outflows, there is an increase in outflow likelihood with far-infrared luminosity, which correlates to an increase in outflow likelihood with star formation rate.
3. While detection rates were generally higher with luminosity bin in Seyfert 2s, the highest velocity outflows occurred in Seyfert 1s. We thus concluded that Seyfert 2 outflows are powered by starbursts alone, whereas Seyfert 1 outflows are primarily powered by AGN.
4. Mass outflow rates in Seyferts and starbursts tend to increase with both star formation rates and host galaxy masses.
5. Neither outflows in infrared-faint Seyfert 1s nor in infrared-faint Seyfert 2s are strong enough to play a major role in galactic feedback, as energy outflow rates were only $\sim 1\%$ of the host galaxy luminosity.
6. Over one-third of infrared-faint Seyferts show inflows, a significantly higher

fraction than infrared-luminous Seyferts and infrared-luminous starbursts, but no obvious trend with star formation rate nor host galaxy mass was found.

7. Mass estimates showed that the inflowing material that we have probed in infrared-faint Seyferts is more than enough to power the AGN for the duration of the expected AGN lifetime.

In **Chapter 3**, we extended the neutral gas outflows and inflows study to PG QSOs and ULIRGs from a gas-rich merger sample:

1. Half of ULIRGs showed outflowing Na I D, whereas very few PG QSOs showed measurable Na I D absorption at all, and none possessed outflows.
2. In combination with data sets from Chapter 2 and previously published work, we again found increasing detection trends with L_{FIR} , implying that IR-luminous starbursts show increasing outflow rates with increasing star formation. This is likely a secondary correlation in IR-luminous AGN, where increasing detection rates are due to increasing amounts of dust and gas in the galaxy.
3. IR-luminous AGN velocities are substantially higher than IR-faint AGN or IR-luminous starbursts, and the AGN is likely the primary driver of outflows in IR-luminous AGN. Statistical tests indicate that IR-luminous AGN and IR-luminous starbursts likely originate from different parent populations.
4. Outflow detection rates were highest in IR-luminous starbursts, and Type 2 AGN detection rates were higher than Type 1 AGN detection rates, but the highest velocities by far were found in Type 1 AGN. The inclusion of PG QSOs

and ULIRGs again bolsters the claim that Type 1 AGN outflows are primarily powered by AGN, whereas Type 2 AGN are primarily powered by starbursts only; statistical tests back up these claims.

5. Substantial increases in detection rates and velocities were found with increasing AGN luminosity, agreeing with the conclusions above.
6. We found that galaxies which have completed the merger process have outflows with higher velocities than galaxies still in the pre-merger stage, though the merger phase is not necessarily the driver of those outflows.
7. According to our rough estimates, with the sole exception of the extremely powerful outflows in Mrk 231, none of the objects in this sample have strong enough outflows to play a significant role in galactic feedback.
8. Again, according to rough estimates, inflow detection rates in our PG QSO and ULIRG sample were too low for us to discern any particular trends, but again, the mass accretion rates in the PG QSOs and ULIRGs which did show inflow were high enough to power the AGN over their lifetimes.

In **Chapter 4**, we used the NEWFIRM camera to attempt a search for high-redshift Ly α emitters:

1. We found four potential $z = 7.7$ Ly α emitter candidates, with line fluxes of $\sim 10^{-17}$ erg s $^{-1}$ cm $^{-2}$.
2. Monte Carlo simulations indicated a likelihood that no more than two of our candidates are high-redshift Ly α emitters.

3. Assuming only two real high-redshift targets, we found that there would be no significant evolution of the Ly α luminosity function between $5.7 < z < 7.7$, implying no significant change in the neutral hydrogen fraction of the IGM over that time.

Chapter 5 focused on follow-up of the $z = 7.7$ Ly α emitter candidates found in Chapter 4:

1. Candidate #3 had an optical detection in the ACS *I*-band data, which, in conjunction with a Subaru detection, ruled it out as a $z = 7.7$ Ly α emitter.
2. Candidates #1 and #4 showed some flux in infrared imaging, potentially a detection of the faint continuum of these objects.
3. Candidate #2 was not detected at all in imaging, neither in optical nor in near-infrared.
4. After 2.5 hours of GNIRS integration on candidate #2, we found no signal.
5. Our collaborators also found non-detections of candidates #1 and #2 after 7.5 hours of LUCI observation on the LBT (candidate #1) and after an extensive observation using MOSFIRE on Keck (candidates #1 and #2). We thus concluded that candidates #1 and #2 are not $z = 7.7$ Ly α emitters.
6. Candidate #4 remained our only viable high-redshift target, but would require spectroscopic confirmation to be sure.

7. We share the conclusion of many other authors working in this field that the IGM is significantly more opaque at $z \sim 8$ than $z \sim 7$ and that reionization is still ongoing at this time.

While some of the questions raised in Section 6.1 remain unanswered, this thesis has addressed and provided initial solutions to a number of major questions in astronomy today. We have quantified the prevalence of winds in local galaxies, determined their main drivers in different host galaxy types, and shown that the majority of galactic-scale winds, at least locally, likely cannot play the role in galactic feedback that many would hope. We have also provided evidence supporting the generally held picture of gas-rich mergers. We have shown the limitations of current ground-based technology in detecting and confirming high-redshift galaxies. We have also shown that it is likely that the intergalactic medium was still rather opaque at $z \sim 8$, although more, independent confirmations in additional target fields will be needed to bolster this claim. This thesis has added much to the current knowledge base in extragalactic astronomy and has laid the groundwork for future discoveries.

Bibliography

- [Abel et al. (2002)] Abel, T., Bryan, G. L., & Norman, M. L. 2002, *Science*, **295**, 93.
- [Alexander et al. (2010)] Alexander, D. M., Swinbank, A. M., Smail, I., McDermid, R., & Nesvadba, N. P. H. 2010, *MNRAS*, **402**, 2211.
- [Alvarez et al. (2006)] Alvarez, M. A., Bromm, V., & Shapiro, P. R. 2006, *ApJ*, **639**, 621.
- [Alvarez et al. (2009)] Alvarez, M. A., Wise, J. H., & Abel, T. 2009, *ApJL*, **701**, L133.
- [Antonucci (1993)] Antonucci, R. 1993, *ARA&A*, **31**, 473.
- [Antonucci & Miller (1985)] Antonucci, R. R. J., & Miller, J. S. 1985, *ApJ*, **297**, 621.
- [Arav et al. (2008)] Arav, N., Moe, M., Costantini, E., et al. 2008, *ApJ*, **681**, 954.
- [Armus et al. (2007)] Armus, L. et al. 2007, *ApJ*, **656**, 148.
- [Arp (1966)] Arp, H.C. 1966, *Science*, **151**, 1214.
- [Bahcall & Salpeter (1965)] Bahcall, J. N., & Salpeter, E. E. 1965, *ApJ*, **142**, 1677.
- [Barnes & Hernquist (1996)] Barnes, J. E., & Hernquist, L. 1996, *ApJ*, **471**, 115.
- [Bautista et al. (2010)] Bautista, M. A., Dunn, J. P., Arav, N., et al. 2010, *ApJ*, **713**, 25.
- [Begelman (1985)] Begelman, M. C. 1985, *ApJ*, **297**, 492.
- [Benson et al. (2003)] Benson, A. J., Bower, R. G., Frenk, C. S., et al. 2003, *ApJ*, **599**, 38.
- [Bertin & Arnouts (1996)] Bertin, E., & Arnouts, S. 1996, *A&AS*, **117**, 393.
- [Bertin et al. (2002)] Bertin, E., Mellier, Y., Radovich, M., Missonnier, G., Didelon, P., & Morin, B. 2002, *Astronomical Data Analysis Software and Systems XI*, **281**, 228.

- [Binney (2004)] Binney, J. 2004, MNRAS, **347**, 1093.
- [Binney et al. (2001)] Binney, J., Gerhard, O., & Silk, J. 2001, MNRAS, **321**, 471.
- [Blandford & Payne (1982)] Blandford, R. D. & Payne, D. G. 1982, MNRAS **199**, 883.
- [Blumenthal et al. (1984)] Blumenthal, G. R., Faber, S. M., Primack, J. R., & Rees, M. J. 1984, Nature, **311**, 517.
- [Blustin et al. (2005)] Blustin, A. J., Page, M. J., Fuerst, S. V., Branduardi-Raymont, G., & Ashton, C. E. 2005, A&A, **431**, 111.
- [Bolton & Haehnelt (2013)] Bolton, J. S., & Haehnelt, M. G. 2013, MNRAS, **429**, 1695.
- [Bouwens et al. (2010)] Bouwens, R. J., et al. 2010, ApJ, **725**, 1587.
- [Bouwens et al. (2006)] Bouwens, R. J., Illingworth, G. D., Blakeslee, J. P., & Franx, M. 2006, ApJ, **653**, 53.
- [Bowler et al. (2012)] Bowler, R. A. A., Dunlop, J. S., McLure, R. J., et al. 2012, MNRAS, **426**, 2772.
- [Bradley et al. (2012)] Bradley, L. D., Trenti, M., Oesch, P. A., et al. 2012, ApJ, **760**, 108.
- [Brammer et al. (2013)] Brammer, G. B., van Dokkum, P. G., Illingworth, G. D., et al. 2013, ApJL, **765**, L2.
- [Bromm et al. (2002)] Bromm, V., Coppi, P. S., & Larson, R. B. 2002, ApJ, **564**, 23.
- [Bromm et al. (2001)] Bromm, V., Kudritzki, R. P., & Loeb, A. 2001, ApJ, **552**, 464.
- [Bromm & Yoshida (2011)] Bromm, V., & Yoshida, N. 2011, ARA&A, **49**, 373.
- [Bromm et al. (2009)] Bromm, V., Yoshida, N., Hernquist, L., & McKee, C. F. 2009, Nature, **459**, 49.
- [Bunker et al. (2013)] Bunker, A. J., Caruana, J., Wilkins, S. M., et al. 2013, MNRAS, **430**, 3314.

- [Burbidge (1967)] Burbidge, E. M. 1967, *ARA&A*, **5**, 399.
- [Burke (1968)] Burke, J. A. 1968, *MNRAS*, **140**, 241.
- [Cano-Díaz et al. (2012)] Cano-Díaz, M., Maiolino, R., Marconi, A., et al. 2012, *A&A*, **537**, L8.
- [Capak et al. (2011)] Capak, P., et al. 2011, *ApJ*, 730, 68.
- [Caruana et al. (2012)] Caruana, J., Bunker, A. J., Wilkins, S. M., et al. 2012, *MNRAS*, **427**, 3055.
- [Castor et al. (1975)] Castor, J., McCray, R., & Weaver, R. 1975, *ApJ*, **200**, L107.
- [Chevalier & Clegg (1985)] Chevalier, R. A. & Clegg, A. W. 1985, *Nature*, **317**, 44.
- [Clément et al. (2012)] Clément, B., Cuby, J.-G., Courbin, F., et al. 2012, *A&A*, **538**, A66.
- [Clements et al. (1996)] Clements, D. L., Sutherland, W. J., McMahon, R. G., & Saunders, W. 1996, *MNRAS*, **279**, 477.
- [Cole et al. (2000)] Cole, S., Lacey, C. G., Baugh, C. M., & Frenk, C. S. 2000, *MNRAS*, **319**, 168.
- [Contursi et al. (2013)] Contursi, A., Poglitsch, A., Grácia Carpio, J., et al. 2013, *A&A*, **549**, A118.
- [Cooper et al. (2008)] Cooper, J., Bicknell, G., Sutherlan, R., & Bland-Hawthorn, J. 2008, *ApJ*, **674**, 157.
- [Couchman & Rees (1986)] Couchman, H. M. P. & Rees, M. J. 1986, *MNRAS*, **221**, 53.
- [Cowie & Hu (1998)] Cowie, L. L., & Hu, E. M. 1998, *AJ*, **115**, 1319.
- [Crenshaw et al. (2003a)] Crenshaw, D. M., Kraemer, S. B., & Gabel, J. R. 2003a, *AJ*, **126**, 1690.
- [Crenshaw et al. (2003b)] Crenshaw, D. M., Kraemer, S. B., & George, I. M. 2003b, *ARA&A*, **41**, 117.

- [Croom et al. (2004)] Croom, S., et al. 2004, AGN Physics with the Sloan Digital Sky Survey Conference Proceedings, **311**, 457.
- [Croston et al. (2008)] Croston, J. H., Hardcastle, M. J., Kharb, P., Kraft, R. P., & Hota, A. 2008, ApJ, **688**, 190.
- [Cuby et al. (2007)] Cuby, J.-G., Hibon, P., Lidman, C., Le Fèvre, O., Gilmozzi, R., Moorwood, A., & van der Werf, P. 2007, A&A, **461**, 911.
- [Curtis-Lake et al. (2012)] Curtis-Lake, E., McClure, R. J., Pearce, H. J., et al. 2012, MNRAS, **422**, 1425.
- [Dadina et al. (2005)] Dadina, M., Cappi, M., Malaguti, G., Ponti, G., & de Rosa, A. 2005, A&A, **442**, 461.
- [Das et al. (2007)] Das, V., Crenshaw, D. M., & Kraemer, S. B. 2007, ApJ, **656**, 699.
- [Dasyra et al. (2008)] Dasyra, K. M., Ho, L. C., Armus, L., et al. 2008, ApJL, **674**, L9.
- [Dasyra et al. (2006a)] Dasyra, K. M., Tacconi, L. J., Davies, R. I., et al. 2006a, ApJ, **638**, 745.
- [Dasyra et al. (2006b)] Dasyra, K. M., Tacconi, L. J., Davies, R. I., et al. 2006b, ApJ, **651**, 835.
- [Dasyra et al. (2007)] Dasyra, K. M., Tacconi, L. J., Davies, R. I., et al. 2007, ApJ, **657**, 102.
- [Davies et al. (2009)] Davies, R., Maciejewski, W., Hicks, E., Tacconi, L., Genzel, R., Engel, H., & Sternberg, A. 2009, ApJ, **702**, 114.
- [Dawson et al. (2004)] Dawson, S., et al. 2004, ApJ, **617**, 707.
- [Dawson et al. (2007)] Dawson, S., Rhoads, J. E., Malhotra, S., Stern, D., Wang, J., Dey, A., Spinrad, H., & Jannuzi, B. T. 2007, ApJ, **671**, 1227.
- [Dekel & Silk (1986)] Dekel, A. & Silk, J. 1986, ApJ, **344**, 1131.
- [Deo et al. (2006)] Deo, R. P., Crenshaw, D. M., & Kraemer, S. B. 2006, AJ, **132**, 321.

- [Dickinson & Valdes (2009)] Dickinson, M., & Valdes, F. A. 2009, Guide to NEW-FIRM Data Reduction with IRAF, NOAO SDM PL017.
- [Di Matteo et al. (2005)] Di Matteo, T., Springel, V., & Hernquist, L. 2005, *Nature*, **433**, 604.
- [Dunn et al. (2010)] Dunn, J. P., Bautista, M., Arav, N., et al. 2010, *ApJ*, **709**, 611.
- [Ebstein et al. (1989)] Ebstein, S. M., Carleton, N. P., & Papaliolios, C. 1989, *ApJ*, **336**, 103.
- [Elston et al. (1985)] Elston, R., Cornell, M. E., & Lebovsky, M. J. 1985, *ApJ*, **296**, 106.
- [Evans et al. (2002)] Evans, A. S., Mazzarella, J. M., Surace, J. A., & Sanders, D. B. 2002, *ApJ*, **580**, 749.
- [Fabian (1999)] Fabian, A. C. 1999, *MNRAS*, **308**, L39.
- [Fabian (2012)] Fabian, A. C. 2012, *ARA&A*, **50**, 455.
- [Falco et al. (1999)] Falco, E. E., Kurtz, M. J., Geller, M. J., et al. 1999, *PASP*, **111**, 438.
- [Faucher-Giguère & Quataert (2012)] Faucher-Giguère, C.-A., & Quataert, E. 2012, *MNRAS*, **425**, 605.
- [Feldmeier et al. (1999)] Feldmeier, J. J., Brandt, W. N., Elvis, M., Fabian, A. C., Iwasawa, K., & Mathur, S. 1999, *ApJ*, **510**, 167.
- [Ferguson et al. (2004)] Ferguson, H. C., et al. 2004, *ApJL*, **600**, L107.
- [Ferrara & Ricotti (2006)] Ferrara, A., & Ricotti, M. 2006, *MNRAS*, **373**, 571.
- [Ferrarese & Merritt (2000)] Ferrarese, L., & Merritt, D. 2000, *ApJL*, **539**, L9.
- [Feruglio et al. (2010)] Feruglio, C., Maiolino, R., Piconcelli, E., et al. 2010, *A&A*, **518**, L155.
- [Finkelstein et al. (2009)] Finkelstein, S. L., Rhoads, J. E., Malhotra, S., & Grogin, N. 2009, *ApJ*, **691**, 465.
- [Fontana et al. (2010)] Fontana, A., et al. 2010, *ApJL*, **725**, L205.

- [Frank et al. (2002)] Frank, J., King, A., & Raine, D., *Accretion Power in Astrophysics* (Cambridge, UK: Cambridge University Press, 2002).
- [Fynbo et al. (2001)] Fynbo, J. U., Möller, P., & Thomsen, B. 2001, *A&A*, **374**, 443.
- [Galli & Palla (1998)] Galli, D., & Palla, F. 1998, *A&A*, **335**, 403.
- [Gallimore et al. (2006)] Gallimore, J. F., Axon, D. J., O’Dea, C. P., Baum, S. A., & Pedlar, A. 2006, *AJ*, **132**, 546.
- [Garnett (2002)] Garnett, D. R. 2002, *ApJ*, **581**, 1019.
- [Gerardy & Fesen (2001)] Gerardy, C. L., & Fesen, R. A. 2001, *AJ*, **121**, 2781.
- [Glikman et al. (2012)] Glikman, E., Urrutia, T., Lacy, M., et al. 2012, *ApJ*, **757**, 51.
- [Gnedin (2000)] Gnedin, N. Y. 2000, *ApJ*, **535**, 530.
- [Gonçalves et al. (1999)] Gonçalves, A. C., Véron-Cetty, M.-P., & Véron, P. 1999, *A&AS*, **135**, 437.
- [González Delgado et al. (2005)] González Delgado, R. M., Cervino, M., Martins, L. P., Leitherer, C., & Hauschildt. P. H. 2005, *MNRAS*, **357**, 945.
- [Granato et al. (2004)] Granato, G. L., De Zotti, G., Silva, L., Bressan, A., & Danese, L. 2004, *ApJ*, **600**, 580.
- [Grazian et al. (2000)] Grazian, A., Cristiani, S., D’Odorico, V., Omizzolo, A., & Pizzella, A. 2000, *AJ*, **119**, 2540.
- [Green et al. (1986)] Green, R. F., Schmidt, M., & Liebert, J. 1986, *ApJS*, **61**, 305.
- [Greif et al. (2007)] Greif, T. H., Johnson, J. L., Bromm, V., & Klessen, R. S. 2007, *ApJ*, **670**, 1.
- [Gronwall et al. (2007)] Gronwall, C., et al. 2007, *ApJ*, **667**, 79.
- [Guillard et al. (2012)] Guillard, P., Ogle, P. M., Emonts, B. H. C., et al. 2012, *ApJ*, **747**, 95.
- [Gunn & Peterson (1965)] Gunn, J. E., & Peterson, B. A. 1965, *ApJ*, **142**, 1633.

- [Guyon (2002)] Guyon, O. 2002, Ph.D. thesis, Univ. Paris VI.
- [Guyon et al. (2006)] Guyon, O., Sanders, D. B., & Stockton, A. 2006, *ApJS*, **166**, 89.
- [Haas et al. (2003)] Haas, M., Klaas, U., Müller, S. A. H., et al. 2003, *A&A*, **402**, 87.
- [Haas et al. (2000)] Haas, M., Müller, S. A. H., Chini, R., et al. 2000, *A&A*, **354**, 453.
- [Haiman (2002)] Haiman, Z. 2002, *ApJL*, **576**, L1.
- [Hardcastle et al. (2012)] Hardcastle, M. J., Massaro, F., Harris, D. E., et al. 2012, *MNRAS*, **424**, 1774.
- [Hazard et al. (1963)] Hazard, C., Mackey, M. B., Shimmins, A. J. 1963, *Nature*, **197**, 1037.
- [Helou (1986)] Helou, G. 1986, *ApJL*, **311**, 33.
- [Henriksen & Cousineau (1999)] Henriksen, M., & Cousineau, S. 1999, *ApJ*, **511**, 595.
- [Hibon et al. (2010)] Hibon, P., et al. 2010, *A&A*, **515**, A97.
- [Higdon et al. (2004)] Higdon, S. J. U., Devost, D., Higdon, J. L., et al. 2004, *PASP*, **116**, 975.
- [Ho (2007)] Ho, L. C. 2007, *ApJ*, **669**, 821.
- [Ho et al. (2008)] Ho, L. C., Darling, J., & Greene, J. E. 2008, *ApJS*, **177**, 103.
- [Ho & Kim (2009)] Ho, L. C. & Kim, M. 2009, *ApJS*, **184**, 398.
- [Hopkins & Elvis (2010)] Hopkins, P. F., & Elvis, M. 2010, *MNRAS*, **401**, 7.
- [Hopkins et al. (2006a)] Hopkins, P. F., Hernquist, L., Cox, T. J., et al. 2006a, *ApJS*, **163**, 1.
- [Hopkins et al. (2006b)] Hopkins, P. F., Hernquist, L., Cox, T. J., et al. 2006b, *ApJ*, **639**, 700.

- [Hopkins et al. (2009)] Hopkins, P. F., Murray, N., & Thompson, T. A. 2009, MNRAS, **398**, 303.
- [Hopkins et al. (2005)] Hopkins, P. F., Somerville, R. S., Hernquist, L., et al. 2006, ApJ, **652**, 864.
- [Hota & Saikia (2006)] Hota, A., & Saikia, D. J. 2006, MNRAS, **371**, 945.
- [Houck et al. (2004)] Houck, J. R., Roellig, T. L., van Cleve, J., et al. 2004, ApJS, **154**, 18.
- [Hoyle & Burbidge (1966)] Hoyle, F. & Burbidge, G. R. 1966, ApJ, **144**, 534.
- [Hu et al. (2002)] Hu, E. M., Cowie, L. L., McMahon, R. G., Capak, P., Iwamuro, F., Kneib, J.-P., Maihara, T., & Motohara, K. 2002, ApJL, **568**, L75.
- [Hu et al. (2004)] Hu, E. M., Cowie, L. L., Capak, P., McMahon, R. G., Hayashino, T., & Komiyama, Y. 2004, AJ, **127**, 563.
- [Hu et al. (2010)] Hu, E. M., Cowie, L. L., Barger, A. J., et al. 2010, ApJ, **725**, 394.
- [Hu et al. (1999)] Hu, E. M., McMahon, R. G., & Cowie, L. L. 1999, ApJL, **522**, L9.
- [Huchra et al. (1999)] Huchra, J. P., Vogeley, M. S., & Geller, M. J. 1999, ApJS, **121**, 287.
- [Hutchings et al. (1987)] Hutchings, J. B., Gower, A. C., & Price, R. 1987, AJ, **93**, 6.
- [Irwin & Saikia (2003)] Irwin, J. A., & Saikia, D. J. 2003, MNRAS, **346**, 977.
- [Iye et al. (2006)] Iye, M., et al. 2006, Nature, **443**, 186.
- [Jeans (1928)] Jeans, J. H., *Astronomy and Cosmogony* (Cambridge, UK: The University Press, 1928).
- [Jensen et al. (2013)] Jensen, H., Laursen, P., Mellema, G., et al. 2013, MNRAS, **428**, 1366.
- [Jiang et al. (2013)] Jiang, L., Bian, F., Fan, X., Krug, H. B., McGreer, I. D., & Stark, D. P. 2013, ApJL, accepted.

- [Jones et al. (2009)] Jones, D. H., Read, M. A., Saunders, W., et al. 2009, MNRAS, **399**, 683.
- [Kashikawa et al. (2006)] Kashikawa, N., et al. 2006, ApJ, **648**, 7.
- [Kashikawa et al. (2011)] Kashikawa, N., Shimasaku, K., Matsuda, Y., et al. 2011, ApJ, **734**, 119.
- [Kennicutt (1998)] Kennicutt, R. C. 1998, ApJ, **498**, 541.
- [Khachikian & Weedman (1974)] Khachikian, E. Y. & Weedman, D. W. 1974, ApJ, **192**, 581.
- [Kim & Sanders (1998)] Kim, D.-C., & Sanders, D. B. 1998, ApJS, **119**, 41.
- [Kim et al. (1995)] Kim, D.-C., Sanders, D. B., Veilleux, S., Mazzarella, J. M., & Soifer, B. T. 1995, ApJS, **98**, 129
- [Klaas et al. (2001)] Klaas, U., Haas, M., Müller, S. A. H., et al. 2001, A&A, **379**, 823.
- [Kleinmann & Low (1970)] Kleinmann, D. E., & Low, F. J. 1970, ApJL, **159**, L165.
- [Koekemoer et al. (2007)] Koekemoer, A. M., Aussel, H., Calzetti, D., Capak, P., et al. 2007, ApJS, **172**, 196.
- [Komatsu et al. (2011)] Komatsu, E., et al. 2011, ApJS, **192**, 18.
- [Koo & McKee (1992)] Koo, B. C. & McKee, C. F. 1992, ApJ, **388**, 93.
- [Kormendy & Kennicutt (2004)] Kormendy, J., & Kennicutt, R. C., Jr. 2004, ARA&A, **42**, 603.
- [Kormendy & Sanders (1992)] Kormendy, J., & Sanders, D. B. 1992, ApJL, **390**, L53.
- [Kornei et al. (2012)] Kornei, K. A., Shapley, A. E., Martin, C. L., et al. 2012, ApJ, **758**, 135.
- [Krolik et al. (1981)] Krolik, J. H., McKee, C. F., & Tarter, C. B. 1981, ApJ, **249**, 422.

- [Krongold et al. (2003)] Krongold, Y., Nicastro, F., Brickhouse, N. S., Elvis, M., Liedahl, D. A., & Mathur, S. 2003, *ApJ*, **597**, 832.
- [Krongold et al. (2007)] Krongold, Y., Nicastro, F., Elvis, M., Brickhouse, N., Binette, L., Mathur, S., & Jiménez-Bailón, E. 2007, *ApJ*, **659**, 1022.
- [Krug et al. (2010)] Krug, H. B., Rupke, D., & Veilleux, S. 2010, *ApJ*, **708**, 1145.
- [Krug et al. (2012)] Krug, H. B., Veilleux, S., Tilvi, V., et al. 2012, *ApJ*, **745**, 122.
- [Larson (1974)] Larson, R. B. 1974, *MNRAS*, **169**, 229.
- [Lebouteiller et al. (2011)] Lebouteiller, V., Barry, D.J., Spoon, H.W.W., Bernard-Salas, J., Sloan, G.C., Houck, J.R., & Weedman, D., 2011, *ApJS* **196**, 8.
- [Lebouteiller et al. (2010)] Lebouteiller, V., Bernard-Salas, J., Sloan, G. C., & Barry, D. J. 2010, *PASP*, **122**, 231.
- [Lee et al. (2012)] Lee, J. C., Ly, C., Spitler, L., et al. 2012, *PASP*, **124**, 782.
- [Lehnert et al. (2010)] Lehnert, M. D., Nesvadba, N. P. H., Cuby, J.-G., et al. 2010, *Nature*, **467**, 940.
- [Leitherer et al. (1992)] Leitherer, C., Robert, C., & Drissen, L. 1992, *ApJ*, **401**, 596.
- [Loeb & Barkana (2001)] Loeb, A., & Barkana, R. 2001, *ARA&A*, **39**, 19.
- [Lord (1992)] Lord, S. D., 1992, NASA Technical Memorandum 103957.
- [Lorenzoni et al. (2013)] Lorenzoni, S., Bunker, A. J., Wilkins, S. M., et al. 2013, *MNRAS*, **429**, 150.
- [Low & Kleinmann (1968)] Low, J., & Kleinmann, D. E. 1968, *AJ*, **73**, 868.
- [Ly et al. (2012)] Ly, C., Malkan, M. A., Kashikawa, N., et al. 2012, *ApJ*, **757**, 63.
- [Lynds (1971)] Lynds, R. 1971, *ApJL*, **164**, L73.
- [Lynds & Sandage (1963)] Lynds, C. R. & Sandage, A. R. 1963, *ApJ*, **137**, 1005.
- [Madau et al. (1999)] Madau, P., Haardt, F., & Rees, M. J. 1999, *ApJ*, **514**, 648.

- [Maiolino et al. (2012)] Maiolino, R., Gallerani, S., Neri, R., et al. 2012, MNRAS, **425**, L66.
- [Malhotra et al. (2005)] Malhotra, S., et al. 2005, ApJ, **626**, 666
- [Malhotra & Rhoads (2002)] Malhotra, S., & Rhoads, J. E. 2002, ApJL, **565**, L71.
- [Malhotra & Rhoads (2004)] Malhotra, S., & Rhoads, J. E. 2004, ApJL, **617**, L5.
- [Malkan et al. (1998)] Malkan, M. A., Gorjian, V., & Tam, R. 1998, ApJS, **117**, 25.
- [Markarian (1967)] Markarian, B. E. 1967, Astrofizika, **3**, 55.
- [Markarian (1969)] Markarian, B. E. 1969, Astrofizika, **5**, 443.
- [Markarian et al. (1971)] Markarian, B. E., Lipovetskij, V. A., & Lipovetsky, V. A. 1971, Astrofizika, **7**, 511.
- [Martin (2005)] Martin, C. L. 2005, ApJ, **621**, 227.
- [Martini et al. (2001)] Martini, P., Pogge, R. W., Ravindranath, S., & An, J. H. 2001, ApJ, **562**, 139.
- [Martini et al. (2003a)] Martini, P., Regan, M. W., Mulchaey, J. S., & Pogge, R. W. 2003a, ApJS, **146**, 353.
- [Martini et al. (2003b)] Martini, P., Regan, M. W., Mulchaey, J. S., & Pogge, R. W. 2003b, ApJ, **589**, 774.
- [Marziani et al. (1996)] Marziani, P., Sulentic, J. W., Dultzin-Hacyan, D., Calvani, M., & Moles, M. 1996, ApJS, **104**, 37.
- [Massey et al. (2010)] Massey, R., Stoughton, C., Leauthaud, A., et al. 2010, MNRAS, **401**, 371.
- [Mathur et al. (1995)] Mathur, S., Elvis, M., & Wilkes, B. 1995, ApJ, **452**, 230.
- [Mathur et al. (1999)] Mathur, S., Elvis, M., & Wilkes, B. 1999, ApJ, **519**, 605.
- [McCracken et al. (2010)] McCracken, H.J., Capak, P., Salvato, M., et al. 2010, ApJ, **708**, 202.

- [McCracken et al. (2012)] McCracken, H. J., Milvang-Jensen, B., Dunlop, J., et al. 2012, *A&A*, **544**, A156.
- [McLure & Dunlop (2002)] McLure, R. J., & Dunlop, J. S. 2002, *MNRAS*, **331**, 795.
- [Mihos (1999)] Mihos, C. 1999, *Ap&SS*, **266**, 195.
- [Mihos & Hernquist (1996)] Mihos, J. C., & Hernquist, L. 1996, *ApJ*, **464**, 641.
- [Miralda-Escudé (2003)] Miralda-Escudé, J. 2003, *Science*, **300**, 1904.
- [Miralda-Escudé (1996)] Miralda-Escudé, J., Cen, R., Ostriker, J. P., & Rauch, M. 1996, *ApJ*, **471**, 582.
- [Moe et al. (2009)] Moe, M., Arav, N., Bautista, M. A., & Korista, K. T. 2009, *ApJ*, **706**, 525.
- [Monier et al. (2001)] Monier, E. M., Mathur, S., Wilkes, B., & Elvis, M. 2001, *ApJ*, **559**, 675.
- [Morganti et al. (2007)] Morganti, R., Holt, J., Saripalli, L., Oosterloo, T. A., & Tadhunter, C. N. 2007, *A&A*, **476**, 735.
- [Morton (1991)] Morton, D. C. 1991, *ApJS*, **77**, 119.
- [Mouri & Taniguchi (2002)] Mouri, H., & Taniguchi, Y. 2002, *ApJ*, **565**, 786.
- [Murphy et al. (1996)] Murphy, T. W., Jr., Armus, L., Matthews, K., et al. 1996, *AJ*, **111**, 1025.
- [Murphy et al. (2001)] Murphy, T. W., Jr., Soifer, B. T., Matthews, K., Armus, L., & Kiger, J. R. 2001, *AJ*, **121**, 97.
- [Murray et al. (2005)] Murray, N., Quataert, E., & Thompson, T. A. 2005, *ApJ*, **618**, 569.
- [Naab et al. (2006)] Naab, T., Jesseit, R., & Burkert, A. 2006, *MNRAS*, **372**, 839.
- [Naoz et al. (2006)] Naoz, S., Noter, S., & Barkana, R. 2006, *MNRAS*, **373**, L98.
- [Nelson & Whittle (1995)] Nelson, C. H. & Whittle, M. 1995, *ApJS*, **99**, 67.

- [Netzer et al. (2007)] Netzer, H., et al. 2007, ApJ, **666**, 806.
- [Nilsson et al. (2007)] Nilsson, K. K., Orsi, A., Lacey, C. G., Baugh, C. M., & Thommes, E. 2007, A&A, **474**, 385.
- [Novak et al. (2012)] Novak, G. S., Ostriker, J. P., & Ciotti, L. 2012, MNRAS, **427**, 2734.
- [Oesch et al. (2010)] Oesch, P. A., et al. 2010, ApJL, **709**, L21.
- [Oesch et al. (2012)] Oesch, P. A., Bouwens, R. J., Illingworth, G. D., et al. 2012, ApJ, **759**, 135.
- [Oesch et al. (2013)] Oesch, P. A., Bouwens, R. J., Illingworth, G. D., et al. 2013, arXiv:1301.6162.
- [Oh (1999)] Oh, S. P. 1999, ApJ, **527**, 16.
- [Omukai & Nishi (1999)] Omukai, K., & Nishi, R. 1999, ApJ, **518**, 64.
- [Ono et al. (2011)] Ono, Y., Ouchi, M., Mobasher, B., et al. 2012, ApJ, **744**, 83.
- [Osterbrock (1960)] Osterbrock, D. E. 1960, ApJ, **132**, 325.
- [Osterbrock (1977)] Osterbrock, D. E. 1977, ApJ, **215**, 733.
- [Osterbrock (1978)] Osterbrock, D. E. 1978, Proceedings of the National Academy of Science, **75**, 540.
- [Osterbrock (1984)] Osterbrock, D. E. 1984, QJRAS, **25**, 1.
- [Osterbrock (1989)] Osterbrock, D. E., *Astrophysics of Gaseous Nebulae and Active Galactic Nuclei* (Mill Valley, CA: University Science Books, 1989).
- [Ostriker & Gnedin (1996)] Ostriker, J. P. & Gnedin, N. Y. 1996, ApJ, **472**, L63.
- [Ostriker & McKee (1988)] Ostriker, J. P. & McKee, C. F. 1988, Reviews of Modern Physics, **60**, 1.
- [Ota et al. (2008)] Ota, K., et al. 2008, ApJ, **677**, 12.
- [Ota et al. (2010)] Ota, K., et al. 2010, ApJ, **722**, 803.

- [Ouchi et al. (2001)] Ouchi, M., et al. 2001, ApJL, **558**, L83.
- [Ouchi et al. (2003)] Ouchi, M., et al. 2003, ApJ, **582**, 60.
- [Ouchi et al. (2005)] Ouchi, M., et al. 2005, ApJL, **635**, L117.
- [Ouchi et al. (2008)] Ouchi, M., et al. 2008, ApJS, **176**, 301.
- [Ouchi et al. (2010)] Ouchi, M., et al. 2010, ApJ, **723**, 869.
- [Padovani & Rafanelli (1988)] Padovani, P., & Rafanelli, P. 1988, A&A, **205**, 53.
- [Parkes et al. (1994)] Parkes, I. M., Collins, C. A., & Joseph, R. D. 1994, MNRAS, **266**, 983.
- [Partridge & Peebles (1967)] Partridge, R. B. & Peebles, P. J. E. 1967, ApJ, **147**, 868.
- [Pentericci et al. (2011)] Pentericci, L., Fontana, A., Vanzella, E., et al. 2011, ApJ, **743**, 132.
- [Petrosian et al. (2007)] Petrosian, A., McLean, B., Allen, R. J., & MacKenty, J. W. 2007, ApJS, **170**, 33.
- [Pogge & Martini (2002)] Pogge, R. W. & Martini, P. 2002, ApJ, **529**, 624.
- [Pritchett (1994)] Pritchett, C. J. 1994, PASP, **106**, 1052.
- [Rafanelli et al. (1995)] Rafanelli, P., Violato, M., & Baruffolo, A. 1995, AJ, **109**, 1546.
- [Rees (1966)] Rees, M. J. 1966, Nature, **211**, 468.
- [Rees (1986)] Rees, M. J. 1986, MNRAS, **218**, 25P.
- [Rees (1993)] Rees, M. J. 1993, QJRAS, **34**, 279.
- [Rhoads et al. (2003)] Rhoads, J. E., et al. 2003, AJ, **125**, 1006.
- [Rhoads et al. (2004)] Rhoads, J. E., et al. 2004, ApJ, **611**, 59.
- [Rhoads et al. (2012)] Rhoads, J. E., Hibon, P., Malhotra, S., Cooper, M., & Weiner, B. 2012, ApJL, **752**, L28.

- [Rhoads & Malhotra (2001)] Rhoads, J. E., & Malhotra, S. 2001, ApJL, **563**, L5.
- [Rhoads et al. (2000)] Rhoads, J. E., Malhotra, S., Dey, A., Stern, D., Spinrad, H., & Jannuzi, B. T. 2000, ApJL, **545**, L85.
- [Ricotti et al. (2002a)] Ricotti, M., Gnedin, N. Y., & Shull, J. M. 2002a, ApJ, **575**, 33.
- [Ricotti et al. (2002b)] Ricotti, M., Gnedin, N. Y., & Shull, J. M. 2002b, ApJ, **575**, 49.
- [Ricotti et al. (2008)] Ricotti, M., Gnedin, N. Y., & Shull, J. M. 2008, ApJ, **685**, 21.
- [Richard et al. (2007)] Richard, J., et al. 2007, ApJ, **662**, 781.
- [Richard et al. (2008)] Richard, J., Stark, D. P., Ellis, R. S., George, M. R., Egami, E., Kneib, J.-P., & Smith, G. P. 2008, ApJ, **685**, 705.
- [Rieke & Low (1972)] Rieke, G. H., & Low, F. J. 1972, ApJL, **176**, L95.
- [Riffel et al. (2008)] Riffel, R. A., Storchi-Bergmann, T., Winge, C., McGregor, P. J., Beck, T., & Schmitt, H. 2008, MNRAS, **385**, 1129.
- [Rodríguez-Ardila et al. (2006)] Rodríguez-Ardila, A. Prieto, M. A., Viegas, S., & Gruenwald, R. 2006, ApJ, **653**, 1098.
- [Rousselot et al. (2000)] Rousselot, P., Lidman, C., Cuby, J.-G., Moreels, G., & Monnet, G. 2000, A&A, **354**, 1134.
- [Rowan-Robinson & Efstathiou (1993)] Rowan-Robinson, M. & Efstathiou, A. 1993, MNRAS, **263**, 675.
- [Ruiz et al. (2001)] Ruiz, J. R., Crenshaw, D. M., Kraemer, S. B., Bower, G. A., Gull, T. R., Hutchings, J. B., Kaiser, M. E., & Weistrop, D. 2001, AJ, **122**, 2961.
- [Ruiz et al. (2005)] Ruiz, J. R., Crenshaw, D. M., Kraemer, S. B., Bower, G. A., Gull, T. R., Hutchings, J. B., Kaiser, M. E., & Weistrop, D. 2005, AJ, **129**, 73.
- [Rupke & Veilleux (2011)] Rupke, D. S. N., & Veilleux, S. 2011, ApJL, **729**, L27.

- [Rupke & Veilleux (2013)] Rupke, D. S. N., & Veilleux, S. 2013, ApJ, **768**, 75.
- [Rupke et al. (2008)] Rupke, D. S. N., Veilleux, S., & Baker, A. J. 2008, ApJ, **674**, 172.
- [Rupke et al. (2005a)] Rupke, D. S., Veilleux, S., & Sanders, D. B. 2005a, ApJS, **160**, 87 (RVS05a).
- [Rupke et al. (2005b)] Rupke, D. S., Veilleux, S., & Sanders, D. B. 2005b, ApJS, **160**, 115 (RVS05b).
- [Rupke et al. (2005c)] Rupke, D. S., Veilleux, S., & Sanders, D. B. 2005c, ApJ, **632**, 751 (RVS05c).
- [Ryan et al. (2005)] Ryan, R. E., Jr., Hathi, N. P., Cohen, S. H., & Windhorst, R. A. 2005, ApJL, **631**, L159.
- [Ryan-Weber et al. (2006)] Ryan-Weber, E. V., Pettini, M., & Madau, P. 2006, MNRAS, **371**, L78.
- [Saez et al. (2009)] Saez, C., Chartas, G., & Brandt, W. N. 2009, ApJ, **697**, 194.
- [Sandage (1960)] Sandage, A.R. 1961, Sky & Telescope, **21**, 148.
- [Sanders et al. (2003)] Sanders, D. B., Mazzarella, J. M., Kim, D.-C., Surace, J. A., & Soifer, B. T. 2003, AJ, **126**, 1607.
- [Sanders & Mirabel (1996)] Sanders, D. B., & Mirabel, I. F. 1996, ARA&A, **34**, 749.
- [Sanders et al. (1989)] Sanders, D. B., Phinney, E. S., Neugebauer, G., Soifer, B. T., & Matthews, K. 1989, ApJ, **347**, 29.
- [Sanders et al. (1988)] Sanders, D. B., Soifer, B. T., Elias, J. H., et al. 1988, ApJ, **325**, 74.
- [Santos (2004)] Santos, M. R. 2004, MNRAS, **349**, 1137.
- [Sato et al. (2009)] Sato, T., Martin, C. L., Noeske, K. G., Koo, D. C., & Lotz, J. M. 2009, ApJ, **696**, 214.
- [Scannapieco et al. (2005)] Scannapieco, E., Silk, J., & Bouwens, R. 2005, ApJL, **635**, L13.

- [Schaye (2001)] Schaye, J. 2001, ApJ, **559**, 507.
- [Schenker et al. (2012)] Schenker, M. A., Stark, D. P, Ellis, R. S., et al.. 2012, ApJ, **744**, 179.
- [Schiano (1985)] Schiano, A. V. R. 1985, ApJ, **299**, 24.
- [Schlesinger et al. (2009)] Schlesinger, K., Pogge, R. W., Martini, P., Shields, J. C., & Fields, D. 2009, ApJ, **699**, 857.
- [Schmidt (1963)] Schmidt, M. 1963, Nature, **197**, 1040.
- [Schmidt (1965)] Schmidt, M. 1965, *Quasi-Stellar Sources and Gravitational Collapse*, 455.
- [Schmidt & Green (1983)] Schmidt, M., & Green, R. F. 1983, ApJ, **269**, 352.
- [Schmidt (1964)] Schmidt, M., & Matthews, T. A. 1964, ApJ, **139**, 781.
- [Schwartz & Martin (2004)] Schwartz, C. M., & Martin, C. L. 2004, ApJ, **610**, 201.
- [Schweitzer et al. (2006)] Schweitzer, M., et al. 2006, ApJ, **649**, 79.
- [Scoville et al. (2000)] Scoville, N. Z., Evans, A. S., Thompson, R., et al. 2000, AJ, **119**, 991.
- [Serjeant & Hatziminaoglou (2009)] Serjeant, S., & Hatziminaoglou, E. 2009, MNRAS, **397**, 265.
- [Seyfert (1943)] Seyfert, C. K. 1943, ApJ, **97**, 28.
- [Shapley et al. (2003)] Shapley, A. E., Steidel, C. C., Pettini, M., & Adelberger, K. L. 2003, ApJ, **588**, 65.
- [Shibuya et al. (2012)] Shibuya, T., Kashikawa, N., Ota, K., et al. 2012, ApJ, **752**, 114.
- [Shimasaku et al. (2006)] Shimasaku, K., et al. 2006, PASJ, **58**, 313.
- [Shlosman et al. (1989)] Shlosman, I., Frank, J., & Begelman, M. C. 1989, Nature, **338**, 45.
- [Silk & Rees (1998)] Silk, J., & Rees, M. J. 1998, A&A, **331**, L1.

- [Simcoe et al. (2011)] Simcoe, R. A., Cooksey, K. L., Matejek, M., et al. 2011, ApJ, **743**, 21.
- [Simkin et al. (1980)] Simkin, S. M., Su., H. J., & Schwarz, M. P. 1980, ApJ, **237**, 404.
- [Sligh (1963)] Sligh, V. I. 1963, Nature, **199**, 682.
- [Smith et al. (2007)] Smith, B. J., Struck, C., Hancock, M., Appleton, P. N., Charmandaris, V., & Reach, W. T. 2007, AJ, **133**, 791.
- [Sobral et al. (2009)] Sobral, D., et al. 2009, MNRAS, **398**, L68.
- [Soifer et al. (1987)] Soifer, B. T., Neugebauer, G., & Houck, J. R. 1987, ARA&A, **25**, 187.
- [Soifer et al. (1984)] Soifer, B. T., Rowan-Robinson, M., Houck, J. R., et al. 1984, ApJL, **278**, L71.
- [Somerville & Primack (1999)] Somerville, R. S., & Primack, J. R. 1999, MNRAS, **310**, 1087.
- [Spitzer (1978)] Spitzer, L., *Physical Processes in the Interstellar Medium* (New York: Wiley-Interscience, 1978).
- [Spoon & Holt (2009)] Spoon, H. W. W., & Holt, J. 2009, ApJL, **702**, L42.
- [Springel et al. (2005)] Springel, V., Di Matteo, T., & Hernquist, L. 2005, MNRAS, **361**, 776.
- [Springel et al. (2005b)] Springel, V., White, S. D. M., Jenkins, A., et al. 2005b, Nature, **435**, 629.
- [Springob et al. (2005)] Springob, C. M., et al. 2005, ApJS, **160**, 149.
- [Stark et al. (2010)] Stark, D. P., Ellis, R. S., Chiu, K., Ouchi, M., & Bunker, A. 2010, MNRAS, **408**, 1628.
- [Stark et al. (2007)] Stark, D. P., Ellis, R. S., Richard, J., Kneib, J.-P., Smith, G. P., & Santos, M. R. 2007, ApJ, **663**, 10.
- [Steidel et al. (1999)] Steidel, C. C., Adelberger, K. L., Giavalisco, M., Dickinson, M., & Pettini, M. 1999, ApJ, **519**, 1.

- [Steigman et al. (1975)] Steigman, G., Strittmatter, P. A., & Williams, R. E. 1975, *ApJ*, **198**, 575.
- [Straughn et al. (2009)] Straughn, A. N., et al. 2009, *AJ*, **138**, 1022.
- [Strauss et al. (1992)] Strauss, M. A., Huchra, J. P., Davis, M., et al. 1992, *ApJS*, **83**, 29.
- [Struve et al. (2008)] Struve, C., Morganti, R., & Oosterloo, T. A. 2008, *MmSAI*, **79**, 1096.
- [Sturm et al. (2011)] Sturm, E., González-Alfonso, E., Veilleux, S., et al. 2011, *ApJL*, **733**, L16.
- [Swaters et al. (2011)] Swaters, R. A., Valdes, F., Dickinson, M. E. 2011, Guide to NEWFIRM Data Reduction, NOAO SDM, in preparation.
- [Szalay et al. (1999)] Szalay, A. S., Connolly, A. J., & Szokoly, G. P. 1999, *AJ*, **117**, 68.
- [Taniguchi et al. (2005)] Taniguchi, Y., et al. 2005, *PASJ*, **57**, 165.
- [Tegmark et al. (1997)] Tegmark, M., Silk, J., Rees, M. J., et al. 1997, *ApJ*, **474**, 1.
- [Teng & Veilleux (2010)] Teng, S. H., & Veilleux, S. 2010, *ApJ*, **725**, 1848.
- [Teng et al. (2009)] Teng, S. H., Veilleux, S., Anabuki, N., et al. 2009, *ApJ*, **691**, 261.
- [Teng et al. (2013)] Teng, S. H., Veilleux, S., & Baker, A. J. 2013, *ApJ*, **765**, 95.
- [Teng et al. (2005)] Teng, S. H., Wilson, A. S., Veilleux, S., et al. 2005, *ApJ*, **633**, 664.
- [Terrell (1964)] Terrell, J. 1964, *Science*, **145**, 918.
- [Thacker et al. (2006)] Thacker, R. J., Scannapieco, E., & Couchman, H. M. P., 2006, *ApJ*, **653**, 86.
- [Tilvi et al. (2010)] Tilvi, V., et al. 2010, *ApJ*, **721**, 1853.
- [Tilvi et al. (2009)] Tilvi, V., Malhotra, S., Rhoads, J. E., Scannapieco, E., Thacker, R. J., Iliev, I. T., & Mellema, G. 2009, *ApJ*, **704**, 724.

- [Tilvi et al. (2013)] Tilvi, V., Papovich, C., Tran, K.-V. H., et al. 2013, ApJ, **768**, 56.
- [Tinney et al. (2003)] Tinney, C. G., Burgasser, A. J., & Kirkpatrick, J. D. 2003, AJ, **126**, 975.
- [Toomre & Toomre (1972)] Toomre, A., & Toomre, J. 1972, ApJ, **178**, 623.
- [Tremonti et al. (2004)] Tremonti, C. A., et al. 2004, ApJ, **613**, 898.
- [Tremonti et al. (2007)] Tremonti, C. A., Moustakas, J., & Diamond-Stanic, A. M. 2007, ApJ, **663**, L77.
- [Trenti & Stiavelli (2008)] Trenti, M., & Stiavelli, M. 2008, ApJ, **676**, 767.
- [Treu et al. (2012)] Treu, T., Trenti, M., Stiavelli, M., Auger, M. W., & Bradley, L. D. 2012, ApJ, **747**, 27.
- [Tumlinson & Shull (2000)] Tumlinson, J. & Shull, J. M. 2000, ApJL, **528**, 65.
- [Urry & Padovani (1995)] Urry, C. M., & Padovani, P. 1995, PASP, **107**, 803.
- [van de Ven & Fathi (2010)] van de Ven, G., & Fathi, K. 2010, ApJ, **723**, 767.
- [Vanzella et al. (2011)] Vanzella, E., Pentericci, L., Fontana, A., et al. 2011, ApJL, **730**, L35.
- [de Vaucouleurs et al. (1995)] de Vaucouleurs, G., de Vaucouleurs, A., Corwin, H. G., Buta, R. J., Paturel, G., & Fouque, P. 1995, VizieR Online Data Catalog, **7155**, 0.
- [Vaughn & Uttley (2008)] Vaughan, S., & Uttley, P. 2008, MNRAS, **390**, 421.
- [Veilleux (1991a)] Veilleux, S. 1991a, ApJS, **75**, 357.
- [Veilleux (1991b)] Veilleux, S. 1991b, ApJS, **75**, 383.
- [Veilleux (1991c)] Veilleux, S. 1991c, ApJ, **369**, 331.
- [Veilleux et al. (2005)] Veilleux, S., Cecil, G., & Bland-Hawthorn, J. 2005, ARA&A, **43**, 769.

- [Veilleux et al. (2006)] Veilleux, S., Kim, D.-C., Peng, C. Y., et al. 2006, *ApJ*, **643**, 707.
- [Veilleux et al. (2009c)] Veilleux, S., Kim, D.-C., Rupke, D. S. N., et al. 2009c, *ApJ*, **701**, 587.
- [Veilleux et al. (1999a)] Veilleux, S., Kim, D.-C., & Sanders, D. B. 1999a, *ApJ*, **522**, 113.
- [Veilleux et al. (2002)] Veilleux, S., Kim, D.-C., & Sanders, D. B. 2002, *ApJS*, **143**, 315.
- [Veilleux et al. (1995)] Veilleux, S., Kim, D.-C., Sanders, D. B., Mazzarella, J. M., & Soifer, B. T. 1995, *ApJS*, **98**, 171.
- [Veilleux et al. (2013b)] Veilleux, S., Meléndez, M., Sturm, E., et al. 2013b, *ApJ*, submitted.
- [Veilleux et al. (2009a)] Veilleux, S., Rupke, D. S. N., Kim, D.-C., et al. 2009a, *ApJS*, **182**, 628.
- [Veilleux et al. (2009b)] Veilleux, S., Rupke, D. S. N., & Swaters, R. 2009b, *ApJL*, **700**, L149.
- [Veilleux et al. (1999b)] Veilleux, S., Sanders, D. B., & Kim, D.-C. 1999b, *ApJ*, **522**, 139.
- [Veilleux et al. (2013a)] Veilleux, S., Trippe, M., Hamann, F., et al. 2013a, *ApJ*, **764**, 15.
- [Véron-Cetty & Véron (2010)] Véron-Cetty, M.-P., & Véron, P. 2010, *A&A*, **518**, A10.
- [Villar-Martín et al. (2011)] Villar-Martín, M., Humphrey, A., Delgado, R. G., Colina, L., & Arribas, S. 2011, *MNRAS*, **418**, 2032.
- [Walker (1968)] Walker, M. F. 1968, *ApJ*, **151**, 71.
- [Wandel & Mushotzky (1986)] Wandel, A., & Mushotzky, R. F. 1986, *ApJL*, **306**, L61.
- [Wang et al. (2005)] Wang, J. X., Malhotra, S., & Rhoads, J. E. 2005, *ApJL*, **622**, L77.

- [Wang et al. (2009)] Wang, J.-X., Malhotra, S., Rhoads, J. E., Zhang, H.-T., & Finkelstein, S. L. 2009, *ApJ*, **706**, 762.
- [Weedman (1977)] Weedman, D. W. 1977, *ARA&A*, **15**, 69.
- [Wegner et al. (2003)] Wegner, G., et al. 2003, *AJ*, **126**, 2268.
- [Weiner et al. (2009)] Weiner, B. J., et al. 2009, *ApJ*, **692**, 187.
- [Werner et al. (2004)] Werner, M. W., Roellig, T. L., Low, F. J., et al. 2004, *ApJS*, **154**, 1.
- [Whittle (1992a)] Whittle, M. 1992a, *ApJS*, **79**, 49.
- [Williams (1963)] Williams, P. J. S. 1963, *Nature*, **200**, 56.
- [Willis et al. (2008)] Willis, J. P., Courbin, F., Kneib, J.-P., & Minniti, D. 2008, *MNRAS*, **384**, 1039.
- [Wilson & Ulvestad (1987)] Wilson, A. S., & Ulvestad, J. S. 1987, *ApJ*, **319**, 105.
- [Wisotzki (2000)] Wisotzki, L., Christlieb, N., Bade, N., et al. 2000, *A&A*, **358**, 77.
- [Wolf & Sheinis (2008)] Wolf, M. J., & Sheinis, A. I. 2008, *AJ*, **136**, 1587.
- [Woo & Urry (2002)] Woo, J.-H., & Urry, C. M. 2002, *ApJ*, **579**, 530.
- [Worrall (2005)] Worrall, D. M. 2005, *MmSAI*, **76**, 28.
- [Yoshida et al. (2007)] Yoshida, N., Omukai, K., & Hernquist, L. 2007, *ApJL*, **667**, L117.
- [Yoshida et al. (2008)] Yoshida, N., Omukai, K., & Hernquist, L. 2008, *Science*, **321**, 669.
- [Yoshida et al. (2006)] Yoshida, N., Omukai, K., Hernquist, L., & Abel, T. 2006, *ApJ*, **652**, 6.
- [Zensus (1997)] Zensus, J. A. 1997, *ARA&A*, **35**, 607.